Modifications of Stratospheric Dynamics and Circulation by Volcanic Eruptions

by

Joseph P. Hollowed

A dissertation submitted in partial fulfillment
of the requirements for the degree of
Doctor of Philosophy
(Physics)
at the University of Michigan
2025

Doctoral Committee:

       Professor Christiane Jablonowski, Co-Chair
       Professor Emanuel Gull, Co-Chair
       Professor Adriana Raudzens Bailey
       Professor Robert Deegan
       Professor Mark Flanner

Joseph P. Hollowed

hollowed@umich.edu

ORCID iD: 0000-0002-8658-1672

To my parents Dan and Judy, for their eternal and unconditional support.
And to my Grandmother Lynn, for her infinite curiosity of the natural world.

ACKNOWLEDGEMENTS

I am grateful to many collaborators, mentors, peers, friends and family members in supporting and encouraging me through the completion of this dissertation. These pages represent only the best of a long five and a half years of work. Five wonderful, awful, joyous, miserable, satisfying years of work. I encountered many crossroads throughout my graduate career where I could have gone another way. Had I taken some of those turns, maybe this dissertation would be better. Or perhaps worse, or perhaps written on the subject of cosmology, or perhaps never written at all. But at each of those crossroads, someone stood to guide the way. Surely there are many people deserving of thanks, and for every one that I mention in these acknowledgments, there is likely at least one more that I've left out. To anyone reading this, I likely owe you a thanks as well.

First, I give great thanks to my research advisor, Professor Christiane Jablonowski, who I was very fortunate to find during my second year at Michigan. Her ability to choose between offering careful guidance or trusting freedom, before I knew which I needed, was very beneficial to my growth as a student and scientist. She has been a kind, caring, and inspiring mentor since we met. I also give thanks to our collaborators at Sandia National Laboratories in Albuquerque, New Mexico, including Diana Bull, Tom Ehrmann, Benj Wagman, Hunter Brown, and Ben Hillman, among others. Diana in particular, always so thoughtful and encouraging, has been like my second "pro bono" advisor, even as she has plenty of bigger fish to fry. All of these Sandia scientists helped me in immeasurable ways, and are co-authors on the publication that resulted from Chapter 2 of this thesis (Hollowed et al., 2024), as well as publications of the remaining chapters, in preparation at the time of this writing. I also thank my research group members at Michigan for many useful discussions and collaborations, especially Owen Hughes, Garrett Limon, and Aaron Johnson.

To my friends and family, really no words could be written to express my fortune in having your support, friendship, and love. My parents Dan and Judy, and my siblings Jenny (plus John), Jim, Jake, Jaxson, and Josh mean everything in the world to me. There is no greater achievement in completing this dissertation than to make them proud. My sanity and happiness through graduate school depended fully on periodically driving home to Chicago, and getting to be a kid again for a weekend. I also thank my grandmother Lynn for being

iii

perhaps more interested than almost anyone in the details of my work, which she understood in her own beautiful way. I'm forever grateful for the astronomy newspaper and magazine clippings that she would share with me over Christmas, which quickly turned instead to climate-change articles as I refocused my research. To my friends from Ann Arbor, I'm grateful for so many memories which I will cherish as I move on in life. Tessa, Haley, Kevin, Mia, Sarah, Adam, Thomas, Matt, David, Kate, Nick, Lisa, Avik, Chami, Nick, Shreya, Bineet, Jem. Many of these friends have graduated and left town before me, and writing their names is bittersweet. I also thank my long-time friends from Chicago, Chris and Isaac, as our annual backpacking trips always gave me something great to look forward to through the hardest of times. And I would be remiss not to give a shoutout to Oslo, Marzie, and Miles. If you know, you know.

A very special thanks to my partner in life and very best friend, Christina. I met Christina on the red brick courtyard of the Kerrytown Market over a concentrated cold brew on a day that I'll never forget, during my first summer in Michigan. Two doctoral degrees later, and we have a wonderful little life with our dog Maple, recently settled in the foothills of the Rocky Mountains. I thank her for her unwavering support and love, through the best and worst of times. I truly don't know if I could have done it without her.

I'd also like to write some words of appreciation for all of the places that brought me such joy during graduate school. I was incredibly fortunate to find the time, the means, the mental bandwidth, and the company to visit these places while completing my studies. Many pages of my preliminary prospectus and my dissertation were written at these places, wherever I could find an outlet, not to mention many homework assignments completed and graded in early morning hours. The Mountain Guides and Yokum's general store at Seneca Rocks, WV, Miguel's Pizza in the Red River Gorge, KY, the Grand Teton Climber's Ranch, WY, the Manistee and Huron Rivers, MI, East Race Waterway in South Bend, IN, Norhouse Dunes, MI, the streets of Slazburg and Gosau, Austria, and the Sandia Mountains, NM. A thanks in particular to the New Mexico Mountain Club, especially Mark and Anna, who were warmly welcoming and taught me much during my stay in Albuquerque, NM while interning at Sandia National Labs. And finally, to the lovely city of Ann Arbor, Michigan; thank you for everything, and please never change.

TABLE OF CONTENTS

CHAPTER

LIST OF FIGURES

LIST OF TABLES

LIST OF APPENDICES

LIST OF ACRONYMS

AGCM atmospheric general circulation model

AoA age of air

AOD aerosol optical depth

AO actic oscillation

BDC Brewer-Dobson circulation

CESM Community Earth System Model

CF counterfactual

CIME Common Infrastructure for Modeling the Earth

CMIP Coupled Model Intercomparison Project

DOE Department of Energy

E3SM Energy Exascale Earth System Model

EAM E3SM Atmosphere Model

ENSO El-Niño-Southern Oscillation

EOF empirical orthogonal function

EP Eliassen-Palm

EPFD Eliassen-Palm flux divergence

ESM Earth System model

ETFD eddy tracer flux divergence

HOMME Higher Order Method Modeling Environment

HS Held-Suarez

HSW Held-Suarez-Williamson

HV high variability

LV low variability

LW longwave

NCAR National Center for Atmospheric Research

NERSC National Energy Research Scientific Computing Center

NH northern hemisphere

OGCM oceanic general circulation model

QBO quasi-biennial oscillation

RCTT residual circulation transit time

SAI stratospheric aerosol injection

SAO semi-annual oscillation

SE spectral element

SH southern hemisphere

SHLS southern hemisphere lower stratosphere

SNL Sandia National Laboratories

SW shortwave

SYPD simulated years per day

TEM Transformed Eulerian Mean

TOA top of atmosphere

WACCM Whole Atmosphere Community Climate Model

ABSTRACT

Tropical volcanic eruptions are capable of delivering enormous quantities for ash and sulfur dioxide (SO_2) to the stratosphere. Once there, SO_2 reacts with atmospheric water to form sulfate aerosols, which persist in the sky for years. Radiative forcing by these aerosols—scattering of sunlight, and absorption of outgoing thermal and near-infrared solar radiation—alters the atmospheric temperature profile. Observations have indicated that the global-average temperature increases in the stratosphere, and decreases at the surface by several degrees Celsius as a result. These changes in turn have far-reaching effects on the global circulation.

In this thesis, Exascale Energy Earth System Model (E3SM) from the U.S. Department of Energy's (DOE) is used to simulate the atmosphere in the years following the 1991 eruption of Mt. Pinatubo in the Philippines. The simulation outputs are then analyzed in order to understand the dynamical processes which govern not only changes in temperature, but also changes in winds and global mass transport that result. Two different types of simulations are used; an idealized atmosphere-only model which couples aerosol concentration directly to atmospheric temperature, and a more complex model which treats aerosol processes more fundamentally, and additionally simulates energy exchange between the atmosphere, ocean, and land.

In Chapter 2, the idealized model is described, which was developed as a part of the research of this thesis. Specifically, the model includes a stratospheric injection of volcanic SO_2 and ash. The ash fallout, conversion of SO_2 to sulfate aerosols, and radiative forcing by the aerosols are parameterized by a set of ordinary differential equations (ODEs). It is shown the model can be tuned to produce post-eruption temperature anomalies that mimic those of the historical Mt. Piantubo eruption.

Chapter 3 and 4 employ the more complex model and a transformed Eulerian mean (TEM) analysis framework in order to study the changes to zonal momentum, wave dynamics, and circulation which are caused by volcanic forcing of temperature. Using two different 15-member simulation ensembles, Chapter 3 describes statistically robust findings of accelerated polar vortex region winds near 8 m s^{-1} for 1 year following the eruption. The cause is identified as enhanced equatorward planetary wave deflection during winter, and an enhanced

meridional circulation during summer. Chapter 4 then investigates the consequences of these dynamical changes on the global transport of trace gases. It is found that age of stratospheric air (measure as time since last contact with the troposphere) decreases by up to 5 months everywhere but for the southern hemisphere's lower stratosphere, where it is increased by up to 3 months. This finding is attributed to an volcanically-induced meridional circulation which accelerates and decelerates the background circulation in the northern and southern hemisphere, respectively. The origin of this difference is shown to be related to both the latitude and the season of the Mt. Pinatubo eruption. It is also found that the strength of this effect on transport scales approximately linearly with the size of the eruption, within a tested range of 3–15 Tg of eruptive SO_2.

CHAPTER I

Introduction

8,200 miles northwest from the city of Ann Arbor, Michigan lies the Bataan Peninsula on the island of Luzon, Philippines. This hilly outcropping of land stands as a geologic guardian for the people of Luzon, forming a narrow mountain-flanked constriction which links the western sea and Manila Bay, the socio-economic gateway to the Filipino archipelago. Bataan is the southern terminus of the much broader Zambales Mountains, which separate the plains of central Luzon from the South China sea. Over it's 150-mile northerly length, the Zambales are adorned with small villages and cities, tropical forests, and a chain of volcanic peaks. Though the range is volcanic in origin, having formed in response to plate subduction along the Manila trench (Defant et al., 1989), all of the Zambales volcanoes are dormant, except for one; Mt. Piantubo.

Mt. Pinatubo is classed as an active *stratovolcano*, which are characterized by large explosive eruptions. Standing in an eerie contrast to this classification is the mountain's relatively low topographic prominence, which allows neighboring peaks to often obscure it from recognition among the people living in its vicinity. In the spring 1991, the nearby population numbered in the millions, including at least 30,000 inhabiting small villages on the sloping flanks of the volcano itself (Wolfe and Hoblitt, 1997). It was during that spring that locals began to feel the murmur of distant seismic activity, and eventually observed explosions of steam from the mountain on April 2, 1991 (Wolfe and Hoblitt, 1997). These events would turn out to be a heralding of a cataclysm which arrived on June 15, 1991—a pivotal moment in time for Luzon, and for the remainder of this thesis.

The main event was first preceded by minor eruptions and increasing earthquakes through the week of June 7–June 14. A photo of a preliminary eruption on June 12th is shown in Fig. 1.1 (top panel), which itself is large enough to evoke mythology. Much to the fortune of the region's people, scientists from the Philippine Institute of Volcanology and Seismology (PHIVOLCS) and the U.S. Geological Survey (USGS) were able to successfully forecast the volcanic events given observations that they had been taking since April, which ultimately enabled mass evacuations that saved countless lives (a story that was chronicled in a 1993

documentary (Hal Holbrook, 1993)). On the afternoon of July 15th, Mt. Pinatubo initiated an explosive eruption which lasted 9 hours, collapsing the summit of the mountain, and ejecting enormous quantities of volcanic material over the surrounding region and into the atmosphere. Among the ejected matter was an estimated 15-20 Tg of sulfur dioxide (SO_2), perhaps 200 Tg of carbon dioxide (CO_2), and an astounding 500 Tg or more of water vapor (Wolfe and Hoblitt, 1997). The amount of particulate matter like ash that escaped into the atmosphere was later estimated near 50 Tg (Guo et al., 2004b). For reference, one Tg (teragram) is approximately 2.2×10^9 pounds. The explosion was energetic enough to launch much of this material into the upper troposphere, where it's thermal energy continued to loft
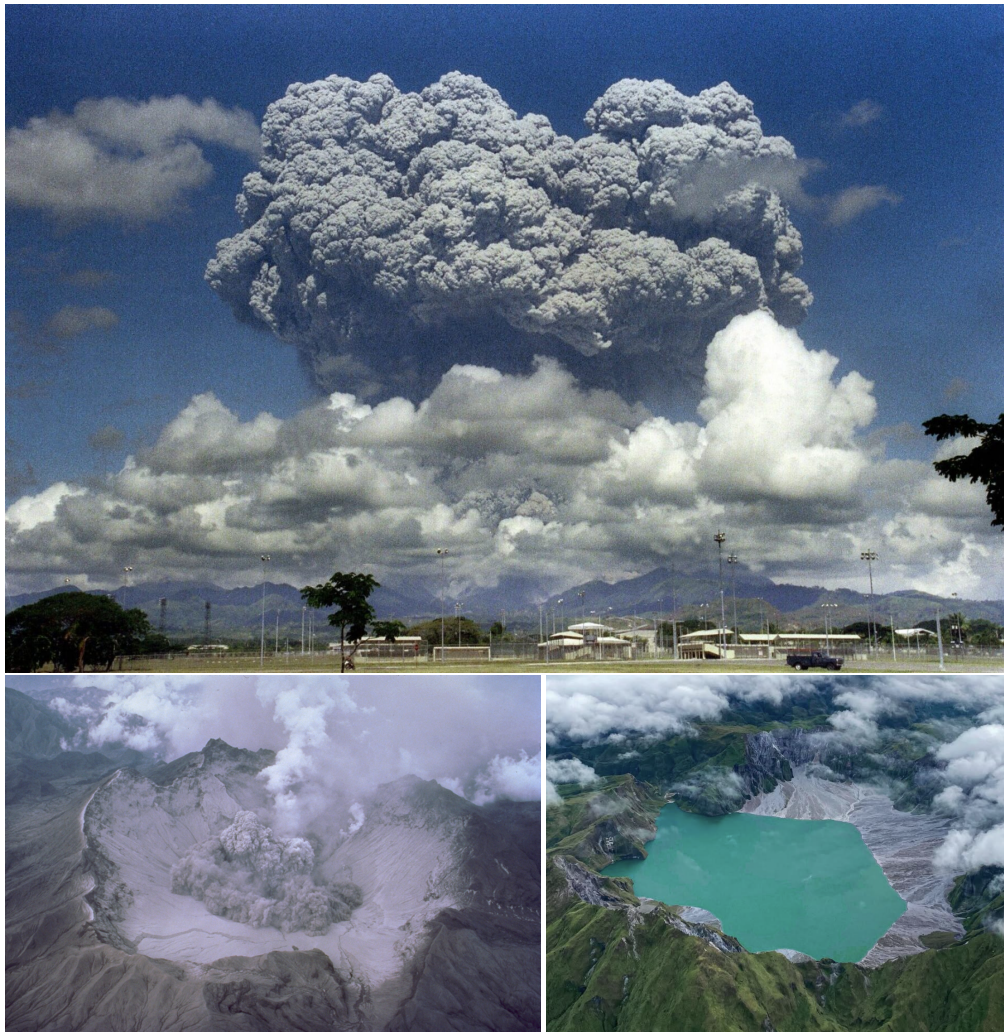
Figure 1.1: **(top)** Preliminary eruption of Mt. Pinatubo as seen from the former US Clark Air Base on June 12, 1991 (Naeg/AFP, 1991) **(bottom left)** Mt. Pinatubo caldera as seen on August 8, 1991 (Casadevall, 1991) **(bottom right)** the caldera as seen in November, 2023, now called Lake Pinatubo (Sierra, 2023).
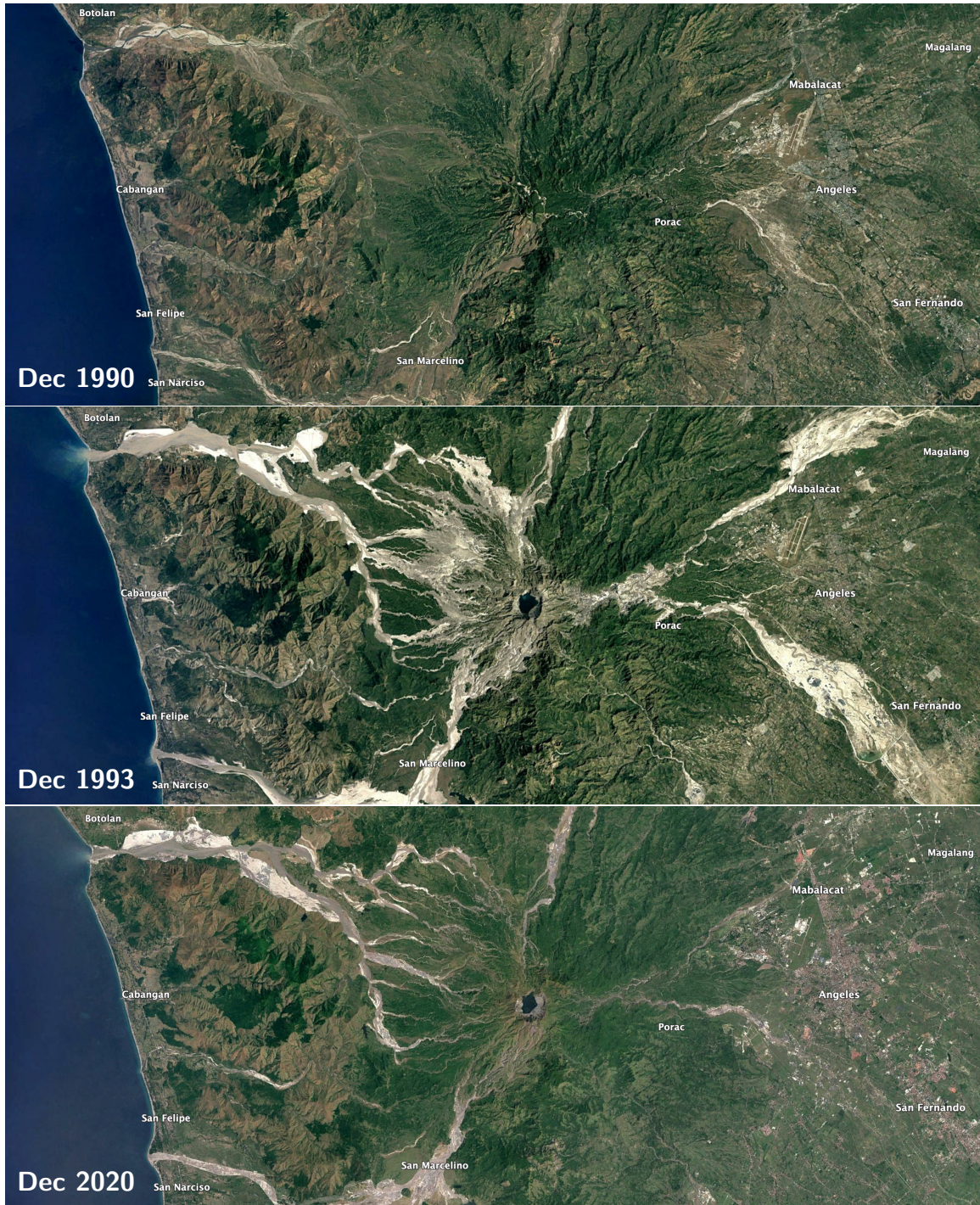
Figure 1.2: Satellite imagery of the Mt. Pinatubo region before and after the 1991 eruption. The Mt. Pinatubo caldera is the dark-colored lake in the image centers. Images from Landset/Copernicus, Google Earth

it further to 20 km, about 65,000 feet (Stenchikov et al., 2021). Once the data was collected, this eruption would prove to be the second-largest of the 20th century, and the largest in the era of modern meteorological observations.

On the ground, the aftermath of the Pinatubo eruption was completely transformative for the local topography, hydrology, and ecology. Pyroclastic flows filled valleys, while pumice and ash covered the surrounding plains. And, in an tragic happenstance of nature, the June 15th eruption coincided with the landfall of typhoon Yunya (Rudolph and Guard, 1995). The introduction of typhoon-level rainfall to the ash-filled environment lead to a proliferation of *lahars*; violet flows of debris in a slurry of water and pyroclastic material. These muddy flows filled river channels, inundated agricultural land, destroyed bridges, and buried smaller towns. Unfortunately, lahars continued to occur seasonally during monsoon rains in 1991 and 1992, which caused continued socio-economic distress (Wolfe and Hoblitt, 1997). The development and gradual recovery of the lahars is shown in Fig. 1.2 in satellite imagery from 1990, 1993, and 2020. Even 30 years later, the scars on the land are clearly visible from afar. All told, the death toll was at least 500 (McClelland, 1991), and tens of thousands more were displaced (Wolfe and Hoblitt, 1997).

In this introduction, a summary of the local destruction imparted by Pinatubo was necessary, out of respect and recognition for the Filipino people that endured the event. Especially because for the remainder of this thesis, the cataclysmic day of June 15, 1991 will be reduced to a set a mere few unimpassioned numbers: (15°N, 120°W), 15–20 Tg of material, 20 km high. This thesis is not about volcanism, but rather is about the climate; from a climatological perspective, explosive volcanic eruptions are, first and foremost, localized and transient inputs of energy to a much larger system. Still, as we will see over the following pages, Mt. Pinatubo has had a climatic legacy (and a scientific legacy) that spans many years, and reaches every corner of the globe.

1.1 Volcanoes and Climate

The main actors in the interaction between volcanoes and the climate are a type of particulate matter known as *volcanic aerosols*. An aerosol is any small particle or liquid droplet suspended in air. There exist a wide diversity of aerosol species traversing the atmosphere at any given time, and many processes of scientific interest that control aerosol genesis, growth, and dissipation. Accurate prediction of the Earth's climatic evolution necessarily involves thorough measurement, understanding and modeling of those aerosol processes (see McNeill (2017) for a recent review), of which volcanic aerosols are no exception.

The volcanic aerosols of most interest to our purposes would not have been ejected di-

rectly from the Pinatubo eruption, but rather would have arisen from a series of subsequent chemical transformations. The process is initiated by the enormous release of SO_2 from the volcano. Once in the free atmosphere, the primary removal process (known as a *sink*) is an oxidation chain mediated by atmospheric water (H_2O), with an end product of sulfuric acid (H_2SO_4). Sulfuric acid is more stable in the atmosphere than sulfur dioxide, and it's tendency is to condense with water vapor to form a material known as *sulfate aerosols*, or simply sulfates (Bekki, 1995). While the removal process of volcanic SO_2 (i.e. the reactions that give rise to the aerosol population) operates on an approximately 30-day timescale (Guo et al., 2004a), removal of sulfate takes much longer. The main sulfate sinks are wet and dry deposition in the troposphere (the lower atmosphere, where we live). However, because Pinatubo-sized eruptions deliver their aerosol-forming gases directly to the stratosphere (the upper atmosphere, where airplanes fly), the sulfate must first be physically transported toward the planet's surface via gravitational settling, and movement with the wind. In the case of the Pinatubo eruption, the result was a global reduction of atmospheric optical transmission for about 5 years, according to measurements taken at the Mauna Loa Observatory on the island of Hawai'i (Barnes and Hofmann, 1997).

Atmospheric aerosols and gases are typically classed as *passive* or *active*. A passive substance is one that is transported with the atmospheric circulation, and may be detectable, but does not participate in any exchange of energy with their environment. An active substance is one that does the opposite. *Chemically active* substances are those that participate in chemical interactions, providing opportunities for sources and sinks of other species, while *radiatively active* substances are those that emit, absorb, or reflect photons in a manner that perturbs the radiative energy balance of the atmosphere. The most famous example of an active substance to the reader may be CO_2, the main character of modern anthropogenic climate change.

The long persistence of volcanic sulfate aerosols in the atmosphere is important because it is a radiatively active material. It's primary pathways of interaction are (1) scattering of incoming solar radiation, and (2) absorption of both outgoing planetary longwave radiation, and near-infrared solar radiation. The net result is a warm anomaly local to the aerosol distribution in the stratosphere due to radiative heating by absorption, and a cool anomaly at the planet's surface due to the reduction of sunlight from the aerosol cloud above. The term *anomaly*, here, refers to an atmospheric state which somewhere differs from average climatological conditions. Following the Pinatubo eruption, observations have indicated an increase in global average stratospheric temperatures, and a decrease in global average surface temperatures of 2–3 degrees Celsius (Dutton and Christy, 1992; McCormick et al., 1995; Robock, 2000).

To the unfamiliar reader, it may not be obvious why a temperature perturbation of a few degrees is relevant to the climate as a whole, beyond the direct experience of the temperature anomaly itself by humans on the surface. But through theoretical and observational developments in climate science over the past century, a picture has emerged of an Earth system which is highly nonlinear, governed in unexpected ways by exchanges of energy over long time and length scales. Because radiative forcing by the Pinatubo aerosols was mostly confined to the tropics, an increased temperature gradient from equator-to-pole was established. We will see through the following chapters that this in turn stirs up anomalous winds in the midlatitudes, alters the character of the jetstream and polar vortex, and the global circulation of mass. It has even been suggested that the excitation of specific climate modes can follow, such as standing patterns of localized warming at the surface in the high northern latitudes, and perturbed global precipitation rates (Robock, 2000). Before we can understand these strange relationships in detail, a primer of basic atmospheric dynamics is on order.

1.2   Numerical Simulation of the Earth System

The core function of climate models is to solve a set of partial differential equations which describe the evolution of atmospheric fluid flow on the spherical Earth. The most common form implemented in modern models are the so-called *primitive equations of motion*. For the sake of simplicity and clarity, the equations as represented on a Cartesian tangential plane and a constant pressure surface in the vertical are

$$\frac{\mathrm{D}u}{\mathrm{D}t} = -\frac{\partial \Phi}{\partial x} + fv \tag{1.1}$$

$$\frac{\mathrm{D}v}{\mathrm{D}t} = -\frac{\partial \Phi}{\partial y} - fu \tag{1.2}$$

$$\frac{\partial \Phi}{\partial p} = -\frac{RT}{p} \tag{1.3}$$

$$\frac{\partial u}{\partial x} + \frac{\partial v}{\partial y} + \frac{\partial \omega}{\partial p} = 0 \tag{1.4}$$

$$\frac{\partial T}{\partial t} + u\frac{\partial T}{\partial x} + v\frac{\partial T}{\partial y} + \omega\left(\frac{\partial T}{\partial p} - \frac{RT}{pc_p}\right) = \frac{J}{c_p}, \tag{1.5}$$

where the *material derivative* operator is

$$\frac{\mathrm{D}}{\mathrm{D}t} \equiv \frac{\partial}{\partial t} + (\mathbf{v} \cdot \nabla) \tag{1.6}$$

6

for a velocity field $\mathbf{v} = (u, v)^T$. This formulation includes the important assumptions that the atmosphere is shallow (relative to the planetary radius) and hydrostatic (motion in the vertical is much smaller than in the horizontal). Eq. (1.1) and Eq. (1.2) are the inviscid *momentum equations*; a reduced form of the Navier–Stokes equations for the zonal wind speed u (along lines of longitude) and meridional wind speed v (along lines of latitude). The right-hand sides indicate that the evolution of the wind velocity is due to a pressure gradient force (horizontal gradients in the geopotential Φ) and a Coriolis force f. Eq. (1.3) encodes the hydrostatic and ideal gas approximations, which relate the geopotential, pressure p and temperature T with the ideal gas constant R. Eq. (1.4) represents the continuity of mass, which balances spatial changes in u, v, and the vertical pressure velocity ω. Finally, Eq. (1.5) is the thermal energy equation for the heat flow per unit time per unit mass J, where c_p is the isobaric specific heat of air.

This equation set is the basis for our predictions of future climate change, but also daily weather forecasts that we routinely access from our pockets. The component of a forecast model which numerically solves for the time evolution of the system on a spatial grid is known as the *dynamical core*. The specific design of a dynamical core, namely it's spatial discretization and timestepping schemes, has important consequences on energy and mass conservation, fluid shape preservation, and the overall accuracy of the forecast. A rich history of dynamical core design since the 1960's is chronicled in Williamson (2007) and Randall (2010). In practice, this Cartesian equation set shown above is adjusted in actual dynamical core implementations to include spherical geometry, mapped vertical coordinates like orography-following coordinates, dissipation processes, and potentially a removal of the hydrostatic assumption. An example of the full equation set used in the U.S. Department of Energy's (DOE) Energy Exscale Earth System Model (E3SM) is shown in Taylor et al. (2020).

However, the dynamical core alone is not capable of simulating the Earth's atmosphere. This is because once the equations of motion are discretized by the dynamical core, phenomena that are unresolved either in space or in time will not be represented. This includes small-scale wave activity, convection, and clouds. Further, the primitive equations govern only the fluid motion, and do not model external sources of energy that are input to the system. The most critical of these sources is radiation from the sun, which must be accounted for in order to establish realistic atmospheric circulations. Additional external sources include temperature perturbations caused by atmospheric chemicals and aerosols, and the emission of those substances. Among the plethora of chemical emissions and processes that are included in today's complex climate models, representations of volcanic eruptions are critical for capturing realistic long-term climate variability.

All of the mentioned unresolved and external processes are included in a climate model in the form of *parameterizations*; sets of differential equations which are used to force a climate model at the gridpoint level, which the modeler *tunes* by the adjustment of free parameters. These parameterizations are often derived from first-principles give the relevant physics, but are also often purely empirical tunings of designed formulae. A comprehensive review of common parameterizations and their design considerations is given by Mcfarlane (2011) and Hourdin et al. (2017). The reader will also get a glimpse into the science (or arguably, art) of parameterization design and tuning in Chapter 2.
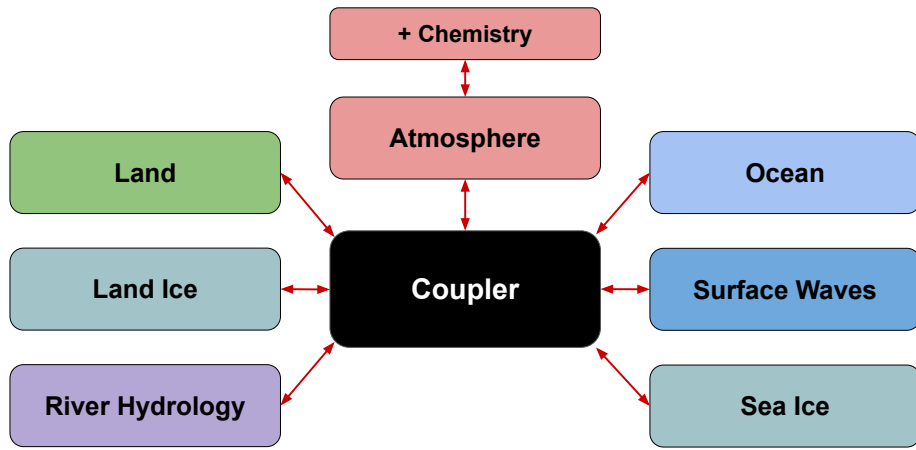
Figure 1.3: Schematic representation of a coupled Earth system model. Each colored box represents an independent model for the named physical component. The centered black box represents the model's coupler, collecting and exchanging information between each of the components.

The dynamical core fluid solver and the library of parameterizations that accompany it are often called *dynamics* and *physics*, respectively. Models that combine dynamics and physics into a single predictive framework are known as Atmospheric General Circulation Models (AGCM). The analog for simulation of the ocean is the OGCM. Flagship models currently run by major scientific and academic institutions couple AGCMs and OGCMs, allowing exchange of energy across the boundary at the surface of the ocean by way of a *coupler*. These models also couple the atmosphere to independent models for the continental land masses, land and sea ice, river hydrology, ocean surface waves, and usually add a library of chemistry calculations to the atmosphere component. The result is known as a "coupled" Earth System Model (ESM), shown schematically in Fig. 1.3. These complex machines are currently the state-of-the-art in climate modeling, and the basis for our modern understanding of climate change. It is within this simulated environment that this thesis

studies the interaction between volcanic aerosols and atmospheric dynamics.

1.3 The CLDERA Collaboration

The preceding introduction to the relationship between volcanism and the climate has lacked some important context. In the current age of anthropogenic climate change, the average global surface temperature of the Earth has risen by 1.1°C compared to the period 1850-1900, most of which has occurred in the last 75 years since 1950, making the modern era the warmest multi-century period in over 100,000 years (Calvin et al., 2023). Given this, interest in processes which are capable of lowering global surface temperatures are of more than purely scientific interest. There is no natural event capable of this feat in such a dramatic fashion as explosive tropical volcanic eruptions.

For this reason, there has been vigorous activity within the community over at least the last decade to study the theoretical implementation of artificial stratospheric aerosol injections (SAI). Indeed, the suggestion is to mimic the action of eruptions like the 1991 Pinatubo event by manually dispersing vast quantities of SO_2 into the stratosphere to enable sulfate aerosol formation, and thus global dimming (Crutzen, 2006). Activities of this kind are known as *geoengineering*.

Of course, SAI is an idea met with controversy, both within and outside of the scientific community. While some authors have argued that something akin to SAI will ultimately be required if we are to lower surface temperatures, others have emphasized that the outcome of such activities is not clear—an uncertainty that incurs even more risk, and distracts from the nevertheless necessary effort to reduce global greenhouse gas (GHG) emissions (e.g. Shepherd and Rayner (2009); American Meteorological Society (2013)). As such, SAI experiments have so far been conducted exclusively in simulated atmospheres. For example, Tilmes et al. (2018) recently introduced the Geoengineering Large Ensemble Project (GLENS), which included a 20-member ensemble of simulated SAI scenarios implemented in a coupled ESM. Various authors have subsequently used the GLENS or similar simulated datasets in attempts to diagnose the side-effects of SAI, beyond the intended surface cooling effect. Through these works, it is becoming clear that SAI may have at least some relation to almost every major mode of climate variability. This includes, but is not limited to, significant changes to precipitation in the tropics and midlatitudes (Simpson et al., 2019), stratospheric ozone and the global circulation of mass (Richter et al., 2017; Bednarz et al., 2023; Henry et al., 2024), the quasi-biennial oscillation of tropical winds (Richter et al., 2017), and the wave-driven coupling between the tropical and midlatitude stratosphere (Karami et al., 2023).

In light of this recent research, the decade-old warnings expressed by McCusker et al.

(2012) remain salient; "Countless other issues abound, both climatic and nonclimatic, including the ignorance of other consequences of increased carbon dioxide, such as ocean acidification. The likelihood of a climate surprise occurring due to geoengineering is high because research into geoengineering is still nascent, unintended consequences are a certainty, and the uncertainties of geoengineering are layered on top of those of global warming, compounding them."

With this understood, we finally note that the majority of work presented in this thesis was performed as a part of the CLDERA collaboration (CLimate impact: Determining Etiology thRough pAthways; Bull et al. (2025)) at Sandia National Laboratories (SNL). The goal of the CLDERA project was to develop statistical methods of attribution of an observed climate condition, and major sources of external forcing in the climate's past history. This is exactly the type of capability that the scientific community needs if we are to quantitatively relate observed conditions on Earth to climate change, or indeed to SAI and other geoengineering activities. To this end, the project oriented itself around the most well-observed and researched natural analogue of SAI; the 1991 eruption of Mt. Pinatubo. The primary role of Prof. Jablonowski and I was to develop methods and codes for investigating the dynamical processes which fundamentally control the atmosphere's response to the Pinatubo event.

1.4   Outline of this dissertation

The results of our efforts as members of the CLDERA project is presented over the following pages. Chapter 2 provides a detailed description of a custom parameterized model of volcanic aerosol injection that we developed for E3SM. This new configuration of the model was used to provide idealized representations of the Pinatubo event to other members of CLDERA, as an environment for attribution method development and testing. In Chapter 3, we use a more realistic version of the coupled E3SM in order to study the Pinatubo-driven effects on northern hemisphere stratospheric winds, with a detailed breakdown of the involved wave and circulation dynamics. Chapter 4 continues the analysis by investigating the changes to global distributions of trace gases. In short, our results will agree with the SAI literature that dynamical impact of Mt. Pinatubo on the climate are subtle yet far-reaching.

Each chapter is meant to mostly stand on its own, with self-contained introductions and conclusions. Appendices A–C accompany each chapter. Appendices D–F represent technical work that contributed to the main chapters, but have not been published elsewhere. They may also be useful as standalone information.

CHAPTER II

Volcanic Aerosol Injection in a Simple General Circulation Model

Abstract

A new set of standalone parameterizations is presented for simulating the injection, evolution, and radiative forcing by stratospheric volcanic aerosols against an idealized Held-Suarez-Williamson (HSW) atmospheric background in the Energy Exascale Earth System Model version 2 (E3SMv2). In this model configuration, HSW-V, sulfur dioxide (SO_2) and ash are injected into the atmosphere with a specified profile in the vertical, and proceed to follow a simple exponential decay. The SO_2 decay is modeled as a perfect conversion to a long-living sulfate aerosol which persists in the stratosphere. All three species are implemented as tracers in the model framework, and transported by the dynamical core's advection algorithm. The aerosols contribute simultaneously to a local heating of the stratosphere and cooling of the surface by a simple plane-parallel Beer-Lambert law applied on two zonally-symmetric radiation broadbands in the longwave and shortwave range. It is shown that the implementation parameters can be tuned to produce realistic temperature anomaly signatures of large volcanic events. In particular, results are shown for an ensemble of runs that mimic the volcanic eruption of Mt. Pinatubo in 1991. The design requires no coupling to microphysical subgrid-scale parameterizations, and thus approaches the computational affordability of prescribed-aerosol forcing strategies. The idealized simulations contain a single isolated volcanic event against a statistically uniform climate, where no background aerosols or other sources of externally-forced variability are present. HSW-V represents a simpler-to-understand tool for the development of climate source-to-impact attribution methods.

2.1 Introduction

Volcanic eruptions are one of the most dominant natural sources of exogenous forcing on the Earth system. In large volcanic events, the stratosphere can be loaded with extraordinary amounts of sulfur dioxide (SO_2), which gradually oxidize to form long-living sulfate aerosols (Bekki, 1995). In the case of tropical eruptions, the radiative properties of long-living aerosols subsequently lead to global stratospheric and surface-level temperature deviations up to a few degrees Kelvin from climatological averages, which can persist for years (Kremser et al., 2016; McCormick et al., 1995; Dutton and Christy, 1992). Variations in the stratospheric sulfate content by the Earth's volcanic history has thus been one of the strongest drivers of interannual climate variability (e.g. Schurer et al. (2013)).

Since volcanic eruptions impact the climate, there is a rich history of implementing volcanic forcing parameterizations for coupled Earth system models (ESMs) in the literature. Simpler techniques prescribe radiative aerosol properties directly from an external dataset or analytic forms (e.g., see DallaSanta et al. (2019); Toohey et al. (2016); Eyring et al. (2013); Gao et al. (2008); Kovilakam et al. (2020)). Prescribed forcing approaches might be chosen for their computational affordability, though they are also used to facilitate climate model intercomparisons by standardizing the forcing scheme (Zanchettin et al., 2016; Clyne et al., 2021). More complex approaches prescribe emissions of volcanic SO_2, which are then handed to separate aerosol, chemistry, and advection codes. These codes then explicitly model the aerosol evolution, transport, and radiative properties (e.g., Mills et al. (2016, 2017); Brown et al. (2024)). Reviews of the wide array of modeling choices for volcanic forcings made by different ESMs are presented in Timmreck (2012) and Marshall et al. (2022).

Prescribed and prognostic methods have also been applied to model other forms of sulfur-based radiative forcing, with significant research recently being devoted to stratospheric aerosol injection (SAI) climate-change intervention activities (Crutzen, 2006; Tilmes et al., 2018, 2017; McCusker et al., 2012). One key goal of SAI research is to quantify the causal connections between an observed climate impact, and an upstream forcing source, i.e. to attribute the SAI source as the cause of a detected, anomalous atmospheric response. Volcanoes are a natural analog to SAI, and thus offer an avenue for developing novel attribution methods of quantifying these causal connections.

The climate impacts that are most societally-relevant tend to be spatially localized (e.g. droughts, heat waves, or fires) and located downstream from their associated sources (e.g. volcanoes, or other solar radiation modification) by multiple causal connections. "Multi-step attribution" involves a sequence of single-step attribution analyses, but is generally not employed, as the single weakest attribution step limits its confidence (Hegerl et al.,

2010). Therefore, there is a need for novel multi-step attribution techniques in both climate change studies (Burger et al., 2020) and climate intervention studies (National Academies of Sciences, 2021; Office of Science and Technology Policy (OSTP), 2023) that overcome these issues to enable attribution of societally-relevant impacts.

As the climate community increasingly relies on advanced statistical inference and machine learning approaches to attribute downstream impacts, it is critical to develop testbeds which can be widely shared and used to understand the accuracy of the methods' inferences. Although the development of verification datasets for advanced data analytic techniques in the climate community is nascent, there are a few examples. Fulton and Hegerl (2021) generated synthetic climate modes to test the accuracy of distinct pattern extraction techniques and show that the most commonly used principal component analysis technique does not perform well. Mamalakis et al. (2022) worked to develop an "attribution benchmark dataset" for which the ground truth is known to enable evaluation of different explainable artificial intelligence (AI) methods.

Currently, developing data analytic methods for multi-step attribution in the context of volcanic forcing is restricted to models that utilize expensive prognostic aerosol treatments. This is because with prescribed forcing approaches in free-running atmospheric simulations, there is a dynamical inconsistency between the transport patterns and aerosol distributions. In particular, the forcing dataset does not respond to the atmospheric state. Accordingly, we suggest that a new idealized representation of prognostic volcanic forcing within a highly simplified atmospheric environment would be a useful testbed for the development of novel multi-step attribution methods (i.e. constructing relationships between stratospheric aerosol forcing and atmospheric temperature perturbations).

Here we outline a simulation strategy which enables an affordable prognostic aerosol implementation for idealized climate model configurations. Our design seeks to maintain a realistic spatio-temporal signature of the atmospheric impacts, while minimizing the terms contributing to temperature and wind tendencies as much as possible. The former is achieved by including a localized injection and subsequent transport of aerosols by a tracer advection scheme. The latter is achieved by coupling the aerosol concentrations directly to the temperature field. While traditional approaches often require the inclusion of an auxiliary radiative transfer code for this second step, our implementation is standalone.

Our approach sacrifices realism by design. The goal is not to simulate an accurate post-eruption climate of a particular historical volcanic event, but rather to produce a plausible realization of a generic volcanic eruption, simulated with a minimal forcing set. This configuration will not offer a deterministic answer to the attribution problem, as the internal variability of the simulated atmosphere implies that there is no single solution to the spatio-

temporal evolution of the affordable prognostic aerosol. Nevertheless, it does represent key process characteristics between a source and downstream impact, and can provide large datasets without the typical computational burden of climate simulations, thereby supporting the development and testing of novel data analyses and attribution techniques.

Our model isolates a single volcanic event from any other external source of forcing or variability, and allows the flexibility to be embedded in a simplified atmospheric environment. Though the implementation is generic, we present here a particular tuning of the parameterizations for an eruption similar in character to the 1991 eruption of Mt. Pinatubo, and the subsequently observed impacts (Karpechko et al., 2010; Robock, 2000; McCormick et al., 1995; Hansen et al., 1992). The atmosphere model is an idealized so-called Held-Suarez-Williamson (HSW; Williamson et al. (1998)) configuration of the Energy Exascale Earth System Model version 2 (E3SMv2; Golaz et al. (2022)). The HSW configuration on a flat earth replaces E3SMv2's physical parameterization package with a temperature relaxation towards a prescribed, hemispherically-symmetric equilibrium temperature and Rayleigh friction near the surface. These two forcing mechanisms mimic radiative effects and the boundary-layer turbulence, respectively. There are no background aerosols, no moisture, and no long-term climate trends. The implementation of the injection, aerosol dissipation, and forcing can be tuned to yield sensible atmospheric impacts for almost any model configuration with qualitatively realistic circulation patterns, even in absence of a standard physical parameterization suite. We call this extension to the HSW model with enabled volcanism HSW-V.

The chapter is structured as follows. The simplified climate model configuration of E3SMv2 is described in Sect. 2.2. Section 2.3 introduces the idealized volcanic injection, sulfate formation, and radiative forcing parameterizations. This is followed by a discussion of the ensemble design, simulation results, and the computational expense in Sect. 2.4. Section 2.5 summarizes the findings and provides an outlook on their utility for the modeling community. Appendix A.1 describes custom modifications that were needed for our chosen simplified climate implementation with E3SMv2. In addition, Appendix A.3 provides recommendations for the tuning of the suggested aerosol parameterizations.

2.2 Climate Model Configuration

When choosing the base model configuration, the goal was to provide an environment in which the volcanic forcing can be nearly isolated. In addition, we aimed at keeping the number of physical subgrid-scale forcing mechanisms small. These simplifications are achieved by running a climate model in an atmosphere-only mode, and replacing the standard suite of

physical parameterizations with simple forcing functions for the temperature and horizontal winds.

Section 2.2.1 introduces the E3SMv2 climate model which serves as the foundation for our developments. E3SMv2's chosen HSW configuration is a modified implementation of the idealized scheme originally described by Held and Suarez (1994) (hereafter HS94), involving a damping of low-level winds and a relaxation of the temperature field to a specified zonally-symmetric reference profile, described in Sect. 2.2.2. The main difference between the HS94 and HSW forcing is the presence of a more realistic relaxation temperature profile above 100 hPa which generates stratospheric polar jets in the HSW variant. Section 2.2.3 describes a simple extension for idealized physics packages which provides global, zonally-symmetric longwave and shortwave radiation profiles.

2.2.1 The E3SMv2 climate model

E3SMv2 is a state-of-the-art climate model that consists of various coupled components for the atmosphere, ocean, land, sea ice, and land ice (Golaz et al., 2022). The dynamical core of the E3SM Atmosphere Model version 2 (EAMv2) uses a spectral-element (SE) solver on a quasi-uniform cubed-sphere grid for a shallow, hydrostatic atmosphere (Taylor et al., 2020), and a semi-Lagrangian tracer transport scheme (Bradley et al., 2022) which ensures local mass conservation and shape preservation. Specifically, the experiments presented here use the $\sim 2°$ "ne16pg2" grid, where each cubed-sphere element features a 2x2 grid of physics columns. The grid for the physical parameterizations is thus coarser than the associated dynamics grid (Hannah et al., 2021; Herrington et al., 2019). The vertical grid consists of 72 vertical levels with a model top near 0.1 hPa, or approximately 60 km.

We use a highly simplified, dry configuration of EAMv2 with no topography, no moisture, and no coupling to other components. The physical parameterization suite is replaced by a set of idealized forcing functions described in Section 2.2.2. Internally, this configuration is labeled as the "FIDEAL" component set— an inheritance of E3SMv2 from its original fork of the Community Earth System Model (CESM, Danabasoglu et al. (2020)). As a part of our work, the FIDEAL component set needed to be revived, and is not functional in the official release of E3SMv2.

We note that the ne16pg2 grid is coarser than the default E3SMv2 $\sim 1°$ "ne30pg2" grid. We have not tested activating our implementation on such a higher-resolution grid, which will require a re-tuning the model parameters. Recommendations for performing the tuning of the volcanic forcing are given in Appendix A.3.

2.2.2 Idealized climate forcing

The HS94 forcing was originally proposed as a benchmark for the intercomparison of statistically steady-states produced by the dry dynamical cores of Atmospheric General Circulation Models (AGCMs) without topography. The forcing includes the Rayleigh damping of low-level winds to represent friction in the boundary layer and a Newtonian temperature relaxation toward an analytic "radiative equilibrium" temperature $T_{eq}(\phi, p)$ given by

$$\frac{\partial T}{\partial t} = \ldots - k_T(\phi, p) \left[T - T_{eq}(\phi, p) \right]. \tag{2.1}$$

Here, T is the temperature, t stands for the time, ϕ represents the latitude, p symbolizes the pressure, and $k_T(\phi, p)$ is the relaxation rate. T_{eq} has no time dependence and therefore does not include any diurnal or seasonal cycles. The temperature variability on any timescale is purely driven by the internal dynamics arising from nudging towards the equilibrium. The form of the equilibrium temperature is designed to mimic the net effects of radiation, convection, and other subgrid-scale processes. Williamson et al. (1998) (hereafter W98) later noted that since the HS94 benchmark deliberately maintains a "passive" stratosphere, supporting none of the typical stratospheric structures such as the polar jets, it would not be applicable to their dynamical core intercomparison studies of tropopause formation. To remedy this deficiency, they provide a modification of the original HS94 equilibrium temperature, which includes realistic lower-stratospheric lapse rates in the tropics and polar regions. Such a HSW configuration was, e.g., also used in Yao and Jablonowski (2016) who explored Sudden Stratospheric Warmings (SSWs) in the idealized environment.

We use the HSW forcing in our simulations, and omit all other physical parameterizations. This setup provides an atmosphere that is characterized by realistic dynamical motions and a quasi-realistic idealized climatology while maintaining a highly simplified inventory of diabatic subgrid forcings. In implementing HSW in E3SMv2, a few notable modifications were made. First, the lapse rate of the equilibrium temperature T_{eq} was set to zero above 2 hPa to maintain realistic upper-stratospheric temperatures. Next, in addition to the HS94 treatment of surface friction, we include a second Rayleigh damping mechanism near the model top as a "sponge layer" for calming the polar jet winds and absorbing spurious wave reflections, as described in Jablonowski and Williamson (2011). Specifics of these HSW modifications are provided in Appendix A.1.

Figure 2.1 shows the equilibrium temperature in the latitude-pressure plane, the vertical profile of the wind damping strength, and the resulting 10-year average zonal-mean temperature and zonal wind fields following a five-year spinup period using these idealized forcings in E3SMv2. The resulting stratospheric temperature and wind structures are quasi-realistic,

16
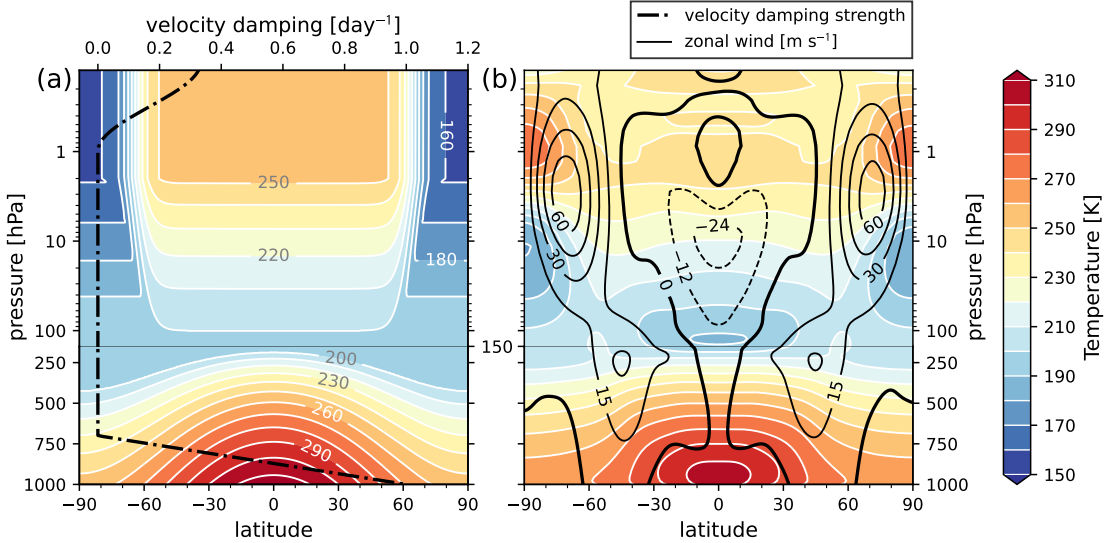
Figure 2.1: **(a)** The modified HSW equilibrium temperature in the latitude-pressure plane. Contours are drawn every 10 K. Overlaid as a thick dashed black line is the vertical profile of the velocity damping coefficient for both the sponge layer and the surface, with its values on the top horizontal axis (see Appendix A.1 for details). **(b)** 10-year average zonal-mean temperature and zonal wind distributions in an E3SMv2 run with temperature relaxation toward the reference temperature of panel (a), after a five-year spinup period. Temperature contours are drawn every 10 K, while positive (negative) wind contours every 15 m s^{-1} (12 m s^{-1}). Negative contours are dashed, and the zero-line is shown in bold. For all variables shown, the vertical (pressure) axis is logarithmic above 150 hPa, and linear below 150 hPa. The separation between these two domains given as gray horizontal lines.

reaching maximum tropical temperatures of about 240 K at the 50-60 km height levels which correspond to the region between 1-0.1 hPa. However, these temperatures are slightly cooler than the observed values near 50 km (1 hPa) which are about 260 K, as documented in Fleming et al. (1990). Temperature minima are seen near the tropical tropopause, as well as the polar middle-stratosphere. Sharp vertical temperature gradients are seen near the polar upper-stratosphere, leading to temperatures in excess of 270 K.

In the zonal wind, we see the formation of tropospheric mid-latitude westerly jets with maximum wind speeds of ~30 m s^{-1}, and strong stratospheric polar jets in excess of 60 m s^{-1}. As there are no seasonal variations present, each hemisphere eternally varies about this winter-like steady state, which is qualitatively representative of observations (Fleming et al., 1990). At the same time, the global circulation, and thus mass transport, is characterized by symmetric thermally-direct circulations (Hadley cells) in the troposphere, and symmetric residual streamfunction cells in the stratosphere, consistent with equinox states in nature (see discussion in Sect. 2.4.2 and Appendix A.2).

In the tropical stratosphere, easterlies with speeds up to -30 m s^{-1} dominate. Note that while the tropical stratospheric winds will vary about this average, the HSW atmosphere does not include any kind of regular quasi-biennial oscillation (QBO) analog. Yao and Jablonowski (2016) showed that whether or not a QBO spontaneously develops in an HSW configuration will largely depend on the dynamical core in use. For a spectral element (SE) dynamical core, they observed that wave forcing was never strong enough to cause a reversal of the tropical stratospheric winds. The same conclusion appears to hold for our configuration of E3SMv2. Despite this, the QBO may be a desirable target for future studies employing this model configuration, as it has been shown that the QBO phase is a significant modulator of the volcanic climate response (Thomas et al., 2009). We do not consider this issue further in the present work, but note that it could be possible to prescribe a QBO by nudging the horizontal winds toward a specified reference state (as has been done for e.g. the Whole Atmosphere Community Climate Model (WACCM) by Matthes et al. (2010)).

2.2.3 Extending the HSW model with simple radiation

The HSW atmosphere does not describe any radiative processes, except by the extent to which they are mimicked in the temperature relaxation toward T_{eq}. Energy balance at the top of the atmosphere (TOA) is implied, though there are no specifications of incoming or outgoing radiative fluxes.

However, in computing the diabatic heating and cooling terms of stratospheric aerosols in Sect. 2.3, it will be both convenient and natural to have expressions for the flux densities of incoming shortwave (SW) and outgoing longwave (LW) broadbands, which are qualitatively consistent with the HSW equilibrium temperature field. We first define a global, zonally-symmetric longwave flux density based on T_{eq} at the surface, and then deduce a shortwave component by setting the total integrated global power equal to that of the longwave component. Both flux density profiles will be constant in time.

In both the HS94 and HSW models, the radiative equilibrium temperature below 100 hPa is

$$T_{\text{eq}}(\phi, p) = \max \left[(200 \text{ K}), \left[(315 \text{ K}) - (60 \text{ K}) \sin^2 \phi - (10 \text{ K}) \log \left(\frac{p}{p_0} \right) \cos^2 \phi \right] \left(\frac{p}{p_0} \right)^{R_d/c_p} \right], \tag{2.2}$$

where $R_d/c_p = 2/7$ is the ratio of the ideal gas constant and specific heat at constant pressure for dry air. At the reference pressure $p_0 = 1000$ hPa, the equation reduces to

$$T_{\text{eq}}(\phi, p_0) = 315 \text{ K} - (60 \text{ K}) \sin^2 \phi. \tag{2.3}$$

We compute a longwave graybody flux density I_{LW} from the Stefan-Boltzman law as

$$I_{LW} = \sigma T_{surf}^4 = \sigma \left[315 \text{ K} - (60 \text{ K}) \sin^2 \phi \right]^4 \tag{2.4}$$

where σ is the Stefan-Boltzman constant. If desired, T_{surf} can be the actual surface temperature on the 2D surface mesh. We instead choose a simplified approach that is both analytic and static in time, by approximating the surface temperature as Eq. (2.3). For incident shortwave radiation, we use a simple cosine form which vanishes at the poles, resembling equinox conditions, given by

$$I_{SW} = I_0 \cos \phi. \tag{2.5}$$

By integrating Eq. (2.4) and Eq. (2.5) over the sphere, we find that a normalization parameter of $I_0 \approx 560 \text{ W m}^{-2}$ enforces that the total globally-integrated power is in balance between I_{LW} and I_{SW}. We note that these radiative fluxes are considerably higher than the annual average solar insolation of the real Earth system. The primary reason for the enhanced values is that there is no attenuation of the upwelling longwave radiation by moisture, clouds, or other background constituents (excluding volcanic aerosols) in the HSW atmosphere. Including such an effect in the HSW configuration would be arbitrary and overly-complicated. Further, we will show in Sect. 2.3 that the aerosol radiative forcing design has sufficient freedom in the number of tunable parameters to achieve desired heating rates, without being preferential about the amplitudes of I_{SW} and I_{LW}.
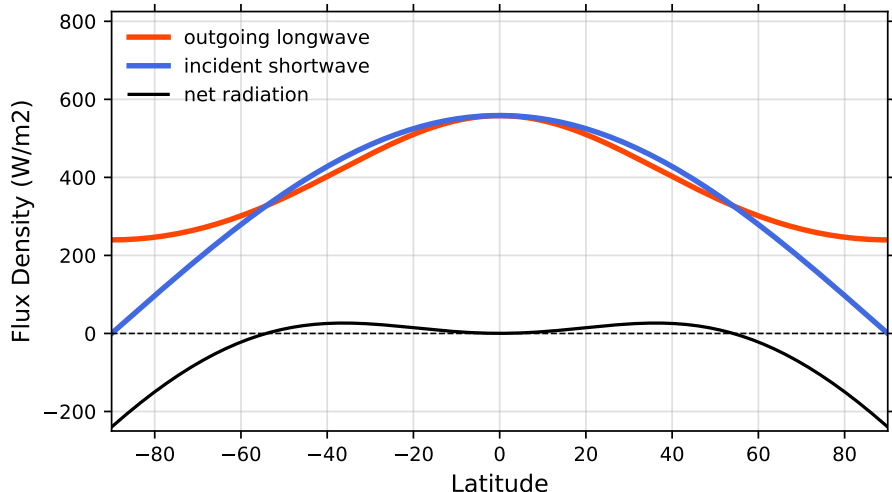
Figure 2.2: Longwave (Eq. (2.4)), shortwave (Eq. (2.5)), and net flux densities as functions of latitude.

The resulting flux profiles are shown in Fig. 2.2. This figure shows an energy deficit poleward of 55°, and a surplus equatorward, with maxima in the net flux in the midlatitudes. We emphasize that the shape of the flux profiles is the important aspect here, and that balancing I_{LW} and I_{SW} is only being done for style and physical legibility. This "radiation" will be used *only* to control the heating and cooling rates imposed by injected aerosols, which will ultimately be subject to model tuning, and will have no effect on mean atmospheric temperatures. The overall climate and energy balance is still controlled independently by the HSW temperature relaxation.

2.3   The HSW-V Volcanic Forcing Approach

We model radiative forcing by stratospheric aerosol injection events in the idealized HSW environment by directly forcing the temperature field via a standalone parameterization. This forcing is done without the need for intermediary aerosol or radiation models. While this approach could be generalized for any local injections of sulfur species to the atmosphere, the implementation used here is designed and tuned to produce a realistic representation of the 1991 eruption of Mt. Pinatubo. Specifically, our model describes the localized simultaneous injection of volcanic ash and sulfur dioxide (SO_2) with a specified vertical profile over a single model column. Decay of the SO_2 in turn leads to production of long-lived sulfate aerosols. These chemical species are implemented as "tracers" within EAMv2 (scalar mixing ratio quantities advected by the model's transport scheme), and contribute independently to local and surface temperature tendencies.

The strategy is to add together various ingredients as follows: (1) define volcanic sources (stratospheric injection), (2) define SO_2 sinks (sulfate aerosol production), (3) compute the aerosol optical depth (AOD) of each model column, and (4) increment the temperature tendency (local radiative heating by absorption, and radiative surface cooling by AOD). Steps (1)-(4) are described in Sect. 2.3.1-2.3.4, respectively. Section 2.3.5 provides a brief summary of the model, a table of the model parameters, and notes on the parameter tuning strategy.

2.3.1   Tracer injection

We model the time tendency of each injected tracer species j (SO_2 and ash) as the sum of a source and sink:

$$\frac{\partial m_j}{\partial t} = R(m_j) + f. \tag{2.6}$$

20

$R(m_j)$ is an exponential removal function with e-folding timescale $1/k_j$, and the source term f describes the spatial distribution of injection:

$$R(m_j) = -k_j m_j, \tag{2.7}$$

$$f = \widetilde{A}_j T(t) H(\phi, \lambda) V(z). \tag{2.8}$$

The separable temporal, vertical, and horizontal dependencies are $T(t)$, $V(z)$, and $H(\phi, \lambda)$, respectively, where z is the geometric height and λ symbolizes the longitude. $\widetilde{A}_j$ is a normalization parameter. This form is then discretized onto the model grid with horizontal column, vertical level, and timestep indices i, k, and n, respectively. We choose to model an injection uniformly distributed over a single column and time period of length δt. Explicitly, the "injection region" S is symbolized as

$$S = \{(\phi_i, \lambda_i, t_n) \mid \phi_i = \phi_{i'}, \ \lambda_i = \lambda_{i'}, \ t_0 \leq t_n \leq t_0 + \delta t\}, \tag{2.9}$$

where i' is the index of the injection column. The product of $T(t_n)$ and $H(\phi_i, \lambda_i)$ in Eq. (2.8) is then replaced by an indicator function $I_{i,n} \equiv I(t_n, \phi_i, \lambda_i)$, which is equal to one inside of S, and equal to zero outside of S. The mass tendency is then

$$\frac{\partial m_{j,i,k}}{\partial t} = -k_j m_{j,i,k} + I_{i,n} A_j V(z_k). \tag{2.10}$$

The source f for tracer j is normalized by the constant A_j, which scales the *total* injected mass to a known parameter M_j, by

$$M_j = A_j \delta t \sum_k V(z_k) \tag{2.11}$$

$$\implies A_j = \frac{M_j}{\delta t \sum_k V_k}, \tag{2.12}$$

where we define $V_k \equiv V(z_k)$. The normalization constant A_j is unique to the vertical grid configuration, and converges to the normalization of the analytic form $A_j \to \widetilde{A}_j$ with increasing resolution. This treatment avoids losing mass to numerical diffusion once the injected mass is placed onto the model grid.

Rather than a mass tendency, the quantity required by EAMv2's physics interface is the tendency of the tracer mixing ratio $q_j \equiv m_j/m_{\text{atm}}$. If $\Delta p_{i,k}$ is the local pressure thickness of the grid cell, g is acceleration due to gravity, and a_i is the column area, the air mass m_{atm}

in this definition can be replaced via the hydrostatic equation, yielding

$$q_{j,i,k} = m_{j,i,k} \, \frac{g}{\Delta p_{i,k} \, a_i} \,. \tag{2.13}$$

Given Eq. (2.10)-(2.13), the final expression implemented for the update of tracer j at column i, vertical level k, and timestep n is

$$\frac{\partial q_{j,i,k,n}}{\partial t} = \frac{g}{\Delta p_{i,k} \, a_i} \left[-k_j \, m_{j,i,k} + I_{i,n} \, \frac{M_j}{\delta t \, \sum_k V_k} V_k \right] \,. \tag{2.14}$$

For the vertical dependence $V(z)$, we follow Fisher et al. (2019) and assume a Gaussian distribution defined by a center of mass altitude μ, and a geometrical standard deviation

$$V(z) = \exp\left(-\frac{1}{2} \frac{(z-\mu)^2}{(1.5 \text{ km})^2} \right). \tag{2.15}$$

The profile deviation of 1.5 km is a compromise between Fisher et al. (2019) and the width of the parabolic injection profile of Stenchikov et al. (2021). In hydrostatic models such as E3SMv2, the height z is a diagnostic quantity. Therefore, the vertical profile needs to be computed at each timestep. We inject both SO_2 and ash at the same height and with the same deviation, and we do not include a normalization coefficient in $V(z)$, since A_j is already scaled by $\sum_k V_k$.

We tuned the center of mass altitude μ by ensuring that the sulfate tracer which eventually arises from the initial SO_2 injection settles in the lower stratosphere, between 20 and 25 km, consistent with estimates from aerosol transport models (Sheng et al., 2015) and forcing reconstructions (see review in Sect. 2 of Toohey et al. (2016)). As in previous works, we might expect to inject just above the tropical tropopause, near $\mu = 17\text{-}18$ km (Stenchikov et al., 2021; Fisher et al., 2019), and then allow the self-lofting process to carry the plume to a level of neutral buoyancy in the lower stratosphere. Per Stenchikov et al. (2021), this process is expected to be driven by a vertical velocity of $w \approx 1$ km day^{-1} due to strong initial radiative heating rates of about 20 K day^{-1} in the dense, fresh volcanic plume. After tuning the model with these considerations in mind, we use the even lower value of $\mu = 14$ km, which we found to result in a realistic settling altitude for the sulfate tracer distribution. The need for this exceptionally low injection height is due to an overly aggressive heating of the initial plume given our parameter choices, which is discussed further in Section 2.3.5 and Appendix A.3.4.

Observations giving the total injected mass and e-folding time for SO_2 (25 days) and ash (1 day) for the Mt. Pinatubo eruption were estimated from satellite data and published

in Guo et al. (2004a,b) and Barnes and Hofmann (1997). Table 2.1 provides the chosen parameter values. In particular, the model describes a 24-hour injection of a plume centered on 14 km in the vertical, uniformly over a single column. We assume no background values for any of the injected species prior to the eruption, as in some other studies (e.g. Bekki and Pyle (1994)).

The remainder of the model formulation as presented in Sect. 2.3.2-2.3.4 is applied uniformly on each timestep, and thus the temporal index n will be omitted for brevity. Optical depths and radiative forcings are computed identically for each tracer species, and so the tracer index j will be also be omitted. Mixtures of multiple tracers j with varying radiative extinction coefficients will be reintroduced in Sect. 2.3.4.3.

Table 2.1: Model parameters. Parameters with a superscript † are tuned parameters. Parameters with a superscript ‡ are constrained by a data-driven calculation, though not necessarily free for tuning. Parameters without a superscript are observations and/or estimates directly from the literature. For information on tuning, see Sect. 2.3.5 and Appendix A.3.

Parameter	Value	Units	Description	Reference
injection				
ϕ_0	15.15	deg	meridional plume center	
λ_0	120.35	deg	zonal plume center	
δt	24	hr	injection duration	
μ	14	km	peak injection altitude	Stenchikov et al. (2021)
tracers				
k_{SO2}	1/25	day^{-1}	SO$_2$ decay rate	Guo et al. (2004a)
$k_{sulfate}$	1/360	day^{-1}	sulfate decay rate	Barnes and Hofmann (1997)
k_{ash}	1	day^{-1}	ash decay rate	Guo et al. (2004b)
M_{SO2}	17	Tg	injected mass of SO2	Guo et al. (2004a)
M_{ash}	50	Tg	injected mass of ash	Guo et al. (2004b)
$\nu^{\ddagger}$	2.04	-	SO$_2 \rightarrow$ sulfate weighting	See Sect. 2.3.2
heating				
$\zeta^{\dagger}$	4×10^{-3}	-	surf. heat transfer efficiency	See Sect. 2.3.4
$\widetilde{\delta z}^{\dagger}$	100	m	max height of surf. cooling	See Sect. 2.3.4
$b_{SW}, ash^{\ddagger}$	400	m^2 kg^{-1}	SW mass extinction coeff.	See Sect. 2.3.3
$b_{SW}, SO_2^{\ddagger}$	400	m^2 kg^{-1}	SW mass extinction coeff.	See Sect. 2.3.3
$b_{SW}, sulfate^{\ddagger}$	1900	m^2 kg^{-1}	SW mass extinction coeff.	See Sect. 2.3.3
$b_{LW}, ash^{\dagger}$	1×10^{-5}	m^2 kg^{-1}	LW mass extinction coeff.	See Sect. 2.3.3
$b_{LW}, SO_2^{\dagger}$	0.01	m^2 kg^{-1}	LW mass extinction coeff.	See Sect. 2.3.3
$b_{LW}, sulfate^{\dagger}$	29	m^2 kg^{-1}	LW mass extinction coeff.	See Sect. 2.3.3

2.3.2 Sulfate formation

Once injected into the atmosphere, SO_2 follows an oxidation chain with an end product of sulfuric acid (H_2SO_4) that condenses with water vapor to form sulfate aerosol particles (Bekki, 1995). Stratospheric sulfate aerosols have an e-folding removal timescale of one year (Barnes and Hofmann, 1997), and are responsible for much of the heating that perturbs the Earth's energy balance and atmospheric circulation after a stratospheric volcanic eruption (McCormick et al., 1995; Robock, 2002).

In fully coupled climate models, aerosol heating will be mediated by chemistry, radiation, and moist subgrid processes. Here, the same heating is rather modeled by a direct, analytic coupling of SO_2 to sulfate, in a way inspired by the so-called "toy chemistry" of Lauritzen et al. (2015), also seen in Toohey et al. (2016). Sulfate will evolve by Eq. (2.6), where the source term f exactly becomes the SO_2 sink $R(m_{SO2})$. The SO_2 removal rate k_{SO2} is then interpreted purely as a reaction rate, and the sulfate tendency mass is

$$\frac{\partial m_{\mathrm{sulf}}}{\partial t} = -k_{\mathrm{sulf}}\, m_{\mathrm{sulf}} + \nu\, k_{SO2}\, m_{SO2} \tag{2.16}$$

or, in terms of mixing ratio on the computational grid,

$$\frac{\partial q_{\mathrm{sulf},i,k}}{\partial t} = -k_{\mathrm{sulf}}\, q_{\mathrm{sulf},i,k} + \nu\, k_{SO2}\, q_{SO2,i,k} \; . \tag{2.17}$$

Here, the reaction weight ν encodes the net production of sulfate per unit mass of SO_2. While ν could be a tuning parameter of the model, we can inform a first choice from chemistry. Since the overall effect of the oxidation sequence yields one aerosol "particle" of sulfate per molecule of SO_2 (Bekki, 1995), ν will just be the ratio of the sulfate to SO_2 molar mass. Though it is known from observation that sulfate particles vary in their composition across latitude, altitude, and season (Yue et al., 1994), depending on specific humidity and temperature, we make the simplifying assumption that all sulfate particles are 75% H_2SO_4 by mass. The same assumption is made in Bekki (1995) and suggested by observation (Rosen, 1971; Yue et al., 1994). Defining this percentage as $f_{\mathrm{acid}} = 0.75$, and the molar masses of H_2SO_4 and SO_2 as $M(H_2SO_4)$ and $M(SO_2)$, the reaction weighting is

$$\nu = \frac{M(H_2SO_4)/f_{\mathrm{acid}}}{M(SO_2)} \approx \frac{1/0.75 \times 98.079 \text{ g/mol}}{64.066 \text{ g/mol}} = 2.04 \; . \tag{2.18}$$

This choice of ν results in a peak sulfate mass of about ~ 28 Mt occurring approximately two months after injection, which is consistent with previous modeling efforts by e.g. Bluth et al. (1997). In that study, however, the authors note that if we assume sulfate production

24

to arise directly from SO_2 depletion, then the inferred sulfate loading does not coincide with observed 0.55 μm AOD anomalies after Pinatubo. Citing the AOD database of (Sato et al., 1993), Bluth et al. (1997) show this peak AOD anomaly to occur nearer to nine months than two months.

For this reason, Toohey et al. (2016) (who also modeled the $SO_2 \rightarrow$ sulfate conversion directly), decided to address this lag in AOD anomaly by artificially inflating the SO_2 dissipation parameter to $k_{SO2} = 1/180$ day^{-1}. This change is said to represent the *net* timescale of all processes resulting in increased global mean AOD, beyond just the oxidation chain producing H_2SO_4, which may not be fully captured in this idealized description. In this way, they delay the peak sulfate loading, and thus peak 0.55 μm AOD anomaly, from two months to six months post-injection. This figure is more consistent with the Pinatubo AOD anomaly time series constructed by the Chemistry-Climate Model Initiative (CCMI; Eyring et al. (2013)).

Rather than following these findings of Bluth et al. (1997) and Toohey et al. (2016), we decide instead to retain the observed value of $k_{SO2} = 1/25$ day^{-1}. This choice causes the peak AOD anomaly to occur simultaneously with the sulfate loading near month two, which is consistent with 0.55 μm AOD results of the prognostic aerosol implementation of Brown et al. (2024), as well as observations of 0.6 μm AOD from the Advanced Very High Resolution Radiometer (AVHRR; Zhao et al. (2013); Heidinger et al. (2014)). We verified that the difference in peak sulfate mass between our model and Toohey et al. (2016) is explained fully by the choice of k_{SO2}, and not the reaction normalization ν.

2.3.3 Aerosol optical depth

A single aerosol species can contribute to extinction of transmitted radiation by absorption and scattering, the combined effect of which is expressed by a spatially-varying extinction coefficient $\beta_e(x, y, z)$. Within a single model column, we will make the parallel plane approximation, i.e. $\beta_e(x, y, z) \approx \beta_e(z)$. This coefficient can further be expanded as

$$\beta_e = b_e \, \rho = b_e \, q \, \rho_{atm}, \tag{2.19}$$

where b_e is the *mass extinction coefficient* of the aerosol species, with dimensions of area per unit mass, ρ is the tracer mass density, and q is the mixing ratio. Consistent with Sect. 2.2.3, the extinction properties of each tracer species j will be modeled with respect to two broadbands: b_{LW} will be used for the extinction of longwave (LW) radiation, which is assumed to be entirely absorption, and b_{SW} will be used for the extinction of shortwave

(SW) radiation, which is assumed to be entirely scattering:

$$b_{\mathrm{LW}} \equiv (b_e \text{ for the longwave band}),$$

$$b_{\mathrm{SW}} \equiv (b_e \text{ for the shortwave band}).$$

For a column with a model top at z_{top}, the dimensionless SW AOD τ at a height z is obtained by vertically integrating the shortwave extinction:

$$\tau(z) = \int_z^{z_{\mathrm{top}}} \beta_e(z')\, dz' = \int_z^{z_{\mathrm{top}}} b_{\mathrm{SW}}\, q(z')\, \rho_{atm}(z')\, dz' \tag{2.20}$$

On the model grid, this extinction becomes

$$\tau_{i,k} = \sum_{k'<k} b_{\mathrm{SW}}\, q_{i,k'}\, \rho_{\mathrm{atm},i,k'}\, \Delta z_{i,k'} \tag{2.21}$$

$$= \sum_{k'<k} b_{\mathrm{SW}}\, \frac{q_{i,k'}\, \Delta p_{i,k'}}{g}. \tag{2.22}$$

where the pressure thickness Δp symbolizes the pressure difference between two neighboring model interface levels that surround the full model level with index k'.

We assume that the indices k and k' decrease toward the model top (as in E3SMv2). We also define a shorthand for the cumulative SW AOD at the surface as $\tau_i \equiv \tau(z=0)$. After summing over k for this case, we have the usual result (Petty, 2006) that each remaining term is just the total column mass burden M_i of the tracer, scaled by the mass extinction coefficient b_{SW} and column area a_i,

$$\tau_i = \sum_k b_{\mathrm{SW}} \frac{q_{i,k}\Delta p_{i,k}}{g} = \sum_k b_{\mathrm{SW}} \frac{q_{i,k} m_{atm,i,k}}{a_i} = b_{\mathrm{SW}} \frac{M_i}{a_i}. \tag{2.23}$$

Hereafter, "AOD" will refer specifically to the column-integrated SW AOD defined in Eq. (2.23).

2.3.4   Radiative forcing

Injected stratospheric aerosols force the Earth system in two primary ways which are (1) local heating of the stratosphere and (2) remote cooling of the surface. The presence of SO_2 and sulfate aerosols in the stratosphere induces a local diabatic heating to the temperature field by absorption of upward-propagating longwave radiation (Kinne et al., 1992; Brown et al., 2024) and incoming near-IR solar radiation (Stenchikov et al., 1998). After the 1991 Mt. Pinatubo eruption, this process resulted in a positive temperature anomaly of up to

$\sim$2–4 K peaking near 50–30 hPa (Rieger et al., 2020; Stenchikov et al., 1998; Labitzke and McCormick, 1992), driven by a maximum net temperature change at a rate of $\sim$1 K month^{-1} during the initial period following the injection.

At the same time, increased aerosol optical depths of the vertical column decrease the flux density of shortwave solar radiation reaching the troposphere. This upper-level scattering of solar radiation contributed to an observed surface cooling of ~ -0.5 K during the two years following the eruption of Mt. Pinatubo (Dutton and Christy, 1992; Self et al., 1997; Fyfe et al., 2013).

We model each of these heating effects by adding new forcing terms to the temperature field of the HSW atmosphere. Heating is applied in the stratospheric aerosol plume, and the lowest few model levels are cooled, via the computation of the energy change that results from the attenuation of the flux densities I_{LW} and I_{SW}.

2.3.4.1 Local heating of the stratosphere

The local warming effect is modeled as an attenuation of upwelling longwave radiation with flux density I_{LW} defined in Eq. (2.4), computed for each model column via the plane-parallel Beer-Lambert law. For simplicity, here we neglect the heating contribution from the absorption of near-infrared solar radiation, which we decided was an unnecessary degree of realism for this simple model. This omission will be compensated for by tuning the LW absorption process to the observed heating rates. To begin, the attenuated flux density after transmission through a particular slab with vertical bounds $[z_0, z_1]$ is an integral of the extinction β_e such as

$$I(z_0, z_1) = I_{\mathrm{LW}} \exp\left(-\int_{z_0}^{z_1} \beta_e(z')\, dz'\right). \tag{2.24}$$

Here we assume that z_0 is the lowest extent of the aerosol plume, and there has been no attenuation between $z = 0$ and $z = z_0$. In this case, the power per unit area absorbed by the slab is

$$\Delta I = I_{\mathrm{LW}} - I(z_0, z_1). \tag{2.25}$$

If we consider another slab located immediately above z_1, on $[z_1, z_2]$, then the incident flux is no longer I_{LW}, but rather $I(z_0, z_1)$, and the power per unit area absorbed is

$$\Delta I = I(z_0, z_1) - I(z_1, z_2)$$

$$= I_{\text{LW}} \exp\left(-\int_{z_0}^{z_1} \beta_e(z')dz'\right) \left[1 - \exp\left(-\int_{z_1}^{z_2} \beta_e(z')dz'\right)\right]. \qquad (2.26)$$

This form generalizes to an arbitrary slab on $[z_n,\, z_{n+1}]$ as

$$\Delta I = I(z_{n-1}, z_n) - I(z_n, z_{n+1})$$

$$= I_{\text{LW}} \exp\left(-\int_{z_0}^{z_n} \beta_e(z')dz'\right) \left[1 - \exp\left(-\int_{z_n}^{z_{(n+1)}} \beta_e(z')dz'\right)\right]. \qquad (2.27)$$

Discretizing these integrals onto the vertical grid with levels k and column i yields

$$\Delta I_{i,k} = I_{\text{LW}} \exp\left(-\sum_{k'>k} b_{\text{LW}} \frac{q_{i,k'}\Delta p_{i,k'}}{g}\right) \left[1 - \exp\left(-b_{\text{LW}} \frac{q_{i,k}\Delta p_{i,k}}{g}\right)\right], \qquad (2.28)$$

where the argument to the leftmost exponent sums over all levels k' which are below level k. The effect here is that aerosols lower in the vertical column "shadow" those above, decreasing the power of incident radiation available for absorption. In this way, the peak of the local aerosol heating may lie below the actual density peak of the plume.

The absorbed power per unit area is then translated to a heating rate per unit mass s, and finally to an associated temperature tendency ΔT, with the assumption that all of the absorbed radiation is perfectly converted to heat. If the flux densities are given in units of W m^{-2}, then by dimensional analysis

$$s_{i,k} = \frac{a_i \Delta I_{i,k}}{m_{i,k}} \frac{\text{J}}{\text{kg s}} \qquad (2.29)$$

$$\implies \Delta T_{i,k} = \frac{1}{c_p} \frac{a_i \Delta I_{i,k}}{m_{i,k}} \frac{\text{K}}{\text{s}}. \qquad (2.30)$$

This temperature tendency is always positive, and will be imposed on the grid cell at $(i,\, k)$ for each tracer at each timestep.

We note that while it has been shown that absorption of solar near-infrared radiation also contributes significantly to the aerosol-induced heating in the stratosphere (Stenchikov et al., 1998; Robock, 2000)

2.3.4.2   Cooling of the surface

The surface cooling is modeled as an AOD attenuation of incident radiation with flux density I_{SW}, as defined in Eq. (2.5). We begin with an analogous form to Eq. (2.24), where the vertical slab on $[z_0, z_1]$ is replaced with the entire vertical column above position z, on $[z, z_{\text{top}}]$. The integral term in brackets is then exactly the AOD as given in Eq. (2.20). The

attenuation is thus

$$I(z) = I_{\text{SW}} \exp\left(-\int_z^{z_{\text{top}}} \beta_e(z')dz'\right) = I_{\text{SW}}\, e^{-\tau(z)}. \tag{2.31}$$

With the notation used in Eq. (2.23), the deficit flux density after attenuation by the aerosol over the full height of the atmosphere on a single model column i is

$$\Delta I_i = I_{\text{SW}}\left(e^{-\tau_i} - 1\right). \tag{2.32}$$

That is, a deficit energy density of ΔI_i W m^{-2} is imposed at the surface. For a model column at the equator with $\tau = 0.2$, this form gives $\Delta I \approx -100$ W m^{-2}, which is roughly consistent with the observed broadband solar transmission deficits of $\sim 20\%$ at Mauna Loa, Hawaii in the months following Pinatubo (Self et al. (1997); see their Fig. 9). By AODs of $\tau \approx 4$, the shortwave attenuation saturates (all available incident radiation has scattered).

The attenuation is next translated to a cooling rate per unit mass s, and an associated temperature tendency ΔT. Since the HSW atmosphere simulates no land-atmosphere coupling processes, we employ a very simple representation of the conduction and convection that would, in reality, be responsible for communicating an energy deficit at the ground to the atmospheric surface layer. We imagine that all of the energy lost over the column heats the planetary surface, which in turn transfers heat to the atmosphere by a function F with some efficiency ζ:

$$s_{i,k} = \zeta F(\Delta I_i). \tag{2.33}$$

The heat transfer "efficiency" ζ should be considered a catch-all for any surface-atmosphere coupling effects which we do not model, and is treated as a tuning parameter for the magnitude of atmospheric surface cooling (see Sect. 2.3.5). As in the local heating treatment of the previous section, the function F can be obtained by dimensional analysis:

$$s_{i,k} = \zeta \frac{a_i \Delta I_i}{\widetilde{m}_i}\; \frac{\text{J}}{\text{kg s}} \tag{2.34}$$

$$\implies \Delta T_{i,k} = \zeta \frac{1}{c_p} \frac{a_i \Delta I_i}{\widetilde{m}_i}\; \frac{\text{K}}{\text{s}}, \tag{2.35}$$

where $\widetilde{m}_i$ is the mass of air in the lowest κ model levels of column i over which the cooling is to be applied. If we apply the cooling only to the lowest model level with $\kappa = K$, then

$$\widetilde{m}_i = m_{i,K} \tag{2.36}$$

29

and otherwise

$$\widetilde{m}_i = \sum_{k=K}^{K-(\kappa-1)} m_{i,k}.$$ (2.37)

In this way, the net cooling (total energy loss over unit time) is conserved as the parameter κ is increased, and the cooling per unit mass is "diluted". The choice of κ will effectively encode whatever missing physical mechanisms would otherwise communicate the cooling higher into the vertical column. For $\kappa > 1$, $\Delta T_{i,k}$ is a 3D quantity, while ΔI_i and τ_i are always 2D quantities. In Table 2.1, rather than setting κ directly we set $\widetilde{\delta z}$, or the height above the surface in meters where the cooling should be applied, from which κ is inferred, given the vertical discretizaiton.

2.3.4.3 Generalization to mixtures of tracer species

When multiple tracer species j are present (SO_2, ash, sulfate), the total radiative heating is not derived from a simple sum of the ΔT solutions found over the proceeding sections. Rather, it is the total extinction which is determined by additive extinction coefficients,

$$\beta_e = \sum_j \beta_{e,j} = \sum_j b_{e,j} m_j.$$ (2.38)

In this case, the total AOD of Eq. (2.23) becomes

$$\tau_i = \sum_k \sum_j b_{\text{SW},j} \frac{q_{j,i,k}\Delta p_{i,k}}{g} = \sum_j b_{\text{SW},j} \frac{M_{j,i}}{a_i} = \sum_j \tau_{j,i}.$$ (2.39)

For the total longwave heating, the expression is somewhat more complicated. Equation (2.28) becomes

$$\Delta I_{i,k} = I_{\text{LW}} \exp\left(-\sum_j \sum_{k'>k} b_{\text{LW},j} \frac{q_{j,i,k'}\Delta p_{i,k'}}{g}\right)\left[1 - \exp\left(-\sum_j b_{\text{LW},j} \frac{q_{j,i,k}\Delta p_{i,k}}{g}\right)\right].$$ (2.40)

Here, each grid cell has an incident flux density that has already been attenuated by *all* species j underneath it, and so the total attenuation is not simply a sum of j separate evaluations of ΔI.

2.3.5 Model summary & parameter tuning

Figure 2.3 provides a summary of the important equations developed in the previous sub-sections, and Table 2.1 gives the chosen parameter values. Some parameter values are taken

directly from observations or previous works in the literature, while others are derived quantities. Five parameters are tuning parameters, including the longwave mass extinction coefficients for SO_2, sulfate, and ash, the maximum height of forced surface cooling, and the surface heat transfer efficiency.

Tracer tendencies

$$\frac{\partial q_{j,i,k,n}}{\partial t} = \frac{g}{\Delta p_{i,k} a_i} \left[-k_j m_{j,i,k} + I_{i,n} \frac{M_j}{\delta t \sum_k V_k} V_k \right]$$
(2.14)

$$\frac{\partial q_{\text{sulf},i,k,n}}{\partial t} = -k_{\text{sulf}} q_{\text{sulf},i,k,n} + w k_{\text{SO2}} q_{\text{SO2},i,k,n}$$
(2.17)

$$V(z) = \exp\left(-\frac{1}{2}\frac{(z-\mu)^2}{(1.5 \text{ km})^2}\right) \qquad (2.15)$$

SW radiative and optical properties

$$I_{\text{SW}} = I_0 \cos\phi \ \frac{\text{W}}{\text{m}^2} \qquad (2.5)$$

$$\tau_i = \sum_j b_{\text{SW},j} \frac{M_{j,i}}{a_i} \qquad (2.39)$$

$$\Delta I_i = I_{\text{SW}} \left(e^{-\tau_i} - 1\right) \ \frac{\text{W}}{\text{m}^2} \quad (2.32)$$

$$s_{i,k} = \zeta \frac{a_i \Delta I_i}{m_i^{\text{cool}}} \ \frac{\text{J}}{\text{kg s}} \qquad (2.34)$$

LW radiative and optical properties

$$I_{\text{LW}} = \sigma \left[315\text{K} - (60\text{K})\sin^2\phi\right]^4 \qquad (2.4)$$

$$\Delta I_{i,k} = I_{\text{LW}} \exp\left(-\sum_j \sum_{k'>k} b_{\text{LW},j} \frac{q_{j,i,k'}\Delta p_{i,k'}}{g}\right) \left[1 - \exp\left(-\sum_j b_{\text{LW},j}\frac{q_{j,i,k}\Delta p_{i,k}}{g}\right)\right] \qquad (2.40)$$

$$s_{i,k} = \frac{a_i \Delta I_{i,k}}{m_{i,k}} \ \frac{\text{J}}{\text{kg s}} \qquad (2.29)$$

Figure 2.3: Summary of the important model equations controlling the tracer injection and removal, and radiative and optical properties for the tracers in shortwave and longwave broadbands. See equation numbers in the text for explanations. The SW and LW equations are written for a mixture of tracer species j at a fixed timestep n. Values for the parameters are given in Table 2.1.

The longwave attenuation mechanism of the model is tuned to produce realistic stratospheric heating rates by sulfate aerosols. The mass extinction coefficient b_{LW} for sulfate is instrumental in tuning the long-term mean temperature anomalies. We note that while we refer to this heating mechanism specifically as a "longwave attenuation", the tuning process implicitly accounts for heating contributions from the near-infrared radiation as well (see Appendix A.3.3). Not as obvious is the importance of b_{LW} for the very short-lived ash tracer. Though radiative forcing by ash does not directly contribute to the eventual stratospheric temperature anomalies, it does control the mechanism by which the aerosols are delivered

31

to the lower stratosphere (Stenchikov et al., 2021). The lofting speed of the dense, fresh plume will be controlled by the aggressive heating of ash, which is the dominant component of the initial injection. As such, the mass extinction coefficient for ash serves as the main tuning parameter which controls the settling height of the aged aerosols. Meanwhile, SO_2 participates both in the initial lofting of the plume, as well as the short-term temperature anomalies for the first couple months. This behavior by SO_2 creates some degeneracy in the longwave extinction tuning parameters which could be avoided with a slight modification; see Appendix A.3.4 for a discussion.

The shortwave mass extinction coefficients b_{SW} do not play the same role in tuning the surface cooling. Instead, we simply constrain b_{SW} of each species to yield an AOD representative of post-Pinatubo zonal-mean observations. During the months and years following the eruption, these values peaked near 0.2-0.5 (Toohey et al., 2016; Mills et al., 2016; Stenchikov et al., 2021; Dutton and Christy, 1992; Stenchikov et al., 1998). Tuning the magnitude of surface cooling is then passed on to the efficiency parameter ζ.

A description of the actual tuning process, as well as recommendations for tuning the model on different simulation grids and varying aerosol injection scenarios can be found in Appendix A.3.

2.4 Implementation in E3SMv2

2.4.1 Ensemble generation

We explored two different ensemble generation strategies, which we are characterized by a "high variability" (HV), or a "limited variability" (LV) set of initial conditions. Both strategies appear in the literature, though not often explicitly named and compared.

In the HV strategy, ensemble member initial conditions are sampled from a base run of the HSW climate (described in Sect. 2.2) at an interval which produces *independent* atmospheric states. The choice of this time interval is unique to the model configuration. In making this determination, we follow the methodology of Gerber et al. (2008). In short, an index measuring the dynamical process which sets the upper-bound on low-frequency variability in the model is defined, and the time that it takes for the autocorrelation of this index to vanish is found. At that time, we consider the initial condition to have been "forgotten". For the HSW forcing, no seasonal cycle or ocean process are imposed, and so the upper-bound variability timescale is set by positional variations of the extratropical jets, encoded as the annular mode index (defined in Gerber et al. (2008)).

For a standard HS94 forcing on a ∼1-degree pseudospectral grid, Gerber et al. (2008)

showed the annular mode index autocorrelation to vanish by day 90–100. Lower resolution grids had progressively longer timescales. We found that this autocorrelation was ∼0.1 by day 90 for the HSW atmosphere on the ne16pg2 grid in E3SMv2, thereafter only slowly converging to zero by day ∼250. Compromising on these diminishing returns for efficiency, our HV ensembles are generated by sampling initial states from a base run every 90 days. Volcanic injections can then begin at any point in the individual member integrations.
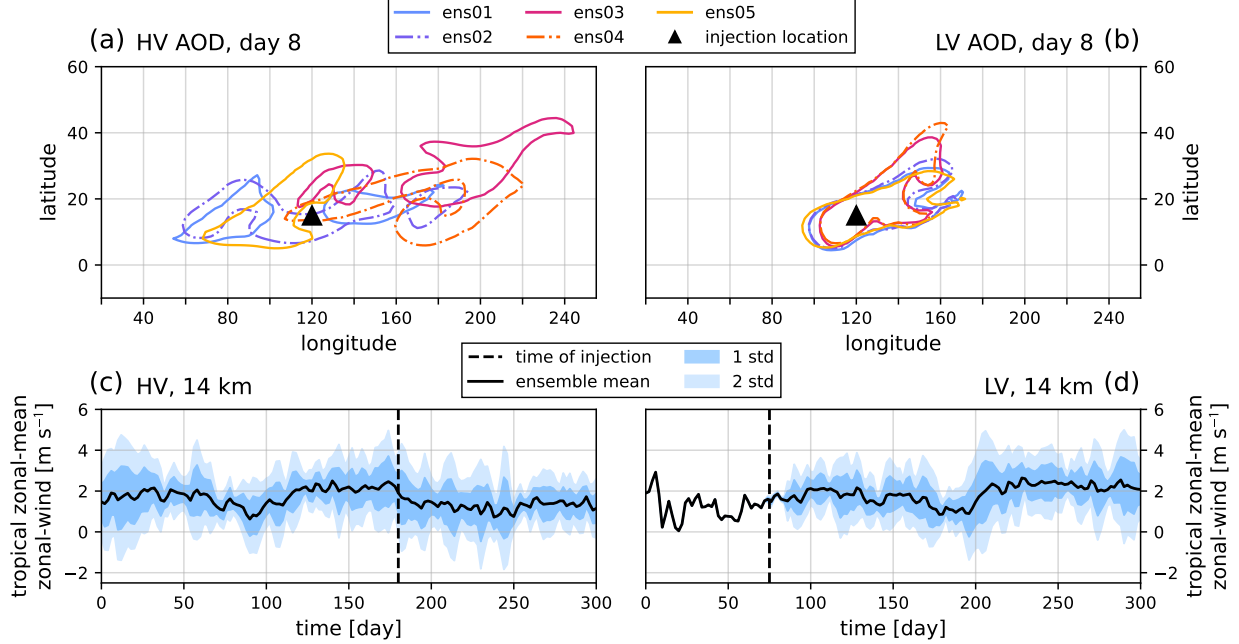
Figure 2.4: **(a)** AOD 0.5 contours for five HV ensemble members at eight-days post-injection. Each ensemble member is given a unique color, and their line styles alternate for visual clarity. **(b)** Identical to panel (a), but for five LV ensemble members. **(c)** Zonal-mean zonal wind averaged over a tropical region bracketing the injection site, from 5°S to 30°N, at 50 hPa, for the HV ensemble. A bold black line shows the ensemble mean. Dark and light blue shading show one and two standard deviations, respectively. A black vertical dashed line shows the time of injection (day 180). **(d)** Identical to panel (c), but for the LV ensemble, with injection at day 75.

In the LV strategy, all ensemble members are initialized with an identical state, which is subjected to a random gridpoint-level temperature perturbation of 1×10^{-4} K. We then wait some amount of time before enabling the volcanic injections. During this pre-injection period, the members will diverge from one another as dynamical feedbacks seeded by the initial temperature perturbations grow. In our experiments, waiting 75 days produced ensemble member background states that are more qualitatively similar in their zonally-averaged flow, but exhibit synoptic-scale variations.

Note that the two timescales quoted above in the generation of the HV and LV ensembles are distinct, and should not be confused. In the former case, the initial conditions lie 90 days apart from one another, while in the latter case, the perturbed initial conditions evolve together, though slowly diverge, for a period of 75 days.

With enough members, the HV ensemble mean will show the average atmospheric response to our volcanic forcing *independent* of the background state. Meanwhile, an LV ensemble mean will show the robust response to a *particular* state, at least for the initial plume evolution. Eventually, the LV members will diverge, and will be statistically similar to the HV ensemble once the aerosol distribution approaches zonal symmetry. Thus, an LV ensemble is perhaps most interesting to studies of this early phase.

Figure 2.4 shows a snapshot of a five-member volcanic injection ensemble at eight-days post-injection for the HV and LV ensemble generation strategies. The differences seen here are principally due to the fact that the HV ensemble samples strongly varying states of the northern polar jet, while the bulk aerosol transport of the plumes of the LV ensemble follow each other more closely. Also shown are time histories of the averaged zonal-mean zonal wind within 20 degrees in latitude of the eruption site (from 5°S to 35°N), at 50 hPa for all ensemble members, demonstrating the difference between the background HV and LV states.

Figure 2.5 displays the zonal-mean of the initial conditions for temperature and zonal wind for ensemble members ens01, ens03, and ens05 for the HV case. These states show the qualitative spread in independent states sampled from an evolving HSW atmosphere, the most notable differences being the balance between (or collapse of) the polar jets, and the strength of the stratospheric equatorial easterlies. Note that the zero-contour rises steeply from the tropical to midlatitude region, and thus the initial transport of a plume for a fixed height will vary strongly with latitude, and will also be particularly sensitive to movements of the jet stream. The combination of the chosen initial condition and the parameter configuration given in Table 2.1 results in the lower-tail of the initial injection distributions catching westerlies, while most of the mass enters the stratosphere and travels East. Note that all of the initial conditions for the LV case were based on perturbations of the HV ensemble member "ens05" (Fig. 2.5 panel (c)).

For the purposes of the present work, the model results of Sect. 2.4.2 are shown only for a HV ensemble. We encourage future studies using this model to present their ensemble generation methods in these terms.

2.4.2 Results

We ran a five-member HV ensemble (Sect. 2.4.1) of E3SMv2 simulations subject to the modified idealized HSW physics (Sect. 2.2, Appendix A.1). A volcanic injection of SO_2 and ash (Sect. 2.3) occurs at day 180, with the parameter configuration of Table 2.1. Figure 2.6 shows the transport of the SO_2 and sulfate aerosol plumes at the 45 hPa model level for days 10, 20, 40, and 80 for the single ensemble member "ens01". At this altitude, the dominant transport is driven by the easterly winds of the tropical stratosphere (see Fig. 2.1). By day 20 the plume has circled the globe, and by day 40 the plume has reached the northern pole. Also during this time, both SO_2 and sulfate concentrations have risen for this fixed vertical level. For SO_2, this effect is purely driven by vertical transport (our model contains no gravitational settling of any tracer species, and so all species will dynamically loft as long as heating is present), while for sulfate, this effect is a combination of transport and actual aerosol production. By day 80, the tracer distributions are well-mixed in the tropical and midlatitude regions, and increasingly more SO_2 has been converted to sulfate.

Figure 2.7 provides a detailed view of the ash plume evolution over the first 20 days of the simulation. Panel (a) shows the zonal-mean ash mixing ratios as a function of time and pressure, averaged over a 20° band centered on the injection in latitude, from 5°S to 35°N. By day 12, the zonal-mean ash mixing ratios in this region have dissipated below 10^{-12}. Also shown for reference is the growing sulfate plume, which is just starting to be produced by SO_2 conversion. Panel (b) shows the total amount of ash removed from the stratosphere
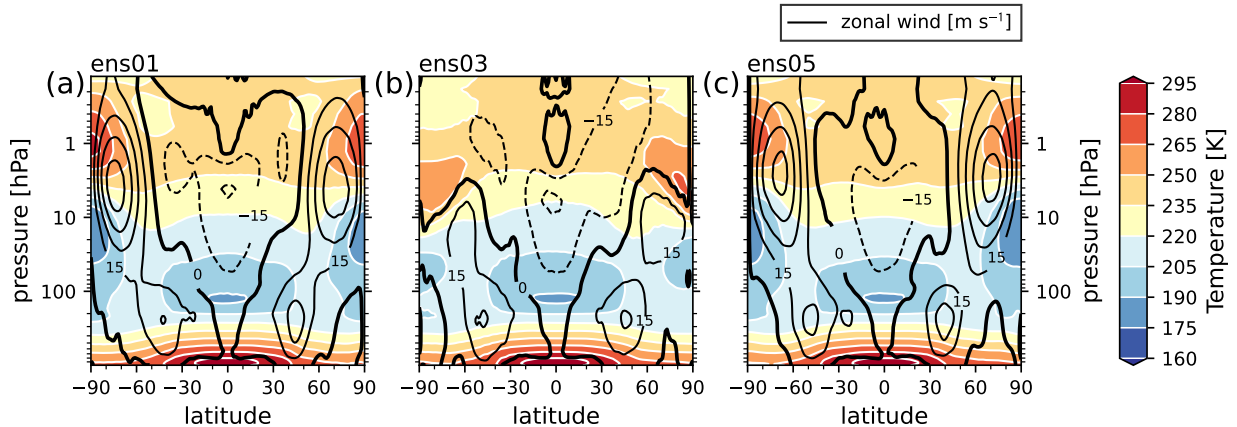
Figure 2.5: Zonal-mean of the initial condition for ensemble members ens01, ens03, and ens05 for the HV ensemble (corresponding to the solid-line AOD distributions of Fig. 2.4). Temperature is shown on the color scale with intervals of 15 K, and zonal wind in black contours with intervals of 15 m s^{-1}. The zero m s^{-1} contour in zonal wind is shown in bold, and negative contours are dashed.
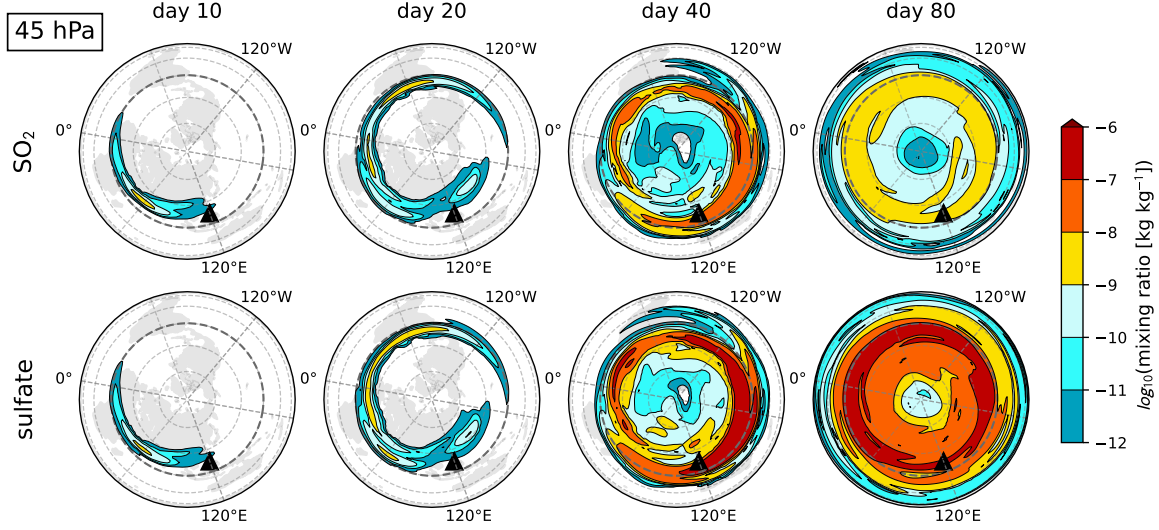
Figure 2.6: SO$_2$ (top row) and sulfate aerosol (bottom row) mixing ratios in (kg tracer)(kg dry air)$^{-1}$ for a single ensemble member at the 45.67 hPa model level, displayed with a logarithmic scale. Columns from left-to-right correspond to 10, 20, 40, and 80 days post-injection. The data is plotted on a Lambert azimuthal equal-area projection extending from the north pole to 60°S, where continental landmasses are shown only for spatial reference (our model features no topography or land processes). A 30°×30° grid is drawn in dashed lines, with the equator in bold dash. The injection location is marked with a black triangle.

over the same time period, in g m^{-2}. That is, we are plotting the cumulative sum of the removal function $R(m_{ash})$ (Eq. (2.7)) over all grid cells above 100 hPa, from days 180 through 200. Our model does not actually implement gravitational settling of ash, though our simple removal process can be thought of as an accumulated "fallout". Thus, this distribution shows both the extent and history of the ash plume after 20 days.

Figure 2.8 displays the evolution of the zonal-mean AOD as a function of latitude and time, as well as the imposed radiative cooling rate at the surface in (K day^{-1}) by SW extinction. The AOD peaks at 0.3 near 15°N after one month, and by day 90 post-injection, zonal-mean optical depths of 0.1 reach the northern pole. Figure 2.9 shows the zonal-mean distribution of sulfate, and the local stratospheric heating rate by LW absorption, as a 30-day time average over days 60 through 90 post-injection. The aerosol density and heating rates coincide with one another in the tropics, while at higher latitudes, the heating rate distribution develops strong meridional gradients that the sulfate mixing ratio does not. These gradients are an imprint of the LW radiation profile of Fig. 2.2, which is minimized at the poles.

Several features of the HSW general circulation are exhibited in Figs. 2.8,2.9. A realistic tropopause is formed by the inversion of the equilibrium temperature T_{eq} near 130 hPa in
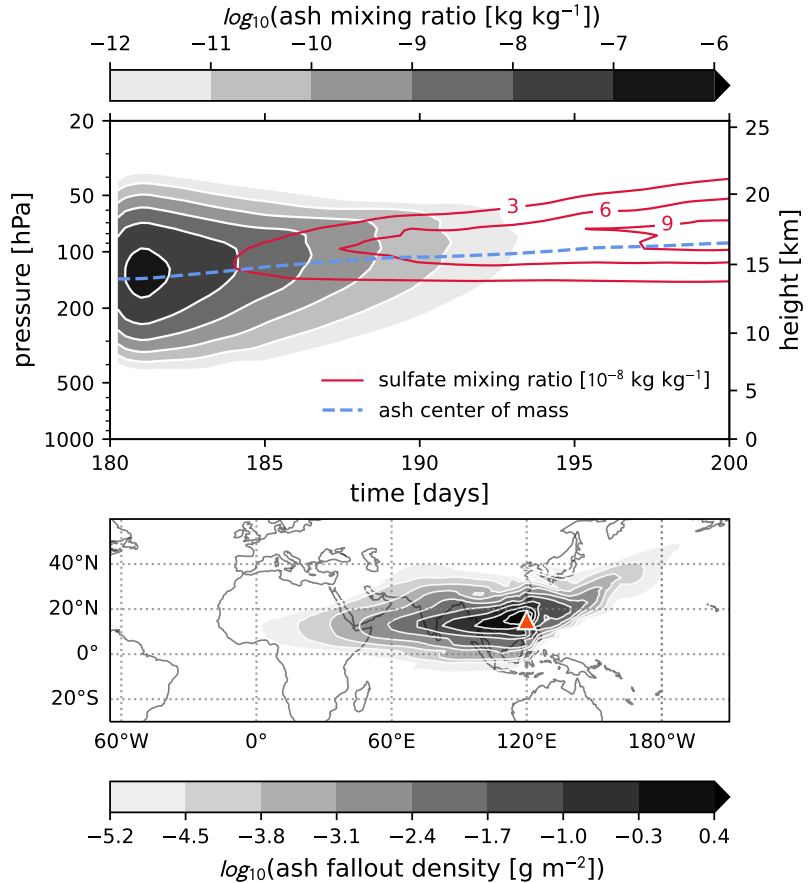
Figure 2.7: Evolution of the ash plume. **(a)** The zonal-mean, ensemble-mean logarithmic ash mixing ratios, averaged over all latitudes within $20°$ of the injection (from $5°$S to $35°$N). A dashed blue line shows the rising center of mass of the ash, and solid red contours show sulfate mixing ratios in intervals of 3×10^8. The eruption occurs at day 180. **(b)** The cumulative sum of removed ("fallout") stratospheric ash $R(m_{\mathrm{ash}})$ over days 0 through 20 post-injection, and all grid cells above 100 hPa, for a single ensemble member. Values are logarithmically-scaled densities in g m^{-2}. A red triangle marks the position of the volcanic injection. Continental landmasses are shown only for spatial reference (our model features no topography or land processes).

the tropics. At the same time, the shape of T_{eq} at the lowest model levels mimics unequal solar insolation of the surface, driving convection in the tropical troposphere. Together, these effects give rise to upper-level divergence at the tropical tropopause, and subsidence in the subtropics. The resulting Hadley cell can be seen in the sulfate distribution tail descending to the surface south of $30°$N. The meridional transport of the zonally-averaged tracer distribution, however, appears not to be hemispherically symmetric, with most of the aerosol population remaining in the northern hemisphere.

For the Mt. Pinatubo eruption, relative hemispheric symmetry of the AOD and temper-
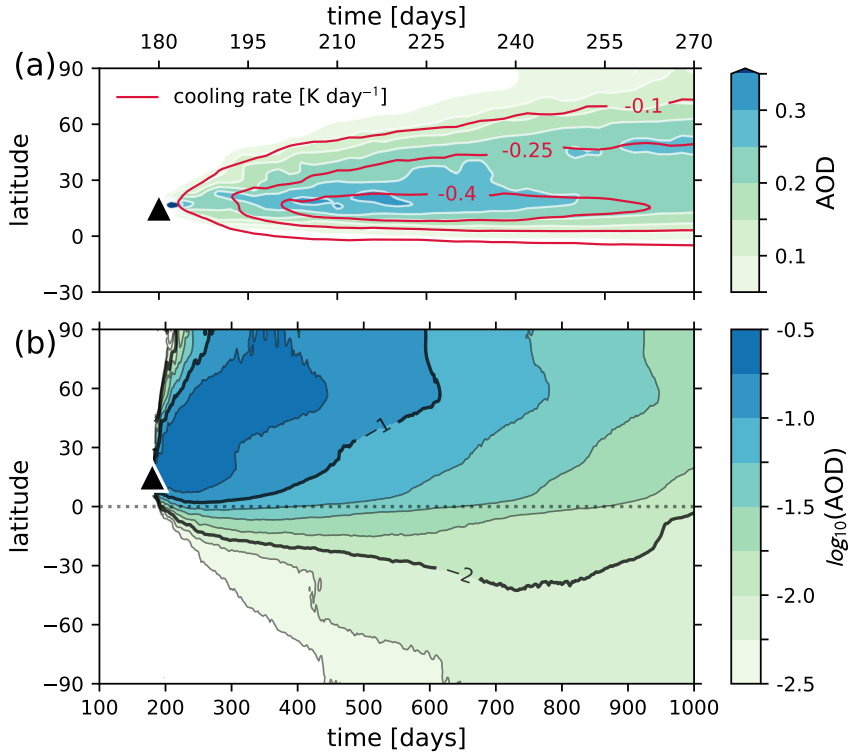
Figure 2.8: **(a)** Zonal-mean AOD in the latitude-time plane for the first 90 days post-injection. Overplotted is the cooling rate imposed on the lowest model level by shortwave extinction every 0.15 K day^{-1} in solid red contours. **(b)** Logarithmic zonal-mean AOD over 1000 days. The 0.1 and 0.001 AOD lines are in bold. Cooling rates are not overplotted in this panel. A faint dotted line shows the equator, and a black triangle shows the time and latitude of the injection.

ature signal is established much more rapidly both in observations (Stenchikov et al., 1998; Mills et al., 2016), and in more realistic models (Mills et al., 2016; Stenchikov et al., 2021; Ramachandran et al., 2000; Karpechko et al., 2010; Brown et al., 2024). This hemispheric symmetry is imposed because, in reality, the mean meridional circulation is characterized during solstice months by a strong winter hemisphere Hadley cell, a relatively weak cell in the summer hemisphere, and a convergence zone north of the equator (Schneider et al., 2014), driven by the seasonal cycle (Schneider, 2006), as well as asymmetry in the northern and southern land-sea distribution (Cook, 2003). During the northern hemisphere summer of July 1991, the upper-level diverging branch of the southern cell would have readily facilitated cross-equatorial transport of lower-stratospheric aerosols (Hoskins et al., 2020). All of these features are absent from our axisymmetric model, where any air masses in the upper troposphere or above will essentially always diverge from the equator. To see this flow feature, the HSW Hadley cells are visualized via the Stokes streamfunction $\psi(\phi, p)$ in Fig. 2.9.
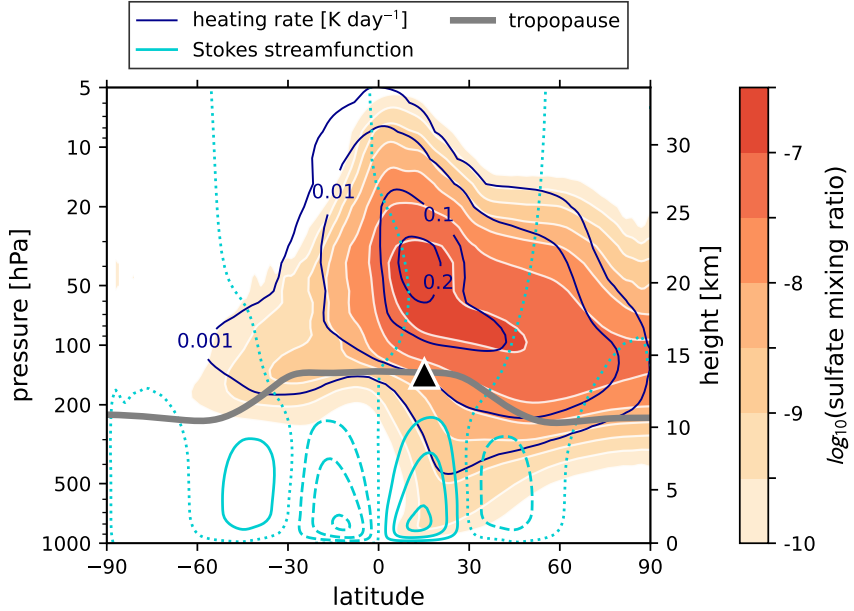
Figure 2.9: 30-day time average over days 60-90 post-injection of the logarithmic zonal-mean sulfate mixing ratio in (kg tracer)(kg dry air)$^{-1}$. Also plotted in solid dark blue contours is the local stratospheric heating rate by longwave absorption in (K day^{-1}), with logarithmic intervals between contours 0.001, 0.01, and 0.1, and a final contour drawn at 0.2. Cyan contours show the Stokes streamfunction (Eq. (2.41)) with intervals of 3×10^{10} kg s^{-1}. Negative (positive) contours are dashed (solid), and the zero line is dotted. A thick gray line shows the tropopause. Height axis is obtained from the model's diagnostic geopotential height.

Following previous studies (Oort and Yienger, 1996; Cook, 2003; Pikovnik et al., 2022), the ψ function is defined by a vertical integration of the zonally-averaged meridional wind $\bar{v}$ as

$$\psi(\phi, p) = \frac{2\pi a \cos \phi}{g} \int_0^p \bar{v}(\phi, p') dp' \qquad (2.41)$$

where a symbolizes the Earth's radius. At a position in pressure and latitude, ψ gives the mean meridional mass transport over the entire stratospheric column above. Thus, positive (negative) peaks in the streamfunction distribution indicate clockwise (counterclockwise) circulation in the zonal average. The HSW streamfunction is anti-symmetric about the equator, more closely resembling an equinox state in nature.

These conclusions about the mean tropospheric circulation can be expressed more generically for the stratospheric mass transport by way of a transformed Eulerian mean (TEM) analysis. Following the specific TEM framework presented in Gerber and Manzini (2016) based on Andrews et al. (1987), we computed residual velocities in the meridional plane for

the HSW atmosphere with no volcanic injections. The five-year average state of the residual velocities between 100 hPa and the the model top near 0.1 hPa are presented in Appendix A.2. This residual circulation is essentially the HSW analog of the Brewer-Dobson circulation (BDC), which describes the global mass circulation through the stratosphere (see e.g. Butchart (2014) for a detailed review). Figure A.2 shows two symmetric overturning circulation features from equator to pole in each hemisphere, characterized by tropical upwelling, a midlatitude surf zone, and polar subsidence. This symmetry is markedly different from the average residual circulation of the northern-hemisphere summer in nature, which sees a single southward pole-to-pole mass transport in the stratosphere (Butchart, 2014). Thus, the volcanic aerosol distribution as manifest in HSW-V remains primarily in the northern hemisphere, unlike the historical Mt. Pinatubo event. This circulation pattern is much more reminiscent of the equinox condition of the BDC. Specifically, the streamfunction presented in Fig. A.2 is in good qualitative agreement with the the observed residual streamfunction during the Spring of 1992 following the historical Mt. Pinatubo eruption (Eluszkiewicz et al., 1996). Similarly, the meridional and vertical residual velocities are in qualitative agreement with those derived from the multi-reanalysis mean presented in Abalos et al. (2021) and reanalysis Springtime means as in Fujiwara et al. (2022) (their Chapter 11). We note that if a solstice condition is desired in the global circulation for future studies with this model, it would be straightforward to replace the HSW equilibrium temperature T_{eq} with a different one designed for that purpose, as in Polvani and Kushner (2002).

Finally, we quantify impacts by the volcanic aerosol forcing on the atmospheric state by atmospheric variable anomalies. Anomalies are defined as a the gridpoint-level arithmetic difference between a particular run (or ensemble mean), and the time-average of a volcanically-quiescent reference simulation. For this reference run, we use a 10-year run of the spun-up HSW atmosphere with no volcanic forcing, which is shown in Fig. 2.1, panel (b). Figure 2.10 shows the resulting ensemble-mean global-mean temperature anomaly as a function of pressure for 1000 days. The temperature anomaly peaks near 2 K at day 120 post-eruption in the stratosphere near 50 hPa, while the surface (lowest model level) anomaly peaks near -1 K. Notice that the surface temperature anomalies exhibit much more noise than those in the stratosphere. In particular, we found that the stratospheric temperature anomaly is positive for any single ensemble members, whereas the negative surface cooling anomaly is often significant (non-zero to at least one standard deviation) only in the ensemble mean.

Also shown in Fig. 2.10 are the total (globally-integrated) tracer mass time series for SO_2 and sulfate, as well as the vertical center-of-mass (COM) of the tropical stratospheric component of the sulfate distribution. The latter is simply defined as a subset of sulfate
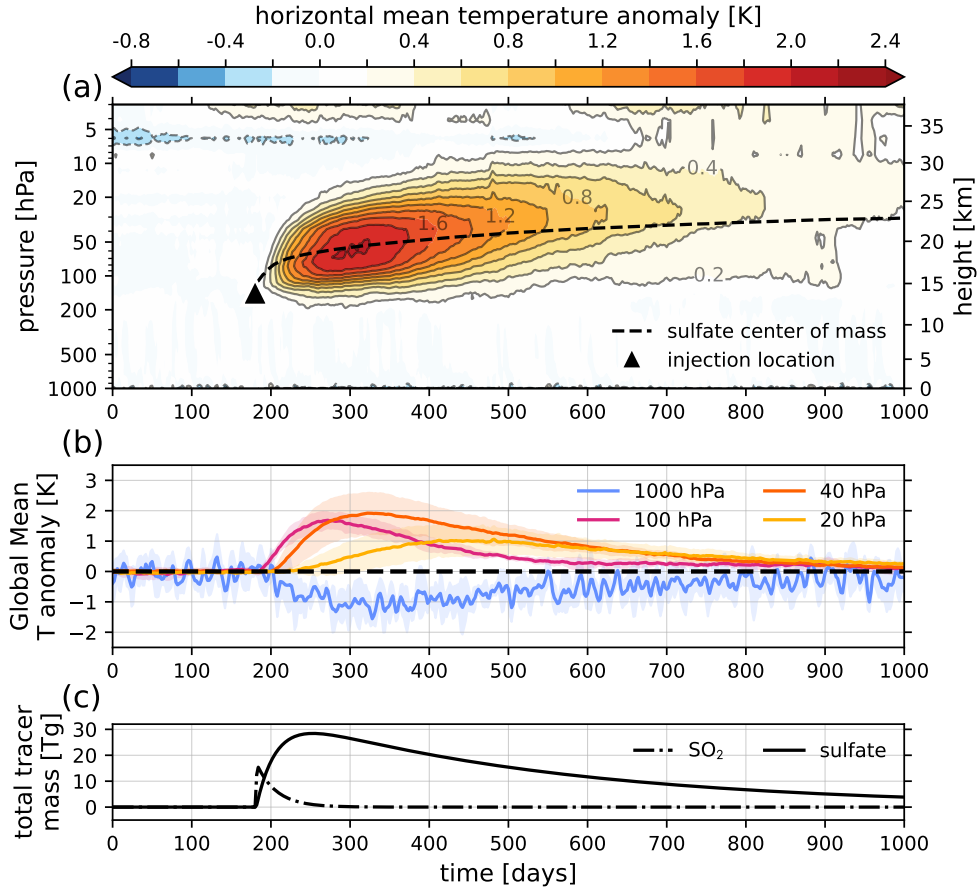
Figure 2.10: **(a)** Ensemble mean temperature anomalies with respect to a volcanically qui-
escent reference period of 10 years, averaged at each model level over all longitudes, and all
latitudes within 20° of the injection (from 5°S to 35°N). Contour intervals are drawn every
0.2 K. Height axis is obtained from the model's diagnostic geopotential height. Black triangle
shows the height of the initial mass injection distribution peak, and time of the eruption at
180 days. A dashed black line shows the center of mass of the volcanic sulfate distribution.
(b) The temperature anomaly data shown in panel (a), chosen for certain pressure levels,
including the surface (1000 hPa). Shading for each curve shows the standard deviation of the
ensemble members. **(c)** The globally-integrated tracer mass time series for SO_2 and sulfate.

which remains above the peak of the vertical injection profile at 14 km or ~130 hPa, and

within 20° of the injection in latitude, from 5°S to 35°N. This sulfate subset is the component

of the plume most sensitive to radiative heating, and thus largely responsible for the global

mean stratospheric temperature anomaly (see Fig. 2.9).

2.4.3 Computational expense

Activating our scheme in E3SMv2 involves minimal computational overhead. We observed that a ne16pg2 HSW simulation with the volcanic parameterizations turned off runs at 175 simulated model years per wallclock day (SYPD) executing on 384 processes (16 physics columns per process) on the Perlmutter supercomputer at the National Energy Research Scientific Computing Center (NERSC). This is equivalent to 52.6 core-hours (or process-element hours) per simulated year, or "pe-hrs/yr". With the same specifications, turning on the volcanic parameterizations reduces the throughput to 58.7 pe-hrs/yr, a decrease of ∼10%.

This performance is in contrast to expensive prognostic aerosol implementations in coupled climate models, which often involve modal aerosol size distributions, more detailed radiative bands, and where aerosol interactions involve an inventory of other chemical species which also must be transported. For comparison, Brown et al. (2024) found 5395 pe-hrs/yr executing their prognostic stratospheric aerosol implementation on the higher-resolution ne30pg2 grid in a nudged atmosphere-only configuration of E3SMv2 on the Cheyenne machine at the National Center for Atmospheric Research (NCAR). For a fully-coupled configuration of E3SMv2, Brown et al. (2024) found 9898 pe-hrs/yr, also on the ne30pg2 grid. Assuming that increasing the resolution from ne16pg2 to ne30pg2 involves a reduction in pe-hrs/yr by a factor of eight our model is ∼11 times faster and ∼21 times faster than atmosphere-only and fully-coupled E3SMv2 simulations, respectively. The assumed factor of eight comes from the fact that when reducing both horizontal dimensions by a factor of two, the timestep must also be halved according to the CFL condition of the dynamical core.

2.5 Conclusions

The injection, evolution, and forcing described in this chapter constitutes an idealized prognostic simulation of volcanic aerosol emission and impact development. Previously, it has not been possible to include volcanic forcing routines in such a simple environment, as they inherently depend upon a complex library of physical subgrid parameterizations. To our knowledge, there is no other option for simulating sulfur forcing with a prognostic aerosol treatment in a Held-Suarez-based atmosphere.

This idealized prognostic simulation has isolated the volcanic event from other sources of variability, and established a direct relationship between forcing (SO_2 emission) and downstream impact (stratospheric and surface temperature anomalies). Delivering these features as a computationally affordable capability facilitates the development of new multi-step data

analytic techniques designed to improve downstream attribution. This simulation has been used in the development of explainable AI techniques which measure the importance of input variables on the prediction of downstream temperature (McClernon et al., 2024). In the near future, we anticipate its broader utility in developing other multi-step attribution methods and in capitalizing on the development of the LV ensemble formulation to establish robust responses to a particular atmospheric state.

This work is a new addition to an idealized AGCM model hierarchy that can be used to study phenomena in isolation. Examples of this model hierarchy include Sheshadri et al. (2015) and Hughes and Jablonowski (2023) who studied the effects of topography on the atmospheric flow, or Polvani and Kushner (2002) and Gerber and Polvani (2009) who assessed polar jets and hemispheric asymmetry. Other idealized configurations focus on simple moist flows with moisture feedbacks (Frierson et al., 2006; Thatcher and Jablonowski, 2016), tropical cyclones (Reed and Jablonowski, 2012), tracer-based cloud microphysics (Frazer and Ming, 2022; Ming and Held, 2018), age-of-air tracers (Gupta et al., 2020), the Madden-Julian oscillation (MacDonald and Ming, 2022), or climate-change forcing (Butler et al., 2010). In addition, this work builds upon previous idealizations of volcanism using simpler prescribed forcing approaches. This includes Toohey et al. (2016) who provide a set of zonally-symmetric volcanic aerosol optical properties tuned to observational data, and DallaSanta et al. (2019) who subjected a set of atmospheric models of increasing complexity to a prescribed aerosol forcing in the form of controlled solar dimming, and steady, zonally uniform lower-stratospheric temperature tendencies.

We illustrated that our implementation can be used to mimic the spatio-temporal temperature anomaly signatures of large volcanic eruptions, and presented one specific parameter tuning that gives rise to a Pinatubo-like event. Our design intentionally leaves out many details which we felt would increase physical complexity, without being necessary for producing realistic atmospheric impacts for attribution studies (e.g. gravitational settling of aerosols). Nevertheless, the formulation remains flexible to modifications. Our parameterizations can:: be tuned toward eruption scenarios other than the 1991 Mt. Pinatubo event. They can also could support any number of co-injected tracer species, concurrence of multiple eruptions, and injections at any latitude and height. In fact, the description is generic enough that by replacing the vertical and/or temporal injection profiles, we could imagine simulating the aerosol direct-effect of various localized emission events of the troposphere (e.g. wildfire smoke) or the stratosphere (e.g. geoengineering SAI experiments) in an idealized model configuration.

CHAPTER III

Volcanic Modification of the Stratospheric Circulation: Wave-Mean Flow Interaction

Abstract

Following large tropical volcanic eruptions, westerly zonal wind accelerations have been observed in the winter hemisphere polar vortex region. This same wind response has been reproduced in some (but not all) simulated eruption studies. As the primary effect of volcanic aerosols is to heat the tropical stratosphere, the midlatitude zonal wind response is often explained as thermal wind effect. Several previous studies have shown that this explanation is insufficient in understanding the relative significance of the aerosol direct effect, and indirect dynamical feedbacks. In this work, we use a Transformed Eulerian Mean (TEM) framework to identify the dynamical origins of stratospheric zonal wind anomalies following the simulated 1991 eruption of Mt. Pinatubo. We employ a paired set of volcanic and non-volcanic 15-member ensembles from the Exascale Energy Earth System Model version 2 (E3SMv2) to identify the isolated volcanic impact. A TEM decomposition of the net zonal wind forcing is then used to close the differenced momentum budget between the two ensembles. Zonal wind accelerations near 30–40°N and 3–30 hPa are identified with significance in the Northern Hemisphere (NH) during both the summer and winter. We find that there are distinct dynamical drivers of these accelerations in each season. In the summertime, the response is primarily governed by an accelerated meridional residual circulation, and thus an associated Coriolis force on the poleward circulation component. In the wintertime, the response is eddy-driven, where a equatorward deflection of planetary waves was robustly identified near 30°N and 30 hPa, acting to reduce wave drag in the region of the westerly anomaly aloft. We additionally identified that a deficit of wave forcing in the tropical stratosphere dampens the amplitude of the quasi-biennial oscillation (QBO) for at least two years following the eruption.

3.1 Introduction

On seasonal to interannual timescales, the mean-flow of the stratosphere exhibits a remarkable diversity of states. The most important modes of stratospheric variability, such as the dramatic development and deterioration of the winter-time polar jets, the oscillation of tropical zonal winds, and the seasonal reversal of the mean-meridional circulation of mass, are highly consequential on the general circulation of the atmosphere (Butchart, 2022). These phenomena also exert influence on conditions near the surface by stratosphere-troposphere coupling, affecting tropospheric weather predictability (Boville and Baumhefner, 1990; Baldwin and Dunkerton, 2001; Scaife et al., 2022).

Much of observed stratospheric variability arises from an internal, dynamical origin. At the same time, there are significant drivers of variability due to sources exogenous to the Earth system, which act to alter the stratosphere's structure and chemical composition. In addition to the anthropogenic depletion and recovery of ozone, one of the most significant natural sources of external forcing on the stratosphere are volcanic eruptions (Schurer et al., 2013). Very large eruptions expel enormous quantities of sulfur dioxide (SO_2) into the free atmosphere, which oxidize to form a long-living population of sulfate aerosols (Bekki, 1995). Once a volcanic aerosol plume is delivered to the upper stratosphere by its own self-lofting (Stenchikov et al., 2021) and the tropical pipe (Kremser et al., 2016), it gradually becomes globally-distributed via the Brewer-Dobson Circulation (BDC; Butchart (2014)). Detectable stratospheric aerosol concentrations will then persist for years. Meanwhile, absorption of longwave radiation by sulfate aerosols drives an increase of tropical stratospheric temperatures, establishing an enhanced equator-to-pole temperature gradient.

Volcanic aerosol-induced temperature perturbations of this nature must give rise to subsequent perturbations in wind—and thus the zonal-mean stratospheric circulation as a whole—such that adiabatic cooling approximately balances diabatic heating in the tropics, and midlatitude thermal-wind balance is maintained at low Rossby number. While the major modes of stratospheric variability such as the quasi-biennial oscillation (QBO) and the arctic/antarctic oscillations (AO/AAO) and their governing mechanisms are well-described in the literature, their quantitative details are controlled by highly nonlinear combinations of forcing terms. Thus, from a theory standpoint, it is difficult to ever know *a priori* how they will respond to a transient source of external forcing, such as radiative heating by volcanic aerosols.

Studies of volcanically-driven changes to the stratospheric circulation typically focus on either the average response to an ensemble of eruptions, or to singular volcanic events in the historical record. Particular attention has been paid to the 1991 eruption of Mt. Pinatubo

in the Philippines, which released 15–20 Tg of SO_2, and induced middle-stratosphere temperature anomalies of a few Kelvin for several years following the event (Self et al., 1997; McCormick et al., 1995). Early observational analyses by Kodera (1994) and Graf et al. (1994) identified a strengthening of the Northern Hemisphere (NH) polar vortex during boreal winter of 1991-1992, despite presence of El-Ninõ conditions (otherwise associated with a weakened vortex). This vortex-strengthening effect is correlated to an enhanced AO (see e.g. Baldwin and Dunkerton (1999)), which itself has been observed by an empirical orthogonal function (EOF) analysis of sea-level pressure data following 13 major volcanic eruptions between 1873 and 2000 (Christiansen, 2008).

Accordingly, positive polar vortex anomalies, and an excitement of the positive AO more generally, are often used as a qualitative benchmark of a climate model's volcanic response. Barnes et al. (2016) used an average of 13 separate model simulations contributed to the Fifth Coupled Model Intercomparison Project (CMIP5; Taylor et al. (2012)), and found a statistically significant strengthening of the polar vortex in austral (boreal) winter of 1991 (1992), accompanied by poleward shifts of the tropospheric jet stream in both hemispheres until February of 1992, suggesting an enhanced AO and AAO. This same result has been found in some additional Pinatubo model studies (Stenchikov et al., 2002; Karpechko et al., 2010; Bittner et al., 2016), but has also been weaker or missing from others (Stenchikov et al., 2006; Driscoll et al., 2012; Toohey et al., 2014; Polvani et al., 2019).

The absence of a robust vortex enhancement is not necessarily indicative of a model's inability to capture the mechanisms which govern that response in nature. Rather, previous studies (Stenchikov et al., 2002, 2006; Toohey et al., 2014) emphasize that this apparent failure is often just a sampling problem; variability of the polar vortex (and thus the AO) is indeed a function of the volcanic forcing structure, but also of internal variability and feedbacks. In the midlatitudes, these effects are comparable in magnitude, and so an ensemble of numerical experiments will not be guaranteed to match any single realization. The conclusion is that in some cases, either a large ensemble size or a very large volcanic eruption may be required for a significant response to be observed. This idea is supported by the robust vortex enhancements simulated in the 700 Tg experiments of Toohey et al. (2011). Likewise, Bittner et al. (2016) found a robust positive vortex response for a 55 Tg eruption, but a weak response and large inter-ensemble spread for a Pinatubo-like eruption with an otherwise comparable experimental setup.

In the tropics, there have also been comparisons between model responses and post-Pinatubo observations. Kinne et al. (1992) reported an increase in observed tropical upwelling, which modifies the vertical wind structure, and by mass continuity, is associated with an accelerated BDC. This effect was previously suggested as early as Dunkerton (1983),

and has since been observed in simulated environments (DallaSanta et al., 2021; Brown et al., 2023), where the consequences of this upwelling on the QBO were studied.

Overall, while some consensus has developed around the qualitative circulation response to volcanic forcing, the causes for differences in the quantitative details between models often remain uncertain. From a process-level point of view, however, we may still be interested in asking: What are the dynamical mechanisms which give rise to a particular post-volcanic state, in a particular model?

An instinctive answer to this question is that the zonal wind must remain in balance with the aerosol-induced temperature perturbations, and thus the enhanced equator-to-pole temperature gradient drives accelerated winds from the subtropics to the midlatitudes. This is the well-known "thermal wind balance" hypothesis, which has been shown to be insufficient by several authors (Toohey et al., 2014; Bittner et al., 2016; DallaSanta et al., 2019). While it is true that the post-eruption atmosphere must indeed be in thermal wind balance at low Rossby number, it is also *not* the case that the net temperature response is solely aerosol-induced. Rather, the net temperature response is a result of aerosol-driven heating, and the nonlinear feedbacks that follow.

The idealized model hierarchy studies of DallaSanta et al. (2019) clearly demonstrated that a zonal-wind field artificially constrained to respond only to the aerosol-induced temperature adjustment is unable to produce accelerations of the NH vortex, shifts of the tropospheric jets, or other features associated with an enhanced AO. Among several factors tested, they show that three-dimensional eddy-driven feedbacks are crucial to establishing the expected zonal-wind response patterns, and thus the balance between temperature and an accelerated extratropical vortex region is only known *a posteriori*.

In an effort to clarify precisely how midlatitude eddies mediate the volcanic response, Bittner et al. (2016) ran a 20-member ensemble of eruption experiments, and analyzed the differences in planetary wave propagation with respect to volcanically-quiescent control runs. They found that the first-order response to the tropical temperature perturbations is an enhancement of westerlies not in the vortex region, but at lower latitudes, near 30°N and 10 hPa. This amounts to a change in the background condition for wave propagation, causing an anomalous equatorward deflection of planetary waves, and thus hampered wave dissipation in the vortex region aloft and poleward. The net result was increased vortex wind speeds during boreal winter following the volcanic event. This effect was observed with weak significance for a Pinatubo-sized eruption, but was shown decisively for an eruption of about 55 Tg SO_2.

In a similar experiment by Toohey et al. (2014) using a 16-member ensemble of Pinatubo simulations, it was likewise found that enhanced wave drag occurs near 30°N and 10 hPa

during boreal winter of 1991–1992, though this did not manifest in a statistically-significant vortex enhancement. The authors further relate the modified large-scale wave activity to balanced changes in the residual meridional circulation, which suggests an acceleration of the BDC.

Incidentally, this observation immediately implies the observed anomalous upwelling in the tropics, and thus coupling to the QBO. In this region, there has also been recent progress made on understanding the driving mechanisms of the volcanic response. In their simulations, Brown et al. (2023) observed that the vertical advection of momentum associated with enhanced upwelling causes a delay of the descending QBO phase, effectively elongating the QBO period for several years following a Pinatubo-like event. Due to feedbacks with the QBO secondary circulation, this delay more strongly affects the QBO in a state of easterly shear than westerly, and the response is thus highly sensitive to the QBO state at the time of eruption.

The essential takeaway from this summary of the literature is that the fundamental atmospheric response to a tropical volcanic eruption is a modification of (predominantly surf-zone) wave activity, and the associated modification to the meridional residual circulation. In this view, specific terms like "vortex strengthening" are perhaps imprecise. For example, volcanically-enhanced midlatitude westerlies are sometimes shown to align with the vortex core, but are often instead shown to align with the equatorward edge of the vortex. We suggest that a description of this response as being either a "vortex strengthening" or a "vortex shift" is really a distinction without a difference, as far as the driving processes are concerned, and that we should instead consider the momentum budget more generically. This idea is also supported by the fact that the "vortex region" anomalies are often shown to be hemispherically symmetric, despite the fact that the southern hemisphere (SH) stratosphere is quiescent during boreal winter (DallaSanta et al., 2019).

In this work, we examine the response to the simulated eruption of Mt. Pinatubo from a Transformed Eulerian Mean (TEM) perspective, in a single coupled climate model. The primary mechanisms controlling large-scale transport of momentum in the stratosphere are advection by the so-called residual (diabatic) circulation, as well as vertical and horizontal wave propagation and dissipation. The TEM framework defines a zonal momentum budget, in which the net local forcing is understood as a combination of these mechanisms. The present goal is to close the TEM budget within regions of interest, in order to understand precisely the dynamical processes which control the development and deterioration of statistically significant post-volcanic wind anomalies. Anomalies are defined as the difference between paired sets of runs, with and without the eruption activated, and otherwise identical initial conditions. The aerosol treatment is prognostic, and so the divergence of each pair

of runs is due to the aerosol forcing, as well as feedbacks to the aerosol distribution. All ensemble members are seeded via precision-level perturbations of a common initial state, which reflects the observed conditions of the real-world Pinatubo event. In this way, we are explicitly ignoring confounding factors such as differences in major climate modes at the time of eruption such as the El-Niño-Southern Oscillation (ENSO) and the QBO phases.

In Sect. 3.2, we describe the climate model employed, and the simulation ensembles. In Sect. 3.3, we define the recipes for our statistical ensemble measures, and the TEM formalism. Section 3.4 shows the characteristics of the background (volcanically-quiescent) runs, and Sect. 3.5 presents the results of the experiments. Section 3.6 and 3.7 provides a discussion of our results in relation to previous works.

3.2   Simulations

The numerical experiments utilized for this study were conducted in a custom version of the Energy Exascale Earth System Model version 2 (E3SMv2; Golaz et al. (2022)) called E3SMv2-SPA, described in Brown et al. (2024). While E3SMv2 describes volcanic eruptions by a prescribed forcing from the GloSSAC reanalysis dataset (Thomason et al., 2018), E3SMv2-SPA instead replaces this treatment with a stratospheric prognostic aerosol (SPA) capability. Rather than prescribing stratospheric light extinction directly, SO_2 is emitted as a tracer into the stratosphere, which forms a sulfate aerosol as governed by the tuned, four-mode version of the Modal Aerosol Module (MAM4; Liu et al. (2016)). Compared to SO_2 emission in standard E3SMv2, this configuration results in a more accurate lifetime of stratospheric sulfate aerosols following the 1991 eruption of Mt. Pinatubo, which is consistent with observations (Baran and Foot, 1994), and the Whole Atmosphere Community Climate Model (WACCM; Garcia et al. (2007)) with its detailed treatment of stratospheric chemistry. The model was run in a standard low-resolution configuration of the model with approximately 1° horizontal resolution. The vertical grid consists of 72 levels extending from 1000 hPa to 0.1 hPa, or approximately 60 km.

This model was used to generate simulation ensembles beginning on June 1st, 1991. Each ensemble member includes a representation of the 1991 eruption of Mt. Pinatubo as an emission of 10 Tg of sulfur dioxide (SO_2) over 6 hours and 9 grid cells between 18 and 20 km near 15° N. The data was output as daily and monthly averages, both of which are used here. Specifically, we utilized the 15-member "limited variability" ensembles, described in Ehrmann et al. (2024). The initial condition for each member was obtained by applying a small, random perturbation of temperature of order 10^{-14} K to a base atmospheric state. This base state was sampled from an auxiliary E3SMv2-SPA simulation run, and exhibits

major climate modes which qualitatively match the real-world conditions at the time of the 1991 Mt. Pinatubo eruption, as derived from the Modern-Era Retrospective Analysis for Research Applications version 2 (MERRA-2; Gelaro et al. (2017)).

Though this initial state was chosen to for it's consistency with the historical scenario, the simulations are free-running (i.e. they are not nudged toward any specific climate modes). Because the ensemble begins on June 1, 1991, the individual members have only two weeks to diverge before the eruption occurs on June 15, 1991. This is enough time to allow for synoptic-scale differences between members to manifest, while the large-scale circulation remains qualitatively consistent. It is in this sense that the intra-ensemble variability is "limited", and thus the ensemble average should capture the robust climatic response to the Mt. Pinatubo event, conditioned on the real-world initial atmospheric state. We will refer to this set of simulations as the limited-variability volcanic ensemble (hereafter LV).

In addition, we utilize the 15-member counterfactual ensemble (hereafter CF) of Ehrmann et al. (2024), where the volcanic sulfate injection is entirely removed. Each member of this ensemble is paired with a corresponding member from the volcanic ensemble. These pairs are identical in their initial conditions, and identical in their evolution until June 15, when the eruption occurs in the volcanic ensemble. After this date, the difference between the volcanic and counterfactual ensembles isolates the net (direct and indirect) impact of the volcanic forcing.

Each pair is run for 8 years. This is enough time for the ensemble members to statistically diverge (from each other, and also from their paired runs) such that the concept of isolating the volcanic impact becomes tenuous, and eventually meaningless. For this reason, most of our analyses will focus on the initial 2-year period from June 1991 through June 1993, which we found to be an appropriate analysis domain for the tropics and midlatitudes (see discussions surrounding Fig. 3.2 and Fig. 3.5).

3.3 Analysis Framework

Rather than use a traditional measure of anomaly as a departure from a reference climatology, we are interested in the pair-wise difference between the LV and CF members. This approach naturally removes structures that are present in the unforced runs from consideration of the volcanic impacts, even if they are anomalous with respect to the climatology (e.g. the QBO, ENSO, and vortex states). To be clear, we will refer to this measure of the volcanic response as an "impact" rather than an "anomaly".

The TEM components of the zonal momentum budget will be used to compute impacts in large-scale wave activity, the global advection of mass, gravity wave drag, and other

parameterized sources. The statistical impact expressions and TEM equation set are defined below.

3.3.1 Impact and Significance

For an N-member ensemble, the ensemble mean variable x, given the data $x^{(n)}$ from each simulation n, is taken independently for both the volcanic ensemble, and the counterfactual ensemble. The counterfactual ensemble mean will be specified as x^{CF}. Following Ehrmann et al. (2024), we define the impact on the variable x as the ensemble mean of the difference between the volcanic and counterfactual data, denoting it as

$$\Delta x \equiv \frac{1}{N} \sum_{n=1}^{N} \left(x^{(n)} - x^{\mathrm{CF},(n)} \right). \tag{3.1}$$

Likewise, the standard deviation of the impact is

$$\mathrm{SD}^{\Delta x} = \sqrt{\frac{1}{N} \sum_{n=1}^{N} (x^{(n)} - x^{\mathrm{CF},(n)} - \Delta x)^2}. \tag{3.2}$$

To identify statistically significant signals in the impact, we apply a paired t-test, where the t-statistic and associated p-value are

$$t\text{-statistic} = \frac{\Delta x}{\mathrm{SD}^{\Delta x}/\sqrt{N}} \tag{3.3}$$

$$p\text{-value} = 2 \times \mathrm{CDF}(-|t\text{-statistic}|, N-1) \tag{3.4}$$

where CDF is the cumulative distribution function of the Student's t distribution, with $N-1$ degrees of freedom, and $-|t\text{-statistic}|$ as the upper bound on the distribution integration. Our null hypothesis states that the volcanic and counterfactual ensembles are statistically indistinguishable. The alternative hypothesis is two-sided, i.e. the volcanic ensemble data is either above or below the counterfactual data, and thus a factor of two also appears in Eq. (3.4). Throughout the results presented in Sect. 3.5, we adopt a p-value threshold of 0.05 (95% confidence) for defining significant impacts. Confidence interval bounds of the impact Δx are computed as

$$\Delta x \pm t_{\mathrm{crit}} \frac{\mathrm{SD}^{\Delta x}}{\sqrt{N}} \tag{3.5}$$

where $t_{\mathrm{crit}} = 2.145$ for $N = 15$.

All processing of the data, including zonal averaging, averaging over latitude bands, selection of vertical levels, and temporal averaging are computed at the member-level. No such processing is done directly on the ensemble means. Rather, a separate ensemble mean, and thus separate impacts and p-values, will be computed for each choice of processing, per Eq. (3.1)–(3.4).

3.3.2 TEM Formulation

To efficiently diagnose the forcing on the zonal-mean flow by the residual circulation and wave activity, we employ the TEM framework originally introduced by Andrews and McIntyre (1976). First, each atmospheric variable x is decomposed into a linear combination of a zonal mean $\overline{x}$ and eddy component x', e.g. $u = \overline{u} + u'$ for the zonal wind u. The TEM momentum equation for the evolution of $\overline{u}$ is written as the sum

$$\frac{\partial \overline{u}}{\partial t} = \frac{\partial \overline{u}}{\partial t}\bigg|_{(\overline{v}^*)} + \frac{\partial \overline{u}}{\partial t}\bigg|_{(\overline{\omega}^*)} + \frac{\partial \overline{u}}{\partial t}\bigg|_{\nabla \cdot \mathbf{F}} + \overline{X}. \tag{3.6}$$

We compute each of the terms on the right-hand side of Eq. (3.6) following the spherical-coordinate formulation specified by Gerber and Manzini (2016) (we also adopt the values of the their constants; see Appendix A2 therein). The first and second terms, which represent zonal momentum forcing by the Coriolis force and residual circulation advection, are

$$\frac{\partial \overline{u}}{\partial t}\bigg|_{(\overline{v}^*)} = \overline{v}^* \left(f - \frac{\partial \overline{u} \cos \phi}{a \cos \phi \partial \phi} \right) \tag{3.7}$$

$$\frac{\partial \overline{u}}{\partial t}\bigg|_{(\overline{\omega}^*)} = \overline{w}^* \frac{p}{H} \frac{\partial \overline{u}}{\partial p} \tag{3.8}$$

for latitude ϕ, pressure p, the Earth's radius a, Coriolis parameter f, and the scale height $H = 7$ km. The meridional (v^*) and vertical (w^*) velocity components of the residual circulation are defined as

$$\overline{v}^* = \overline{v} - \frac{\partial \psi}{\partial p} \tag{3.9}$$

$$\overline{w}^* = -\frac{H}{p}\overline{\omega}^* = -\frac{H}{p}\left(\overline{\omega} + \frac{\partial \psi \cos \phi}{a \cos \phi \partial \phi} \right) \tag{3.10}$$

where v is the meridional velocity, ω is the vertical pressure velocity, and

$$\psi = \frac{\overline{v'\theta'}}{\partial \overline{\theta}/\partial p} \tag{3.11}$$

is the eddy streamfunction, involving the potential temperature θ. It will also be useful to introduce the residual circulation streamfunction Ψ^*,

$$\Psi^* = \frac{2\pi a \cos\phi}{g_0} \left(\int_p^0 \overline{v}^* dp \right), \tag{3.12}$$

were g_0 is the global-mean acceleration due to gravity at mean sea level. The third term on the right of Eq. (3.6) is the forcing of zonal momentum by resolved wave dissipation and breaking,

$$\frac{\partial \overline{u}}{\partial t}\bigg|_{\nabla \cdot \mathbf{F}} = \frac{\nabla \cdot \mathbf{F}}{a \cos\phi}. \tag{3.13}$$

Here, $\mathbf{F}$ is known as the Eliassen-Palm (EP) flux vector, with meridional and vertical components

$$F_{(\phi)} = a \cos\phi \left(\frac{\partial \overline{u}}{\partial p} \psi - \overline{u'v'} \right) \tag{3.14}$$

$$F_{(p)} = a \cos\phi \left(\left[f - \frac{\partial \overline{u} \cos\phi}{a \cos\phi \partial\phi} \right] \psi - \overline{u'\omega'} \right), \tag{3.15}$$

and the EP-flux divergence (EPFD) is

$$\nabla \cdot \mathbf{F} = \frac{\partial F_{(\phi)} \cos\phi}{a \cos\phi \partial\phi} + \frac{\partial F_{(p)}}{\partial p}. \tag{3.16}$$

It is this divergence that represents the sole internal forcing of the zonal flow by transient, nonconservative waves.

Finally, the fourth term on the right of Eq. (3.6), $\overline{X}$, represents all unresolved forcing of $\overline{u}$, including small-scale eddies, and other parameterized sources. We will further split this into contributions from parameterized gravity waves $\overline{X}_{\mathrm{GW}}$, and a (usually small) residual which we will generically call the diffusion $\overline{X}_d$:

$$\overline{X} \equiv \overline{X}_d - \overline{X}_{\mathrm{GW}} \tag{3.17}$$

The diffusion term is inferred by taking the difference

$$\overline{X}_d = \frac{\partial \overline{u}}{\partial t} - \left(\frac{\partial \overline{u}}{\partial t}\bigg|_{(\overline{v}^*)} + \frac{\partial \overline{u}}{\partial t}\bigg|_{(\overline{\omega}^*)} + \frac{\partial \overline{u}}{\partial t}\bigg|_{\nabla \cdot \mathbf{F}} + \overline{X}_{\mathrm{GW}} \right), \tag{3.18}$$

so that the overall zonal momentum budget is closed. For the monthly-mean ensemble data, gravity wave drag outputs were available, and so it was possible to do the separation of $\overline{X}$

in Eq. (3.17). These outputs were not available for the daily-mean data; in that context, we keep $\overline{X}_{\mathrm{GW}}$ on the left-hand side of Eq. (3.18) and can only represent the net parameterized drag $\overline{X}$ in the momentum budget.

The philosophy behind the TEM equations of motion as a diagnostic tool for wave-mean flow interaction has been articulated in several foundational works (e.g. Edmon et al. (1980); Dunkerton et al. (1981); Andrews et al. (1983)). For our purposes, the framework will allow us to identify the mechanisms that are responsible for volcanic aerosol-induced changes to the zonal flow. Specifically, by applying the methods of Sect. 3.3.1 to $\overline{u}$, we will identify statistically significant impacts on the zonal-mean zonal wind. We then separate the forcing of $\overline{u}$ into the contributions from the residual circulation (Eq. (3.7) and Eq. (3.8)), from resolved eddy forcing (Eq. (3.13)), and parameterized forcings and dissipation (Eq. (3.18)). By statistically comparing the closed TEM budgets of each ensemble, we may diagnose which of these dynamical mechanisms control the separation between the volcanic and counterfactual simulations at certain locations and times. The important quantities and equations used in this procedure are summarized in Table 3.1, which may be useful in reading the later figures.

Table 3.1: Essential quantities of the TEM framework and TEM zonal momenutm budget. The second column ("Label") refers to the labels given to the corresponding quantity in figure titles and legends throughout this work. Quantities without a label are labeled either with their name (first column), or their symbol. Units provide the SI units, though different units may appear in figures. All quantities are computed on daily-averaged simulation data, except for the GW forcing and diffusion components of the TEM budget, which are computed on monthly-averaged data.

Quantity	Label	Symbol	Equation	Units
TEM quantities:				
Meridional residual velocity	—	v^*	Eq. (3.9)	m s^{-1}
Vertical residual velocity	—	w^*	Eq. (3.10)	m s^{-1}
Residual circulation streamfunction	RC streamfunction	Ψ^*	Eq. (3.11)	kg s^{-1}
EP flux vector	EP flux	$\left[F_{(\phi)}, F_{(p)}\right]$	Eq. (3.14, 3.15)	m^3 s^{-2}, m^2 s^{-2} Pa
EP flux divergence	EPFD	$\nabla \cdot \mathbf{F}$	Eq. (3.16)	m^2 s^{-2}
TEM budget (zonal-meanzonal wind forcings):				
Net forcing	—	$\frac{\partial \overline{u}}{\partial t}$	Eq. (3.6)	m s^{-2}
Meridional residual velocity advection	v^* forcing	$\frac{\partial \overline{u}}{\partial t}\Big|_{(v^*)}$	Eq. (3.7)	m s^{-2}
Vertical residual velocity advection and Coriolis force	w^* forcing	$\frac{\partial \overline{u}}{\partial t}\Big|_{(\omega^*)}$	Eq. (3.8)	m s^{-2}
Total residual circulation forcing	RC forcing	—	Eq. (3.7+3.8)	m s^{-2}
Resolved eddy forcing (large-scale wave drag)	EPFD forcing	$\frac{\partial \overline{u}}{\partial t}\Big|_{\nabla \cdot \mathbf{F}}$	Eq. (3.13)	m s^{-2}
Unresolved (parameterized and implicit) forcings	unresolved	$\overline{X}$	Eq. (3.17)	m s^{-2}
Gravity wave drag	GW forcing	$\overline{X}_{\mathrm{GW}}$	Eq. (3.17)	m s^{-2}
Unresolved forcings beyond gravity waves	diffusion	$\overline{X}_{\mathrm{d}}$	Eq. (3.18)	m s^{-2}

Note that all zonal averages throughout this chapter are taken by the spectral spherical-harmonic method described in Appendix B.2, which avoids the need to remap the data from the E3SMv2 native cubed-sphere grid to a structured latitude-longitude format. In computing Eq. (3.18), the total tendency $\partial \overline{u}/\partial t$ was not available to us as a model output in the simulation ensembles, and so it is constructed from the daily-mean $\overline{u}$ by a first-order finite forward difference. Meridional and vertical derivatives are computed with a second-order centered finite-difference. See Appendix B.1 for details.

3.4   Reference State

3.4.1   Midlatitudes

In order to establish the behavior of the unforced simulations during the Pinatubo period, Fig. 3.1(a)–(d) shows the seasonal zonal-mean zonal-wind structure for a single year of the CF ensemble mean, spanning June 1991 to June 1992. The stratospheric winds in the E3SMv2-SPA model appear to be broadly consistent with climatological averages deduced from the ERA5 reanalyses dataset (Fig. 2 in Butchart (2022)), with the SH winter-time polar vortex reaching maximum wind speeds in excess of 80 m s^{-1} toward the model top and near 60°S, and the NH polar vortex reaching speeds above 50 m s^{-1} near 60°N. In each summer hemisphere, easterlies peak at 30–40 m s^{-1} near 20°N and 20°S. These wind speeds are slightly low for the SH, and slightly high for the NH with respect to the reanalysis climatology, but are well within the range of observed variability (Fig. 8 in Butchart (2022)). There is similar accuracy in the tropospheric jets.

In addition, EP flux vectors and contours of the residual circulation streamfunction are plotted over the seasonal winds in Fig. 3.1(a)–(d). Negative values in streamfunction (dashed contours) indicate counter-clockwise circulation the meridional plane, and vice-versa for positive values (solid contours). The zero-line between these regions is drawn in bold. Qualitatively, this shows equator-to-pole overturning cells in the lower stratosphere and below, and a single pole-to-pole circulation from summer-to-winter hemisphere during the solstitial seasons. These two regimes represent the advective components of the well-known shallow and deep branches of the BDC, respectively (Birner and Bönisch, 2011; Butchart, 2014).

The EP flux vectors show the relative magnitude and direction of resolved wave propagation in the meridional plane (Edmon et al., 1980; Andrews, 1987). In the summer hemisphere, wave activity forced by surface processes is largely constrained below the tropopause (e.g. Fig. 3.1(a), NH), since the stratospheric easterlies aloft prevent the vertical propagation of Rossby waves (Charney and Drazin, 1961). During the following autumn, the development

of upper-level westerlies acts as a valve for wave propagation into the stratosphere (e.g. Fig. 3.1(b), NH). This persists through the winter, when stratospheric wave activity (and thus, zonal-wind variability) is at its highest (e.g. Fig. 3.1(c), NH).

The seasonal TEM momentum balance is shown in Fig. 3.1(e)–(h) at 3 hPa (winter vortex core) and 30 hPa (lower vortex edge). Forcing by the EPFD, the residual circulation, parameterized gravity wave drag, subgrid diffusion, and their sum are plotted as functions of latitude, along with the CF ensemble mean $\overline{u}$. Scaling of the vertical axis is unique in each panel. This reveals the familiar result (e.g. Andrews et al. (1983)) that the net tendency $\partial \overline{u}/\partial t$ in the stratosphere is due to a relatively small imbalance between negative wave-driven forcing (dissipation and breaking of resolved large-scale waves and parameterized gravity waves), and positive forcing by the residual circulation (Coriolis torque and advection of momentum).

In the summer hemisphere, both the wave-driven and residual circulation forcing magnitudes are low, and the compensation between them is nearly complete (e.g. Fig. 3.1(e), NH). The result is mild easterly wind speeds with low variability. In the winter hemisphere (e.g. Fig. 3.1(g), NH), approximate balance between the forcing terms remains, but the relative contributions are much larger. The result is a strong polar jet. The equinoctial seasons serve as the transitions between the two quasi-steady states found in the summer and winter stratosphere, at which time the force balance must break, and the total mean forcing on $\overline{u}$ departs from zero (Fig. 3.1(f,h)). In the autumnal hemisphere, net positive forcing arises as the polar vortex is spun-up by the Coriolis torque of the strengthening meridional residual velocity, while in the vernal hemisphere, net negative forcing results as wave drag erodes the vortex.

Note that in both winter hemispheres at 3 hPa (Fig. 3.1(e), SH and Fig. 3.1(g), NH) there tends to be a sign change in the EPFD on each side of the polar vortex, such that wave breaking and dissipation (EPFD< 0) occurs equatorward, in the surf zone (McIntyre and Palmer, 1984), and wave divergence (EPFD> 0) occurs poleward. This is qualitatively consistent with some reanalysis climatology results, e.g. ERA-Interim (Díaz-Durán et al., 2017). The parameterized gravity wave drag (yellow curve) in the model tends to exhibit the opposite behavior.

At 30 hPa, well below the vortex peak, there is broad negative EPFD from the midlatitudes to the poles. This westward wave driving is about a factor of 2 larger in magnitude in the NH than the SH due to the continental land masses—an effect which might have the capacity to trigger a breakdown of the vortex (Baldwin et al., 2021) in a different realization.
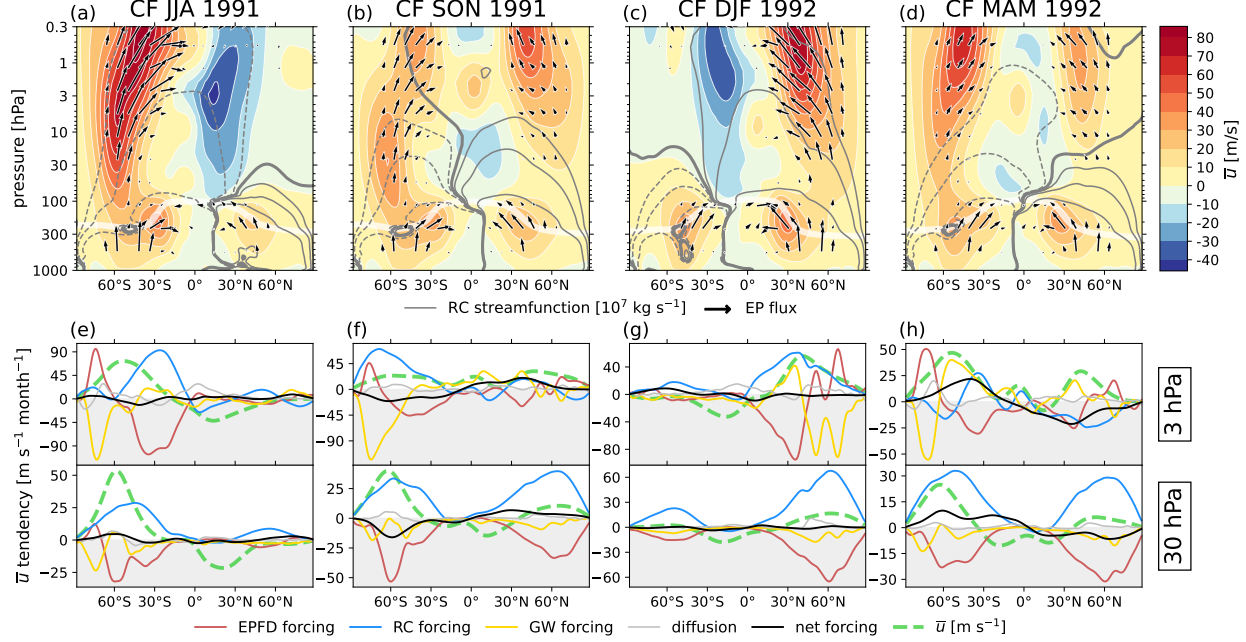
Figure 3.1: Seasonal zonal wind and TEM momentum balance for the first year of the CF ensemble mean. **(a–d)** $\overline{u}$ averaged over 3-month seasons in contours of 10 m s^{-1}, with EP flux vectors, gray Ψ^* contours, and the tropopause overplotted as a thick, faint white contour. The EP flux vectors are scaled following Jucker (2021). The Ψ^* contours are drawn at 30, 100, and 500 in units of 10^7 kg s^{-1} on each side of zero (bold contour). Negative contours are dashed. **(e–h)** seasonal contributions to $\partial \overline{u}/\partial t$ in [m s^{-1} month^{-1}] from the EPFD (red solid), the residual circulation (blue solid), gravity waves (gold solid), and diffusion (thin gray solid) as functions of latitude at 3 hPa (top panels) and 30 hPa (bottom panels). Also shown is the net tendency (black solid), as well as $\overline{u}$ itself (thick green dashed) in [m s^{-1}]. The negative tendency (and wind speed) domain is shaded in light gray. Note that each panel of (e)–(h) has unique scaling of the vertical axis, such that all curves are contained within the plotting region.

3.4.2 Tropics

The tropical zonal-mean zonal wind averaged over 5°S–5°N in the CF ensemble mean is shown in Fig. 3.2 for the full 8-year simulated time period. In Fig. 3.2(a), the initial QBO phase is easterly, and its first cycle has a period of approximately 24 months with peak winds of about -10 m s^{-1} and 7 m s^{-1} in January of 1991 and 1992 respectively, at 30 hPa in the ensemble mean. This is weak by a factor of 2 to 3 compared to ERA5, which is a known bias of E3SMv2 (Yu et al., 2024).

In addition to a weak amplitude compared to reanalyses, the semi-annual oscillation (SAO) penetrates deeper into the stratosphere, and the descent of QBO phases is typically hastened in E3SMv2, resulting in a shortened period at fixed pressure. Yu et al. (2024)
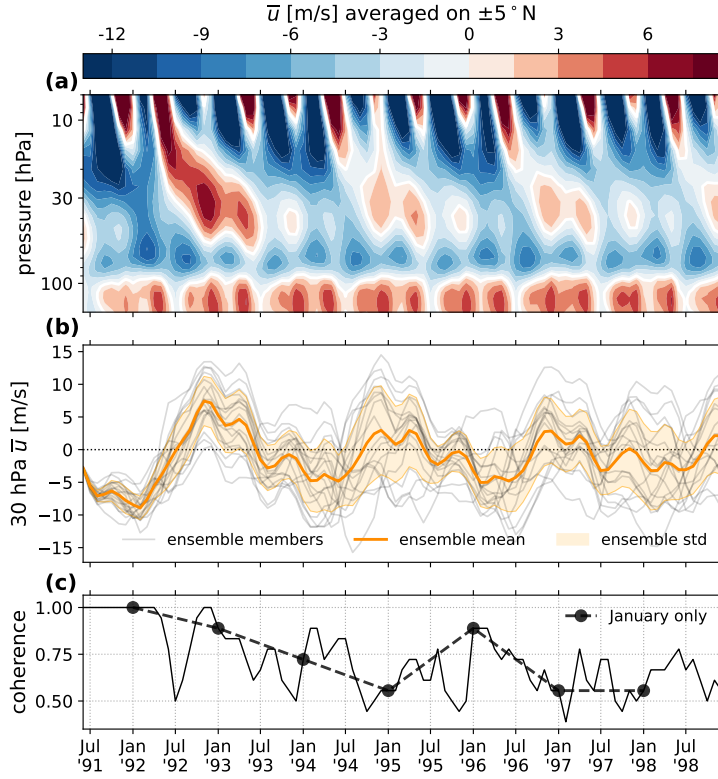
Figure 3.2: The QBO shown as $\overline{u}$ averaged over [5°S, 5°N] for the CF ensemble mean. **(a)** time–pressure plane centered on the lower stratosphere. **(b)** zonal wind time series at 30 hPa. The ensemble mean and standard deviation in $\overline{u}$ is shown as a bold orange line and light orange shading, respectively. Individual ensemble members are shown as faint gray lines, and the zero-line is dotted. **(c)** the ensemble coherence, defined as the fraction of ensemble members in agreement with the sign of the ensemble mean in panel (b). A bold dashed line with points displays the coherence evaluated only at each January.

showed that the spectral density of the QBO computed over 1985–2015 at 20 hPa in E3SMv2 is approximately uniform in power from 20 to 30 months in period, with no distinct peak. For our realizations in E3SMv2-SPA, the QBO manifests with a period of about 24 months. This causes a seasonal phase lock, where maxima and minima in QBO wind speeds occur during alternating boreal winters.

Following the first cycle, the QBO signal in the ensemble mean weakens further, by an additional factor of ∼2. Most of this weakness is explained by the increasing intra-ensemble spread, as the members diverge from their common initial condition, demonstrated at 30 hPa in Fig. 3.2(b). Alternatively, Fig. 3.2(c) shows the 30 hPa ensemble "coherence", or the fraction of the members which agree in sign with the ensemble mean. The coherence is variable, unsurprisingly dropping to 50% whenever $\overline{u}$ crosses zero. More useful is the

January coherence (bold dashed line and points) which, because of the seasonal phase lock of the QBO in the model, shows the ensemble phase agreement during each easterly and westerly maximum. We observe that the January coherence drops below 80% near July of 1993, and so for the remainder of this study we will focus only on this early 2-year period. In the midlatitudes, we should expect the ensemble coherence to fall off faster, though we will still conduct the analysis over this same period.
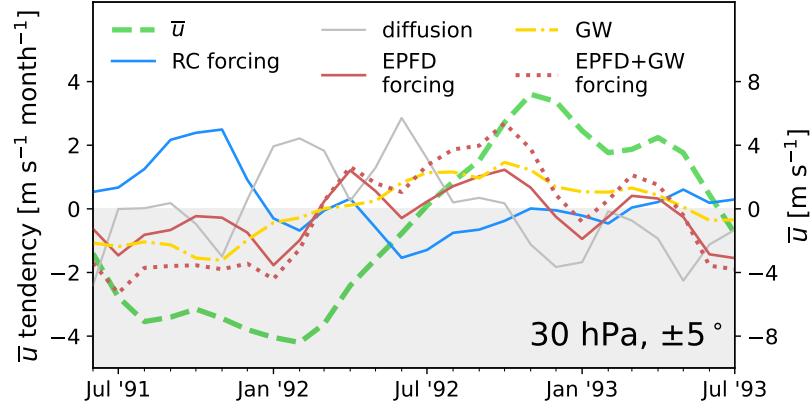
Figure 3.3: The TEM momentum balance of the QBO for the first two years of the CF ensemble mean, averaged over [5°S, 5°N] at 30 hPa. Shown are the contributions to $\partial\overline{u}/\partial t$ in [m s^{-1} month^{-1}] from the EPFD (red solid), gravity waves (gold dotted), the combined EPFD and gravity waves (red dotted), the residual circulation (blue solid), and diffusion (thin gray solid) as functions of latitude at 3 hPa (top panels) and 30 hPa (bottom panels). Also shown is $\overline{u}$ itself (thick green dashed) in [m s^{-1}], values read on the left vertical axis. The negative tendency or wind speed domain is shaded in light gray.

The TEM balance describing the QBO evolution at 30 hPa over the initial 2-year period is shown in Fig. 3.3. Curves show the monthly-mean time series of the forcing on $\overline{u}$ by the EPFD and gravity waves, the residual circulation, and diffusion (this is the same data as in Fig. 3.1(e)–(h) before seasonal averaging, but with the net forcing omitted). The sum of the EPFD and gravity wave drag is also drawn (red dotted line), which shows the usual result that wave-driving is the dominant process controlling the QBO phase descent (Baldwin et al., 2001). However, momentum transport by vertically propagating tropical waves is actually much larger than the net motion of the QBO would suggest (peaking at $\sim$3 m s^{-1}month^{-1} in NH autumn of 1992, while the net tendency is nearer to $\sim$1.3 m s^{-1}month^{-1}), since it is partially canceled by the residual circulation (blue solid line), which hinders the descending phase (Dunkerton, 1997). As the Coriolis force is negligible at these latitudes, and v^* is small, this forcing can be interpreted primarily as a diabatic effect, where upwelling of momentum by w^* is in control (see steamfunction contours in Fig. 3.1). The result is positive (negative)

forcing by the residual circulation in westerly (easterly) shear zones (as in e.g. Brown et al. (2023)).

3.5 Volcanic Impact Results

With an understanding of the seasonal TEM balance in the CF ensemble established, we now investigate disruptions to this balance by the Pinatubo aerosol forcing. Figure 3.4 shows the monthly-averaged global $\Delta \overline{u}$ for select months in the autumn of 1991, winter of 1992, and autumn of 1992 (panels (a)–(c)), as well as meridionally-resolved impacts over 70°S–70°N as a function of time at 10 hPa and 30 hPa (panels (d, e)). On all panels, the counterfactual winds are drawn in black contours every 10 m s^{-1}. Regions where the statistical significance of the impact is above 95% are enclosed by a bold white contour, and regions below 95% are marked with white hatching.

Midlatitude and tropical impacts are discussed in Sect. 3.5.1 and 3.5.2, respectively. The strategy is to (1) identify localized regions of significant $\Delta \overline{u}$ in space and time, (2) over the each identified region, decompose $\Delta(\partial \overline{u}/\partial t)$ into the TEM form of Eq. (3.6), and (3) analyze the imbalance between the impact of the TEM terms. If the result of this process is a set of TEM impacts which are themselves statistically significant, then we will consider the specific mechanism in control of the associated $\Delta \overline{u}$ to have been found.

In the midlatitudes, this process amounts to answering the question; if thermal wind balance is to be approximately maintained after a source of external forcing is introduced, then what processes govern the required adjustments to the zonal-wind to that end? From a TEM perspective, it might be assumed that the residual circulation and large-scale wave drag conspire in this purpose, but as we will show, the quantitative details of this balance change notably with at least season and latitude.

This type of analysis has precedent in the literature, most notably Bittner et al. (2016) and Toohey et al. (2014), but we are not aware of another work on volcanic aerosol forcing that attempts to give a complete accounting of the closed TEM budget in this way. We take some inspiration from similar closed-budget analyses that have been done for climate trends in tracer distributions, e.g. Abalos et al. (2013, 2017, 2020).

3.5.1 Impacts in the Surf Zone & Polar Vortex

Figure 3.4(d, e) shows that until 2 years post-eruption, essentially all stratospheric $\overline{u}$ impacts outside of the tropics are westerly in nature, consistent with aerosol-driven enhancements of the meridional temperature gradient. These features correspond to either zonal acceleration
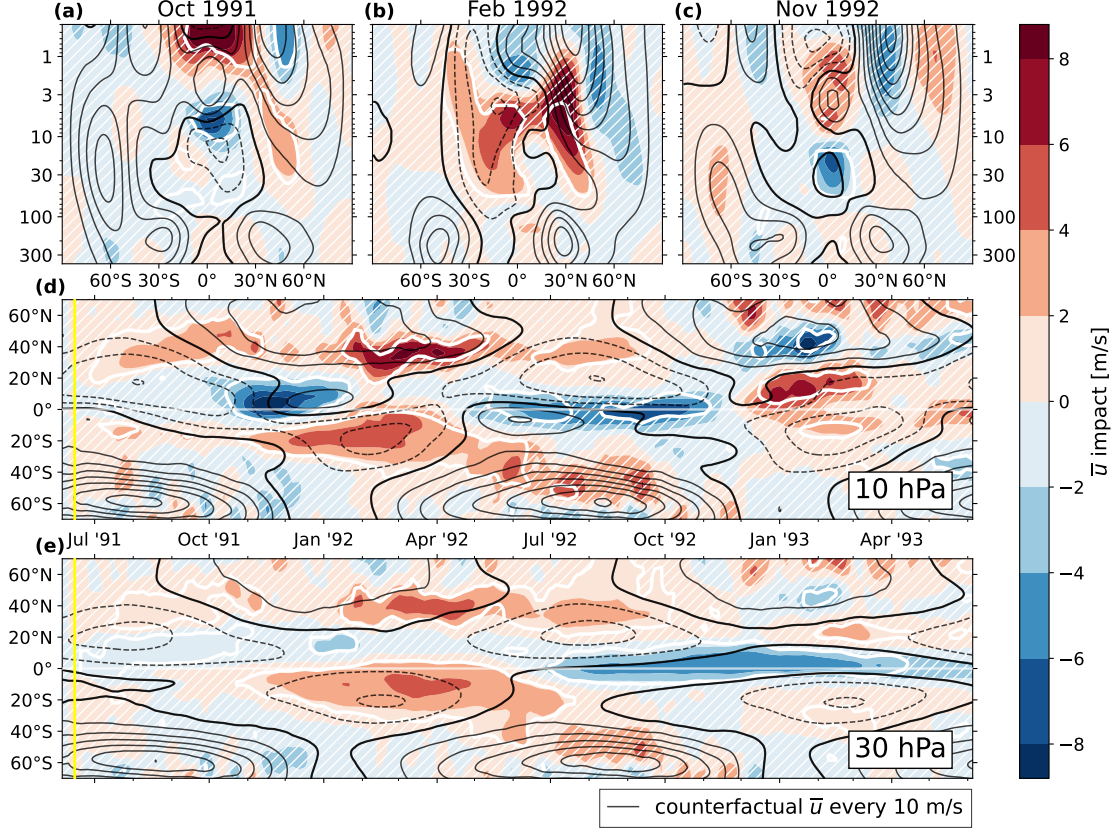
Figure 3.4: The ensemble-mean $\Delta\bar{u}$ as filled contours (colorscale), with the CF ensemble-mean $\bar{u}$ overplotted as black contours, drawn every 10 m s^{-1}, with negative contours dashed and the zero-line in bold. A bold white contour is drawn at 95% significance, with the $\Delta\bar{u}$ p-value computed as in Sect. 3.3.1. Regions of insignificance are filled with white hatching. The upper three panels show the latitude-pressure plane for time averages over **(a)** October 1991, **(b)** February 1992, and **(c)** November 1992. The lower two panels show the time-latitude plane for pressure levels at **(d)** 10 hPa, and **(e)** 30 hPa. In panels (d) and (e), a vertical yellow line shows the time of eruption, and a faint white line is drawn on the equator.

or deceleration with respect to the reference, depending on the season.

The significant response begins near 10 hPa in both hemispheres (Fig. 3.4(d)). In the northern hemisphere, a westerly impact of $\sim3 \text{ m s}^{-1}$ develops near 30°N, decelerating easterly winds (black dashed contours) from July through the end of the NH summer of the eruption. This impact moves poleward toward 60°N throughout autumn, acting to hasten the spin-up of the polar vortex along its equatorward edge, before becoming insignificant in early November. The vertical structure averaged over October 1991 is given in Fig. 3.4(a), which suggests that this feature is perhaps part of a subtle equatorward shift of the vortex, given the accompanying easterly impact near the vortex core above 1 hPa. We will refer to this impact signature as an the "summer response" (SR). Note that a similar summer response

occurs again from July to October of 1992 near 30°N, as well as in the southern hemisphere between December and April 1992, albeit at lower latitudes.

Following the 1991 SR is a stronger westerly impact of up to ∼6 m s^{-1} occurring at both 10 and 30 hPa near 40°N, between January and May 1992 (Fig. 3.4(d, e)). This impact serves to accelerate westerlies in the surf zone (equatorward edge of the polar vortex). Figure 3.4(b) shows the vertical structure averaged over February of 1992, in which we again see easterly impacts near and poleward of the vortex core, indicative of equatorward vortex shift (though it is insignificant). We will refer to this impact as the "winter response" (WR), and we identify this response most closely with the claims of an "accelerated vortex region" that are well-represented in the literature, as discussed in Sect. 3.1. A similar (but less significant) repose also occurs in the southern hemisphere near 50°S between June and October 1992.

The summer and winter responses are summarized in Fig. 3.5, which shows the separation of the LV and CF ensembles in one-dimension as $\overline{u}$ and $\Delta\overline{u}$ at 20 hPa, averaged over 30–50°N. Also plotted are the 95% confidence intervals on the ensemble means and the impact, as well as a curves at two standard deviations. In the lower panel, the confidence interval is shaded in green where the impact is significant, which clearly shows the 1991 SR, 1992 WR, and 1992 SR. This view illustrates that the relatively strong winter-time stratospheric variability in the vortex region sets a kind of lower-bound on the forcing magnitude that is required to illicit a significant response, which our simulations are only just managing to overcome. In the summer-time quiescent stratosphere, on the other hand, the noise floor is much lower, and so even small impacts can be detected. This is consistent with the findings of previous work that has demonstrated a statistically weak response from Pinatubo-like forcing, even for much larger ensemble sizes (Bittner et al., 2016).

For the remainder of this section, our analysis will be restricted to the northern hemisphere, since those impacts occur earlier and with more significance, and have more representation in the literature. There is some suggestion of an easterly impact in boreal winter of 1993 (Fig. 3.4(d)), but it is largely insignificant. Hence, we will also restrict the analysis of this section to the the first 12–16 months post-eruption.

3.5.1.1   TEM Balance of the Surf Zone & Polar Vortex

We now investigate the impacts to the TEM balance associated with both the summer and winter midlatitude responses. Figure 3.6 picks out the 30–50° latitude band at 10 hPa from Fig. 3.4(d), and reproduces it in its panel (a). Panel (b) shows the vertically-resolved meridional average over this band. Over this domain, in addition to $\Delta\overline{u}$, we also obtain the impact (as Eq. (3.1)) of the net tendency $\partial\overline{u}/\partial t$, the large-scale wave drag (Eq. 3.13), the residual circulation forcing (Eq. (3.7) + Eq. (3.8)), gravity wave drag, and diffusion (Eq.
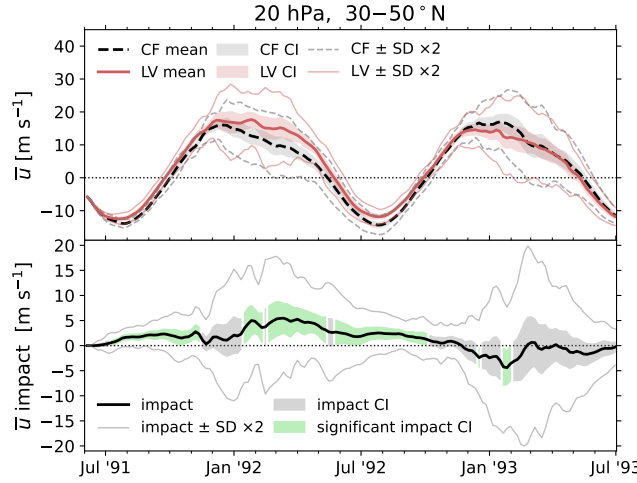
Figure 3.5: Time series of the CF ensemble-mean $\overline{u}$ and LV ensemble-mean $\overline{u}$ (upper panel) as well as the ensemble-mean $\Delta\overline{u}$ (lower panel) at 20 hPa, averaged over 30–50°N. In both panels, shaded bands give the confidence intervals, as computed in the way of Sect. 3.3.1, and thin lines give two standard deviations on each side of the mean. In the lower panel, the confidence interval is shaded in light green where the impact is statistically significant at the 95% level.

(3.18)). We then define time windows which span the 1991 SR, 1992 WR, and 1992 SR. Next, we individually integrate the TEM forcing terms from the left (time t_0) to the right (time t_1) ends of each window, all of which are given a common initial condition of $\overline{u}(t_0)$ as evaluated in the LV ensemble mean.

In this way, the sum of the integrated TEM impacts are identical to the integration of the $\Delta(\partial\overline{u}/\partial t)$, which in turn is identical to the observed $\Delta\overline{u}$. This procedure is described in detail in Appendix B.1, and the result is shown in Fig. 3.6(c)–(e). The intention is to visualize the *accumulated* contribution to the observed $\Delta\overline{u}$ by each of the large-scale TEM processes. In other words, each curve shown in panels (c)–(e) show the anomalous evolution of the wind in absence of all other forcings, given the shared initial condition. This is preferable to showing the forcing impacts themselves, since those often change sign on small temporal scales, and thus the noise would visually dominate over the meaningful trend.

Each integration time window is shown as a highlighted yellow-green strip in panel (b) at 10 hPa. The integrated tendency contributions are shown in panel (c) for the 1991 SR, panel (d) for the 1992 WR, and panel (e) for the 1992 SR. It is immediately apparent that while these westerly impacts appear similar from a thermal-wind perspective, they are in fact brought about by different mechanisms.

The summer-time responses of 1991 and 1992 (panels (c) and (e)), are characterized by a
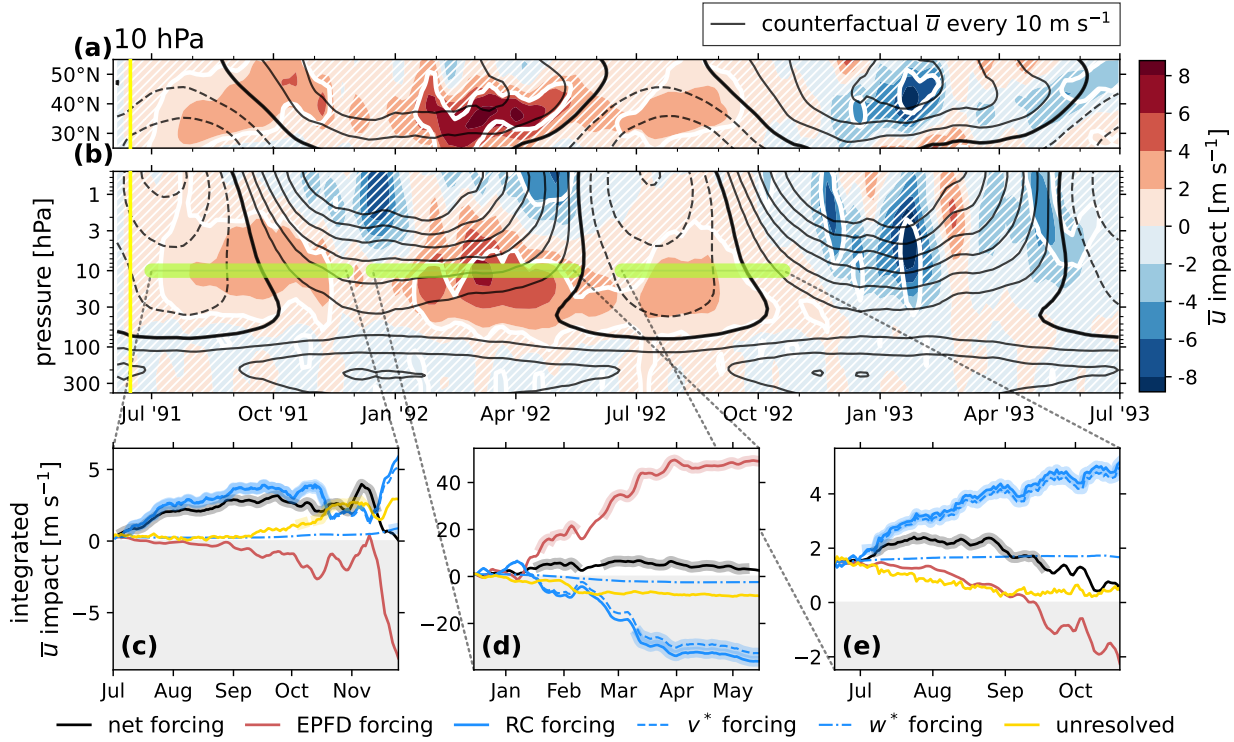
Figure 3.6: Vertical structure of the midlatitude zonal wind impacts, and the TEM balance impact at 10 hPa. Panels **(a)** and **(b)** show the ensemble-mean $\Delta\overline{u}$ as filled contours (colorscale), with the CF ensemble mean $\overline{u}$ overplotted as black contours, drawn every $10\ \mathrm{m\ s^{-1}}$, with negative contours dashed and the zero-line in bold. A bold white contour is drawn at 95% significance, with the $\Delta\overline{u}$ p-value computed as in Sect. 3.1. Regions of insignificance are filled with white hatching. **(a)** shows the latitude band from 25°N to 55°N at 10 hPa, reproduced from Fig. 3.4(b). **(b)** shows the meridional mean over 30–50°N, from 400 to 0.5 hPa, for two years following the eruption (which is indicated with a vertical yellow line). In panels **(c–e)**, curves show the integrated forcing imapct by the EPFD (red solid), by w^* advection (dash-dotted blue), by v^* advection and the associated Coriolis force (dashed blue), and by $\overline{X} = \overline{X}_{\mathrm{GW}} + \overline{X}_d$ (yellow solid). Also shown is the cumulative residual velocity forcing (blue solid), and the total forcing (black solid). The curves are backed by a thick shading of a matching color where they are statistically significant. Each term has units of $\mathrm{m\ s^{-1}}$ after time integration. The total forcing curve (black solid) matches the data on the colorscale in the corresponding highlighted region of panel (b). These data are computed according to Appendix B.1. The negative domain is shaded.

deficit of large-scale wave forcing, and a surplus of forcing by the residual circulation. While the magnitude of impact on each of these effects is comparable, it is the residual-circulation forcing that is favored in the imbalance, and is ultimately responsible for the manifest $\Delta\overline{u}$. Specifically, the forcing is almost entirely due to the impact on the meridional component, Δv^*, and can be interpreted primarily as a Coriolis-driven acceleration, while Δw^* is very

small (as expected in the extratropics). Toward the end of the integration time windows, it appears that an increasingly negative $\Delta(\text{EPFD})$ eventually dominates and brings the summer responses to an end. Impacts on gravity wave and diffusion forcing play a more minor role, and have opposite signs in 1991 and 1992.

On the other hand, the winter-time response is primarily wave-driven (panel (d)). From January to April 1992, $\Delta(\text{EPFD})$ and Δv^* are both large (nearly an order of magnitude larger than the previous summer), though the imbalance favors the former. This drives a net westerly acceleration. By spring of 1992, the TEM forcings are re-aligning with the reference runs (the integrated tendency curves are flattening), and the restored balance brings the winter response to an end.

In order to clarify the nature of these mechanisms of impact, Fig. 3.7, Fig. 3.8, and Fig. 3.9 show the complete TEM budget for the zonal-wind impact $\Delta \overline{u}$ in the meridional plane for select monthly means during the 1992 WR, 1991 SR, and the 1992 SR, respectively. In each of these figures, panel (a) shows $\Delta \overline{u}$, $\Delta \overline{u}$ significance, and $\overline{u}^{\text{CF}}$, in the way of Fig. 3.4. Panels (b)–(e) then show the impacts of the TEM forcing terms, and their significance, while panels (f)–(i) show the reference forcings from the CF ensemble. In panels (f) and (b), the CF EP flux vectors and their impacts are shown, respectively. Likewise, in panels (g) and (c), the CF Ψ^* tangent vectors and their impacts are shown, which have been scaled using a method detailed in Appendix B.3. In all panels (b)–(i), the significance contours from panel (a) are reproduced in black, for spatial reference. The monthly averaging periods were informed by Fig. 3.6, chosen such that we analyze times when the forcing impacts are strong (i.e. integrated curves in Fig. 3.6(c)–(e) are steep).

Figure 3.7 reiterates that the winter-time acceleration of westerly winds at the equatorward vortex edge are primarily a consequence of perturbed wave activity. Panel (b) shows a statistically significant surplus of large-scale wave drag (negative forcing impact) at the lower, equatorward edge of the region of significance in $\Delta \overline{u}$, and a deficit of drag aloft (positive forcing impact). Comparing the vectors of panel (b) and panel (f) reveals the cause for this effect. Relative to the CF ensemble mean, vertical and equatorward wave propagation is decreased near 50°N and 10 hPa, while it is enhanced near 30°N and 30 hPa. This result is exactly the "wave deflection" mechanism proposed by Bittner et al. (2016), where enhanced westerlies near 30°N alter the background condition for wave propagation in the surf zone, serving to steer Rossby waves away from the vortex. With those waves breaking at relatively lower latitudes, the vortex experiences less drag, and higher wind speeds. In our simulations, this effect does not extend to the vortex core, but the mechanism appears to be the same.

At the same time, the residual circulation contribution to the forcing impact opposes the CF condition at 10 hPa, but reinforces it at 30 hPa, and near the model top. Comparing
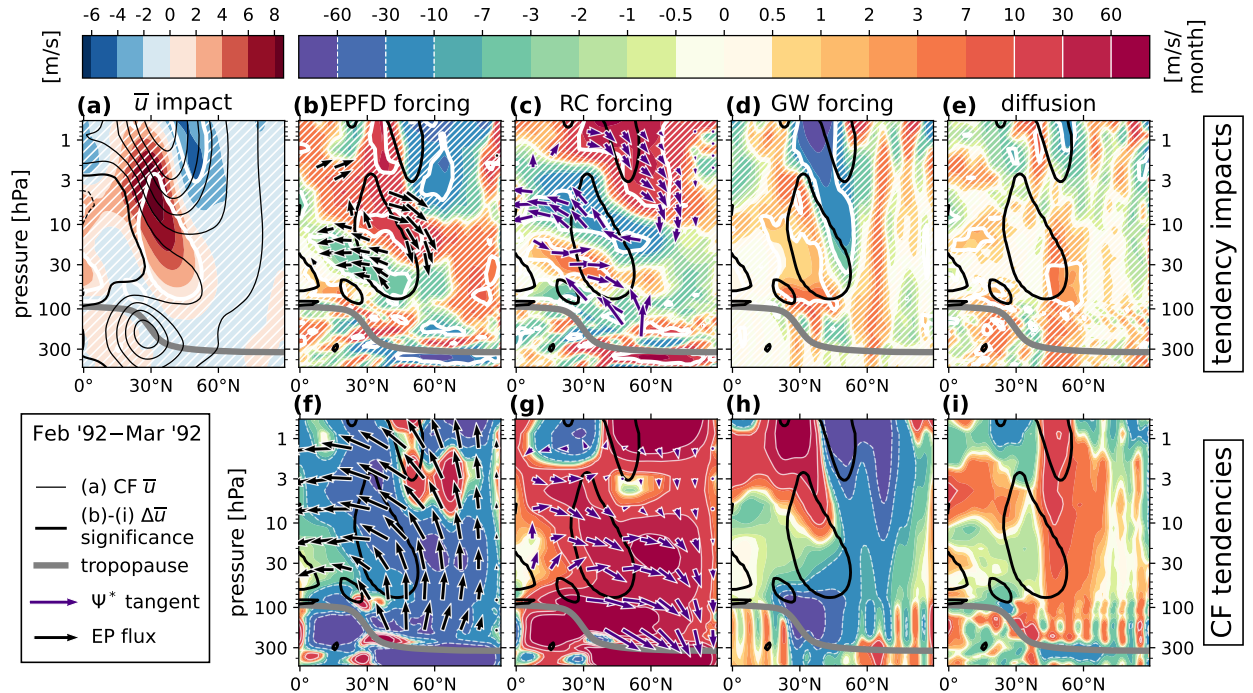
Figure 3.7: The complete TEM budget in the northern hemisphere meridional plane from 500 hPa to 0.5 hPa, averaged from February 1 1992 to March 1 1992. **(a)** the ensemble-mean $\Delta\overline{u}$ as filled contours (red/blue color scale), with the CF ensemble-mean $\overline{u}$ overplotted as black contours, drawn every 10 m s^{-1}, with negative contours dashed and the zero-line in bold. For every other vertical pair of panels, the top and bottom panels show the ensemble-mean impact and CF ensemble-mean of a variable as filled contours (rainbow colorscale). Specifically, **(b)** and **(f)** shows the EPFD forcing (Eq. (3.13)). Black vectors drawn in these panels show the significant ensemble-mean impact and the CF ensemble-mean EP flux vectors (Eq. (3.14, 3.15)), respectively, scaled according to Jucker (2021). The vector lengths are additionally log-scaled equally in length, in order to effectively visualize the vector directions. **(c)** and **(g)** show the residual-circulation forcing (Eq. (3.7) + Eq. (3.8)). Purple vectors drawn in these panels show the significant ensemble-mean impact and the CF ensemble-mean Ψ^* tangent vectors (Eq. (3.11)), respectively, scaled according to Appendix B.3. For both Ψ^* and the EP flux, vectors near and below the tropopause are removed. **(d)** and **(h)** show the gravity-wave forcing. **(e)** and **(i)** show the forcing by diffusion (Eq. (3.18)). On all panels, regions of 95% statistical significance are enclosed with a bold white contour for the variable plotted on the colorscale, and regions of insignificance are filled with white hatching. For spatial reference, the significance contour of the net impact $\Delta\overline{u}$ (bold white contour in panel (a)) is reproduced as a solid black contour in all other panels. Also plotted on all panels is the tropopause, as a bold grey curve. In the rainbow colorscale used for the tendencies, thin solid (dashed) white contours are drawn between all values larger than positive (negative) 10 m s^{-1}month^{-1} in magnitude.

66
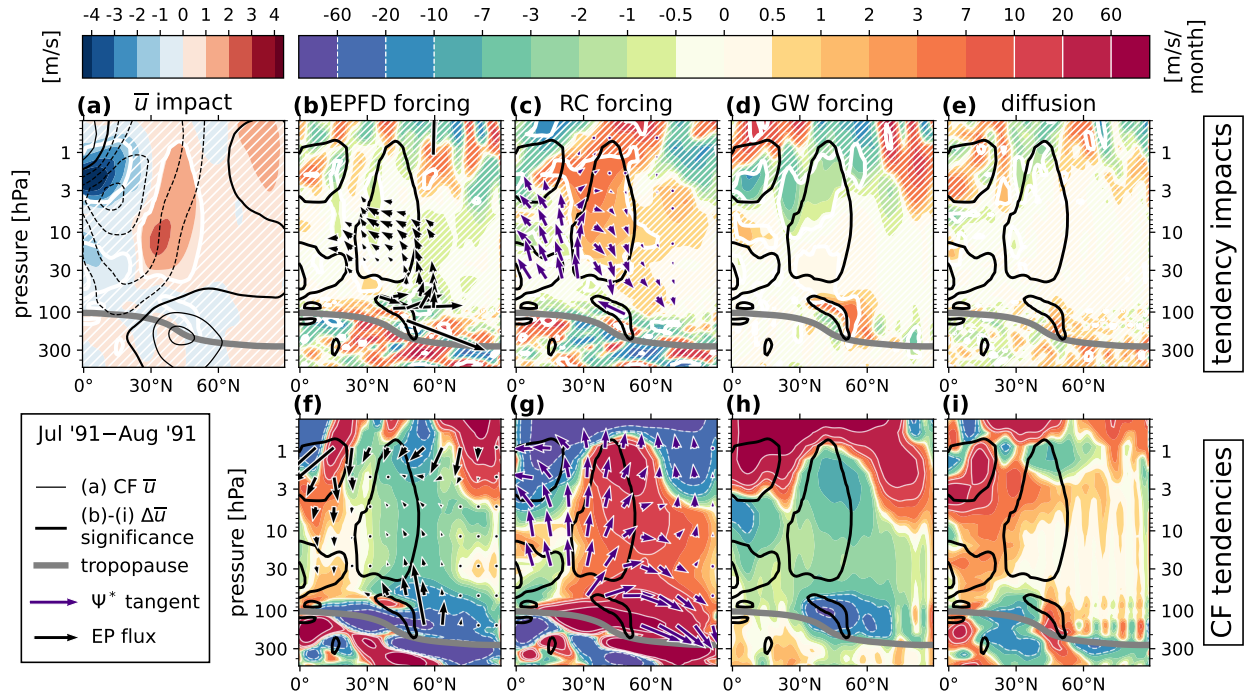
Figure 3.8: The complete TEM budget in the northern hemisphere meridional plane from 500 hPa to 0.5 hPa, averaged from July 1 1991 to August 1 1991. See the caption of Fig. 3.7 for full panel descriptions, considering the following modifications: In panel (**b**), the EP flux vectors are scaled in length to an order of magnitude smaller than the CF vectors in panel (**f**), and both set of vectors are linearly-scaled in length rather than log-scaled. In panels (**c**) the Ψ^* tangent vectors are scaled to two orders of magnitude smaller than the CF vectors in panel (**g**) in length, and both sets of vectors are log-scaled.

the vectors of panel (c) and panel (g), this appears to simultaneously suggest (1) a localized deceleration of the midlatitude shallow branch and (2) an acceleration of the deep branch of the advective BDC. In addition, panels (d,e,h,i) show that while positive impacts to the forcing by gravity wave drag and diffusion are present, they are minor contributors to the net response.

Figures 3.8 and 3.9 show the analogous results for the 1991 SR and 1992 SR, which reiterate that the summer-time westerly impacts are primarily a consequence of enhanced Coriolis torque from positive impacts on v^*. This is demonstrated in panels (c), which shows a strengthened poleward meridional circulation (vector fields), and an associated positive forcing impact over the entire region of $\Delta\overline{u}$ significance. These anomalous circulation cells project strongly onto the counterfactual residual circulation (panels (g)) at 10 hPa and below, which we interpret as an acceleration of the shallow branch of the advective BDC. During the summer of 1991, this acceleration is limited to the subtropics, but has expanded to the
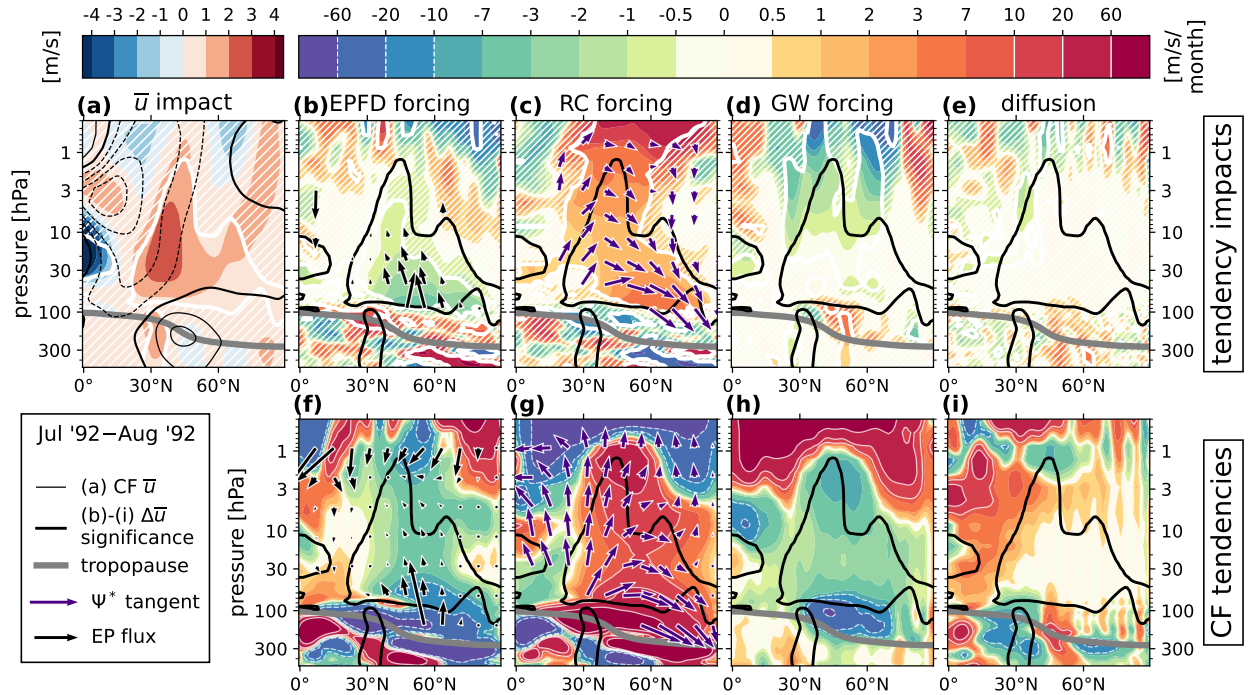
Figure 3.9: The complete TEM budget in the northern hemisphere meridional plane from 500 hPa to 0.5 hPa, averaged from July 1 1992 to August 1 1992. See the caption of Fig. 3.7 for full panel descriptions, considering the following modifications: In panel **(b)**, the EP flux vectors are scaled in length to an order of magnitude smaller than the CF vectors in panel **(f)**, and both set of vectors are linearly-scaled in length rather than log-scaled. In panels **(c)** the Ψ^* tangent vectors are scaled to two orders of magnitude smaller than the CF vectors in panel **(g)** in length, and both sets of vectors are log-scaled.

pole by the summer of 1992.

Meanwhile, in panels (b,f,d,h), we see that impacts to both resolved and unresolved wave drag are either weak, or oppose the sign of the net westerly impact. In the case of resolved Rossby waves, the EP flux vector impacts shown in panels (b) indicate that expanded regions of westerly $\overline{u}$ near 30 hPa and below are allowing vertical wave propagation, which would otherwise have been prevented by the presence of easterlies (especially in Figure 3.9).

3.5.2 Impacts in the Tropics

Figure 3.4(d, e) shows that the significant impacts to the zonal circulation in the tropics arise and persist over a much longer timescale than those in the midlatitudes. The first of these occur in the NH autumn 1991 at 10 hPa (Fig. 3.4(d)) as strong easterly, followed by westerly impacts between 20°S–20°N. The October 1991 mean given in Fig. 3.4(a) shows that this feature is paired with a complimentary tropical impact above 1 hPa, which may
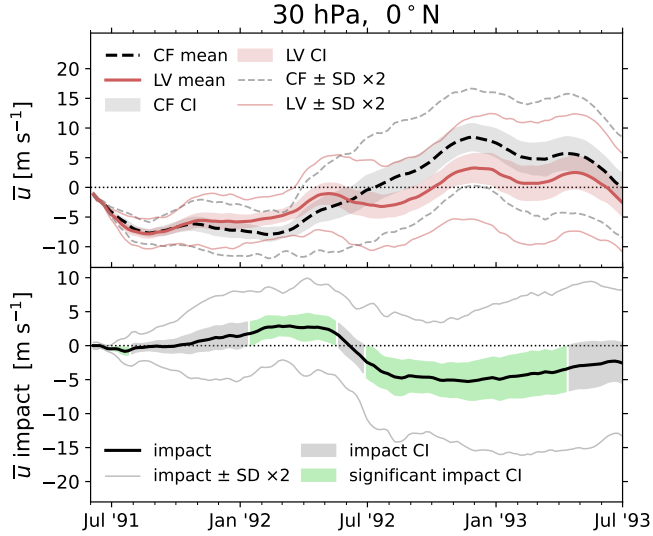
Figure 3.10: Time series of the CF ensemble-mean $\overline{u}$ and LV ensemble-mean $\overline{u}$ (upper panel) as well as the ensemble-mean $\Delta\overline{u}$ (lower panel) at 30 hPa, averaged over 5°S–5°N. In both panels, shaded bands give the confidence intervals, as computed in the way of Sect. 3.3.1, and thin lines give two standard deviations on each side of the mean. In the lower panel, the confidence interval is shaded in light green where the impact is statistically significant.

be understood as a lag in the descent of the westerly phase of the SAO. For the remainder of this study, we choose to ignore the SAO impacts for brevity and instead focus on the response of the QBO.

In our simulations, the Pinatubo eruption occurs during a descending easterly QBO phase, with easterly wind shear (see Fig. 3.2). This state persists for around 6 months, at which point a westerly shear develops in January 1992, and westerly winds descend to 30 hPa by July 1992. Figure 3.4(e) shows that a significant positive $\Delta\overline{u}$ occurs in the tropics from December 1992 to May 1992, and subsequently a significant negative $\Delta\overline{u}$ occurs from July 1992 to April 1993. We will refer to these features as the "westerly response" and the "easterly response", respectively. Both the westerly and easterly responses oppose their simultaneous QBO phase. Fig. 3.4 panel (b) suggests that the westerly response is a part of a broader summer impact in the low latitudes of the SH, while panel (c) shows that the easterly response is a localized feature which alters the QBO in particular. Together, we interpret these impacts as a significant (yet subtle) weakening of the QBO during the 2-year post-eruption period.

This QBO weakening is seen clearly in Fig. 3.10, which shows the separation of the LV and CF ensembles in one-dimension as $\overline{u}$ and $\Delta\overline{u}$ at 30 hPa, averaged over 5°S–5°N. The

69

standard deviation and confidence intervals are analogous to those shown in Fig. 3.5. This indicates that the easterly and westerly QBO phases are weakened by $\sim$3 m s^{-1} and $\sim$5 m s^{-1}, respectively (which approaches 50% of the CF ensemble mean values). The arrival of the westerly phase at 30 hPa also appears delayed by $\sim$2-3 months.

3.5.2.1 TEM Balance of the Tropics

We now investigate the impacts to the TEM balance associated with the weakened QBO. Figure 3.11 picks out the 5°S–5°N latitude band from Figure 3.4(e), and reproduces it in its panel (a). Panel (b) shows the vertically-resolved zonal-wind impacts averaged over this band. In the same way as Fig. 3.6, the integrated impacts of the individual TEM forcing terms are shown as functions of time over two targeted time windows. The first window (panel (c)) is positioned to study the TEM imbalance which generates the westerly $\Delta\overline{u}$ during the easterly QBO phase. The second window (panel (d)) is positioned to show the TEM imbalance which drives the transition from a westerly to easterly $\Delta\overline{u}$, as the westerly QBO phase descends.

Figure 3.11(c) indicates that the westerly response is driven by some combination of decreased large-scale wave drag (a positive EPFD impact) and an increased forcing by the residual circulation, though this effect is opposed by unresolved sources, implying enhanced gravity wave drag. Because of the high-Rossby-number environment in the tropics, forcing by the residual circulation is primarily advective. There are approximately equal contributions from v^* and w^*, as the zero-line of the streamfunction Ψ^* is generally located far from the equator at 30 hPa except near the equinoxes (see Fig. 3.1(a)–(d)). On the other hand, Fig. 3.11(d) shows that the transition from the westerly response to the easterly response, and thus the opposition to the descent of the westerly QBO phase, is due primarily to enhanced resolved and unresolved wave drag at 30 hPa, and has only an mild inhibiting contribution from residual circulation advection.

For a more complete picture of these mechanisms of impact, Fig. 3.12 and 3.13 show the complete TEM budget and its associated impacts in the meridional plane, averaged over one-month periods. The structure of these figures and the analysis is exactly analogous to that presented in Sect. 3.5.1.1. The averaging periods were again chosen to align with times of most rapid change in Fig. 3.11(c, d) (i.e. strongest TEM tendency impacts).

Fig. 3.12 shows the result for the easterly response during June of 1992. In panels (f)–(i), clearly the primary driver for the development of the QBO westerlies during this time is a positive gravity wave forcing (as also seen in Fig. 3.3). Panel (b) and (d) show that in opposition to this development is enhanced wave drag by resolved equatorial (Rossby and Kevlin) waves, and gravity waves. In particular, Panel (b) shows that the response is driven
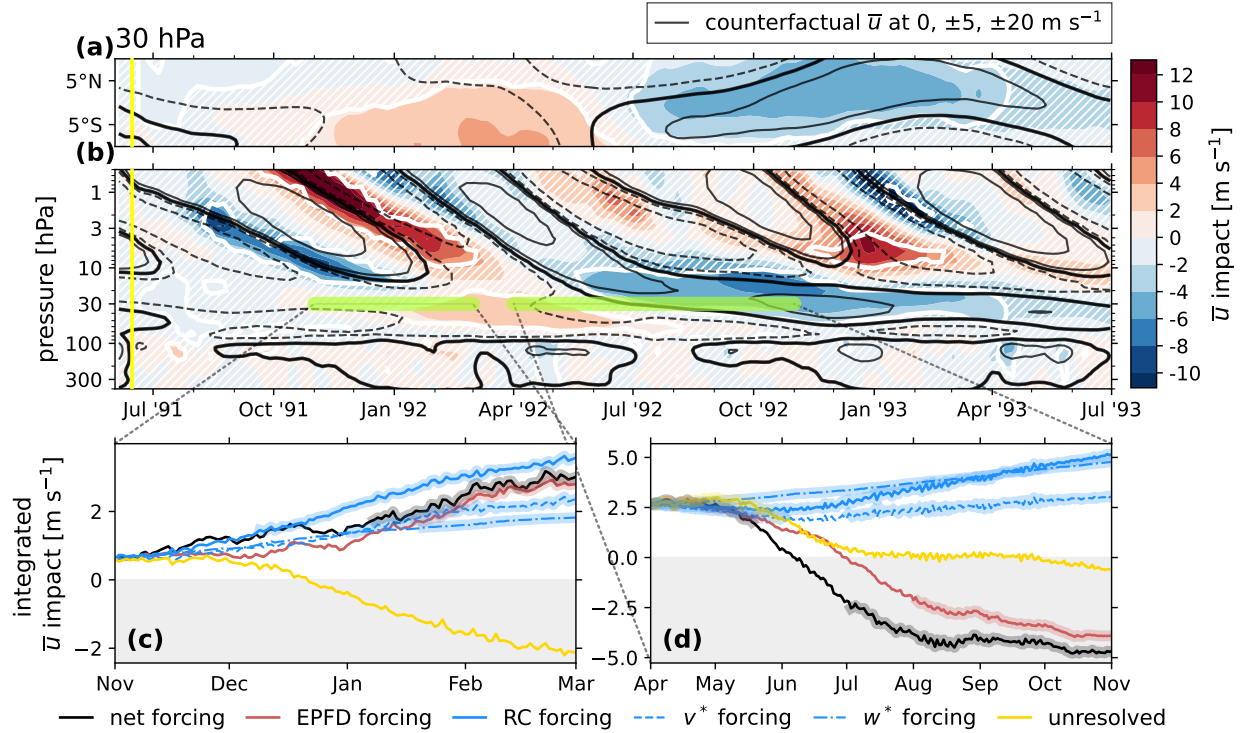
Figure 3.11: The same as Fig. 3.6, with the following modifications: panels (a), (c), and (d) are shown for the 30 hPa level. In panels (b), (c), and (d), the latitude band average is taken over 5°S–5°N. The CF $\overline{u}$ contours in panels (a) and (b) are drawn at 0, ± 5, and ± 20 m s^{-1}.

by an increased convergence of the EP wave activity flux, due to an enhancement of wave propagation from 30 hPa and below, near 5–10°S. The origin of this enhanced wave activity may be related to the westerly $\Delta \overline{u}$ observed south of the equator and below 30 hPa, but we did not investigate this further. We also note that there is a significant deficit to the meridional residual advection between 30-100 hPa (panels (c, g)), though this does not play a role in the easterly response in the QBO region.

Finally, Figure 3.13 provides the equivalent result for the westerly response during January of 1992. Most of the significant regions in the forcing impacts (panels (b)–(e)) are located near 10 hPa and above, which are associated with perturbations to the SAO. Focusing instead on the narrow QBO region near 30 hPa on 5°S–5°N, the suggestions of Fig. 3.11(c) are reiterated; the westerly response (and thus weakening of the easterly QBO winds) during this time are due in equal part to an enhanced EPFD (panel (b)), as well as a simultaneous strengthened w^* and weakened v^* (panels (c, g)).

We note that it is not immediately clear whether or not these results of Fig. 3.12 and 3.13 are congruent with previous studies of the QBO response to Pinatubo-like volcanic forcing

(e.g. Brown et al. (2023)), which often do not use a TEM framework. This comparison is considered further in Sect. 3.6.
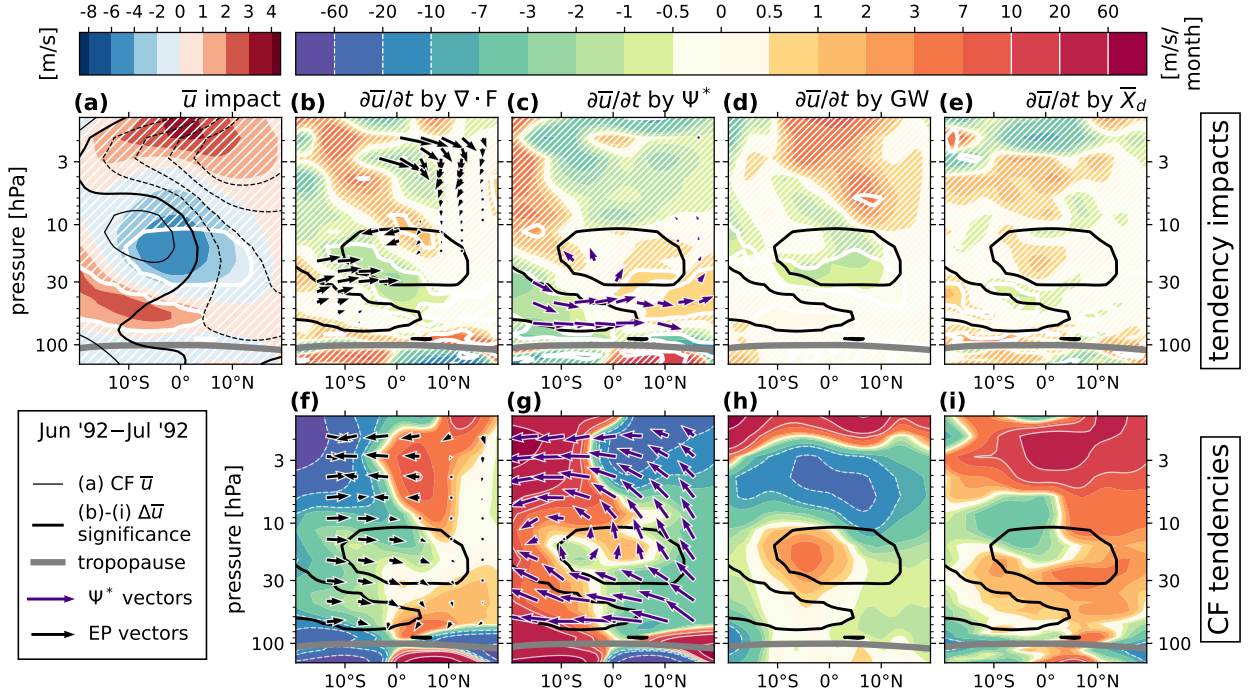
Figure 3.12: The complete TEM budget in the northern hemisphere meridional plane from 500 hPa to 0.5 hPa, averaged from June 1 1992 to July 1 1992. See the caption of Fig. 3.7 for full panel descriptions, considering the following modification: In panel **(b)**, the EP flux vectors are scaled in length to two orders of magnitude smaller than the CF vectors in panel **(f)**.
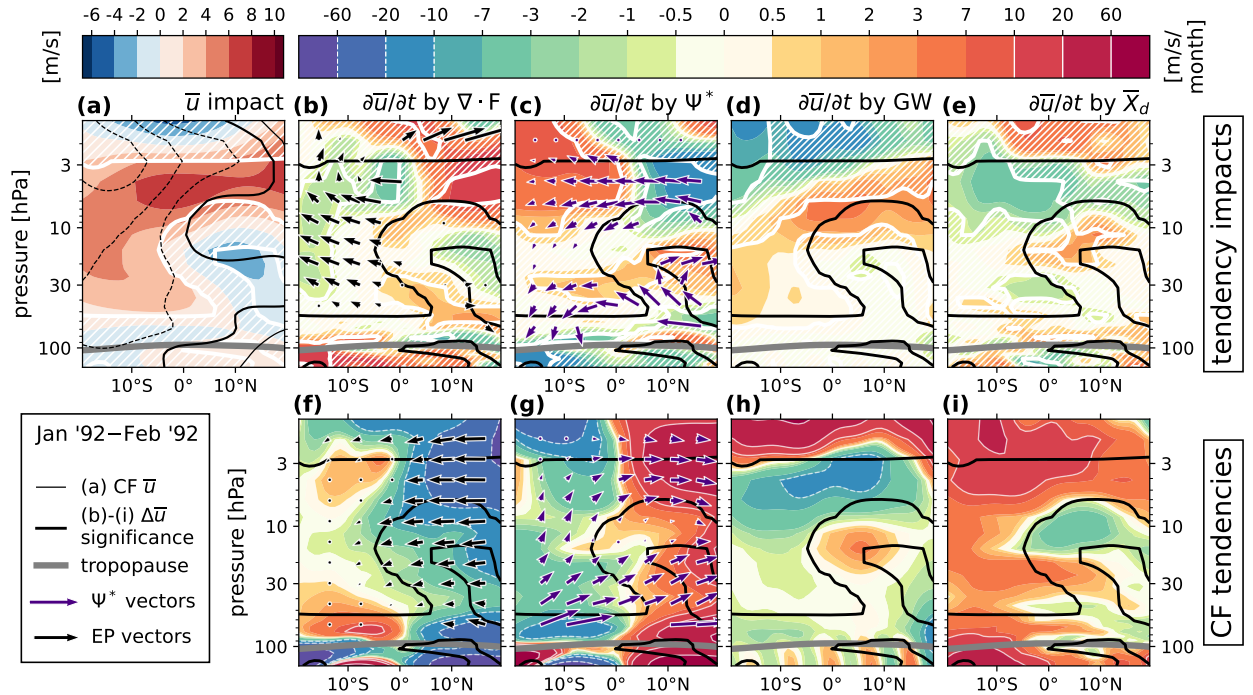
Figure 3.13: The complete TEM budget in the equatorial meridional plane from 500 hPa to 0.5 hPa, averaged from January 1 1992 to February 1 1992. See the caption of Fig. 3.12 for full panel descriptions.

3.6   Discussion of Comparable Results in the Literature

As noted in Sect. 3.5.1.1, the winter-time wave-deflection mechanism that we have identified is consistent with that proposed by Bittner et al. (2016). In that study, the effect is showcased for a much larger 55 Tg eruption. The authors noted, but did not show, that the effect was also detectable in their Pinatubo-sized eruption simulations, but was less robust. The fact that we are able to robustly identify the wave-deflection for a 10 Tg eruption may be due to several factors. First, the model employed by Bittner et al. (2016) was described as showing excessive interannual variability compared to observations, which as they suggest, "masks the response to the forcing of the volcanic aerosols". To demonstrate this, they show that while a 55 Tg eruption was able to force both a positive anomaly in the mean *and* a negative anomaly in the variability of the vortex region, a Pinatubo-sized eruption was only able to force the mean. In fact, they show that variability of the vortex instead *increased* during the winter of 1992, suggesting that the vortex had not been coherently forced across the ensemble members, despite the departure of the ensemble mean.

In our experiments, we don't observe the same masking by internal variability, at least not to the same extent, nor do we draw the same conclusion about the variability anomaly in
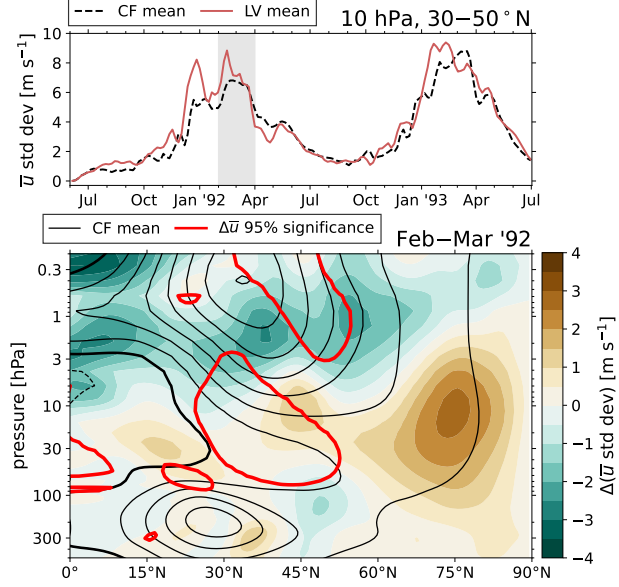
Figure 3.14: Variability of the polar vortex region in the LV and CF ensembles. **(top)** standard deviation of $\overline{u}$ at 10 hPa, averaged from 30° to 50°N, for the LV (red solid) and CF (black dashed) ensemble means. **(bottom)** the impact (difference between LV and CF ensemble means) of the $\overline{u}$ standard deviation averaged over February and March 1992, as filled contours (colorscale). The time average was chosen to match Fig.3.7(a), and is indicated by a grey band in the top panel. Also plotted is the CF ensemble mean $\overline{u}$ (black contours), with negative values dashed and the zero-line in bold. Solid red contours show the $\Delta\overline{u}$ statistical significance (i.e. the bold white contours of Fig.3.7(a)) for reference.

the vortex region. Figure 3.14 compares the northern-hemisphere variability between the CF and LV ensemble members. The top panel shows a time series of the standard deviation in $\overline{u}$ at 10 hPa, averaged over 30–50°N (matching the latitude band of Fig. 3.7). This shows that the midlatitude variability in the LV ensemble does exhibit intermittent increases during the winter of 1992. However, in the bottom panel, we see that the largest increases in variability are located at the lower poleward edge of the vortex (near 75°N, 3–30 hPa), and are not necessarily associated with the significant westerly response that we observed. Within the region of significant $\Delta\overline{u}$ (red contours), the variability either increases by less than 1 m s^{-1}, or decreases. The variability also decreases near the vortex core (near 35°N, 0.3–3 hPa). Indeed, comparing our Fig. 3.7(a) and Fig. 3.14 to Fig. 4 and Fig. 10 in Bittner et al. (2016) suggests that our more robust detection of the wave-deflection mechanism is owed to a relative lack of interference from background internal variability.

Bittner et al. (2016) state that the reason for the increases of vortex-region variability in their volcanic simulations is unclear. At present, we can only speculate as to the relevant dynamical differences between their model and E3SMv2-SPA. It may be that the QBO is

playing a role. Because an easterly QBO phase exists throughout the winter of 1992 in our simulations, we might expect that the vortex should be weakened, and thus destabilized, by the Holton-Tan effect (Holton and Tan, 1980; Lu et al., 2020). However, Fasullo et al. (2024) recently demonstrated that in general, E3SMv2 fails to represent any Holton-Tan-type coupling between the QBO and the extratropics—that is, winter vortex speeds do not decrease relative to a climatological average during easterly QBO states. Not only does this suggest lesser vortex variability than expected, but it also hints that the background wave activity needs to be fully understood if we are to properly interpret significant post-eruption EP flux anomalies. As the Holton-Tan effect essentially describes QBO-induced changes in Rossby waveguiding in the midlatitudes, it's plausible that the strength (or lack thereof) of the effect could directly interfere with the volcanic aerosol wave-deflection mechanism. A potential avenue for future works is to investigate this interaction more directly, by inspecting e.g. post-eruption anomalies in potential vorticity and Rossby refraction index distributions. Similar work has recently been done in a stratospheric aerosol injection (SAI) geoengineering context (Karami et al., 2023).

On another note, Post-Pinatubo summer-time anomalies have received less attention in the literature. In their idealized model studies, DallaSanta et al. (2019) observed that the quiescent summer stratosphere experiences a westerly forcing similar to that of the winter vortex region, which they attribute generically to eddy-driven effects. Toohey et al. (2014) gave more specific consideration to westerly anomalies in the austral summer of 1991 through their simulations with prescribed volcanic forcing. They observed that these anomalies were associated with a statistically significant increase in large-scale wave drag (EPFD), and an accelerated residual circulation (consistent with our Fig. 3.6), though they did not show how these effects contribute to the TEM momentum budget. Moreover, Bittner et al. (2016) did not analyze summer-time anomalies in either hemisphere, and so it has been left unclear whether or not some form of wave-deflection effect acts there as well. Our study has shown that if a similar wave-driving is present, it does not rise to a level that exerts control over the manifest wind anomalies. Rather, the summer-time response is primarily driven by enhanced Coriolis torque due to an acceleration of the advective BDC.

In the tropics, our results read differently than the studies of Brown et al. (2023), though they are not necessarily contradictory. In that paper, the authors describe that the fundamental interaction between volcanic aerosol forcing and the QBO is an increased tropical upwelling, which slows the descent of the coming QBO phase. Our results agree that enhanced diabatic upwelling is the dominant initial response in the tropical region (Fig. 3.8(c)), but this does not immediately result in robust impacts on the QBO itself. This is likely because the Pinatubo eruption is offset from the equator, near 15°N, whereas the aerosol injection

used by Brown et al. (2023) was on the equator. However, by the time significant tropical impacts do arise in our simulations (during boreal spring of 1992) the TEM balance does not indicate that anomalous diabatic vertical motion is responsible. In fact, the weakening of the QBO amplitude and delay of the westerly phase descent during boreal summer of 1992 is due largely to increased large-scale and gravity wave drag (Fig. 3.11).

This apparent contradiction is resolved by the differences in the analysis framework. It must be emphasized that what Brown et al. (2023) calls "vertical momentum advection" is specifically $w \times \partial u / \partial z$. This is not the same as $w^* \times \partial u / \partial z$; the difference is a contribution of the meridional derivative of the eddy streamfunction ψ (Eq. (3.10)). In other words, an Eulerian-mean upwelling impact Δw evaluated on a pressure-based vertical coordinate will always be some combination of eddy effects and residual-circulation advection from a TEM perspective. Our results indicate that the former can often dominate over the latter in controlling the response of the QBO region. Given the extent of our analysis, we are unable to determine if this conclusion is generic, or if it is particular to an easterly-to-westerly QBO transition. It also may be that the conclusion would change for anomalies that occur closer in time to the eruption.

3.7 Conclusions

The goal of this study was to use the TEM analysis framework to identify the dynamical processes in control of the development and deterioration of statistically significant zonal wind anomalies following a large tropical volcanic eruption. The essential result is that, in E3SMv2, while midlatitude westerly anomalies appear consistently for over one year in the post-eruption atmosphere, the processes controlling those anomalies are different during the summer and winter. For Pinatubo-sized eruptions occurring during summer in the NH, the initial response is enhanced tropical upwelling, which by mass continuity drives an accelerated BDC, and thus increased zonal wind speeds northward of 30°N (Fig. 3.6, Fig. 3.8). With these westerly anomalies established, the winter stratosphere is primed for lower-stratosphere equatorward wave-deflection, which acts to further intensify upper-level westerly winds in the vortex region (Fig. 3.6, Fig. 3.7).

The initial upwelling response is as close to a direct aerosol effect that we observed, while the subsequent midlatitude accelerations are indirect consequences of the modified mean meridional circulation, and wave propagation. Moreover, the initial upwelling effect does not result in robust wind responses even in the tropical region. Rather, we did not identify significant volcanic impacts on the QBO until the winter of 1992, which were largely wave-driven effects in opposition of the simultaneous QBO phase (Fig. 3.11).

Our specific conclusions are as follows:

1. We concur with Bittner et al. (2016) that large-scale equatorward wave deflection near the surf zone contributes to post-eruption westerly anomalies in the winter vortex region.

2. We found that the wave-deflection argument holds only in the winter hemisphere. Westerly anomalies in the midlatitude summer stratosphere are instead explained almost entirely by an accelerated residual circulation, and thus an anomalous Coriolis forcing of momentum.

3. We observed that a weakened QBO amplitude and a delayed descent of the westerly QBO phase during summer of 1992 was caused primarily by enhanced large-scale and gravity wave drag near 30 hPa. This finding is not necessarily inconsistent with previous studies that instead emphasize the role of perturbed tropical upwelling, as noted in Sect. 3.6. Effectively, we have identified that the anomalous Eulerian-mean upwelling of momentum affecting the QBO in this context is eddy-driven, rather than simply an enhanced diabatic vertical motion.

4. Practically, we find that regions of robust zonal-wind anomalies can indeed be associated with equally robust forcing anomalies as diagnosed in a TEM framework. However, co-location of these wind and forcing anomalies in space and time is not required; regions where forcing anomalies are insignificant can give rise to significant wind responses, and those responses, once established, may persist after the forcing anomaly ceases.

To our knowledge, this is the only work after Bittner et al. (2016) to demonstrate the wave-deflection pathway in the post-eruption winter stratosphere, and the first to provide a full-accounting of the TEM momentum balance during specific periods of anomalous stratospheric zonal-winds in a volcanic forcing experiment. At this point, we see at least two directions for continued research. As we did not know whether robust wave-driven mechanisms of impact would arise in our simulations, our analysis stopped short of investigating the origin and behavior of the anomalous wave activity in more detail, which could be pursued (see discussion in Sect. 3.6). In an upcoming work using these same datasets, we will explore the volcanic impacts to the residual streamfunction more directly, as well as the resulting pertubations to stratospheric transit times of trace gases, and stratosphere-troposphere mass exchange.

CHAPTER IV

Volcanic Modification of the Stratospheric Circulation: Tracer Transport

Abstract

Great attention has been paid to the short-term climate response to large volcanic eruptions, by observational and modeling campaigns alike, in order to understand effects on zonal winds, the polar vortex, and surface temperature effects across latitude. In contrast, several works have shown that evidence of a strong tropical radiative forcing can persist for much longer in the chemical composition of the stratosphere, even after the instigating aerosol population has dissipated. Heating by volcanic aerosols accelerate tropical upwelling, and thus drive an acceleration of the global Brewer-Dobson Circulation (BDC), and enhance troposphere-to-stratosphere mass exchange. Once the average tropical motion, and thus the BDC returns to their climatological mean, the introduction of excessive tropospheric air remains detectable for at least 5 years. In this work, we use two artificial inert tracers, age of air (AoA) and e90, in order to diagnose the change to stratospheric composition following the simulated 1991 eruption of Mt. Pinatubo. Specifically, we employ a paired set of volcanic and nonvolcanic 15-member simulation ensembles from the E3SMv2 climate model in order to identify statistically significant effects on the AoA and e90 zonal-mean mixing ratios. In addition, we use a Transformed Eulerian Mean (TEM) tracer framework, as well as the Residual Circulation Transit Time (RCTT) diagnostic to separate the effects of advective transport, and two-way mixing. We find that the Pinatubo eruption lowers AoA in the middle-to-upper stratosphere globally. This response is primarily due to an accelerated residual meridional circulation, but a robust contribution from midlatitude mixing is also identified. In particular, we see a localized increase of AoA near 20–100 hPa in the hemisphere opposite the eruption, which we attribute to a dampening of the seasonal BDC cycle by the volcanic aerosols. In addition, we show that volcanic impacts on both AoA and e90 scale approximately linearly with eruption magnitude in the range 3–15 Tg of initial SO_2.

4.1 Introduction

Thus far, this thesis has focused primarily on dynamics; Chapter 2 provided an idealized picture of post-volcanic perturbations of atmospheric temperature, and Chapter 3 investigated the large-scale mechanisms which control subsequent zonal wind anomalies. We saw that the wind response was intermittent, with a notable seasonal dependence, but that the timescale of both the temperature and wind anomalies are ultimately governed by the volcanic sulfate aerosol decay. From a climatological point of view, the response is approximately instantaneous with respect to the radiative forcing, and we can generally expect that the stratospheric dynamics and sulfate concentrations will return to their climatological averages in tandem. In our simulations, this timescale is about 2 years.

We now turn our attention to stratospheric composition. In Chapter 3, the residual circulation (v^*, w^*) was discussed, primarily in regards to it's seasonal forcing of zonal wind. This forcing mechanism, as expressed in the TEM framework, is a combination of direct advection of momentum, and a Coriolis torque induced by the meridional component of the circulation. The strength of these effects develop and deteriorate over the year, with minimum (maximum) forcing in the summer (winter) hemisphere. This may naively lead us to conclude that the most important modes of stratospheric variability are essentially seasonal-to-annual. However, advection of trace gases by the residual circulation, and thus the genesis and depletion of stratospheric chemical concentrations, operate on much longer timescales. In this chapter, it will be demonstrated that the volcanic effects on zonal temperature and momentum are progenitors for robust, decadal-scale anomalies in the distributions of trace gases in the stratosphere. To this end, we will make use of two artificial diagnostic tracer species; one to measure the residence times of trace gases in the stratosphere, and another to measure rates of troposphere-stratosphere mass exchange.

First, a brief primer is in order. The Brewer-Dobson circulation (BDC) was first inferred and described in the works of Brewer (1949) and Dobson (1956) in an effort to explain observed concentrations of ozone, water vapor, and other stratospheric tracer constituents. The BDC describes the net flux of mass in the meridional plane, as the superposition of an advective component, and an eddy-driven component. Tracer isopleths (surfaces of constant mixing ratio) are raised and lowered in the tropics and polar regions, respectively, by the thermally-direct overturning cell that is the residual circulation. In the midlatitudes, isopleths are homogenized by two-way adiabatic mixing of mass along isentropes, caused by breaking planetary waves in the surf-zone (e.g. Plumb (2007)). In other words, the BDC is essentially an expression of TEM balance from a tracer perspective.

Through both observations and model studies, it is now understood that the full traversal

of the BDC, in a Lagrangian sense, takes up to 5–7 years (Butchart, 2014; Waugh and Hall, 2002). This traversal timescale can measured by the so-called stratospheric age of air (AoA), which has a rich history in the literature since at least the 1990's (see Waugh and Hall (2002) for a comprehensive review). The "age" of an air parcel is defined as the elapsed time since its last contact with some reference location, which is usually taken to be the tropical tropopause. In a modeling context, AoA is often implemented as a scalar "clock tracer", with a globally uniform source (it "ticks"), and local concentrations corresponding to mean age.

Early implementations were published by Hall and Prather (1993), Hall and Plumb (1994) and Neu and Plumb (1999). More recently, Gupta et al. (2020, 2021) implemented AoA tracers in a variety of dynamical cores in order to test their sensitivity to numerical schemes and spatial discretizations. Meanwhile, several recent works have made strides in disentangling the advective and eddy-driven components of the BDC, and their contributions to the climatological AoA distribution. A key development was by Birner and Bönisch (2011), who introduced the residual circulation transit time (RCTT), which identifies the age distribution arising purely from transport. The RCTT is obtained by solving for "backward trajectories" connecting each point in the latitude-altitude plane to a crossing of the tropopause, by integrating over the time-varying residual circulation (v^*, w^*) in reversed time. Later, Garny et al. (2014) pointed out that the difference (AoA−RCTT) could be used to isolate aging by isentropic mixing, which throughout much of the upper atmosphere was shown to be at least as important as aging by transport. While this type of differencing is a useful procedure, it is also a blunt one, as it cannot separate contributions of mixing by resolved wave breaking, and diffusion.

On the other hand, we know from the analysis outlined in Chapter 3 that a more fine-grained decomposition of AoA tendencies should be theoretically feasible. Ploeger et al. (2015a,b) and Dietmüller et al. (2017) demonstrated a method to this end, by computing a set of RCTT trajectories, and then integrating the the local tracer mixing tendency $\mathbf{M}$ over those paths. As we will see in Sect. 4.3, the quantity $\mathbf{M}$ is exactly analogous to the EP-flux divergence (EPFD) in the TEM equation for the zonal-wind $\overline{u}$.

AoA anomalies arising in response to both persistent and transient forcing sources are numerous in the literature. Long-term AoA trends in coupled historical simulations have been used to study the response of the BDC to anthropogenic climate change, where the typical finding is decreased age (an accelerated BDC) throughout the lower stratosphere (Muthers et al., 2016; Garfinkel et al., 2017; Ploeger et al., 2019; Abalos et al., 2021). In the case of the SAI geoengineering simulation studies of Richter et al. (2017), the authors showed anomalies in the residual vertical velocity w^* consistent with an accelerated BDC, but did

not show the associated AoA effects. Several works have also concluded a likely accelerated BDC after large volcanic eruptions (Pitari, 1993; Eluszkiewicz et al., 1996; Toohey et al., 2014), while some (Garcia et al., 2011; Pitari et al., 2016) have directly shown decreases in stratospheric AoA by several months for the 1991 Pinatubo event specifically.

The goal of the present chapter is to study the significant post-volcanic impacts on the AoA tendency balance, as we did for $\overline{u}$ in Chapter 3. The key question is this: what are the relative contributions of perturbed transport and perturbed mixing in producing the net impact on stratospheric AoA post-eruption?

To this end, we draw some inspiration from adjacent works which pose the same problem to different tracers species. (Abalos et al., 2013) showed the closed TEM tracer budget in the meridional plane for ozone (O_3) and carbon monoxide (CO) over a 6-year dataset. In a generalization of this work, they later investigated the closed TEM budget for the so-called e90 tracer (Abalos et al., 2017). e90 has a uniform and constant surface emission, and a 90-day e-folding timescale throughout the atmosphere. The steady-state includes high e90 concentrations in the troposphere, low concentrations in the stratosphere, and a steep mixing-ratio gradient at the tropopause. The vertical gradient makes the e90 distribution uniquely sensitive to perturbations to troposphere-stratosphere mass exchange, and it thus qualitatively resembles the behavior of real-world substances in this region, like O_3 and CO.

In addition to the AoA investigations outlined above, this chapter will also study the significant volcanic effects on the e90 tendency budget. In combination, the e90 impacts will identify perturbations to cross-tropopause mass exchange, and the AoA impacts will identify how the broader stratospheric circulation changes as a result. Section 4.2 will describe the simulated datasets employed. Section 4.3 introduces the analysis framework, including the tracer definitions, the tracer TEM balance, and the method of computing the RCTT. Section 4.4 presents the climatological behavior of AoA and e90 in our simulations, and Sect. 4.5 explores the identified impacts in the two diagnostic tracers. Section 4.6 considers the sensitivity of the identified impacts with eruption magnitude, and finally section 4.7 provides a discussion on the results and concluding remarks.

4.2 Simulations

This chapter utilizes the same simulations as in Chapter 3, described in detail in Sect. 3.2. Briefly, we used the E3SMv2-SPA model (Brown et al., 2024) to simulate the eruption of Mt. Pinatubo, which evolves volcanic SO_2 and sulfate aerosols via a prognostic treatment, on a $\sim 1°$ horizontal grid and a 72-level vertical discretization extending to approximately 60 km. We again use the paired limited-variability volcanic ensemble (LV) and its counterfactual

ensemble (CF), introduced by Ehrmann et al. (2024), for the impact analysis. Both ensembles include 15 members covering an approximately 7.5-year time period from June 1 1991 to January 1 1999. The CF ensemble omits the volcanic eruption, and each LV–CF member pair shares identical initial conditions. Statistically-significant departures of the LV ensemble mean from the CF ensemble mean are thus interpreted as the isolated volcanic impact. For this chapter, we primarily use the same 10 Tg SO_2 eruption as Chapter 3, while Sect. 4.6 will additionally include a brief analysis of the tracer sensitivity with respect to eruption magnitude, by employing additional LV ensembles with 3, 5, 7, 13, and 15 Tg SO_2 eruptions.

The AoA and e90 tracer mixing ratios were computed at each gridpoint during the model run. Here, we will use the zonal-average of the tracer fields. For computing the residual circulation transit time, history of the residual velocity components v^* and w^* was required for a period of 10 years prior to the time of analysis. Because the LV ensembles were all initialized on June 1 1991, we were required to concatenate the v^* and w^* time series from the LV runs, and the simulation run from which the perturbed LV initial conditions were seeded. We will refer to the latter as the first prior simulation (PS1). The PS1 included only 3-years of model integration prior to the LV initialization, and so 7 more years were also required from a second prior simulation (PS2), which in turn seeded the PS1. The concatenation of the PS1, PS2 and a single LV ensemble member is illustrated in Fig. 4.1 for a midlatitude gridpoint at 10 hPa. RCTT integration bounds on select dates are plotted for reference.

The PS1 and PS2 were derived from E3SMv2-SPA with a configuration equivalent to the LV and CF runs, though in principle there are discontinuities at the concatenation points. In part, this is because the PS2-to-PS1 and the PS1-to-LV transitions involve random temperature perturbations on the order of 10^{-14} K, as those times both served as points of ensemble initial condition generation (the PS1 is a member of different ensemble, which is not discussed here). In addition, while the winds across the PS1-to-LV transition are approximately continuous, non-volcanic climate forcing sources are not. This is because the PS1 and LV calendars are different, and needed to be manually aligned (see Ehrmann et al. (2024) for details). Because the RCTT results from long-time integrations over monthly-averaged v^* and w^*, we expect the consequences of this feature on the results to be minimal. To whatever extent this discontinuity is present in the recovered transit times, it is present equally in the LV and CF ensembles, and thus will be removed when taking the (LV−CF) impact.
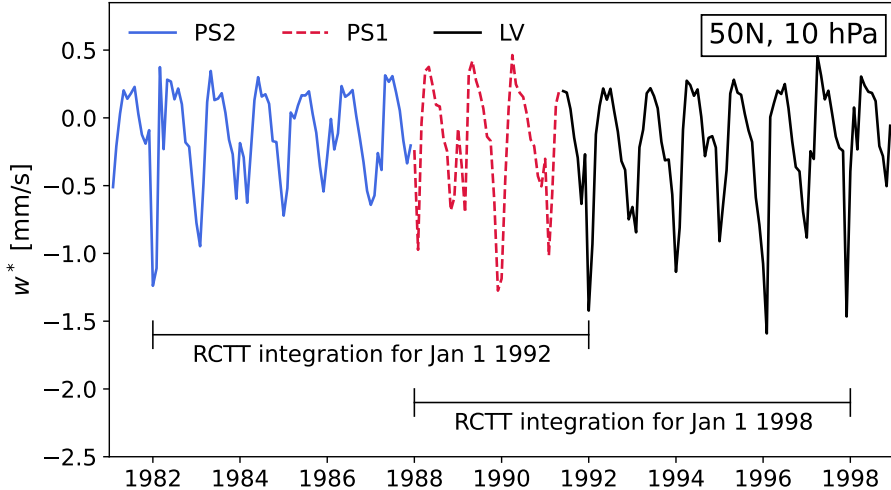
Figure 4.1: Concatenated time series of the residual vertical velocity w^* at 50°N, 10 hPa for a single LV ensemble member (June 1 1991 to Jan 1 1999; black solid line), the PS1 simulation (Jan 1 1988 to June 1 1991; red dashed line), and the PS2 simulation (Jan 1 1982 to Jan 1 1988; solid blue line). Two example RCTT integrations are annotated as bracketed black lines. The RCTT on Jan 1 1992 is computed by residual velocity integration over the decade 1982–1992, and likewise for the RCTT on Jan 1 1998 and the decade 1988-1998.

4.3   Analysis Framework

As in Chapter 3, we express the post-eruption anomalies in AoA and e90 as impacts, defined as the ensemble mean of the difference (e.g. $\Delta\mathrm{AoA} \equiv \mathrm{AoA}_{\mathrm{LV}} - \mathrm{AoA}_{\mathrm{CF}}$), as in Eq. (3.1). See Sect. 3.3.1 for details. Both a tracer-form of the TEM equations and the RCTT will be used to diagnose the impacts on transport and mixing separately. The tracer sources and sinks, as well as the TEM and RCTT formulations are defined below.

4.3.1   Tracer definitions

Recall from Chapter 2 that tracers in E3SM are stored as dimensionless mixing ratios, i.e. (kg of tracer)/(kg of air), within each cell in the simulation grid. While this is an appropriate choice for material substances, the interpretation changes for age of air, where instead the dimensionless tracer value equals a number with an implicit unit of time. As such, we implemented the AoA tracer with a constant production rate of

$$\frac{\partial \mathrm{AoA}}{\partial t} = \frac{1}{86400}\mathrm{s}^{-1} = 1\,\mathrm{day}^{-1}. \tag{4.1}$$

everywhere above 700 hPa. Below 700 hPa, we impose an "instantaneous sink", by directly setting

$$\text{AoA} = 0, \tag{4.2}$$

$$\frac{\partial \, \text{AoA}}{\partial t} = 0 \, \text{s}^{-1}$$

The result is a tracer with a dimensionless mixing ratio that is equal in value to the mean age since last contact with the < 700 hPa layer, in number of days. This is similar to the implementation of Gupta et al. (2020), but with the source located above rather than below the surface layer threshold (the opposite approach requires subtraction of the model time from the AoA mixing ratios, but is funcitonally identical).

The e90 tracer is emitted at the lowest model level, with a surface flux chosen to agree with Abalos et al. (2017),

$$\Phi_s = 28 \times A^{-1} \left(2.7736 \times 10^{11}\right) \text{g cm}^{-2}\text{s} \tag{4.3}$$

where A is Avogadro's constant, and 28 is the molecular weight of CO in g mol^{-1}. Once emitted, the tracer is subject to a constant 90-day e-folding decay rate as

$$\frac{\partial \, \text{e90}}{\partial t} = -\frac{\text{e90}}{90 \times 86400} \, \text{s}^{-1} \tag{4.4}$$

These tracers are were present in E3SMv2, so we implemented them as a part of this research. For readers interested in the technical implementation, a detailed code-level tutorial for the E3SMv2 model is provided in Appendix F.

4.3.2 Tracer TEM framework

The TEM formulation for the evolution of a zonal-mean tracer mixing ratio $\overline{q}$ is analogous to the formulation for zonal momentum $\overline{u}$ (see Sect. 3.3.2). The time-tendency of $\overline{q}$ is written as

$$\frac{\partial \overline{q}}{\partial t} = \frac{\partial \overline{q}}{\partial t}\bigg|_{(v^*)} + \frac{\partial \overline{q}}{\partial t}\bigg|_{(\omega^*)} + \frac{\partial \overline{q}}{\partial t}\bigg|_{\nabla \cdot \mathbf{M}} + \overline{X} + \overline{S}. \tag{4.5}$$

The first and second terms represent tracer transport by the residual circulation,

$$\frac{\partial \overline{q}}{\partial t}\bigg|_{(v^*)} = -v^* \frac{\partial \overline{q} \cos \phi}{\cos \phi \partial \phi} \tag{4.6}$$

$$\frac{\partial \overline{q}}{\partial t}\bigg|_{(\omega^*)} = w^* \frac{p}{H} \frac{\partial \overline{q}}{\partial p} \tag{4.7}$$

which are analogous to Eq. (3.7) and Eq. (3.8), except that there is no Coriolis force acting on $\overline{q}$. The residual velocities v^* and w^* are defined in Eq. (3.9) and Eq. (3.10), respectively. The third term on the right of Eq. (4.5) is the eddy-driven tracer mixing tendency,

$$\frac{\partial \overline{q}}{\partial t}\bigg|_{\nabla \cdot \mathbf{F}} = \frac{\nabla \cdot \mathbf{M}}{a \cos \phi}. \tag{4.8}$$

The vector $\mathbf{M}$ is the eddy-tracer flux vector, with meridional and vertical components

$$M_{(\phi)} = a \cos \phi \left(\frac{\partial \overline{q}}{\partial p} \psi - \overline{q'v'} \right) \tag{4.9}$$

$$M_{(p)} = a \cos \phi \left(-\frac{\partial \overline{q} \cos \phi}{a \cos \phi \partial \phi} \psi - \overline{q'\omega'} \right) \tag{4.10}$$

where ψ is the eddy streamfunction defined in Eq. (3.11). The eddy-tracer flux divergence (ETFD) is

$$\nabla \cdot \mathbf{M} = \frac{\partial M_{(\phi)} \cos \phi}{a \cos \phi \partial \phi} + \frac{\partial M_{(p)}}{\partial p} \tag{4.11}$$

These forms are analogous to the E-P flux vector and it's divergence which governs the TEM momentum forcing by resolved waves (Eq. (3.13)), except that $\overline{u}$ is replaced with $\overline{q}$ and the Coriolis terms are again removed.

The final terms of Eq. (4.5), $\overline{X}$ and $\overline{S}$, are the forcing by parameterized processes and diffusion, and the net tracer sources and sinks, respectively. As we did for the TEM momentum equation (Eq. (3.18)), $\overline{X}$ is inferred by taking the difference between the sum of Eq. (4.6)–(4.8) and the net tendency $\partial \overline{q}/\partial t$:

$$\overline{X} = \frac{\partial \overline{q}}{\partial t} - \frac{\partial \overline{q}}{\partial t}\bigg|_{(v^*)} - \frac{\partial \overline{q}}{\partial t}\bigg|_{(\omega^*)} - \frac{\partial \overline{q}}{\partial t}\bigg|_{\nabla \cdot \mathbf{M}} - \overline{S}. \tag{4.12}$$

The net tendency is estimated by a first-order finite difference taken on the daily-mean $\overline{q}$ data as in Eq. (B.1), as it was not available as a model output. The parameterized production and loss $\overline{S}$ are those defined in Sect. 4.3.1.

The formulation provided here is qualitatively equivalent to Eq. (1) of Abalos et al. (2017), and Eq. (9.4.13) of Andrews et al. (1987). There are some differences in convention that we included in order to maintain consistency with Gerber and Manzini (2016) (and thus Chapter 3), namely the transformation to spherical coordinates. To ensure equivalency between

Gerber and Manzini (2016) and Abalos et al. (2017) specifically, Appendix E provides a detailed accounting of the transformations involved.

4.3.3 Residual circulation transit time

We compute residual circulation transit times following Birner and Bönisch (2011) and Garny et al. (2014). First, we define a latitude-pressure grid on which to compute the RCTT, $(\phi^\dagger, p^\dagger)$, which is a subset of the simulation grid that hosts the LV and CF data (though it does not need to be). We took every-other latitude (for a $\sim 2°$ spacing), and took all 37 pressure levels between 1 hPa and 400 hPa. Backward-trajectories are then "launched" from each of these points, and the motion is solved for by two standard fourth-order Runge-Kutta (RK4) procedures in the meridional and vertical dimensions. Each dimension is transformed to Cartesian meters ($\phi \rightarrow y$, $p \rightarrow z$) before integration. We use a step size of $h = 5$ days, and define

$$x_{n+1} = x_n + \frac{h}{6} \left(k_1 + 2k_2 + 2k_3 + k_4 \right) \tag{4.13}$$

where $x \in [y, z]$, and x_{n+1} is the trajectory position at time $t_{n+1} = t_n + h$. The RK4 slopes are

$$k_1 = f(t_n, y_n) \tag{4.14}$$
$$k_2 = f\left(t_n + h/2, x_n + hk_1/2\right)$$
$$k_3 = f\left(t_n + h/2, x_n + hk_2/2\right)$$
$$k_4 = f\left(t_n + h, x_n + hk_3\right)$$

where the function f is a linear interpolator in t and x of the monthly-mean residual velocity components (v^* for $x \equiv y$, and w^* for $x \equiv z$).

Once the trajectories are obtained, determining the transit time requires finding the intersection of each trajectory with the tropopause. This first involves a linear interpolation of the tropopause position to the integration timesteps $t_n + nh$, and to the horizontal trajectory positions y given by the Eq.4.13. We then search for the intersection of two one-dimensional time series (trajectory and tropopause) in the time-altitude plane, and linearly interpolate between the left and right sides of the intersection in order to estimate the precise crossing time. The difference between the crossing time and the trajectory launch time finally gives the transit time. The trajectory information itself is transformed back to lattiude and pressure before being stored.

This procedure must be completed for a total backward-integration domain spanning 10

years prior to the point when the RCTT is being estimated. 10 years is chosen since we do not know a-priori how long the longest transit times will be, but we can reasonably expect them to typically be a less than a decade. For the present experiments, we launched RCTT trajectories for each month from June 1 1991, to Jan 1 1999. It turns out that while the 10-year integration time is sufficient in the average, some individual trajectories get "stuck" in an oscillating motion between the south and north polar upper stratosphere, in a reflection of the seasonal cycle of the deep branch of the BDC. These trajectories may not reach the tropopause within 10 years, which results in missing RCTT data at certain (ϕ, p) gridpoints near the poles. Averaging over many launch times generally fills in this missing data. The fraction of the affected gridpoints seemed to increase with growing h, though we did not perform a convergence test to understand the behavior fully.

4.4 Tracer Climatology

Before investigating the volcanic impacts on the AoA and e90 tracers, their climatological behavior in the CF ensemble should be understood for reference. Figure 4.2 shows the 5-year average ensemble-mean AoA and e90 distributions from Jan 1 1994 to Jan 1 1999. AoA is younger than 6 months throughout the troposphere, and quickly increases vertically from the tropopause. Because tropospheric air reliably enters the stratosphere through the tropical pipe, The youngest air at a given pressure level is found in the tropics, and the oldest is found at the poles, with flattening age contours throughout the midlatitudes. The oldest air is less than 5.5 years old, which occurs as low as 30 hPa at the poles, and near 1 hPa in the tropics.

   This age distribution is well within the intra-model spread derived from reanalyses, both by in-situ and offline transport models (Chabrillat et al., 2018; Ploeger et al., 2019; Fujiwara et al., 2022). It is also comparable to but slightly older than results from other coupled models simulating a similar historical period. For example, the E3SMv2-SPA mean age distribution is older than published results for the Whole Atmosphere Community Climate Model (WACCM) by up to ∼6 months (Garcia et al., 2011; Davis et al., 2023). This is primarily because those studies compute the AoA with respect to a reference point at the tropical tropopause, which we did not. We did not test this or conduct a specific intercomparison, though we note that the 6-month contour in Fig 4.2 correlates with the average position of the tropopause.

   The e90 distribution exhibits values in excess of 150 parts-per-billion (ppb) below 700 hPa, which decreases to 90 ppb near the tropopause. The vertical tracer gradient is relatively steep at the poles, while the tropospheric tropical pipe is seen clearly in the 110 ppb contour. e90

87
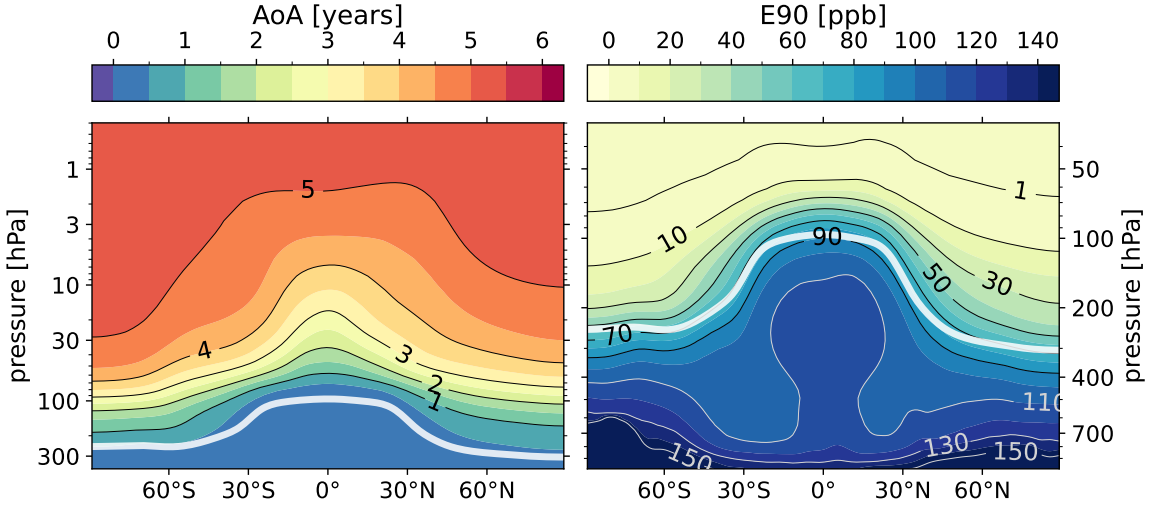
Figure 4.2: 5-year averages of the zonal-mean ensemble-mean AoA and e90 for the CF ensemble, from Jan 1 1994 to Jan 1 1999. **(left)** AoA in the stratosphere, in years. **(right)** e90 in the troposphere and lower stratosphere, in parts-per-billion (ppb). In each panel, the tropopause is plotted as a thick white line.

concentrations in the lower stratosphere fall off rapidly in the vertical. This distribution is broadly consistent with the experiments in WACCM by Abalos et al. (2017), where in particular the 90 ppb contour was determined to be an effective transport-based proxy for the thermal tropopause.

We now turn to the climatological tracer flux balance for the AoA and e90 in turn. Figure 4.3 again shows the CF ensemble mean AoA averaged over 1994-1999, as well as the RCTT over the same period, and the difference (AoA−RCTT). The residual circulation streamfunction is overplotted in each panel. In order to visualize the backward trajectory integration which computes the RCTT at each point in the meridional plane, Fig. 4.4 shows the 5-year mean trajectories, as well as the trajectories for the last month in the averaging period, Dec 1998. The 1998 trajectories exhibit oscillations in the midlatitudes, which are imprints of the seasonal movement of BDC. This seasonal signal is smoothed out in the time-averaged trajectories.

The RCTT in Fig 4.3 shows the age due to transport alone, which has a diminished vertical gradient in the tropics with respect to the AoA, and a much steeper meridional gradient in the midlatitudes. It appears that when wave-driven isentropic mixing is removed from the aging process, older and younger air are effectively segregated on either side of the surf zone. At 100 hPa, the mean age poleward and equatorward of 80°N is about 6 years and 3 years, respectively. Following Garny et al. (2014), we then interpret the difference in panel (c) as the

"aging by mixing", i.e. aging that is not captured by residual circulation transport. There are positive signals of up to 2.5 years of aging between 20–60° throughout the stratosphere in each hemisphere, and negative signals of −4 years in the high-latitude lower stratosphere. This difference in principle also includes any other non-transport parameterized forcing or diffusion, though Dietmüller et al. (2017) showed those effect to comprise 10% of the net aging or less in their simulations. Thus, the primary mechanism is two-way exchange of old and young air across the meridional RCTT gradient by breaking resolved (Rossby) waves in the surf zone.
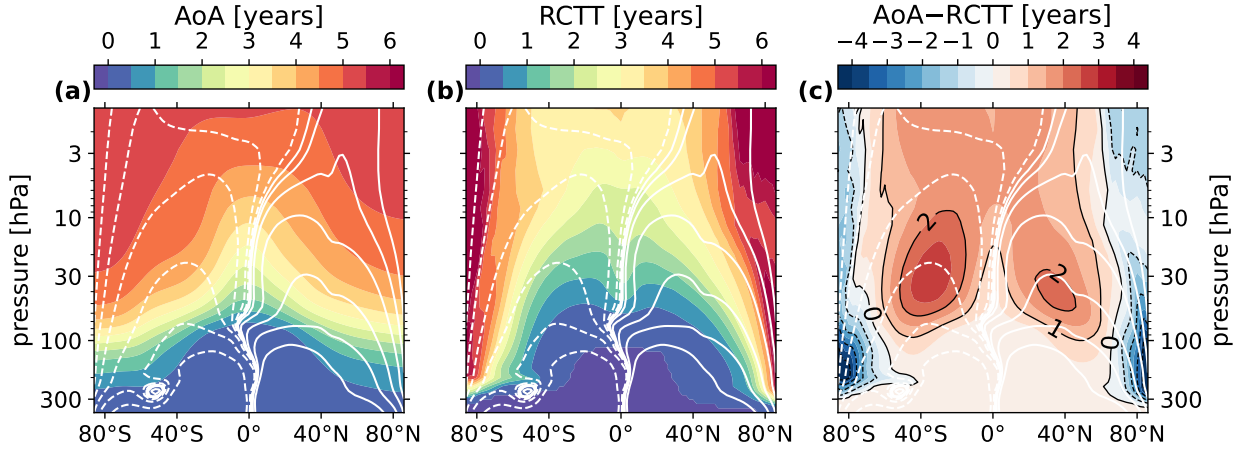
Figure 4.3: 5-year mean CF ensemble mean of **(a)** the AoA, **(b)** the residual circulation transit time, and **(c)** their difference. Age contours are shown every 6 months, and labeled in black every year in panel (c). Overplotted is the residual circulation streamfunciton at 3, 10, 30, 100, 300, and 1000 kg s^{-1} on each side of zero, in white contours, with ngative contours are dashed.

While the RCTT and its implied aging by mixing provide a view of the time-integrated tendencies along transport trajectories, further insight can be gained by instead considering *local* age tendencies. By "local", we mean the instantaneous forcing imposed on the AoA in an Eulerian sense. For this, we recruit the TEM decomposition of the net age tendency, shown in Fig. 4.5. Panels (a)–(e) show advection by the residual circulation (Eq. (4.6) + Eq. (4.7)), the local tracer mixing tendency by resolved waves (Eq. (4.8)), diffusion (Eq. (4.12)), the sum of the resolved mixing and diffusion, and the net tendency, respectively. The data is averaged over the same 5-year time period as Fig. 4.3. The annual-mean AoA is very stable, and so the net tendency has been multiplied by a factor of 100 for visibility.

This figure tells the same story as Fig. 4.3, i.e. transport decreases age in the tropics, and increases age poleward, peaking near the polar tropopause. The mixing tendency has
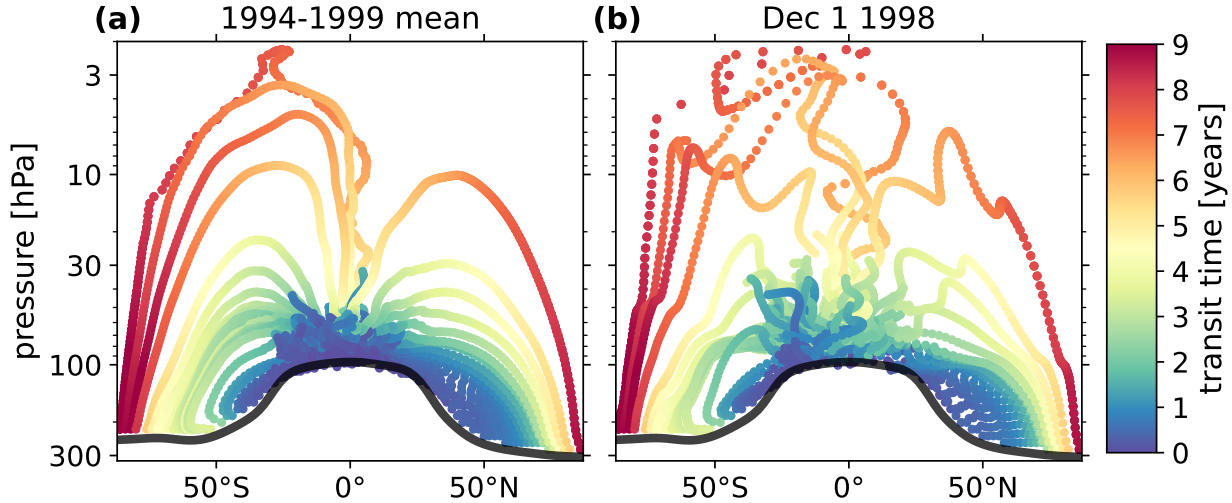
Figure 4.4: Select CF ensemble-mean RCTT trajectories for gridpoints near the tropopause, every 2° in latitude, from 20°–90° on each side of the equator. **(a)** the 5-year mean trajectories **(b)** the trajectories computed on Dec 1 1998.

the opposite behavior. At 100 hPa, the positive and negative diffusion signals peak near ±1 or less days per day, while the net mixing peaks in excess of ±4 days per day. Diffusion thus contributes at most 25% of the mixing signal in the lower stratosphere, usually less. Above 30 hPa and poleward of 60°N, there are stronger diffusion contributions, which serve to nearly cancel large resolved mixing tendencies.

Note that the meridional position of the sign reversal in each of these quantities is located near 40°N, which is equatorward of the same feature as identified by the RCTT. To be clear, this difference is due to the local nature of the measurement; rather than being integrated, panel (a) shows the age by transport *given* the simultaneous, pre-mixed AoA distribution.

Dietmüller et al. (2017) went on to show that one can obtain the cumulative effect of diffusion by integrating the resolved local mixing tendency (Fig. 4.5(b)) along RCTT backward-trajectories, and subtracting it from the RCTT inferred mixing (Fig. 4.3(right)). We did not perform this calculation, but the relatively small local diffusion tendencies we see throughout the tropical column are consistent with the result of Dietmüller et al. (2017) that aging by diffusion is a secondary contribution.

Finally, Fig. 4.6 shows the TEM balance for e90 for the troposphere and upper stratosphere. Panels (a)–(c) and (e) are the same as Fig. 4.5. In panel (d), instead of showing the net mixing, the tracer loss function (Eq. (4.4)) is shown. This is because in the troposphere, there are parameterized processes other than diffusion which are relatively large contributors to the e90 tendency. We did not have the simulation outputs in order to explicitly show these

90

parameterized forcings in the balance, though we note that the distribution shown in panel (c) is consistent with the contributions from parameterized convection and vertical diffusion near the surface shown in the WACCM e90 studies of Abalos et al. (2017) (their Fig. 2).

For e90, troposphere-to-stratosphere mass exchange appears to be a coordination of at least three processes; diabatic upwelling in the tropics, horizontal mixing by large-scale waves
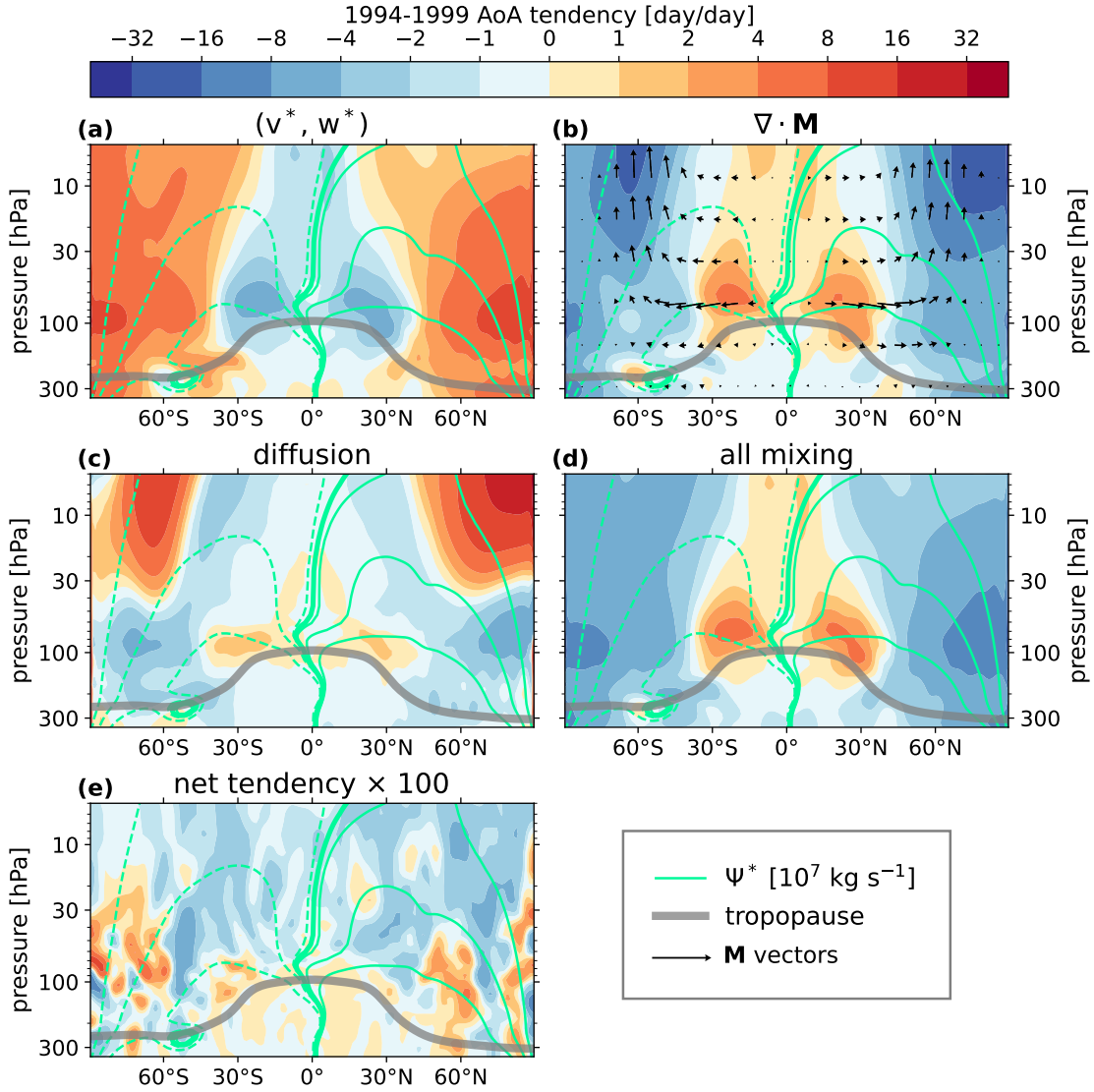
Figure 4.5: The 1994-1999 average TEM balance for the CF ensemble mean AoA. **(a)** advection by the residual circulation **(b)** mixing by resolved waves **(c)** mixing by diffusion **(d)** net mixing by resolved waves and diffusion (sum of panels (b) and (c)) **(e)** net tendency multiplied by 100. Overplotted in each panel is the tropopause in grey, and the resiudal circulation streamfunction in light green at 10, 70, and 300 on each side of zero in units of 10^7 kg s^{-1}, with negative contours dashed. The **M** vector field is plotted in panel (b).

across the midlatitude tropopause (increasing concentrations poleward of 60°), and sub-grid effects in the region of the jetstream. The results of Abalos et al. (2017) suggest that the latter is primarily diffusion, rather than the convection parameterization.

As in the case of the AoA, the annual-mean e90 distribution is very steady, thus the net e90 tendency is multiplied by a factor of 100 in panel (e). For both tracers, how-
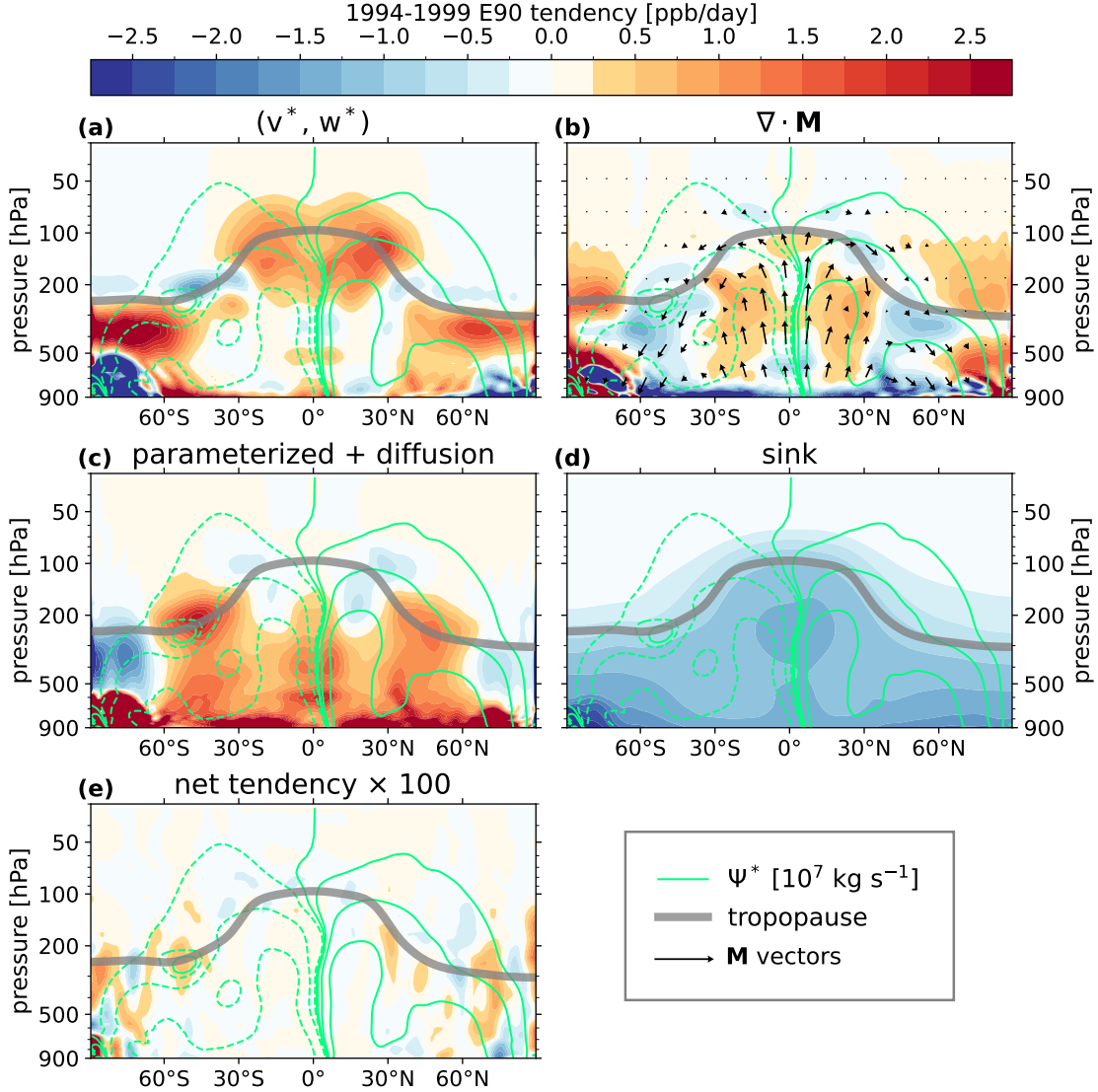
Figure 4.6: The 1994-1999 average TEM balance for the CF ensemble mean e90 in the troposphere and lower stratosphere. **(a)** advection by the residual circulation **(b)** mixing by resolved waves **(c)** mixing by parameterized processes and diffusion **(d)** e90 sink **(e)** net tendency multiplied by 100. Overplotted in each panel is the tropopause in grey, and the resiudal circulation streamfunction in light green at 200, 1000, and 4000 on each side of zero in units of 10^7 kg s^{-1}, with negative contours dashed. The **M** vector field is plotted in panel (b).

ever, the net tendency is much larger in seasonal averages. Seasonal TEM balances for summer and winter are provided in Appendix C.1, in Fig. C.2 and Fig. C.1 for AoA, and Fig. C.4 and Fig. C.3 for e90. There, the e90 tendency exhibits an asymmetric behavior, with net troposphere-to-stratosphere exchange occurring in the summer hemisphere, and net stratosphere-to-troposphere exchange occurring in the winter hemisphere. This behavior is jointly enforced by the residual circulation and resolved mixing, and shows that the exchange of mass actually occurs over a much broader range in latitude than the annual mean would suggest. Meanwhile, the AoA tendency also exhibits a seasonal signal, with enhanced aging occurring in the midlatitude winter hemisphere, and decreased negative aging shifted from the equator to 30° in the summer hemisphere. These effects are explained by the vortex-associated wave activity in the winter hemisphere (and lack of wave-driven mixing in the quiescent summer hemisphere), and the shift of the residual circulation streamfunction zero-line into the summer hemisphere. We note that these findings are consistent with Konopka et al. (2015), where a Lagrangian transport model driven by reanalysis winds was used to estimate the seasonality of the TEM AoA forcing.

4.5   Volcanic Impacts

With the mean and seasonal counterfactual behavior established for the AoA and e90 tracers, we now investigate the Pinatubo impacts on the tracers and the force balance governing their evolution in the LV ensemble. First, it is useful to look at the volcanic effect on the residual circulation itself. Recall from Chapter 3 that the most significant dynamical impacts on zonal momentum in the northern hemisphere occur during boreal summer 1991, late winter 1992, and summer 1992. Moreover, the primary impact driver was a strengthened residual circulation and the associated Coriolis effect during the boreal summer months, and modification of the EP flux divergence involving equatorward deflection of planetary waves near 30 hPa during the winter months. With this in mind, Fig. 4.7 shows the LV ensemble-mean Δw^* and $\Delta \Psi^*$ averaged over August 1991, January 1992, and August 1992.

In each of the seasons shown, there is enhanced residual (diabatic) vertical motion in the tropics, and enhanced downwelling in the high latitude upper stratosphere, though the strength and significance of these features are notably diminished by August of 1992, one year post-eruption. By continuity, this implies an accelerated residual circulation, which is observed in panels (d) and (f). In particular, the impact pattern indicates an enhanced overturning circulation centered on the aerosol forcing, which is near the injection latitude at 15°N in summer of 1991, and migrates poleward thereafter (Brown et al., 2024). The result is that the volcanic effect lacks the seasonality of the background residual circulation, and does
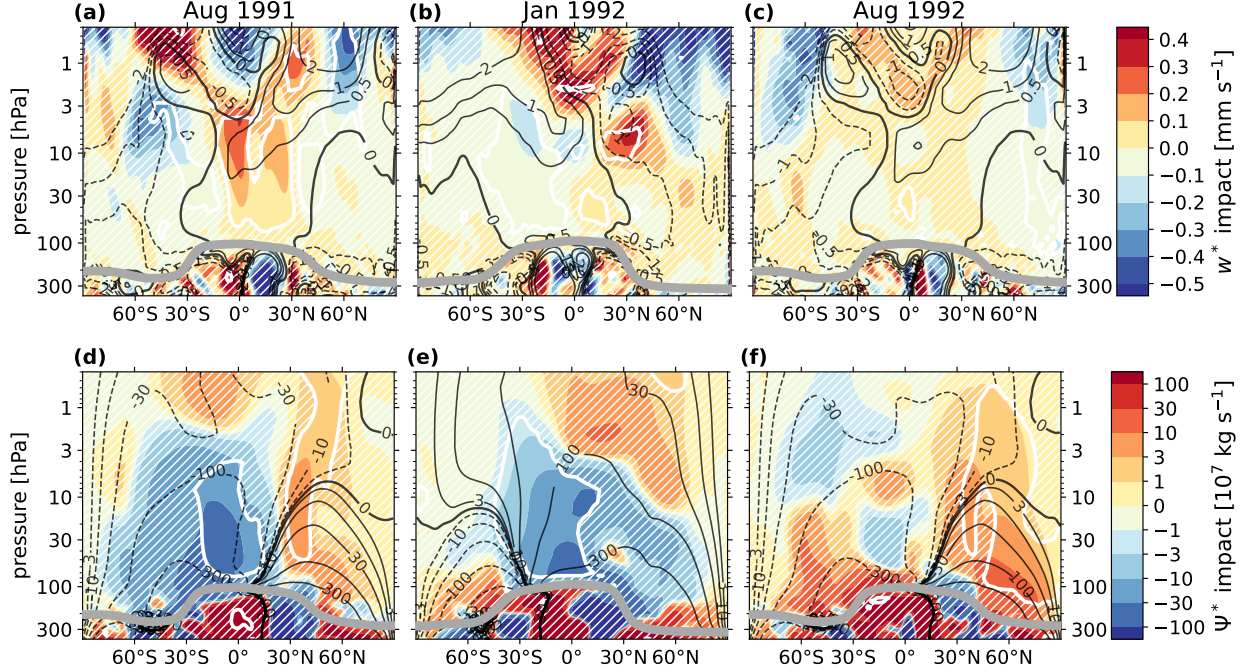
Figure 4.7: Ensemble-mean residual circulation impact, significance, and counterfactual reference for Aug 1991, Jan 1992, and Aug 1992. **(a–c)** the vertical residual velocity impact Δw^* in mm s^{-1}. A white contour is drawn at $p = 0.05$, and regions of $p > 0.05$ are filled with white hatching. Overplotted in black contours is the CF ensemble-mean w^* at 0.5, 1, and 2 mm s^{-1} on each side of zero, with the zero line plotted in bold. **(d–f)** the residual streamfunction impact $\Delta \Psi^*$ in 10^7 kg s^{-1}. Significance is displayed as in panels (a)-(c). Overplotted in black contours is the CF ensemble mean Ψ^* at 3, 10, 30, 100, and 300 on each side of zero, in the same units, and the zero line plotted in bold.

not always project onto the CF Ψ^*. In August of 1991 and 1992, the robust $\Delta \Psi^*$ indicates acceleration of the shallow branch of the BDC in both hemispheres, while the deep branch in the summer hemisphere is weakened. During January of 1992, the southern shallow-branch cell is enhanced along it's northern edge, the Ψ^* zero line moves northward, and the positive overturning circulation in the SH is decelerated.

We found that the statistical significance of the residual velocity impacts extend to about 2 years post-eruption, after which the magnitude decreases and becomes statistically insignificant (not shown), which matches the timescale of the dynamical anomalies presented in Chapter 3. However, these relatively short-lived perturbations to the residual circulation are able to establish much more persistent changes to stratospheric composition, as indicated by the AoA.

4.5.1 AoA impacts

The AoA impact is shown for select monthly means and pressure levels between June 1991 and June 1998 in Fig. 4.8. Panels (d) and (e) show ΔAoA as a function of time and latitude at 10 hPa and 40 hPa, respectively. Panels (a)-(c) show the monthly-averaged vertically resolved impacts during boreal winter of 1992, 1993, and 1994. These monthly means were chosen as the occurrence of peak impact, the arrival of significant impact to the poles, and the initial return of the tropical AoA to the CF condition respectively, at 10 hPa.

The w^* impacts in Fig. 4.7 generally indicate an enhanced tropical pipe following the eruption, and as such the AoA signal is by-and-large an intrusion of younger air into the stratosphere. This feature migrates vertically and then poleward, which persists in sig-
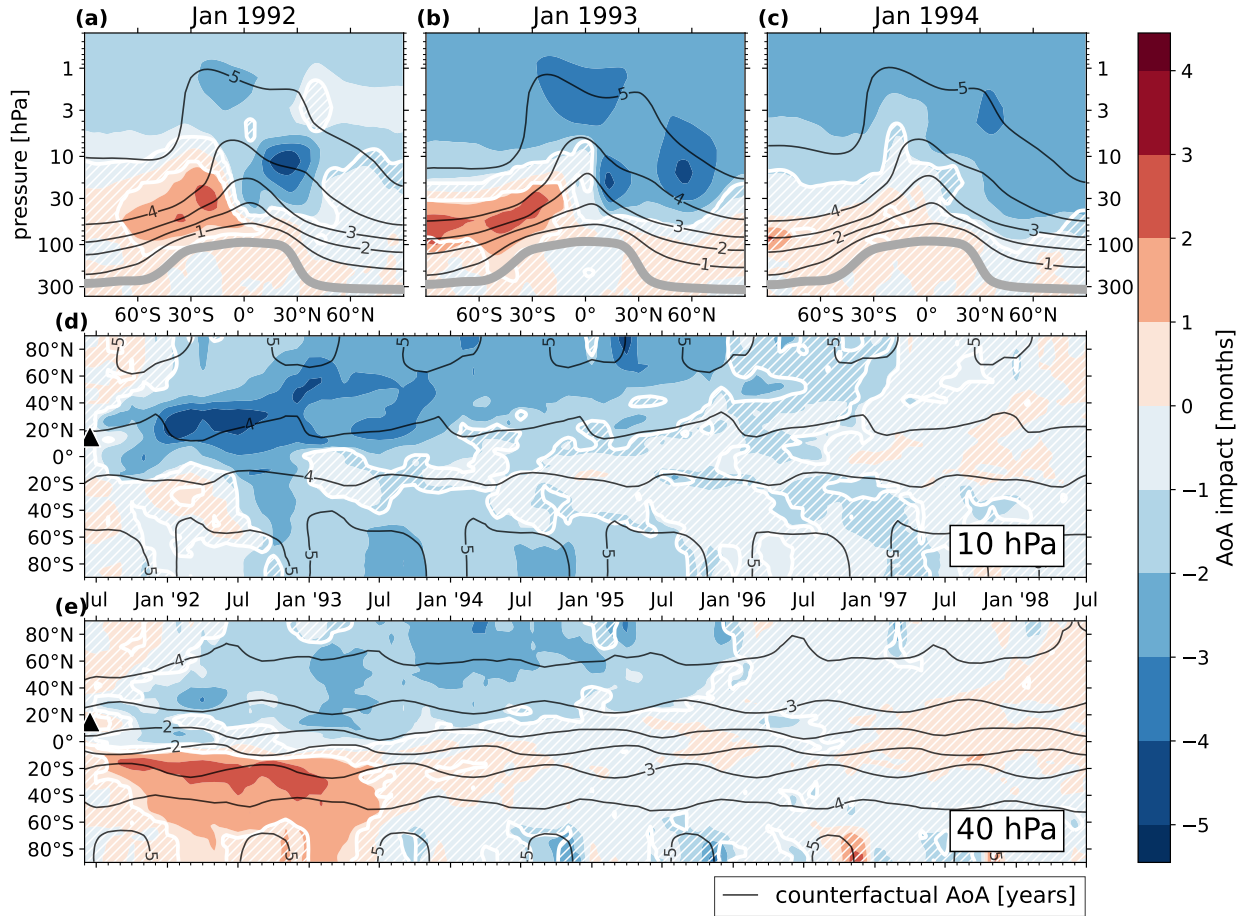
Figure 4.8: Ensemble-mean AoA impact, significance, and counterfactual reference for Jan 1992, Jan 1993, and Jan 1994. **(a–c)** the AoA impact in months. A white contour is drawn at $p = 0.05$, and regions of $p > 0.05$ are filled with white hatching. Overplotted in black contours is the CF ensemble-mean AoA in years. **(d)** the same as panels (a)-(c), but for the time-latitude plane at 10 hPa **(e)** the same as panel (d), but at 30 hPa.

nificance for several years after the anomalous upwelling has ceased. The tropical impact diminishes from January 1993 to January 1994 at 10 hPa, while the impacts poleward of 60°N remain until at least 1996. This timescale can be thought of as the transit time of a "pulse" of young tropical air, and hence is itself a measurement of the BDC traversal timescale.

Also observed in panels (a)-(c) and (e) is a significant positive age anomaly in the SH between 30 hPa and 100 hPa, lasting until July of 1993. We'll refer to this feature as SH lower stratosphere (SHLS) aging. Because the SHLS aging is a robust finding, and yet does not obviously follow from the expectation of an accelerated residual circulation, we will center the following discussion of the AoA flux balance on attributing its cause. This exercise should also provide insight into the volcanic aging process more generally. As a working hypothesis, the observation seems to be related to (1) the fact that $\Delta\Psi^*$ generally does not project onto the CF Ψ^* in austral summer, and (2) the fact that the relatively slow migration of the AoA signal means that the interannual aging impact is dependent on the relatively early transport modification.

Figure 4.9 shows ΔAoA, ΔRCTT, and their difference (aging by mixing) for boreal winters from 1991–1995. Panel (b) shows a robust symmetric signal about the equator, where air is refreshed and aged by transport in the NH and SH subtropics, respectively. This transport anomaly explains most of the net aging signal (panel (a)). Visually scanning down panels (b,e,h,k) shows that the RCTT impact in each hemisphere strengthens and advects along the residual circulation, crossing lines of constant transit time poleward. In the NH, as the the signal reaches the polar lower stratosphere in 1995 (panel (k)) it becomes insignificant, and is canceled by a strong positive aging by mixing anomaly (panel (l)).

In panels (d,e,f), the SHLS aging can be described by both enhanced transport and eddy tracer flux, though the impacts on each are larger than the net age increase. A momentum-based interpretation of this might be that the enhanced aging in the RCTT implies a decelerated residual circulation in the SH, which in turn implies accelerated summertime easterlies (decreased westerly Coriolis torque), and thus hampered diffusion in order to approximately maintain thermal wind balance. Indeed, our results of Chapter 3 showed that residual circulation anomalies were usually associated with anomalous wave driving of approximately equal and opposite sign, and the net impact was a relatively small imbalance. From a tracer perspective, the equivalent statement is that enhanced aging by transport (panel (e) SH) tends to be associated with decreased aging by mixing (corresponding feature in panel (f)). This cancellation (above 30 hPa) is achieved by a downward displacement of mixing contours, which in turn yields an excess aging by mixing below the RCTT anomaly (below 30 hPa), which in part drives the net aging signal in panel (d).
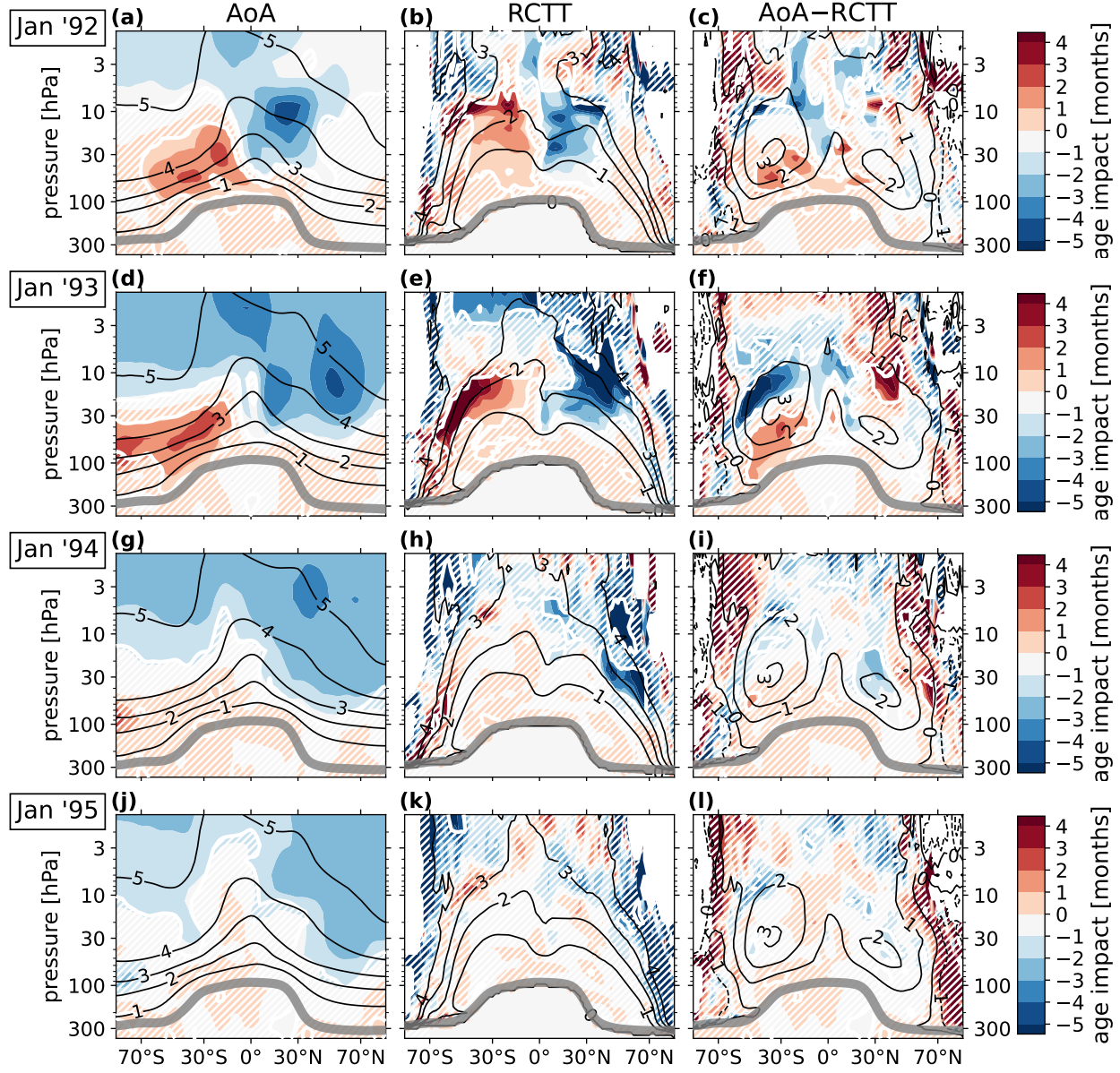
Figure 4.9: LV ensemble-mean aging impacts and their statistical significance in the total AoA (left column), the RCTT (middle column), and aging by mixing (right column) for Januarys from 1992-1995 (rows). In each panel, the CF ensemble mean of each age variable in years is plotted as labeled black contours. Also plotted in each panel is a white contour in p-value at $p = 0.05$, and white hatching in regions of $p > 0.05$. Solid white areas in the polar regions of the center and right column panels are missing-value locations where originating RCTT backward trajectories did not reach the tropopause within the integration domain.

Whatever the dynamical explanation of the transport-mixing balance at play here, it appears to be initiated by the anomalous transport in the first place. Therefore, we will limit our focus here to an explanation of the anti-symmetric hemispheric signal in the RCTT at
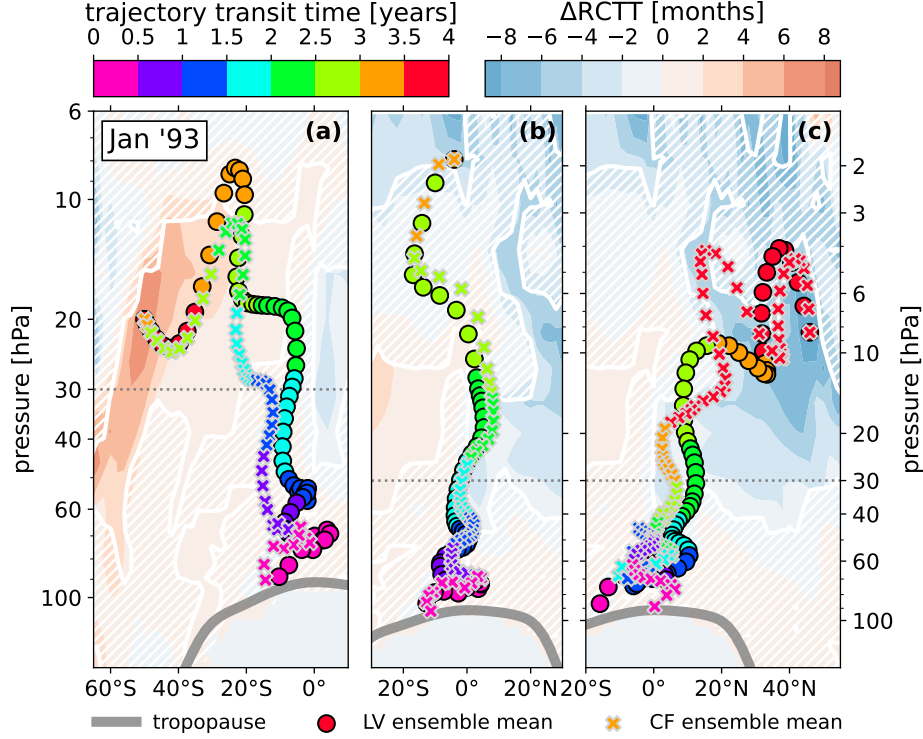
Figure 4.10: Comparison of select LV and CF ensemble-mean RCTT trajectories averaged over January of 1993. The trajectories were chosen as those corresponding to peak RCTT impact in **(a)** the midlatitude SH, **(b)** the tropics, and **(c)** the midlatitude NH. Colored points show the steps of the RK4 backward-integration of the time-varying residual velocity field (Sect. 4.3.3). Times on the top-left colorbar are reported as the difference between the trajectory launch time, and the tropopause intersection time. Circles and crosses are used for the LV and CF trajectories, respectively. Background contours show ΔRCTT, with statistical significance as white contours and hatching. A faint dotted line is drawn at 30 hPa for reference. Panels (b) and (c) share a vertical axis.

early times. Figure 4.10 reproduces the RCTT impacts for three overlapping latitude bands centered on the positive southern ΔRCTT feature, the equatorial region, and the negative northern ΔRCTT feature averaged over January 1993. For each region, a pair of CF and LV ensemble-mean RCTT trajectories are shown. The particular trajectories chosen are those that connect the tropopause to the peaks of significant ΔRCTT near (60°S, 20 hPa), (0°, 6 hPa), and (40°N, 10 hPa). The intention is to clarify whether the difference in transit time are primarily due to difference in trajectory, or difference in transport speed.

We can see that while the trajectories are in fact different, their behavior is qualitatively comparable, and it seems that the more important effect is a difference in the background residual velocity, particularity w^*. In the SH (panel (a)), the total transit time lag is about 6 months, which is already established by the time the trajectories cross the 30 hPa isobar,

before they turn southward toward their destination. A similar but opposite conclusion is reached from the NH trajectory (panel (c)), where the total lag of -8 months appears to have been reached by 30 hPa. The equatorial trajectory in panel (b) exhibits almost exclusively vertical motion, and reaches its destination with a lag of several months.

These findings reinforce one of our initial hypotheses, that relatively early transport anomalies, specifically Δw^*, control the ultimate RCTT impact distribution. But the question remains as to why exactly the RCTT lag in each hemisphere is of opposite sign, if the fundamental effect is enhanced upwelling. To address this problem, Fig. 4.11 shows Δw^*, ΔRCTT, and the impact in the local transport flux as diagnosed by the advective TEM contribution (Eq. (4.6) + Eq. (4.7)) in the latitude-time plane at 30 hPa. Overplotted is the zero-line of the CF ensemble-mean w^*, with bold arrows indicating regions of upwelling and downwelling. Also shown is the position of the Pinatubo eruption, and the latitude of the maximum temperature impact ΔT.

Now, wherever positive (negative) contours in Δw^* coincide with regions of upwelling (downwelling), the aerosol forcing is enhancing the local vertical motion, and thus the RCTT is decreased with respect to the counterfactual. This means that the notable $\Delta w^* > 0$ feature centered on the eruption latitude in panel (a) brings relatively young air into the upper stratosphere, as expected. On the other hand, when the signs of Δw^* and the CF w^* are different, the opposite effect on the RCTT will result. Importantly, this means that the $\Delta w^* < 0$ feature south of the equator from June 1991 to April 1994 is acting to *increase* transit times through the vertical column aloft. This results in a concomitant increase in the local transport flux (panel (b)), which necessarily gives rise to a delayed effect in the integrated measure ΔRCTT. In other words, the early negative upwelling impact in the southern subtropics releases a "pulse" of old air which remains robustly detected for several years as it traverses the BDC.

There are two effects which cause this particular response; (1) after the eruption occurs at 15°N, the maximum ΔT, and thus maximum Δw^*, remains in the NH for at least one year at 30 hPa. By continuity, this must involve enhanced downwelling north and south of the forcing, which occurs north of 45°N and south of 0°. The result is anomalous upwelling and downwelling on opposite sides of the equator. (2) The seasonal shift of the BDC exacerbates this meridional asymmetry, since the region of upwelling (i.e. the diverging region of the residual streamfunciton) migrates into the southern hemisphere (black contours in panel (a)), which we saw in Fig 4.7(e). This means that the positive aging effects of the anomalously low vertical motion in this region is strengthened.

To be clear, if the eruption had instead occurred at the equator, the SHLS aging might still be observed due to the seasonal southern migration of the shallow BDC branches. If the
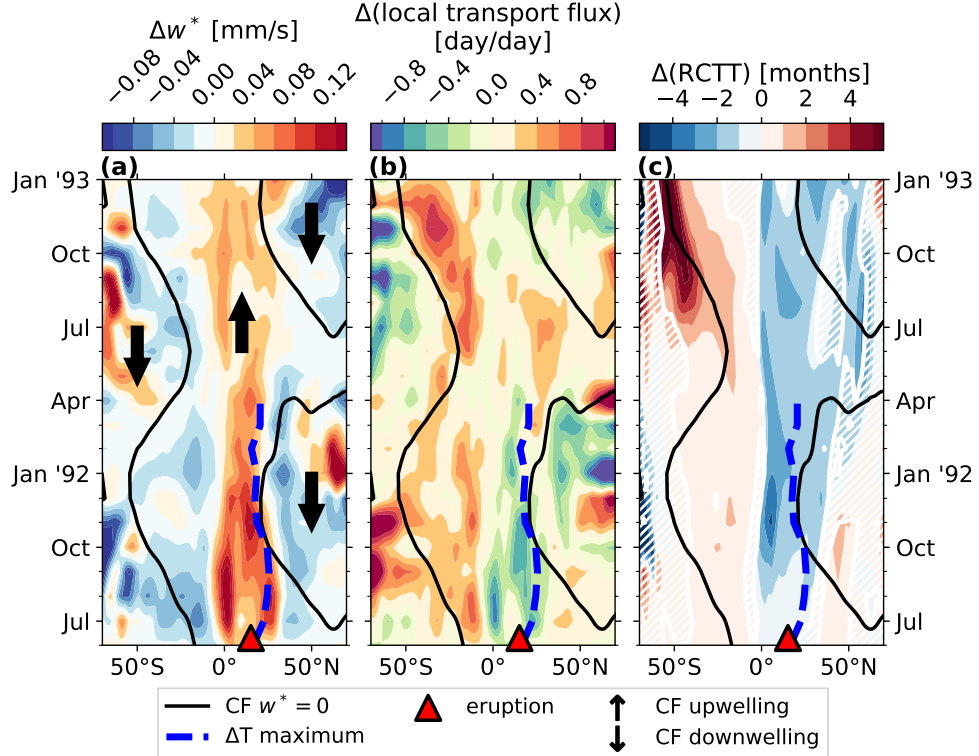
Figure 4.11: Relationship between the ensemble-mean impacts in vertical residual velocity, and aging by transport at 30 hPa from July 1991 to January 1993. In all panels, solid black contours are drawn at $w^* = 0$ in the CF ensemble mean, a thick dashed blue line shows the latitude of maximum ΔT from July 1991 to April 1992, and a red triangle shows the position of the Pinatubo eruption. **(a)** Δw^* in mm s^{-1}. Thick black arrows show regions of upwelling and downwelling in the CF data. **(b)** impact in AoA local transport flux (Eq. (4.6) + Eq. (4.7)) in days per day. **(c)** RCTT impact in months. Statistical significance is shown as white contouring and hatching.

eruption had instead occurred during boreal winter, then the seasonal BDC signal would be the opposite, and we would perhaps see aging in the NHLS instead. In any case, we have arrived at the second of our initial hypotheses, which was that the SHLS aging effect is a result of the misalignment of $\Delta\Psi^*$ and the CF Ψ^*, though the eruption localization also plays a notable role. Specifically, while the split between the BDC shallow branch cells exhibit a meridional oscillation, the volcanic forcing of the residual circulation in contrast is fixed near the eruption location, which alters the relative sign between Δw^* and w^*. This seasonal mechanism also explains why the SHLS aging abruptly ends near June of 1992 (Fig. 4.8(e)); by this time, the southern w^* zero line has moved sufficiently far west such that the southern $\Delta w^* < 0$ feature no longer opposes the sign of the background motion (Fig. 4.11(a)). This pulls relatively young air into the southern BDC cell, which ushers out the roughly year-long

era of diminished transport in the SHLS.

4.5.2   e90 impacts
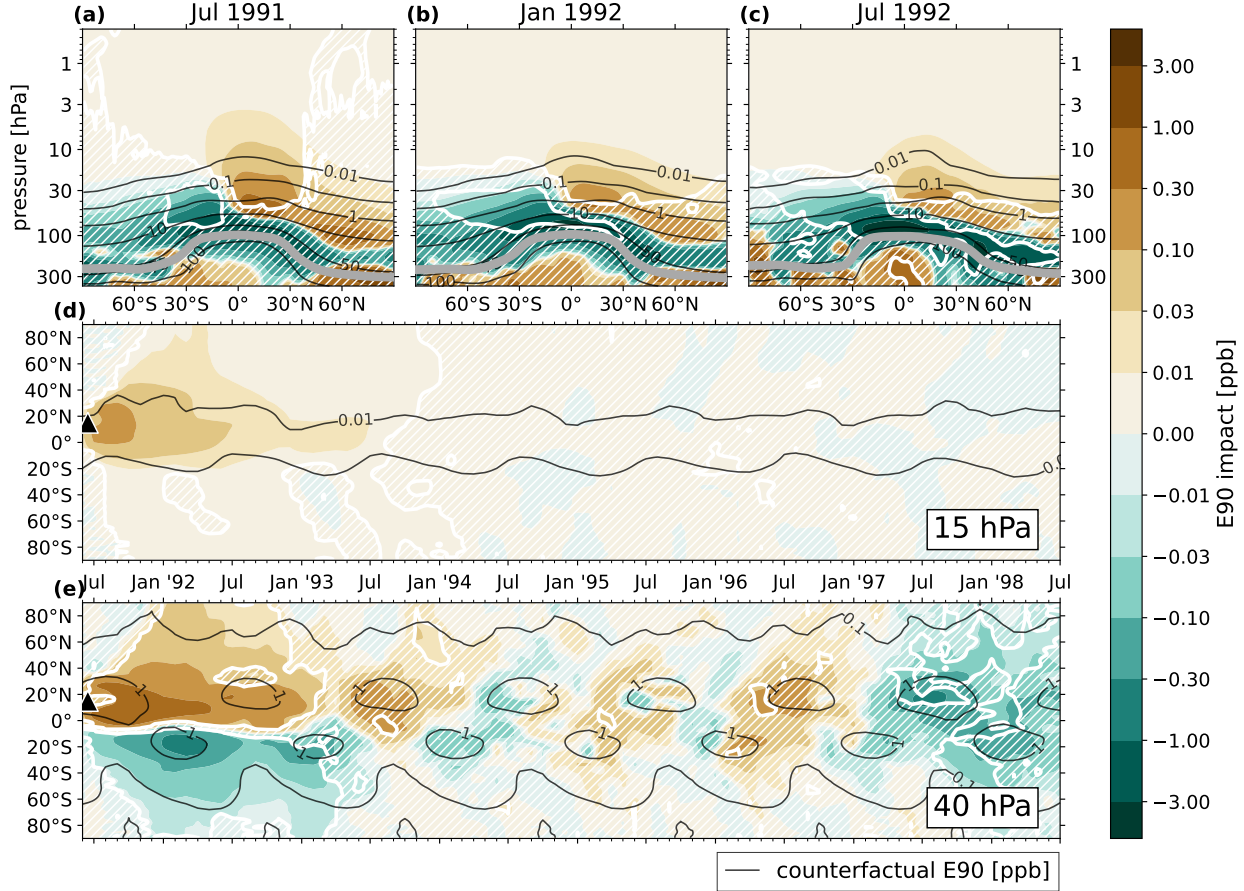
Figure 4.12: Ensemble-mean e90 impact, significance, and counterfactual reference for Jan 1992, Jan 1993, and Jan 1995. **(a–c)** Δe90 in ppb. A white contour is drawn at $p = 0.05$, and regions of $p > 0.05$ are filled with white hatching. Overplotted in black contours is the CF ensemble-mean e90 in ppb. **(d)** the same as panels (a)-(c), but for the time-latitude plane at 15 hPa **(e)** the same as panel (d), but at 40 hPa.

We now briefly discuss the volcanic impacts of e90, which offers another view of the hemispheric asymmetry in the anomalous transport response, as identified in the previous section. Figure 4.12 shows Δe90 for select monthly means and pressure levels between June 1991 and June 1998. Panels (d) and (e) show Δe90 as a function of time and latitude at 15 hPa and 40 hPa, respectively. Panels (a)-(c) show the monthly-mean signal during boreal summer of 1991, winter of 1992, and summer of 1992.

Because the e90 decay is much faster than the BDC traversal timescale, volcanic effects

on this tracer are relatively short-lived. Still, statistical significance persists long enough that we reliably identify the e90 analog of the SHLS aging that was seen previously. Above ∼30 hPa, there is a uniform and robust (albeit small) increase of e90 established by July of 1991 from the north to south polar regions. This is consistent with the global decrease of
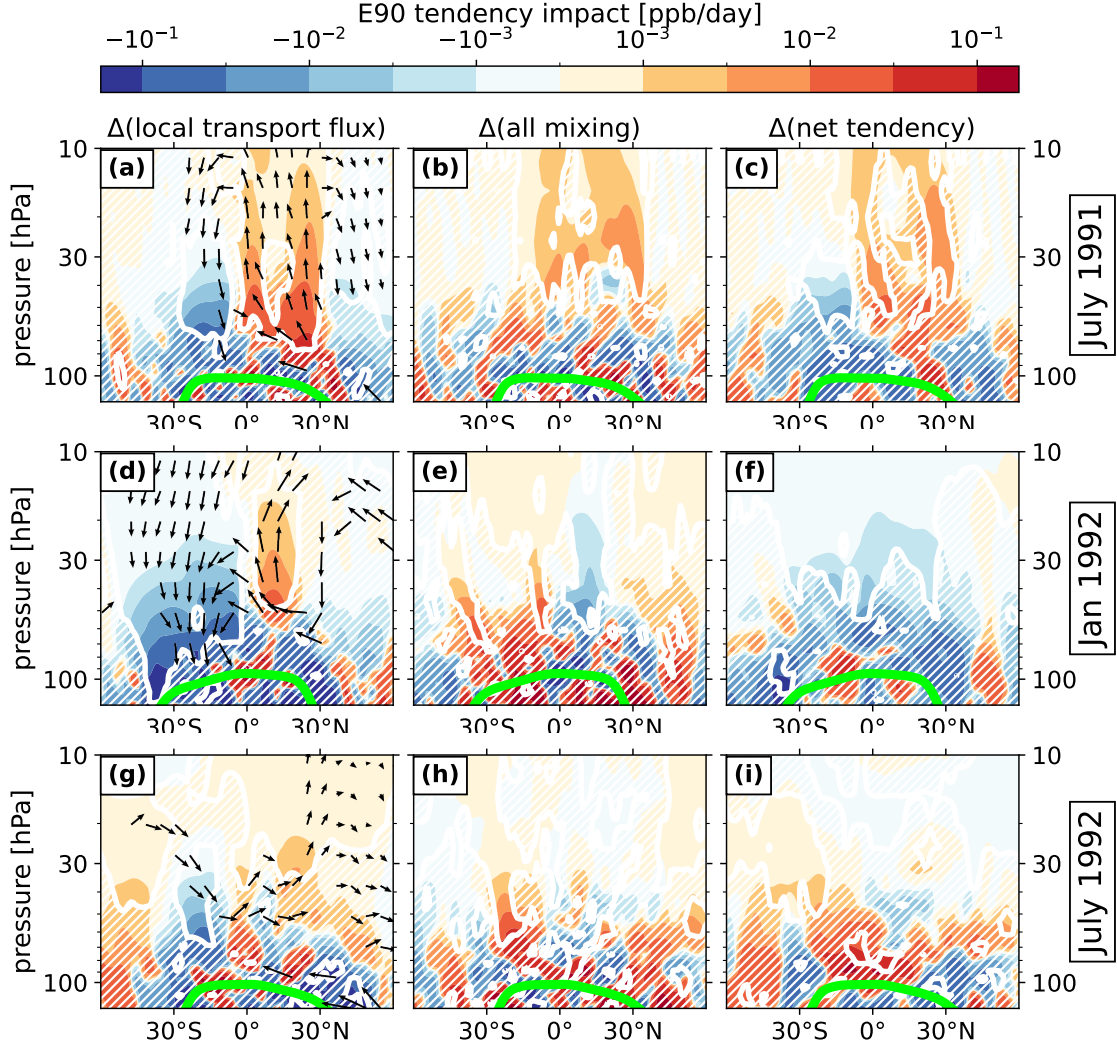
Figure 4.13: The ensemble-mean e90 tracer TEM balance from 60°S–60°N averaged over July 1991 (top row), Jan 1992 (center row), and July 1992 (bottom row). Each panel shows a particular contribution to the total e90 tendency impact as colored contours, with its statistical significance plotted as white contours and hatching. The panels in each row, from left to right, are the local transport flux (forcing by the residual circulation; Eq. (4.6) + Eq. (4.7)), the sum of isentropic mixing by resolved eddies, and diffusion (Eq. (4.8) + Eq. (4.12)), and the net tendency. A thick green line in each panel shows the tropopause. In panels (a,d,g), arrows show the statistically significant tangent vectors of $\Delta\Psi^*$, as computed by the method in Appendix B.3.

AoA in the upper stratosphere, associated with enhanced vertical residual velocities in the tropics. Below 30 hPa, the impact is characterized by rising mixing-ratio isopleths in the NH, and sinking isopleths in the SH, and a robust region of diminished e90 mixing ratio in the SHLS. We now know this to be the signature of a negative streamfunction effect south of the equator, which means diminished upwelling in the southern subtropics. In the e90 context, this is equivalently a decrease in upward troposphere-stratosphere mass exchange, and/or a sinking of the tropopause in this region

To see the anomalous transport more clearly, Fig 4.13 shows the e90 TEM balance between local transport flux, local eddy tracer flux plus mixing, and the net tendency impact (changes to the e90 loss also contributes, but is not shown, since it is simply a scaling of Δe90). Note that we are inferring the total balance residual $\overline{X}$ as mixing here. In the discussion around Fig. 4.6, we described that convection and vertical diffusion are also notable components of this quantity, but those contributions are greatly diminished above the tropopause. In panels (a,d,g), vectors represent the statistically significant circulation given by $\Delta\Psi^*$. In panel (a), the initial response in the month following the eruption is enhanced upwelling centered on 15°N, and anomalous subsidence near 15°S and 60°. As previously discussed, the seasonal southward shift of the shallow BDC cells serves to exaggerate the negative transport flux impact. This effect is expected to peak in boreal winter, shown in panel (d). During this time, the net Δ e90 is in fact negative throughout the stratosphere, as the relatively minor positive upwelling signal in the NH subtropics is canceled by mixing (panel (e)). Finally the negative southern signal is greatly reduced by July of 1992 (panel (g)), once the shallow BDC cells have again shifted northward.

4.5.3   Effect on the BDC seasonality

With the volcanic effects on AoA and e90 reviewed, let us step back for a brief qualitative interpretation. We observed that a robust feature of increased age and diminished e90 concentrations develops in the SHLS soon after the eruption, and ceases abruptly one year later. We noted that this is due in part the occurrence of the eruption in the northern hemisphere, but that the effect is ultimately controlled by the seasonal drift of the BDC with respect to the aerosol forcing, which modulates the relative sign between Δw^* and w^*.

A more general understanding can be gleaned from this collection of evidence, which is that tropical volcanic aerosol forcing occurring during a particular season tends to nudge stratospheric tracer tendencies toward that of the *opposite* season. Indeed, the ΔAoA that we've presented for austral summer, characterized by excessive SHLS aging, minimics the climatological AoA net tendency of austral winter (see Fig. C.2(e)). At the same time,

the observed Δe90 during this period, consisting of enhanced and diminished mixing ratios above the tropopause in the NH and SH respectively, is also reminiscent of the austral winter climatology in that tracer (Fig. C.4(e)).

Considering other hypothetical Pinatubo-like eruptions occurring throughout the year, it appears that the generic effect on global mass transport of tropical eruptions is to dampen the seasonality of the BDC. If true, then surely this effect should be accompanied by corresponding modifications to global EP wave activity, which may in turn offer a more generalized interpretation of the results of Chapter 3. Future work could perhaps design simulated experiments toward this end. For the time being, we'd like to at least make one more incremental advance, by inspecting the dependence of the BDC seasonal damping with eruption size.

4.6   Eruption Magnitude Sensitivity

Thus far, we have not subjected the results of these chapters to sensitivity tests in forcing strength, and have instead limited our focus to a single volcanic scenario. This section provides a brief inspection of the qualitative relationship between the AoA and e90 tracer distributions, and initial eruption magnitude expressed in Tg of the aerosol precursor SO_2. As we have seen, the volcanic effect on global tracer concentrations is an indirect one, depending on interactions with the simultaneous background conditions. As such, it is difficult to make any a-priori estimate of the trend. A naive model of the aerosol forcing as an exponential attenuation of longwave radiation (as we did in e.g. Eq. (2.28)) suggests that the local heating rates should respond linearly at small mixing-ratio, but we should not make the extrapolation that the local temperature response shares this scaling, let alone the non-local response after the downstream dynamical development.

Fig. 4.14 shows the ΔAoA time series and eruption magnitude trend at 10 hPa and 30 hPa averaged over 20–40° in each hemisphere. These positions were chosen to match the impact peaks in Fig. 4.8 panels (d,e). In the lower panels of Fig. 4.14(a-d), the trend of the maximum $|\Delta\text{AoA}|$ is shown as a function of SO_2 mass, normalized such that the result for the 15 Tg eruption is set to unity. The maximum $|\Delta\text{AoA}|$ is identified uniquely for each SO_2 mass choice, and thus the occurrence of each in time are not always the same (marked with colored triangles in the figure). A linear fit to the normalized data is also shown for reference.

In the NH, the trend is approximately linear from 3 Tg to 10 Tg, after which there is a hint of saturation in the ΔAoA from 10 Tg–15 Tg. The positive aging anomaly in the SH at 30 hPa qualitatively shows this effect as well, while at 10 hPa the trend is approximately linear from 3 Tg to 15 Tg. Once the peak impacts are realized, panels (a), (b) and (d)

suggest that larger anomalies also remain detectable for longer, as seen in the persistence of the significance of each impact curve with time.

Figure 4.15 shows the same analysis for the e90 tracer. The response appears to approximately vary linearly with forcing magnitude. In the NH in particular, saturation is again suggested for SO_2 loading above 10 Tg, though this is not decisive. We further note that while the e90 tracer is sensitive to changes in cross-tropopause mass exchange, it's concentration at a fixed pressure level is also highly sensitive to displacements of the tropopause itself. In order to clarify this, we checked that the total stratospheric e90 mass does increase when controlling for tropopause height for the 10 Tg SO_2 eruption (not shown). However, we did not evaluate the statistical significance of this finding, or trends with eruption size. Further research could be directed to evaluating the post-volcanic troposphere-stratosphere mass exchange more specifically.

The combination of Fig. 4.14(c,d) and Fig. 4.15(c,d) shows that both of the opposing southern and northern hemisphere responses scale together with eruption size, which implies that the seasonal damping effect on the BDC in general is linearly controlled over at least the tested forcing range. It is an open question whether or not the effect should saturate given even larger SO_2 loading. Either way, some nonlinear behavior should probably be expected, since the interaction between volcanic impacts and background dynamics could change approaching the condition $|\Delta w^*| \approx |w^*|$.
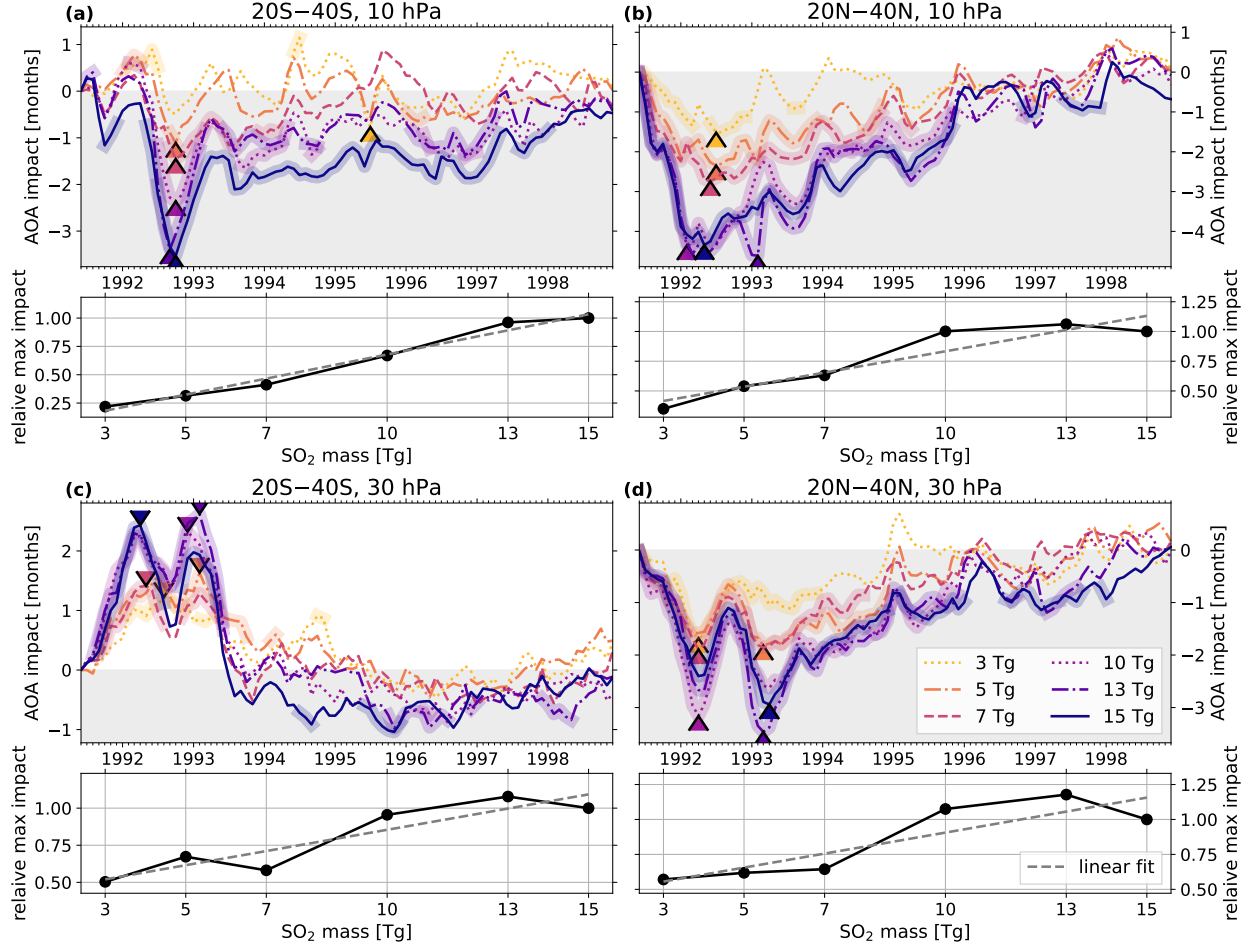
Figure 4.14: ΔAoA following eruptions with 3, 5, 7, 10, 13, and 15 Tg of eruptive SO_2. **(a)** top panel shows the ΔAoA time series at 10 hPa and averaged over 20–40°S for each eruption mass (legend in panel (d)). Each line is highlighted in color where the impact is statistically significant. Bottom panel shows max($|\Delta$AoA$|$), normalized such that the result for the 15 Tg eruption has a value of 1. Occurrence of the max impact is labeled in the top panel with a caret of matching color for each curve. A gray dashed line shows the linear fit to the data. **(b,c,d)** the same as panel (a), but for the pressure levels and meridional averaging as given in their titles above each top panel.

106
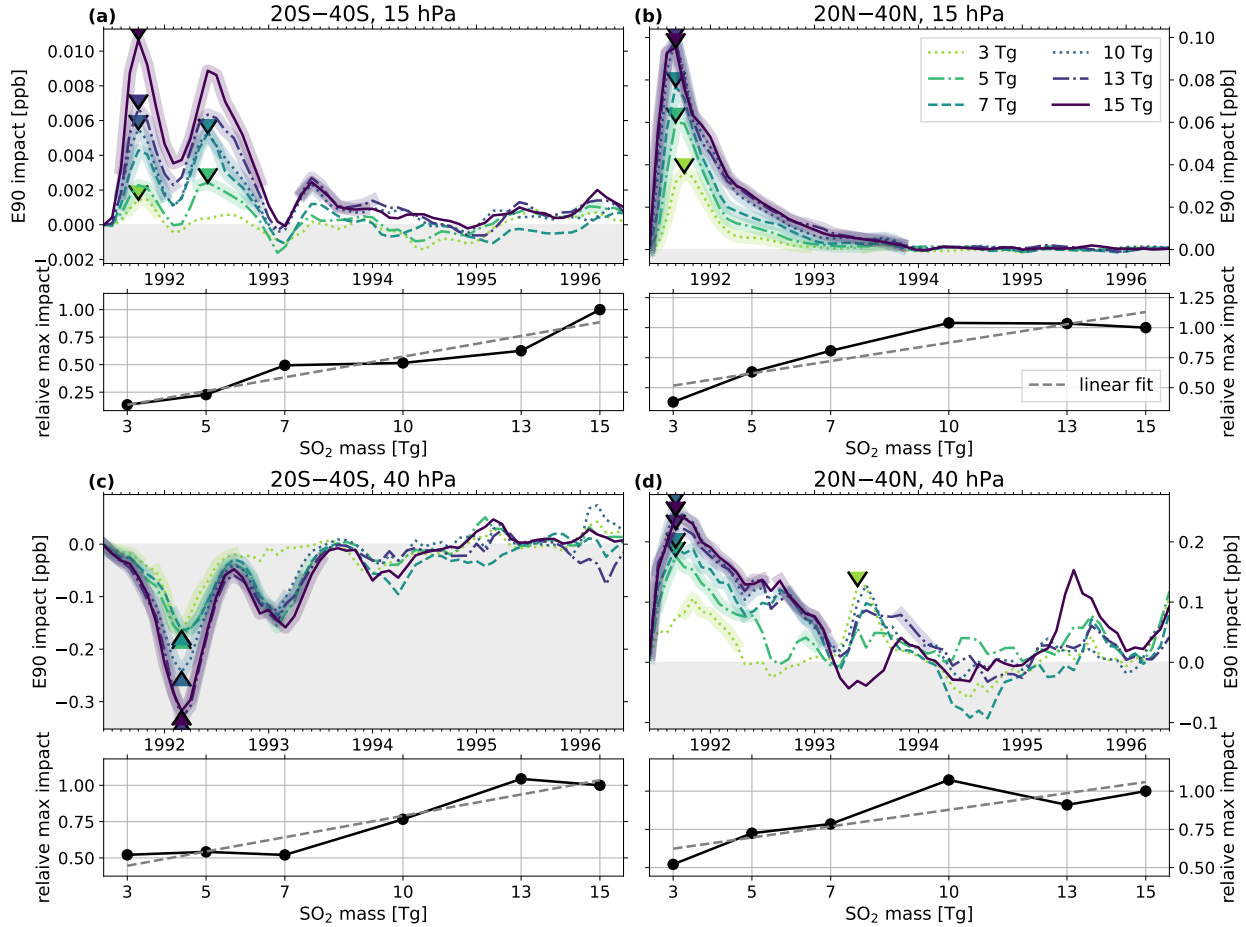
Figure 4.15: The same as Fig. 4.14, but for the Δe90 at 15 hPa (top row of panels) and 40 hPa (bottom row of panels), and the eruption mass legend given in panel (b).

4.7 Discussion & Conclusions

Our conclusions are as follows

1. The main effect of the Pinatubo eruption on tracer transport is to strengthen the tropical pipe, which lowers age of air throughout the tropics, and in the middle-to-upper stratosphere globally.

2. Age impacts remain detectable long after the instigating dynamical perturbations have relaxed, and generally persist until they traverse the deep BDC (about 2 years in the tropics, and about 5 years at higher latitudes).

3. Stratospheric concentrations of tracers with sources in the troposphere (e90) are also enhanced with the strength of the tropical pipe.

107

4. There is a hemispherically asymmetric response in the lower stratosphere, involving increased aging and decreased e90 concentrations in the southern hemisphere, spanning one year post-eruption. We called this feature SHLS aging.

5. The SHLS aging is due to a combination of anomalous aging by both transport and mixing.

6. The anomalous transport component of the SHLS aging is primarily attributed to vertical residual velocity impacts Δw^*. The sign of the age impact in each hemisphere depends on the relative sign between Δw^* and the background condition w^*

7. The relative sign between Δw^* and w^* (or between $\Delta \Psi^*$ and Ψ^*) is controlled by two properties: (1) meridional position of the eruption, and (2) the configuration of the lower branch of the BDC during the season following the eruption.

8. The generic interaction between tropical volcanic forcing and the global tracer transport appears to be a damping of the BDC seasonal cycle, though this would need to be verified with additional studies

Our interpretation of the BDC seasonal damping is an extrapolation from the observations presented here; while the finding in the SHLS is robust across the ensemble and also across the tested eruption magnitude range, it is limited to a single year and eruption location. Verification of this conclusion generically would be better suited to an experiment involving persistent and hemispherically symmetric aerosol forcing, rather than a transient and localized volcanic event. Fortunately, the plethora of simulated stratospheric aerosol injection (SAI) geoengineering experiments conducted during the past decade offer some insight. Bednarz et al. (2023) published a model intercomparison study of meridionally-varying aerosol injections, and concluded that w^* anomalies are generally positive in the NH subtropics, and negative in the SH subtropics for injections near 15°. Notably, the negative anomalies in the SH occur north of the climatological w^* zero-line (their Fig. 6). This resulted in excess concentrations of ozone in the SHLS in three out of four models they analyzed, consistent with our finding of increased AoA in that region (their Fig. 7). For the case of an equatorial injection, they showed positive anomalous upwelling near the equator, and downwelling poleward in each hemisphere, all of which occurred mostly within a region of climatological $w^* > 0$. Associated with this vertical motion effect was an ozone increase symmetric about the equator near 70 hPa.

Later, Henry et al. (2024) performed a similar series of SAI simulations with varying injection latitudes, and analyzed the resulting AoA anomalies (their Fig. 5). Consistent

with Bednarz et al. (2023), they identified increases in aging of up to ∼3 months, near 70 hPa and within ±40° in latitude. They also reported AoA anomaly results from the ARISE-SAI-1.5 simulations (Richter et al., 2022; Henry et al., 2023). Those simulations included simultaneous injection locations at ±30° and ±15° in latitude, but with overall more SO_2 injected in the NH (see Henry et al. (2023) Fig. 2(a)). Consistent with both our work and Bednarz et al. (2023), for this scenario they identified AoA anomalies of nearly 3 months in the SHLS.

Though our results are consistent with the highlighted findings of Bednarz et al. (2023) and Henry et al. (2024), neither of those authors describe the aging effect in the lower stratosphere in terms of the BDC, saying instead that "The response results from local deceleration of upwelling in the tropical troposphere... brought about by the increase in static stability associated with heating in the lower stratosphere and cooling in the troposphere... This deceleration of tropospheric upwelling slows down the transport of ozone-poor tropospheric air into the lower stratosphere, thus increasing ozone in the region." (Bednarz et al., 2023). This is perhaps at odds with our findings, since we observe robust SHLS aging and enhanced e90 despite the fact that the tropospheric vertical velocity impacts are not insignificant (Fig 4.7(a)-(c)), though admittedly we did not pay special attention to the troposphere and did not plot Δw^* below 400 hPa. If there is a contribution from negative stratospheric w^* anomalies to the lower stratosphere increases in age and ozone in Bednarz et al. (2023) and Henry et al. (2023), then it is also unclear if the seasonal effect that we have proposed here is contributing to the hemispherically symmetric response that they demonstrated for equatorial injections. In particular, they did not consider the meridionally-resolved time series of the response, which might have clarified the seasonal contributions to the long-time mean of their tracers. We hypothesize that their symmetric aging in the subtropical lower stratosphere is an average of SHLS aging in austral winter, and NHLS aging in boreal winter, which would be consistent with our conclusions.

In terms of volcanic eruption simulations, there are several works which support our findings. Pitari et al. (2016) used a paired-ensemble strategy similar to ours, and showed that changes of up to 0.1 mm s^{-1} in w^* follow the eruption of Mt. Pinatubo averaged on ±20° at 30 hPa. In latitude, the positive w^* anomaly peaked near 10°N, and became negative at 10°S and 30°N. This is most likely consistent with our finding that the residual streamfunction anomaly does project onto the background condition during the summer of the eruption (Fig. 4.7(d)). They further showed that tropical and northern subtropical AoA decreased by several months, as well as the meridional age gradient. They did not show changes in age below 30 hPa, and so they may or may not have simulated the SHLS aging. Toohey et al. (2014) looked at the circulation response to the Pinatubo eruption with a

64-member ensemble, composed of four sets of 16 simulations, which averaged over different prescribed forcing datesets. They observed that the residual circulation averaged over boreal winter of 1991 was accelerated between 0° and 60°N below 1 hPa, and decelerated in the SH between 0° and 50°S (their Fig. 10(f)), the latter of which is consistent with our Fig. 4.7(e).

A future study could be designed to test our seasonal BDC hypothesis more specifically, by simulating similar volcanic eruptions occuring at different latitudes and/or seasons, or by studying the meridionally- and vertically-resolved temporal evolution of residual circulation anomalies in SAI simulations. There could be any number of other variables to consider as well. An aspect that we did not discuss here is whether the phase of the quasi-biennial (QBO) complicates a potential interaction between volcanic forcing and BDC seasonality. A hint of this complication is found in Brown et al. (2023), who showed that the global symmetry of the post-eruption vertical velocity response depended strongly on the simultaneous QBO phase for equatorial eruptions in their simulations (their Fig. 10). It would also be enlightening to understand how exactly wave activity balances (or fails to balance) the global residual circulation response, which we only described in a more local sense in Chapter 3.

CHAPTER V

Conclusion

This thesis has presented important new developments in idealized modeling of volcanic eruptions (Chapter 2), and has enhanced our understanding of the interaction between volcanic aerosols and global stratospheric dynamics (Chapter 3) and transport (Chapter 4).

In Chapter 2, a new standalone parameterization set called HSW-V was introduced, allowing for simulation of volcanic eruptions in idealized climate models. Specifically, we used a Held-Suarez-Williamson (HSW) forcing set within the Energy Exascale Earth System Model version 2 (E3SMv2) which gives rise to an eternal, quasi-realistic steady state climatology. Against this background state, our method introduces new species of prognostic tracers for volcanic sulfur dioxide (SO_2), ash, and sulfate aerosol. The SO_2 and ash tracers are deposited in the stratosphere by a short-lived and localized massive injection, and are subsequently handed to E3SM's tracer advection code for transport. Chemical production of sulfate aerosol from the SO_2, local radiative aerosol heating, and radiative cooling at the planetary surface are controlled by a small set of differential equations. It was shown that these equations can be tuned to produce atmospheric temperature impacts which mimic those that were observed in nature following the eruption of Mt. Pinatubo in 1991. We suggested that alternative tunings of the equations could enable the idealized representation of other volcanic eruptions, or stratospheric aerosol injection (SAI) geoengineering scenarios.

Prior to this work, only prescribed approaches of volcanic forcing have been available in idealized climate configurations like HSW. Prescribed forcings can be tuned to historical forcing datasets, but cannot represent indirect feedbacks, since the forcing distribution does not respond to changing atmospheric state. Prognostic approaches, on the other hand, typically rely on a complex interplay between chemistry, aerosol, and radiation packages, which are often unavailable in idealized settings. HSW-V finds a middle-ground solution, where the accuracy of proper chemistry and aerosol modeling is sacrificed in favor of simplicity and flexibility, without losing the ability for the aerosols to interact with the environment.

In Chapter 3, a Transformed Eulerian Mean (TEM) framework was used to study the dynamical processes which govern the stratosphere's response to volcanic aerosol radiative

forcing. Two paired ensembles of 15 simulations from the fully-coupled E3SMv2-SPA model were used in this analysis. The first ensemble included the 1991 eruption of Mt. Pinatubo in the form of a large stratospheric injection of SO_2, and the other did not. The ensemble-averaged differences between each pair of simulations from the volcanic and non-volcanic simulations were used to isolate the volcanic impact on the atmospheric state.

This analysis found that westerly zonal winds in the midlatitude polar vortex region of the stratosphere increased following the Pinatubo eruption. However, the nature of this response goes beyond the traditional "thermal wind balance" interpretation. Specifically, we found that the anomalous summertime and wintertime westerlies have very different driving mechanisms. The summer response involves enhanced tropical upwelling, and by mass continuity, an accelerated poleward circulation cell. The Coriolis force associated with the poleward branch of this anomalous circulation primarily drives the observed midlatitude zonal accelerations. The winter response, on the other hand, is characterized by an equatorward deflection of large-scale Rossby waves, due to the altered zonal wind profile. This deflection leads to a deficit of Rossby wave breaking in the midlatitude stratosphere, and thus westerly wind accelerations.

This work is the first to present a full accounting for the volcanic impact on the TEM budget that we are aware of, and the only work after Bittner et al. (2016) to identify the wintertime wave deflection mechanism. We conclude that the TEM framework is a very effective tool for diagnosing dynamical drivers of change following external forcing episodes. We additionally observed that the quasi-biennial oscillation (QBO) of the tropical stratosphere was significantly disturbed by the volcanic aerosols, and saw some suggestion that this is a consequence of not only perturbed upwelling, but also tropical wave characteristics. Further analysis to elucidate the contributing wave mechanisms should be the subject of future studies.

In Chapter 4, we used the same simulations as in Chapter 3 to study the volcanic impact on global mass transport in the years following the Pinatubo eruption. Two inert species were activated for this purpose; the age-of-air (AoA) and e90 tracers. The AoA measures transit times throughout the Brewer-Dobson circulation (BDC) of the stratosphere, and the e90 measures troposphere-stratosphere mass exchange. We found that the main effect of the Pinatubo eruption on global mass transport is to strengthen the so-called *tropical pipe*, which introduces a new population of "young" tropospheric air to the lower tropical stratosphere. This young air takes at least 5 years to traverse the global circulation, meanwhile lowering the average stratospheric AoA post-eruption.

We further investigated the dynamical origins of the changing AoA and e90 tracer concentrations by again utilizing the TEM framework, as well as the residual circulation transit

time (RCTT) measure. Both approaches serve to isolate the changes to tracer transport by advection, and by wave mixing. While the dominant impact was driven by the advective impact, there were also notable findings of perturbed midlatitude wave activity and diffusion altering the AoA and e90 distributions. Notably, we also saw indications that a generic effect of tropical volcanic forcing is to dampen the seasonal signal in the BDC. Finally, we also showed that these effects to the AoA and e90 tracer distributions scale approximately linearly with eruption magnitude, over a range of 3 Tg to 15 Tg initial SO_2 loading, with some suggestion of saturation toward higher masses. Whether that trend continues or not to even higher masses would require further studies in order to be understood.

The chapters of this thesis represent important contributions to the CLDERA project (Chapter 1), to the improvement of the E3SMv2 climate model, and to our ever-evolving understanding of the climate and its interactions with stratospheric aerosols. This progress could not have been made without my collaborators and mentors, and the generations of hard-working scientists that established the foundational literature upon which this work was built. We hope that this research further enriches the field of climate science, contributing in some small way to humanity's collective pursuit for knowledge, and the safety and security of the future people of Earth.

APPENDIX A

This appendix accompanies Chapter 2; Localized Injections of Interactive Volcanic Aerosols in a Simple General Circulation Model.

A.1 Modification of the HSW forcing to Accommodate Higher Model Tops

As suggested in Sect. 2.2.2, we make two modifications to the implementation of the HSW forcing scheme which are (1) the adjustment of the radiative equilibrium temperature T_{eq} near the model top, and (2) the inclusion of an additional sponge-layer wind damping mechanism, described in Sect. A.1.1-A.1.2. Figure 2.1, panel (a) shows the radiative equilibrium temperature with our modifications, and the employed vertical profiles for the sponge layer and surface-layer damping.

A.1.1 Modified radiative equilibrium temperature

The model employed in the experiments of W98 features a top at $\sim$3 hPa, while the standard E3SMv2 model top is located at $\sim$60 km, or 0.1 hPa. Applying the temperature relaxation profile as published in W98 to E3SMv2 therefore results in undesired reversals in the polar lapse rate near 2 hPa, as well as temperatures at the tropical model top at around 60 km in excess of 300 K. Observed monthly-mean zonal-mean tropical temperatures peaks near 50 km are closer to $\sim$260 K (Holton and Hakim, 2013). We experimented with modifying the lapse rate parameters in the HSW T_{eq} as suggested by W98 and implemented by Yao and Jablonowski (2016), but ultimately chose to attempt to retain more realistic temperatures of the upper-stratosphere by simply imposing a lapse rate of zero for p <2 hPa in T_{eq}. Specifically, the equilibrium temperature used in our modified HSW forcing is

$$T_{\mathrm{eq}}(\phi, p) = T_{\mathrm{eq,HSW}}(\phi, \max(p, p^*)) \tag{A.1}$$

where $T_{\mathrm{eq,HSW}}(\phi, p)$ is the form presented in Appendix A of Williamson et al. (1998), and $p^* = 2$ hPa.

Other than this modification, the design and parameter choices of T_{eq} are identical to those defined in HS94 and W98. From W98, we inherit the property that the original implementation of HS94 applies below 100 hPa. Figure A.1 shows zonally-averaged tropical temperature profiles resulting from five-year E3SMv2 runs responding to the specifications of HS94, W98, and our modified HSW forcings. The three implementations exhibit no difference in tropopause structure. Above the tropopause, the HS model approaches a constant temperature near 200 K, while W98 and the modified HSW forcings share a lapse rate of approximately 2.6 K km^{-1} until 2 hPa, where they diverge.

A.1.2   Sponge layer Rayleigh damping

Following HS94 and W98, we use the inverse timescales $k_v(p)$ and $k_T(\phi, p)$ for Rayleigh damping of the velocity $\vec{v}$ and relaxation temperature T toward T_{eq}, respectively. In addition, we also add a second Rayleigh damping mechanism in the "sponge layer" (so-called since it acts to absorb vertically propagating waves near the model top). The vertical profile that we choose for the damping strength follows the implementation of Harris et al. (2021) (their Eq. (8.15)), having a monotonic onset from $\sim$100 Pa to the model top:

$$k_s(p) = k_0 \sin\left(\frac{\pi}{2} \frac{\log(\eta_c/\eta)}{\log(\eta_c/\eta_T)}\right)^2 . \tag{A.2}$$

Here, the normalized pressure coordinate is $\eta \equiv p/p_0$, with $p_0 = 1000$ hPa. We define an onset position at $\eta_c = (1 \text{ hPa})/p_0$, and the normalized pressure at the model top as $\eta_T \equiv p_{\text{top}}/p_0$. The maximum strength of the damping is set via $k_0 = 1/(3 \text{ days})$.

Given these modifications, the wind and temperature tendencies will be updated at each physics timestep by

$$\frac{\partial T}{\partial t} = -k_T(\phi, p)\,(T - T_{\text{eq}}) \tag{A.3}$$

$$\frac{\partial \vec{v}}{\partial t} = (-k_s(p) - k_v(p))\,\vec{v} \tag{A.4}$$

which is the totality of parameterized forcings in our model (in absence of volcanic injections). The vertical profile of the total wind damping $(k_s(p) + k_v(p))$ is shown in Fig. 2.1, panel (a).
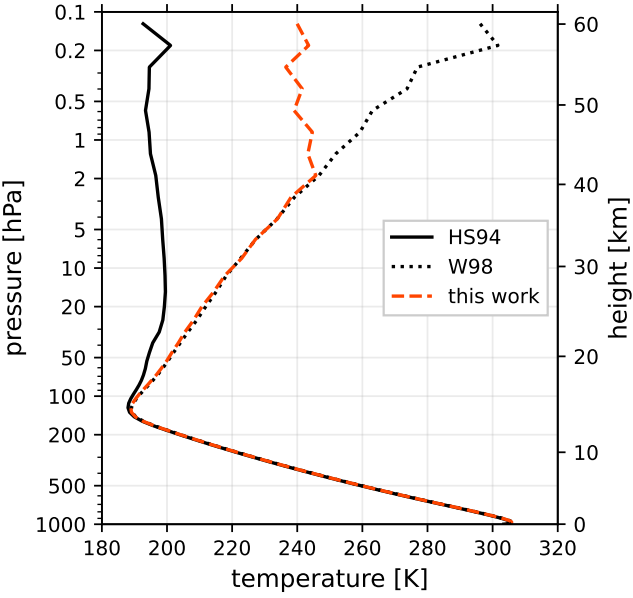
Figure A.1: Zonal-mean tropical temperature profiles resulting from E3SMv2 runs of the HS94 (solid black), W98 (dotted black), and our modified HSW (dashed red) forcing schemes, averaged over $-7°$S to $7°$N. The runs were done at the ne16pg2 resolution for 10 years, with the first five years discarded as spin-up, and the time mean of the latter five-year period shown here. The height axis is derived from the geopotential height of the modified HSW run, with the same averaging performed.

A.2 Residual Circulation of the Modified HSW Atmosphere

A discussion of the residual circulation of the HSW atmosphere was presented in Section 2.4.2. Figure A.2 shows the vertical and meridional components of the residual velocity in the meridional plane from 100 hPa to 0.1 hPa averaged over five years of integration of a HSW run with no volcanic injections, after a five-year spinup period. Also shown is the residual circulation mass streamfunction. The meridional residual velocity, vertical residual velocity, and residual velocity sreamfunction are exactly the forms presented as Eq. A6, A7, and A8 of Gerber and Manzini (2016), respectively.

The residual vertical and meridional velocities agree qualitatively well with those computed from Springtime averages of reanalysis data as presented in Fujiwara et al. (2022) (their Figures 11.12 and 11.15). A curious feature of the HSW residual velocities are the sign reversals in both residual velocity components, as well as the streamfunction, in the polar stratosphere near 10-30 hPa. These features appear in some, but not all, of the Springtime reanalysis results of Fujiwara et al. (2022) in the meridional residual velocity, though not in

116
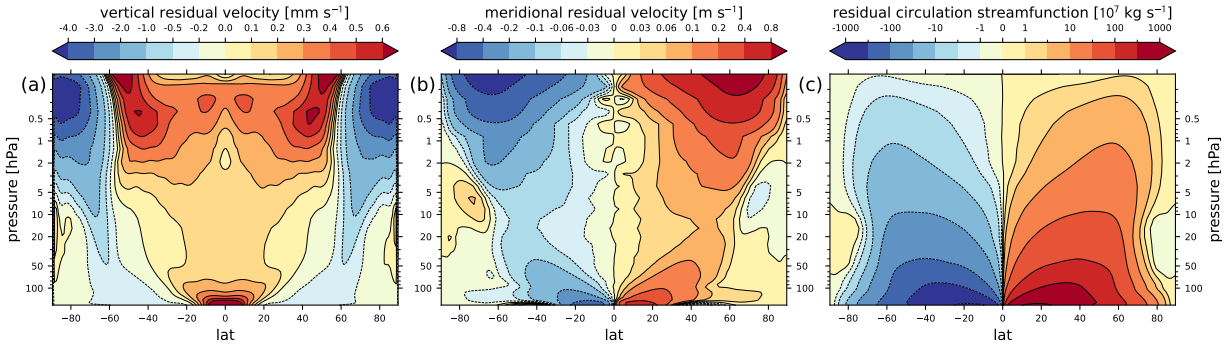
Figure A.2: Stratospheric residual circulation of the HSW atmosphere averaged over five years, after a five-year spinup period. The vertical scale extends from 100 hPa to the model top near 0.1 hPa. **(a)** The vertical residual velocity in mm s^{-1}. Contours are irregularly spaced. **(b)** The meridional residual velocity in m s^{-1}. Contours are irregularly spaced. **(c)** The residual streamfunction in units of 10^7 kg s^{-1}. Contours unlabeled on the colorbar are three times their neighboring contour toward zero. That is, the positive contours are $1, 3, 10, 30, 100 \ldots$

the vertical residual velocity.

A.3 Recommendations for Model Parameter Tuning

This section provides recommendations for re-tuning the idealized volcanic forcing model presented in this work. This information may be useful if the parameterizations are to be activated with a different dynamical core resolution, or if the model parameters are altered to represent a different aerosol injection scenario. The results shown in Sect. 2.4.2 only represent the Pinatubo-like parameter configuration given in Table 2.1 for a grid of nominal 200 km horizontal spacing (the ne16pg2 grid).

In our original implementation, the parameter tuning was done by manually perturbing parameter values after a preliminary estimate, running simulations, and observing the result of certain target metrics. In practice, the tuning process is an iterative one, since changing the extinction coefficients changes the local aerosol heating rates, which in turn changes the local circulation and thus plume transport. Achieving a plume that leads to both a realistic stratospheric distribution and global mean temperature anomalies was the goal.

Each subsection below describes the tuning of a certain effect, first listing the relevant parameters, the target metric used, and the method of the initial estimate. We suggest that future tuning efforts of our parameterizations follow these procedures. In what follows, we refer to a "passive" run as one where the tracer injection and sulfate production occurs as

described in Sect. 2.3.1-2.3.2, but all radiative feedback is disabled, and the tracers are only transported.

A.3.1   SW mass extinction coefficients

Parameters: $b_{\mathrm{SW,ash}}$, $b_{\mathrm{SW,SO2}}$, $b_{\mathrm{SW,sulfate}}$
Target metric: maximum zonal-mean AOD
Initial estimate method: passive simulation runs

In tuning the shortwave extinction coefficients, we can make a preliminary constraint of b_{SW}, such that the resulting AOD τ_i is representative of post-Pinatubo observations. Zonal-mean AODs observed in the months and years following the Pinatubo eruption peaked near 0.2-0.5 (Dutton and Christy, 1992; Stenchikov et al., 1998; Mills et al., 2016), and passive runs of our injection protocol yield maximum zonal-mean column mass burdens (as a sum of all species) which peak near 2×10^7 kg approximately three weeks post-injection near the equator. Constraining columns of this mass burden to have an AOD of 0.35, Eq. (2.23) then suggests

$$\tau_i = 0.35 = b_{\mathrm{SW}} \frac{M_i}{a_i}$$
$$\implies b_{\mathrm{SW}} = \frac{0.35 a_i}{2 \times 10^7 \ \mathrm{kg}} = 700 \ \frac{\mathrm{m}^2}{\mathrm{kg}} \tag{A.5}$$

where we took $a_i = (200 \times 200)$ km^2, consistent with a $\sim$2 degree resolution near the equator. Starting with this initial estimate, we then manually and iteratively altered the b_{SW} parameters until converging upon the desired peak zonal-mean AOD (see Fig. 2.8), with the final parameter values given in Table 2.1. These final values are an acceptable starting estimate for new tuning efforts. Since Eq. (A.5) involves a factor of (area)/(mass), the b_{SW} parameters should be, in principle, independent of resolution. However, higher resolutions could resolve finer, higher-density structures in the tracer fields and might therefore be indirectly dependent on the grid spacing.

A.3.2   Surface heat transfer efficiency

Parameters: ζ
Target metric: minimum mean surface temperature anomaly
Initial estimate method: derived constraint from literature

As we do not a priori know the relationship between surface cooling rates and the realized surface temperature anomaly in the HSW atmosphere, we make a preliminary tuning of ζ, assuming a known maximum negative cooling rate. In their model experiments of the Pinatubo initial plume dispersion, Stenchikov et al. (2021) observed that spatial-mean values of the surface cooling in the equatorial belt from $0°$-$15°$N post-injection are around $\Delta T = -0.02$ K/day (their Fig. 6), which is also qualitatively consistent with Stenchikov et al. (1998) and Ramachandran et al. (2000). In this region, we have already roughly constrained τ to be near 0.35 in Eq. (A.5). Solving Eq. (2.35) for ζ in this case gives:

$$
\left(-0.02\ \frac{\text{K}}{\text{day}}\right) = \zeta \frac{1}{c_p} \frac{a_i}{m_{i,\text{surf}}} \frac{(1\ \text{day})}{(86400\ \text{s})} I_{\text{SW}} \left(\exp(-0.35) - 1\right)
$$

$$
\implies \zeta^{-1} = \frac{1}{c_p} \frac{a_i}{m_{i,\text{surf}}} \frac{(1\ \text{day})}{(86400\ \text{s})} \frac{1}{\left(-0.02\ \frac{\text{K}}{\text{day}}\right)} I_{\text{SW}} \left(\exp(-0.35) - 1\right) . \tag{A.6}
$$

Using I_{SW} from Eq. (2.5) at latitude $\phi = 0$, and $m_{i,\text{surf}} = (\Delta p_{i,k} a_i / g)$ with $\Delta p_{i,k} = 10$ hPa (corresponding to ~ 100 meters or $\kappa = 2$ for Eq. (2.37) in E3SMv2), this gives

$$
\zeta \approx 1.5 \times 10^{-3}
$$

which is independent of horizontal resolution, since a_i cancels in Eq. (A.6) (though it is dependent on vertical resolution). The tuned value of 4.0×10^{-3} is several times larger than this estimate, since we ultimately required average tropical cooling rates significantly lower than -0.02 K day^{-1} (see Fig. 2.8, panel (a)) to obtain a significant surface-level temperature anomaly near -1 K. This requirement may simply be due to the strength of the HSW temperature relaxation at the lowest model levels needing a stronger forcing to overcome.

A.3.3   LW mass extinction coefficients

Parameters:	$b_{\text{LW,ash}}$, $b_{\text{LW,SO2}}$, $b_{\text{LW,sulfate}}$
Target metric:	maximum mean stratospheric temperature anomaly, and lofted sulfate plume height
Initial estimate method:	passive simulation run, and derived constraint from literature

In making initial estimate of the LW mass extinction parameters, we first simplify Eq. (2.28) to an approximate form where the aerosol radiative shadowing effect is not allowed (assuming

I_{LW} is incident on all vertical positions of the column):

$$\Delta I_{i,k} = I_{\mathrm{LW}} \left[1 - \exp\left(-b_{\mathrm{LW}} \frac{q_{i,k} \, \Delta p_{i,k}}{g} \right) \right] . \tag{A.7}$$

This simplified attenuation implies a stratospheric heating rate in the form of Eq. (2.30) of

$$\begin{aligned}
\Delta T_{i,k} &= \frac{1}{c_p} \frac{a_i}{m_{i,k}} I_{\mathrm{LW}} \left[1 - \exp\left(-b_{\mathrm{LW}} \frac{q_{i,k} \, \Delta p_{i,k}}{g} \right) \right] \\
&\approx -\frac{1}{c_p} \frac{a_i}{m_{i,k}} I_{\mathrm{LW}} \, b_{\mathrm{LW}} \frac{q_{i,k} \, \Delta p_{i,k}}{g} ,
\end{aligned} \tag{A.8}$$

where the approximation $e^x \approx (1 + x)$ was used. From observations by previous modeling studies (Stenchikov et al., 2021; Ramachandran et al., 2000; Stenchikov et al., 1998), we expect monthly-mean zonal-mean values for the stratospheric heating rate during month three post-injection to approach $\Delta T = 0.3$ K day^{-1} in the tropics. Note that in the works cited for this figure, this is the *total* heating rate due to contributions of visible, near-infrared, and infrared radiation. In this work, though we refer to this heating effect specifically as "longwave", we are tuning to the *total* heating rate of 0.3 K day^{-1}.

The estimate of b_{LW} can now proceed analogously to Sect. A.3.1-A.3.2, by inverting Eq. (A.8) for b_{LW}. Passive runs of our injection protocol yield sulfate monthly-mean zonal-mean mixing ratios at this time and location of about 10^{-6} kg kg^{-1}. The preliminary b_{LW} estimate is then

$$\implies b_{\mathrm{LW}} = \frac{\left(0.3 \frac{\mathrm{K}}{\mathrm{day}} \right)}{\left(10^{-6} \frac{\mathrm{kg}}{\mathrm{kg}} \right)} \frac{g \, c_p \, m_{i,k}}{a_i \, I_{\mathrm{LW}} \, \Delta p_{i,k}} \frac{(1 \text{ day})}{(86400 \text{ s})} \frac{\mathrm{m}^2}{\mathrm{kg}} . \tag{A.9}$$

Evaluating this form with $I_{\mathrm{LW}}(\phi = 0)$ from Eq. (2.4), and using $m_{i,\mathrm{surf}} = (\Delta p_{i,k} a_i / g)$ gives

$$b_{\mathrm{LW}} \approx 6.2 \ \frac{\mathrm{m}^2}{\mathrm{kg}} . \tag{A.10}$$

Comparing this estimate with Eq. (A.5), our formulation implies that the aerosols are much more efficient at attenuating shortwave radiation (by scattering) than longwave radiation (by absorption).

From this estimate, we then manually and iteratively adjust the three b_{LW} parameters for ash, SO$_2$, and sulfate. As suggested in Sect. 2.3.5, this tuning is done with two target metrics in mind: (1) $b_{\mathrm{LW, \, sulfate}}$ is tuned to give rise to maximum stratospheric temperature anomalies of 2-3 K, and (2) $b_{\mathrm{LW, \, ash}}$ is tuned to control the initial lofting of the fresh, dense

plume, such that the aged sulfate population converges upon the 20-30 km vertical layer. The parameter $b_{\text{LW, SO2}}$ contributes to both the initial lofting and short-term temperature anomalies. Thus, the final tuned parameters (given in Table 2.1) arrive at very different values.

A.3.4 Avoiding a low injection height by revising the LW mass extinction coefficient tuning

As alluded to in Section 2.3.5 and Appendix A.3.3, there is some degeneracy between $b_{\text{LW,ash}}$ and $b_{\text{LW,SO2}}$ for controlling the initial heating of the aerosol plume, as well as degeneracy between $b_{\text{LW,sulfate}}$ and $b_{\text{LW,SO2}}$ for controlling the stratospheric temperature anomalies during the first few months post-injection. This makes the manual process of iteratively tuning the parameters more laborious. In the present case, it also results in the implementation of a unusually low initial injection height of $\mu = 14$ km. Specifically, we did not tune $b_{\text{LW,SO2}}$ along with $b_{\text{LW,ash}}$ and instead needed to compensate for the aggressive early plume lofting by lowering μ.

The tuning process would be easier, and a higher initial injection height of 18-20 km could be more easily supported, if the degeneracy between these three extinction parameters were removed. We suggest having the SO_2 tracer instead behave as a radiatively passive tracer, acting only as the vehicle for sulfate production, by setting $b_{\text{LW,SO2}} = 0$ and $b_{\text{SW,SO2}} = 0$. In this case, the LW mass extinction coefficients for ash and sulfate would be independent knobs for the lofting height, and long-term temperature anomalies, respectively. We would consider this tuning choice an improvement of the parameterization.

APPENDIX B

This appendix accompanies Chapter 3; Volcanic Aerosol Modification of the Stratospheric Circulation in E3SMv2 Part I: Wave-Mean Flow Interaction

B.1   Numerical Recipes for Tendencies and Their Integration

The total tendency in the zonal-mean zonal wind $\overline{u}_i$ at time t_i is computed by the first-order accurate forward finite difference

$$\frac{\partial \overline{u}_i}{\partial t} \approx \frac{\overline{u}_{i+1} - \overline{u}_i}{\Delta t} \tag{B.1}$$

for an integer $i \in [1, N]$, where N is the total number of time samples in the dataset, $\Delta t = (t_{i+1} - t_i)$, and $\overline{u}_i \equiv \overline{u}(t_i)$. Occurrences of Δ in this appendix take the conventional meaning, rather a notation of impact as in the rest of this paper.

For the analysis presented in Sect. 3.5, we compute the integrated tendency of a particular component x of the TEM momentum budget (those terms on the right-hand side of Eq. (3.6)) as

$$\overline{u}_i^{(x)} \equiv \overline{u}_n + \Delta t \sum_{i'=n}^{i} \frac{\partial \overline{u}_{i'}}{\partial t} \bigg|_{(x)} \tag{B.2}$$

for an integer $i \in [n, N]$. This form estimates the total "accumulated" eastward wind speed by the forcing mechanism x over the time period from t_n to t_i, given a common initial condition $\overline{u}_n$. If this recipe is applied to the *total* tendency $\partial \overline{u}/\partial t$, then Eq. (B.2) is just a reversal of the finite difference procedure Eq. (B.1), and the model data $\overline{u}_i$ is recovered exactly. That is, starting the integration from a certain time n does not alter the time series $\overline{u}$, as expected.

For the TEM components, on the other hand, the choice of n does make a material difference to the time series $\overline{u}^{(x)}$. This is a important step in the analysis, since there is strong cancellation between the residual circulation and the EP-flux divergence forcings, especially in the midlatitudes. There, the net resulting zonal-wind is only a relatively small

imbalance between these effects. In addition, there is a seasonal asymmetry in the both the residual circulation speed and large-scale wave activity, such that more zonal wind speed is accumulated by each of these forcing sources during the winter than the summer. Thus, applying Eq. (B.2) with $n = 1$ results in two time series $(\overline{u}^{(v^*)} + \overline{u}^{(w^*)})$ and $\overline{u}^{(\nabla \cdot \mathbf{F})}$ which simply diverge across the dataset. Choosing $n > 1$ instead calibrates the data to a time period of interest.

In order to apply the significance tests of Sect. 3.3.1 to the resulting integrated tendencies, Eq. (B.2) is computed per-ensemble-member, for all x and for each unique choice of n. Note that because the unresolved forcing term $\overline{X}$ (Eq. (3.18)) closes the momentum budget by construction, the sum of $\overline{u}_i^{(x)}$ over all of the TEM components x also recovers the model data $\overline{u}_i$ exactly.

For the meridional and vertical gradients required for the TEM equations of Sect. 3.3.2, we use second-order accurate central differences for interior points, and either forward or backward finite differences at the boundaries. For a quantity $f(\phi_i)$, this is

$$\frac{\partial f_i}{\partial \phi} \approx \begin{cases} \frac{f_{i+1} - f_i}{\phi_{i+1} - \phi_i} & i = 1 \\ \frac{f_{i+1} - f_{i-1}}{\phi_{i+1} - \phi_{i-1}} & 1 < i < N \\ \frac{f_i - f_{i-1}}{\phi_i - \phi_{i-1}} & i = N. \end{cases} \tag{B.3}$$

An analogous form is used for $\partial f / \partial p$. Note that the TEM equations only require meridional derivatives of zonally-averaged quantities. Therefore, the recipe Eq. (B.3) need only be applied to the data after remapping to a uniform latitude grid via Eq. (B.12), and is not used on the native grid.

B.2 Spherical Harmonic Zonal Averaging

For taking zonal averages, rather than interpolating the data to a latitude-longitude grid, we use a spectral method which allows us to obtain atmospheric variable eddy components on the native cubed-sphere simulation grid. For a 2D scalar $A(\phi, \lambda)$, we may write it's zonal average $\overline{A}$ as a superposition of orthonormal basis functions:

$$\overline{A}(\phi) = \sum_{l=0}^{\infty} b_l Y_l^0(\phi) \tag{B.4}$$

Here, b_l are coefficients which scale each contributing basis function, and the basis functions are the set of zonally-symmetric spherical harmonics $Y_l^{m=0}$ of degree l:

$$Y_l^0(\phi) = \sqrt{\frac{2l+1}{4\pi}} P_l(\cos \phi).$$ (B.5)

where $P_l(\phi)$ are the Legendre polynomials. To justify this definition of $\overline{A}$, it can be shown that decomposing the dataset $A(\phi, \lambda)$ into the full set of spherical harmonics $Y_l^m(\phi, \lambda)$ for $0 \leq l < \infty$ and $-l \leq m \leq l$, and zonally-averaging the resulting superposition causes all of the non-symmetric terms ($m \neq 0$) to vanish, yielding Eq. (B.4).

Computationally, this expression for $\overline{A}$ can be approximated for a finite set of basis functions on $0 \leq l \leq L$ as

$$\overline{A}(\phi) \approx \sum_{l=0}^{L} b_l Y_l^0(\phi)$$ (B.6)

Consider a sampling of A resulting in the data vector $\mathbf{A}$ defined on a discrete set of N gridpoints with latitudes ϕ_i. The zonal-mean of this data, $\overline{\mathbf{A}}$ is found by solving for the coefficients b_l at each ϕ_i. The spherical harmonic amplitudes for each (ϕ, l) pair are stored in an $N \times (L+1)$ matrix $\mathbf{Y}_0$, and the coefficients b_l in a column vector $\mathbf{B}$:

$$\mathbf{Y}_0 = \begin{array}{c} \\ \phi_1 \\ \phi_2 \\ \vdots \\ \phi_N \end{array} \begin{array}{c} l=0 \quad l=1 \quad \ldots \quad l=L \\ \left[\begin{array}{cccc} Y_0^0(\phi_1) & Y_1^0(\phi_1) & \ldots & Y_L^0(\phi_1) \\ Y_0^0(\phi_2) & Y_1^0(\phi_2) & \ldots & Y_L^0(\phi_2) \\ \vdots & \vdots & \ddots & \vdots \\ Y_0^0(\phi_N) & Y_1^0(\phi_N) & \ldots & Y_L^0(\phi_N) \end{array} \right] \end{array}, \quad \mathbf{B} = \begin{bmatrix} b_0 \\ b_1 \\ \vdots \\ b_L \end{bmatrix}$$ (B.7)

In matrix notation, Eq. (B.6) is

$$\overline{\mathbf{A}} \approx \mathbf{Y}_0 \mathbf{B},$$ (B.8)

and the coefficients $\mathbf{B}$ are solved for by decomposition of the native grid data $\mathbf{A}$ onto the zonally-symmetric basis set. This requires inversion of $\mathbf{Y}_0$:

$$\mathbf{B} = \mathbf{Y}_0^{-1} \mathbf{A}$$ (B.9)

and so

$$\overline{\mathbf{A}} \approx \mathbf{Y}_0 \mathbf{Y}_0^{-1} \mathbf{A}$$ (B.10)

The inversion $\mathbf{Y}_0^{-1}$ can be obtained by computing a least-squares solution to the equation

124

$\mathbf{Y}_0^{-1}\mathbf{Y}_0 = \mathbf{I}$, where $\mathbf{I}$ is the $(L \times L)$ identity matrix. Alternatively, it can be obtained by $\mathbf{Y}_0^{-1} \equiv \mathbf{Y}_0^{\mathrm{T}}\mathrm{diag}(\mathbf{w})$ where $\mathrm{diag}(\mathbf{w})$ is an $(N \times N)$ matrix with a vector $\mathbf{w}$ of N data weights on the diagonal. The weights provide the areas of the model grid cells, normalized such the the sum of the weights is 4π.

This procedure results in zonal-means, and thus eddy components, at all gridpoints N. Alternatively, an analogous procedure can be followed to recover the zonal mean $\overline{\mathbf{A}}$ on a different, coarser latitude grid. This is more appropriate for visualization and storage of the zonal-mean components. Given a uniform set of latitudes ϕ' of length $M \ll N$, we store the $l = 0$ spherical harmonics at those latitudes in an $M \times (L+1)$ matrix $\mathbf{Y}_0'$:

$$
\mathbf{Y}_0' =
\begin{array}{c}
\\
\phi_1' \\
\phi_2' \\
\vdots \\
\phi_M'
\end{array}
\begin{array}{cccc}
l = 0 & l = 1 & \ldots & l = L \\
\left[\begin{array}{cccc}
Y_0^0(\phi_1') & Y_1^0(\phi_1') & \ldots & Y_L^0(\phi_1') \\
Y_0^0(\phi_2') & Y_1^0(\phi_2') & \ldots & Y_L^0(\phi_2') \\
\vdots & \vdots & \ddots & \vdots \\
Y_0^0(\phi_M') & Y_1^0(\phi_M') & \ldots & Y_L^0(\phi_M')
\end{array}\right]
\end{array}
\tag{B.11}
$$

and the zonal mean of the data is again a composite of these basis functions,

$$
\overline{\mathbf{A}}' \approx \mathbf{Y}_0'\mathbf{B} = \mathbf{Y}_0'\mathbf{Y}_0^{-1}\mathbf{A}.
\tag{B.12}
$$

This equation transforms the data from a N-point grid in real space, to the set of $L + 1$ coefficients b_l in spectral space, before transforming back to a M-point grid in real space.

The matrices $\mathbf{Y}_0$, $\mathbf{Y}_0^{-1}$, and $\mathbf{Y}_0'$ need only be computed once for a given pairing of computational grid ϕ, remap grid ϕ', and choice of L, after which they can be saved to file for use in subsequent computations.

B.3 Physically Consistent Vector-Field Representation of the Meridional Circulation

It is common in the literature for authors to visually represent the circulation in the meridional-vertical plane as a vector field with components $(\overline{v}, \overline{w})$. However, because meridional velocities are typically several orders of larger than vertical velocities, $\overline{w}$ is often multiplied by a post-hoc scaling factor. This scaling factor is usually of order 100, though the specific choice depends on the data localization and processing. In any case, the choice is usually not explicitly justified, and it is often difficult to discern if the direction of the vectors are providing the correct physical picture of the circulation.

Inspired by the scaling recommendations of Jucker (2021) for the EP-flux vectors, here we introduce a method of constructing a vector field of the meridional circulation which is physically-consistent with rotation in the meridional-vertical plane. Specifically, we define a vector field which is everywhere tangent to isolines in a mass streamfunction Ψ (in the form of Eq. (3.12), with a sign convention such that positive structures in Ψ indicate clockwise rotation, and vice-versa. In other words, the curl of the visualized vector field will "look" correct, and regions of zero curl with correspond to $\Psi = 0$. This is usually the implicit goal of manual scaling of the vertical velocity w.

We will assume that the data is provided in a ϕ-p plane, with latitude ϕ in degrees and pressure p in hPa, with p decreasing toward the positive end of the vertical axis. The gradient of Ψ in data units is

$$\nabla\Psi = \begin{bmatrix} \partial\Psi/\partial\phi \\ \partial\Psi/\partial p \end{bmatrix}, \tag{B.13}$$

which we compute by the finite difference methods of Appendix B.1. With Ψ given in kg s^{-1}, the units of the meridional and vertical components of $\nabla\Psi$ are kg s^{-1} deg^{-1} and kg s^{-1}hPa^{-1}, respectively. Because these derivatives are in different units, they must be scaled such that plotting the vector field $\nabla\Psi$ shows the correct direction and amplitude at any location in the plot.

This amounts to a coordinate transformation from data units to "display units". Following Jucker (2021), we define the display coordinates in the plot as X and Y, respectively, which have units of length (e.g. inches). We also define a pair of normalized coordinates $x, y \in [0, 1]$ which give the fractional distance along each axis. For any other coordinate $\alpha \in [\phi, X]$ mapping to $d \equiv x$, or $\alpha \in [p, Y]$ mapping to $d \equiv y$, we use the notation $\alpha_0 \equiv \alpha(d = 0)$, $\alpha_1 \equiv \alpha(d = 1)$, and $\Delta\alpha \equiv \alpha_1 - \alpha_0$ (occurrences of Δ in this appendix take the conventional meaning, rather a notation of impact as in the rest of this paper). If the axes are linear, then the data and display units are related by

$$\phi(X) = \frac{\Delta\phi}{\Delta X}X + \phi_0 \tag{B.14}$$

$$p(Y) = \frac{\Delta p}{\Delta Y}Y + p_0 \tag{B.15}$$

The streamfunction gradient in the display units is then obtained via the transformations

$$\frac{\partial\Psi}{\partial X} = \frac{\partial\Psi}{\partial\phi}\frac{\partial\phi}{\partial X} = \frac{\partial\Psi}{\partial\phi}\frac{\Delta\phi}{\Delta X}, \tag{B.16}$$

$$\frac{\partial \Psi}{\partial Y} = \frac{\partial \Psi}{\partial p}\frac{\partial p}{\partial Y} = \frac{\partial \Psi}{\partial p}\frac{\Delta p}{\Delta Y}, \tag{B.17}$$

Since we can freely make scaling changes to the components which maintain the vector lengths to a constant factor, we will express this as

$$\nabla \Psi_{(X,Y)} \equiv \begin{bmatrix} \Delta X \times \partial \Psi/\partial X \\ \Delta X \times \partial \Psi/\partial Y \end{bmatrix} = \begin{bmatrix} \Delta \phi \partial \Psi/\partial \phi \\ \Delta p(\Delta X/\Delta Y)(\partial \Psi/\partial p) \end{bmatrix} \tag{B.18}$$

where $\Delta X/\Delta Y$ is the plot aspect ratio. Finally, we obtain the tangent vector field $\nabla \Psi^\perp$ by swapping the components and applying the desired sign convention:

$$\nabla \Psi^\perp_{(X,Y)} = \begin{bmatrix} -\Delta p(\Delta X/\Delta Y)(\partial \Psi/\partial p) \\ \Delta \phi \partial \Psi/\partial \phi \end{bmatrix} \tag{B.19}$$

This is the vector field that we plot for visualizing the meridional circulation on linear latitude-pressure axes. Note that if the display coordinates X and Y are expressed in e.g. inches, then Eq. (B.16) and Eq. (B.17) have units of kg s^{-1} in^{-1}. The components of Eq. (B.18) and Eq. (B.19) thus have units of kg s^{-1} y-unit^{-1}, where y-unit represents a unit-length of the y-axis, defined by $\Delta Y = 1$ y-unit.

If we are instead visualizing the vector field in a log-pressure vertical coordinate $z = \log_{10}(p)$, then a different transformation for the vertical component is required. If we define a normalized coordinate $y \in [0,1]$, giving the fractional length along the vertical axis, then the relation between y and p is given by Jucker (2021) as

$$y(p) = \frac{\log_{10}(p_0) - \log_{10}(p)}{\log_{10}(p_0) - \log_{10}(p_1)} = \frac{\ln(p_0/p)}{\ln(p_0/p_1)} \tag{B.20}$$

which implies

$$p(y) = p_0 \left(p_1/p_0\right)^y . \tag{B.21}$$

The derivative of p with respect to the display coordinate Y is then

$$\frac{\partial p}{\partial Y} = \frac{\partial p}{\partial y}\frac{\partial y}{\partial Y} = \frac{1}{\Delta Y}\frac{\partial p}{\partial y} \tag{B.22}$$

and Eq. (B.17) is replaced with

$$\frac{\partial \Psi}{\partial Y} = \frac{\partial \Psi}{\partial p}\frac{\partial p}{\partial Y} = \frac{\partial \Psi}{\partial p}\frac{1}{\Delta Y}\left(p_0 \ln\left(\frac{p_1}{p_0}\right)\left(\frac{p_1}{p_0}\right)^y\right) . \tag{B.23}$$
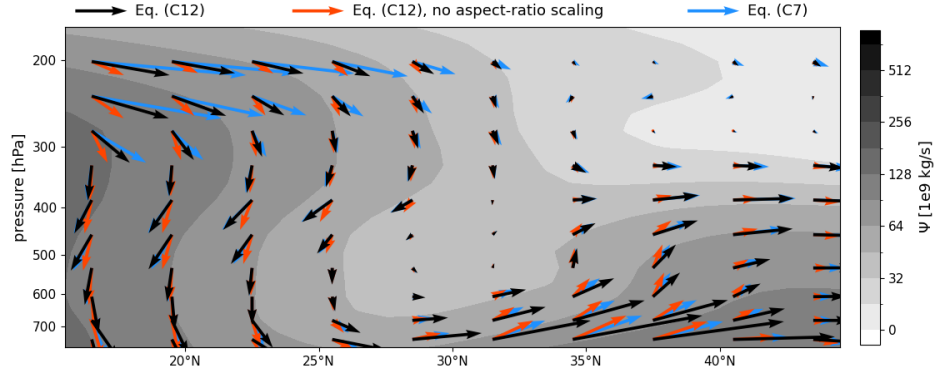
Figure B.1: A comparison of three representations of the gradient-normal vector field of a winter-time streamfunction Ψ in the northern hemisphere on a log-scaled vertical pressure axis, with a figure aspect ratio of 2.4. Ψ is shown in the greyscale contours. Black arrows show the vectors tangent to isolines in Ψ, as computed by Eq. (B.24). Red arrows show the same vectors, but with the aspect-ratio scaling removed (the horizontal component of Eq. (B.24) is multiplied by $\Delta Y/\Delta X$). Blue arrows shows the vectors as computed by Eq. (B.19) without the log-pressure correction. The black arrows are the only ones which are everywhere tangent to the Ψ contours. The blue arrows would be tangent if the vertical pressure axis were linearly-scaled. The vector lengths correspond to the magnitude $\nabla\Psi$ at each point. The arrows presented in the figure legend represent 4×10^{11} kg s^{-1} per unit length of the y-axis.

where y in this equation is the evaluation of Eq. (B.20) at p. Following the procedure in Eq. (B.18)–Eq. (B.19) above, the vector field that we plot for visualizing the meridional circulation on latitude-log-pressure aces is thus

$$
\nabla\Psi^{\perp}_{(X,Y)} = \begin{bmatrix} -\frac{\Delta X}{\Delta Y}\frac{\partial\Psi}{\partial p}\left(p_0\ln\left(\frac{p_1}{p_0}\right)\left(\frac{p_1}{p_0}\right)^{y}\right) \\ \Delta\phi\partial\Psi/\partial\phi \end{bmatrix} \tag{B.24}
$$

Figure B.1 shows the effect of these different choices for plotting the gradient-normal vector field of Ψ for a logarithmic vertical pressure axis, with and without the plot aspect ratio scaling and derived log-pressure scaling. This demonstrates that for rendering a vector field parallel to isolines of Ψ while maintaining physically correct vector directions in plots of arbitrary shape, the scalings presented here are the correct ones.

APPENDIX C

This appendix accompanies Chapter 4: Volcanic Modification of the Stratospheric Circulation: Tracer Sensitivity

C.1 Seasonal Tracer TEM Balance

This section provides the seasonal TEM balance for the evolution of the age of air (AoA) and e90 tracers. The summer and winter balance is shown in Fig. C.2 and Fig. C.1 for AoA, Fig. C.4 and Fig. C.3 for e90, respectively. See Sect. 4.4 for discussion.
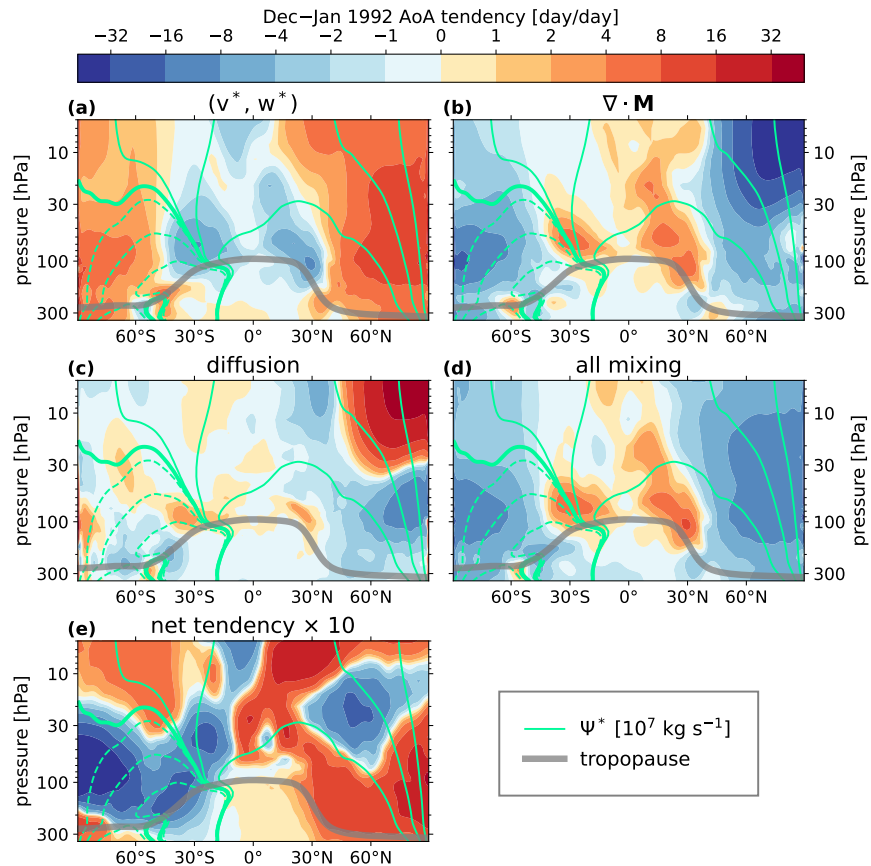
Figure C.1: The same as Fig. 4.5, but for a winter climatological average.
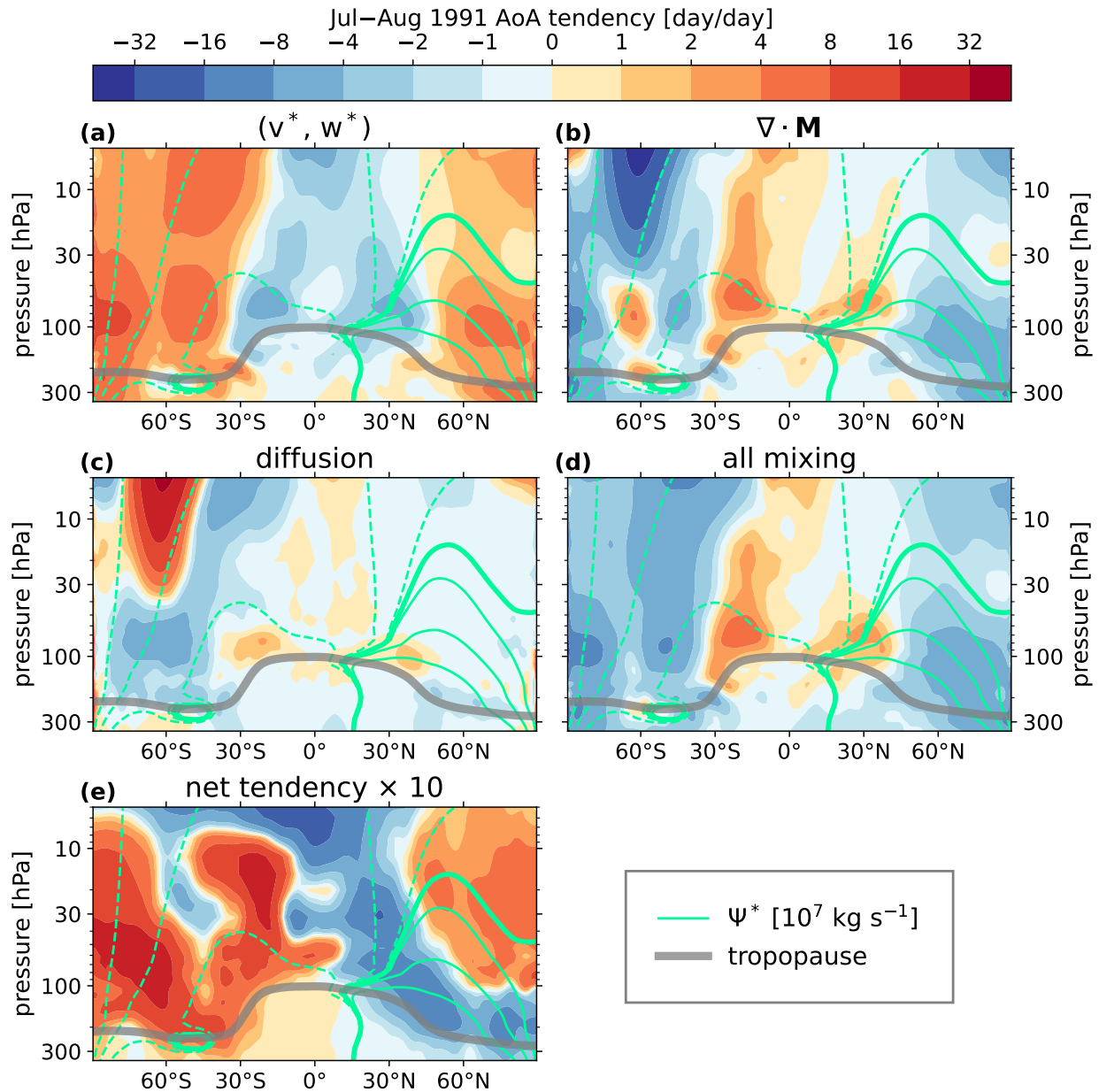
Figure C.2: The same as Fig. 4.5, but for a summer climatological average.
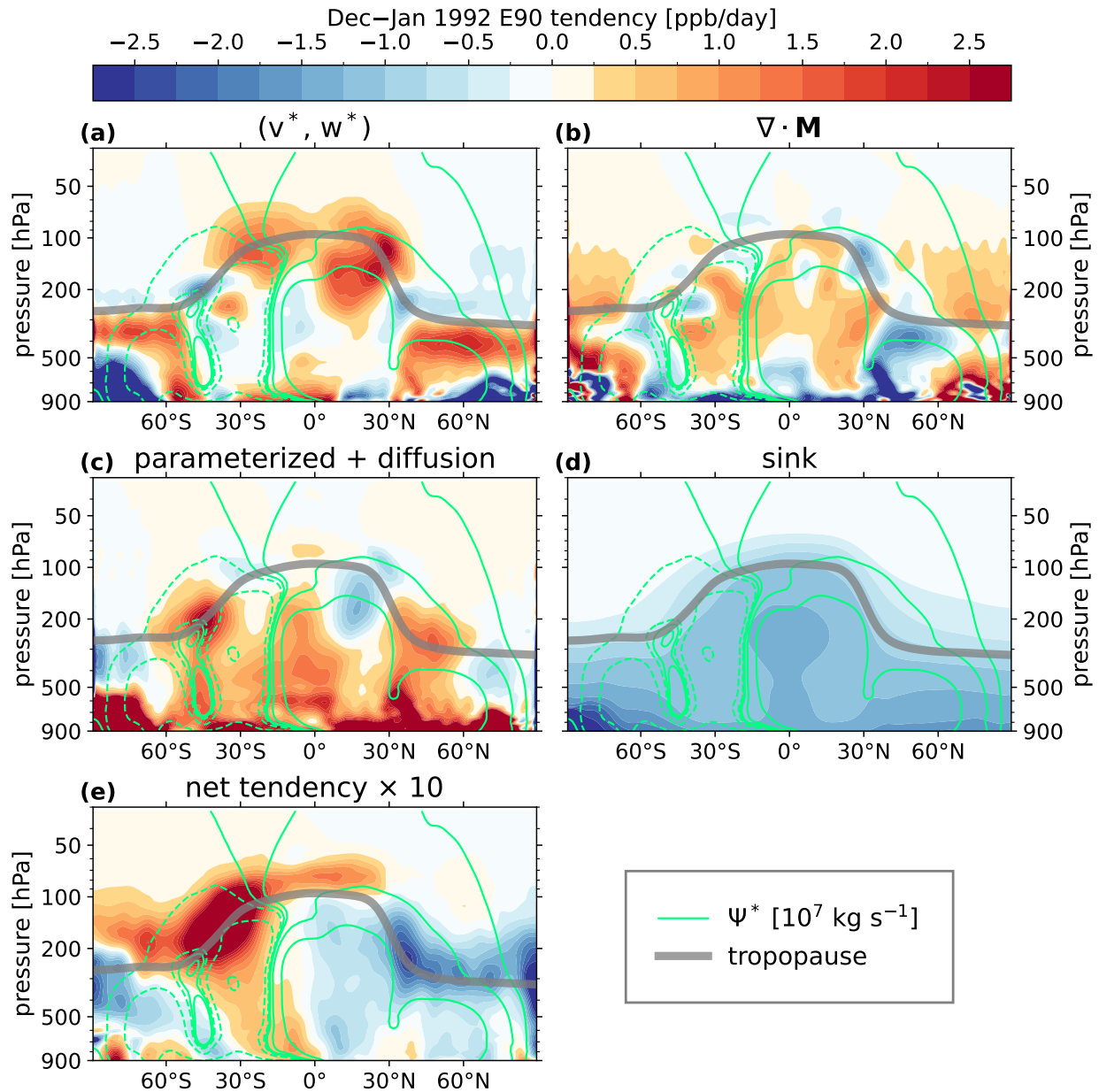
Figure C.3: The same as Fig. 4.6, but for a late-winter climatological average.
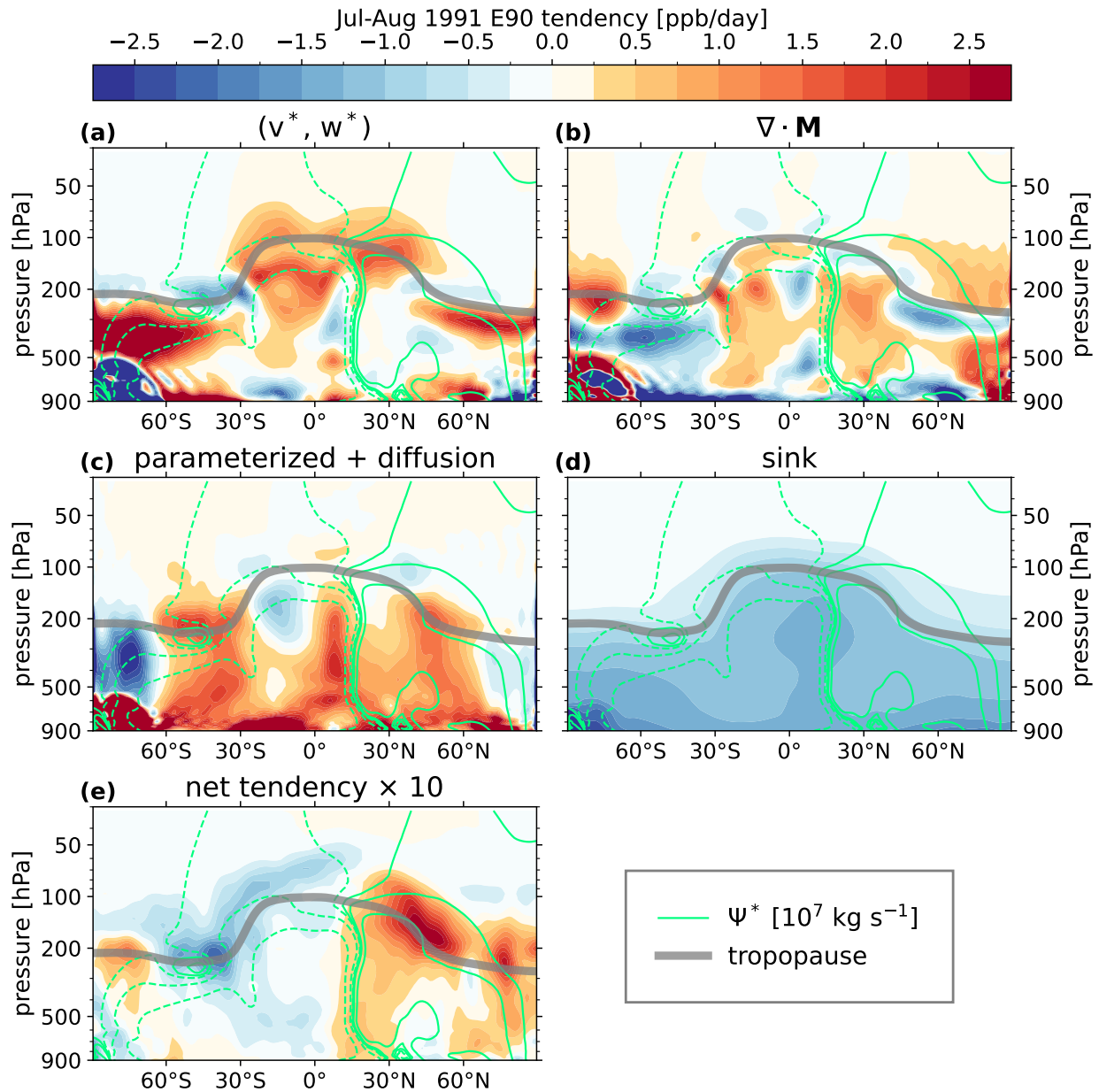
Figure C.4: The same as Fig. 4.6, but for a summer climatological average.

APPENDIX D

This appendix describes the process of taking weighted averages of climate model data on structured latitude-longitude grids with a vertical hybrid pressure coordinate. The vertical averaging (Appendix D.2) described here will equally apply to data stored on unstructured horizontal grids, but the horizontal averaging (Appendix D.3) will not. For a spherical-harmonic-based spectral method for taking zonal averages of unstructured data, see Appendix B.2.

D.1 Vertical Hybrid Coordinate

Consider a 3D variable $A(\phi, \lambda, p)$ with orthogonal dimensions latitude ϕ and longitude λ, and a vertical pressure coordinate p. A is known on a $N \times M$ horizontal grid with coordinates (ϕ_i, λ_j), and a vertical grid composed of K *model levels* at reference pressures p_k. In general, the horizontal grid has unequal grid-cell area, and the vertical grid has non-equidistant spacing.

At the north and south pole, $\phi_1 = \pi/2$ and $\phi_N = -\pi/2$ by convention, respectively. The vertical index $k = 1$ is the model level at nearest (but not touching) the top of the vertical domain, and index $k = K$ is the model level nearest (but not touching) the surface.

In addition, there are $K + 1$ *interface levels* that straddle each model level. These start at the model top, and the lowest interface level coincides with the surface. Symbolically, we can use a half-index notation to distinguish between model levels (index k) and interface levels (index $k \pm 1/2$). The reference pressure at each model level is simply defined as a linear average of the two surrounding interfaces,

$$p_k = \frac{1}{2}(p_{k-1/2} + p_{k+1/2}) \tag{D.1}$$

where

$$p_{k \pm 1/2} = p_0(a_{k \pm 1/2} + b_{k \pm 1/2}) \tag{D.2}$$

Here, $a_{k \pm 1/2}$, $b_{k \pm 1/2}$ are known as the *hybrid coefficients* and are constant per model level.

p_0 is a constant, most often $p_0 = 10^5$ Pa. From Eq. (D.1)-(D.2), we see that

$$p_k = \frac{1}{2}p_0 \left(a_{k\pm1/2} + b_{k\pm1/2}\right) = p_0(a_k + b_k) \tag{D.3}$$

with the definitions

$$a_k \equiv \frac{1}{2}(a_{k+1/2} + a_{k-1/2}) \tag{D.4}$$

$$b_k \equiv \frac{1}{2}(b_{k+1/2} + b_{k-1/2}) \tag{D.5}$$

The vertical dependence of the $a_{k\pm1/2}$ and $b_{k\pm1/2}$ may be different for the choice of vertical resolution and model height, and in general is manually constructed as a part of the model design. But why have these coefficients at all? Note that while the reference pressure p_k of Eq. (D.1) defines the fixed vertical grid, the *actual* pressure at a given gridpoint, $p_{i,j,k}$, varies with the prognostic surface pressure variable p_s as

$$p_{i,j,k} = a_k p_0 + b_k (p_s)_{i,j} \tag{D.6}$$

where $(p_s)_{i,j}$ is the surface pressure at index (i, j), in Pa. Likewise, the actual pressure at the interface levels is

$$p_{i,j,k\pm1/2} = a_{k\pm1/2}p_0 + b_{k\pm1/2}(p_s)_{i,j} \tag{D.7}$$

This kind of discretization is known as a *hybrid* vertical coordinate or *η-coordinate*, since for $a_k = 0$, p_k is an orography-following coordinate (a *σ-coordinate*), and for $b_k = 0$, p_k is a purely pressure-based coordinate which has no knowledge of topography (a *p-coordinate*). The design of the hybrid coefficients a_k, b_k control the transition between these two regimes. See a diagram and notes on the *η*-coordinate on this CESM page.

If p_s is not known, then the best that can be done is assume $p_s = p_0$, in which case Eq. (D.6) reduces to Eq. (D.3), and Eq. (D.7) to Eq. (D.2).

In the CESM and E3SM climate models, p_k and $p_k \pm 1/2$ are supplied with any model output as the `lev` and `ilev` fields. The actual pressure $p_{i,j,k}$ and $p_{i,j,k\pm1/2}$ is not provided, and must be calculated by Eq. (D.2), (D.7) with the provided `PS` and `P0` fields, corresponding to p_s and the constant p_0.

D.2   Vertical Averaging

We can reduce A to a 2-dimensional horizontal field by taking a vertical average, incorporating pressure-weights to reflect the varying thickness of each model level. The pressure-

weighted average $\langle A \rangle_p$ is

$$\langle A \rangle_p = \frac{1}{p_s - p_{\text{top}}} \int_{p_s}^{p_1} A(p) dp \tag{D.8}$$

where, as a reminder, $p_{\text{top}} = p_{k=1/2}$ is the pressure at the model top, or the pressure of the highest interface level. Discretized onto the vertical grid, this is

$$\langle A \rangle_p = \frac{1}{p_s - p_{\text{top}}} \sum_{k=1}^{K} A_k \Delta p_k \tag{D.9}$$

$$= \frac{1}{p_s - p_{\text{top}}} \sum_{k=1}^{K} A_k (p_{k+1/2} - p_{k-1/2}) \tag{D.10}$$

Here we have defined the pressure thickness of each level to be the separation of the surrounding reference interface levels, $\Delta p_k \equiv (p_{k-1/2} - p_{k-1/2})$. Without knowledge of p_s, this is the best we can do.

If, on the other hand, the surface pressure $(p_s)_{i,j}$ is known, then a more accurate expression per-gridpoint is

$$(\langle A \rangle_p)_{i,j} = \frac{1}{(p_s)_{i,j} - p_{i,j,1/2}} \sum_{k=1}^{K} A_{i,j,k} \Delta p_{i,j,k} \tag{D.11}$$

$$= \frac{1}{(p_s)_{i,j} - p_{i,j,1/2}} \sum_{k=1}^{K} A_{i,j,k} (p_{i,j,k+1/2} - p_{i,j,k-1/2}) \tag{D.12}$$

for which the pressure terms can be computed given the procedure described at the end of Appendix D.1.

We can also view this equation as a weighted average of A, where the weights are the model level pressure thicknesses, normalized by the sum of all the weights. If we call those normalized weights

$$\widetilde{\Delta p}_{i,j,k} = \frac{\Delta p_{i,j,k}}{\sum_{k=1}^{K} \Delta p_{i,j,k}} = \frac{\Delta p_{i,j,k}}{((p_s)_{i,j} - p_{i,j,1/2})} \tag{D.13}$$

then we can write

$$(\langle A \rangle_p)_{i,j} = \sum_{k=1}^{K} A_{i,j,k} \widetilde{\Delta p}_{i,j,k} \tag{D.14}$$

D.3 Horizontal Averaging

In general, weighting a horizontal average requires knowledge of the grid cell areas. For unstructured grids, this is necessary (though in practice, we will often omit weighting entirely for e.g. unstructured cubed-sphere grids, which are quasi-uniform). Lat-lon grids are far from uniform, and hence this weighting is needed, else values near the poles will contribute disproportionately to horizontal means. We can take advantage of the properties of this grid to deduce the appropriate weighting, and avoid computing cell areas.

On the lat-lon grid, all grid cells are uniformly sized in longitude, and only vary in latitude, where cell areas are largest at the equator, and vanish at the poles. Thus, the horizontal weights $w_{i,j}$ need only be a function of ϕ, with the limiting behavior suggesting

$$w_{i,j} = \cos(\phi_i) \tag{D.15}$$

To see this more rigorously, note that our convention of having the latitudinal zero-point at the equator, with $\phi \in [-\pi/2, \pi/2]$ is non-standard in most of math and physics; with this convention, then radial unit vector on the unit-sphere is

$$\mathbf{r} = \begin{bmatrix} \cos\phi\cos\lambda \\ \cos\phi\sin\lambda \\ \sin\phi \end{bmatrix} \tag{D.16}$$

and thus

$$\frac{\partial \mathbf{r}}{\partial \phi} = \begin{bmatrix} -\sin\phi\cos\lambda \\ -sin\phi\sin\lambda \\ cos\phi \end{bmatrix}, \quad \frac{\partial \mathbf{r}}{\partial \lambda} = \begin{bmatrix} -cos\phi\sin\lambda \\ \cos\phi\cos\lambda \\ 0 \end{bmatrix} \tag{D.17}$$

The product of the magnitudes of these vectors gives the surface element dS_r:

$$dS_r = \left| \frac{\partial \mathbf{r}}{\partial \lambda} \times \frac{\partial \mathbf{r}}{\partial \phi} \right| d\phi d\lambda = \cos\phi d\phi d\lambda \tag{D.18}$$

Horizontal averages $(\langle A \rangle_h)_k$ at vertical level k can then be computed by integrating the A over the surface of the sphere, dividing by the total surface area

$$(\langle A \rangle_h)_k = \frac{1}{4\pi} \int_0^{2\pi} \int_{-\pi/2}^{\pi/2} A(\phi, \lambda) \cos\phi d\phi d\lambda \tag{D.19}$$

Discretized onto the grid, this is

$$\frac{1}{\sum_{i,j} \cos\phi_i \Delta\phi_i \Delta\lambda_j} \sum_{i=1}^{N} \sum_{j=1}^{M} A_{i,j,k} \cos\phi_i \Delta\phi_i \Delta\lambda_j \qquad (D.20)$$

where the factor out front is the inverse of the total sum of the weights, approximating the sphere's total surface area. $\Delta\phi$ and $\Delta\lambda$ are the grid cell angular dimensions in *radians*. If $\Delta\lambda_j$ is constant, then this becomes

$$\frac{1}{M \sum_i \cos\phi_i \Delta\phi_i} \sum_{i=1}^{N} \sum_{j=1}^{M} A_{i,j,k} \cos\phi_i \Delta\phi_i \qquad (D.21)$$

The factors $\cos\phi_i \Delta\phi_i$ we will call the *Gaussian weights* $(w_g)_i$, which are used in the weighted horizontal means for lat-lon grids with non-uniform gridpoint spacing in ϕ, e.g. Gaussian grids. The sum in the denominator is approximating the integral

$$\sum_i (w_g)_i \approx \int_{-\pi/2}^{\pi/2} \cos\phi \, d\phi = 2 \qquad (D.22)$$

which even for very coarse grids (e.g. N=25) has an error of $\sim 1\%$. For this reason, Eq. (D.21) is usually written as

$$\frac{1}{M} \frac{1}{2} \sum_{i=1}^{N} \sum_{j=1}^{M} A_{i,j,k} (w_g)_i \qquad (D.23)$$

If, however, we know that we have constant $\Delta\phi$, then Eq. (D.21) again simplifies to

$$\frac{1}{M \sum_i \cos\phi_i} \sum_{i=1}^{N} \sum_{j=1}^{M} A_{i,j,k} \cos\phi_i \qquad (D.24)$$

$$= \frac{1}{M} \frac{1}{\sum_i w_i} \sum_{i=1}^{N} \sum_{j=1}^{M} A_{i,j,k} w_i \qquad (D.25)$$

where w_i are the cosine weights as introduced in Eq. (D.15). For constant $\Delta\phi$, the weighted averaging approaches Eq. (D.23) and (D.25) are equivalent. For non-equidistant $\Delta\phi$, Eq. (D.25) is only approximately correct.

As was done in Appendix D.2, let us define normalized weights $\widetilde{w}_i$, which are just the cosine weights normalized by the sum of all the weights,

$$\widetilde{w}_i = \frac{\cos\phi_i}{\sum_i \cos\phi_i} \qquad (D.26)$$

in which case, the weighted average is concisely

$$(\langle A \rangle_h)_k = \frac{1}{M} \sum_{i=1}^{N} \sum_{j=1}^{M} A_{i,j,k} \widetilde{w}_i \qquad \text{(D.27)}$$

D.4 Global Average

Weighted vertical averages at a gridpoint (i,j) in a hybrid $\eta-$coordinate are taken by Eq. (D.14):

$$(\langle A \rangle_p)_{i,j} = \sum_{k=1}^{K} A_{i,j,k} \widetilde{\Delta p}_{i,j,k}$$

Weighted horizontal averages at level k on a standard lat-lon grid (with equidistant gridpoint spacing in ϕ and λ) are taken by Eq. (D.27):

$$(\langle A \rangle_h)_k = \frac{1}{M} \sum_{i=1}^{N} \sum_{j=1}^{M} A_{i,j,k} \widetilde{w}_i$$

Global averages over the entire simulation domain at a time t are thus

$$\langle A \rangle = \frac{1}{M} \sum_{i=1}^{N} \sum_{j=1}^{M} \sum_{k=1}^{K} A_{i,j,k} \widetilde{\Delta p}_{i,j,k} \widetilde{w}_i \qquad \text{(D.28)}$$

APPENDIX E

This appendix details the step-by-step conversion between various forms of the Transformed Euelrian Mean (TEM) equations commonly used in the literature. The version originally introduced by Andrews and McIntyre (1976) is provided on a midlatitude β-plane with a height coordinate z. This is also the version included in *Middle Atmoshere Dynamics* (Andrews et al. (1987); hereafter A87). More recently, a more general spherical-coordinate version with a pressure-based vertical coordinate was chosen for the use by the Dynamics and Variability Model Intercomparison Project (DynVarMIP) protocol (Gerber and Manzini (2016); hereafter GM16), which is also the version that was employed in Chapters 3–4 of this thesis.

The β-plane version has been used in many works, including in the tracer-based studies of Abalos et al. (2017) and Abalos et al. (2013). There, the authors borrow a quantity known as the eddy-tracer flux vector field from Andrews et al. (1987). While the dynamical TEM equations appears in various forms in the literature, alternative expressions of the tracer equations are more rare.

Conversions between these different expressions are straightforward, but cumbersome to carry through the framework. We will detail the steps here, with a preference for obtaining the result in the spherical-coordinate formulation of GM16. For the informed reader, this appendix is intended to stand on it's own, and so will have some redundancies of definitions and derivations with Chapter 3.

E.1 Spherical and Local Beta-plane TEM Formulations

In the GM16 formulation, the residual velocities are

$$v^* = \overline{v} - \frac{\partial}{\partial p}\frac{\overline{v'\theta'}}{\partial\overline{\theta}/\partial p} \tag{E.1}$$

$$\omega^* = \overline{\omega} + \frac{\partial}{a\cos\phi\partial\phi}\frac{\overline{v'\theta'}}{\partial\overline{\theta}/\partial p}\cos\phi \tag{E.2}$$

where the factor involving the eddy heat flux is the eddy streamfunction $\psi = \overline{v'\theta'}/(\partial\overline{\theta}/\partial p)$. The zonal and vertical Eliassen-Palm (EP) components are

$$F_{(\phi)} = a\cos\phi\left\{\frac{\partial\overline{u}}{\partial p}\frac{\overline{v'\theta'}}{\partial\overline{\theta}/\partial p} - \overline{u'v'}\right\} \tag{E.3}$$

$$F_{(p)} = a\cos\phi\left\{\left[f - \frac{\partial\overline{u}\cos\phi}{a\cos\phi\partial\phi}\right]\frac{\overline{v'\theta'}}{\partial\overline{\theta}/\partial p} - \overline{u'\omega'}\right\}, \tag{E.4}$$

or in a log-pressure coordinate,

$$\widehat{F}_{(\phi)} = \frac{p}{p_0}F_{(\phi)}, \qquad \widehat{F}_{(z)} = \frac{p}{p_0}F_{(z)} = -\frac{H}{p_0}F_{(p)} \tag{E.5}$$

The time tendency of the zonal-mean zonal-wind is a sum of four terms—advection by the meridional residual flow and the Coriolis force, advection by the vertical residual flow, forcing by wave activity (EP flux divergence), and subgrid processes. This is written as

$$
\begin{aligned}
\frac{\partial\overline{u}}{\partial t} &= \frac{\partial\overline{u}}{\partial t}\bigg|_{\mathrm{adv}(v^*)} + \frac{\partial\overline{u}}{\partial t}\bigg|_{\mathrm{adv}(\omega^*)} + \frac{\partial\overline{u}}{\partial t}\bigg|_{\nabla\cdot\mathbf{F}} - \overline{X} \\
&= v^*\left[f - \frac{\partial\overline{u}\cos\phi}{a\cos\phi\partial\phi}\right] - \omega^*\frac{\partial\overline{u}}{\partial p} + \frac{\nabla\cdot\mathbf{F}}{a\cos\phi} - \overline{X} \\
&= v^*\left[f - \frac{\partial\overline{u}\cos\phi}{a\cos\phi\partial\phi}\right] - \omega^*\frac{\partial\overline{u}}{\partial p} + \frac{1}{a\cos\phi}\left[\frac{\partial F_{(\phi)}\cos\phi}{a\cos\phi\partial\phi} + \frac{\partial F_{(p)}}{\partial p}\right] - \overline{X}
\end{aligned}
\tag{E.6}
$$

where $\overline{X}$ is subgrid dissipation, or more generally any acceleration imposed on $\overline{u}$ not accounted for in the other terms (notably parameterized gravity waves). GM16 state that these diagnostics are formulated following the textbook A87, with the following important modification: GM16 does not follow A87 in multiplying the EP flux vector components by a factor of the background density profile $\rho_0 = \rho_s e^{-z/H} = (p_0/RT_s)e^{-z/H}$. They also replace vertical derivatives in z with derivatives in p by assuming a log-pressure vertical coordinate:

$$\frac{\partial\alpha}{\partial z} = \frac{\partial\alpha}{\partial p}\frac{\partial p}{\partial z} = \frac{\partial\alpha}{\partial p}\frac{\partial}{\partial z}\left(-p_0 e^{-z/H}\right) = -\frac{\partial\alpha}{\partial p}\frac{p}{H} \tag{E.7}$$

where α is a generic variable. Thus, occurrences of the vertical velocity transform as

$$w = \frac{\partial z}{\partial t} = \frac{\partial z}{\partial p}\frac{\partial p}{\partial t} = \frac{\partial}{\partial p}\left[-H\ln\left(-\frac{p}{p_0}\right)\right]\frac{\partial p}{\partial t} = -\frac{H}{p}\omega. \tag{E.8}$$

Let's verify that we can recover the equations of GM16 from those presented in A87 given these transformations. The relevant forms are Eq. (3.5.2a–3.5.3b) of A87 (which we'll denote with squiggly hats). Substitutions made according to the log-pressure rules given above will

be highlighted in red. First the meridional component:

$$\widetilde{F}_{(\phi)} = \rho_0 a \cos\phi \left\{ \frac{\partial \overline{u}}{\partial z} \frac{\overline{v'\theta'}}{\partial \overline{\theta}/\partial z} - \overline{u'v'} \right\} \tag{E.9}$$

$$= \rho_0 a \cos\phi \left\{ -\frac{\cancel{p}}{H} \frac{\partial \overline{u}}{\partial p} \frac{\overline{v'\theta'}}{\cancel{-(p/H)}\partial\overline{\theta}/\partial p} - \overline{u'v'} \right\}$$

$$= \rho_0 a \cos\phi \left\{ \frac{\partial \overline{u}}{\partial p} \frac{\overline{v'\theta'}}{\partial\overline{\theta}/\partial p} - \overline{u'v'} \right\}$$

$$\implies \widetilde{F}_{(\phi)} = \rho_0 F_{(\phi)}$$

and the vertical component:

$$\widetilde{F}_{(z)} = \rho_0 a \cos\phi \left\{ \left[f - \frac{\partial \overline{u} \cos\phi}{a \cos\phi \partial\phi} \right] \frac{\overline{v'\theta'}}{\partial\overline{\theta'}/\partial z} - \overline{u'w'} \right\} \tag{E.10}$$

$$= \rho_0 a \cos\phi \left\{ \left[f - \frac{\partial \overline{u} \cos\phi}{a \cos\phi \partial\phi} \right] \frac{\overline{v'\theta'}}{-(p/H)\partial\overline{\theta'}/\partial p} - \left(-\frac{H}{p} \right) \overline{u'\omega'} \right\}$$

$$\implies \widetilde{F}_{(z)} = -\frac{H}{p} \rho_0 F_{(p)}$$

By pulling out a factor of $\rho_s = p_0/RT_s$, we recover the log-pressure EP flux given in Eq. (A13–A14) of GM16, and so these two formulations are consistent:

$$\widehat{F}_{(\phi)} = \frac{1}{\rho_s} \widetilde{F}_{(\phi)} = \frac{\rho_0}{\rho_s} F_{(\phi)} = e^{-z/H} F_{(\phi)} = \frac{p}{p_0} F_\phi \,\checkmark \tag{E.11}$$

$$\widehat{F}_{(z)} = \frac{1}{\rho_s} \widetilde{F}_{(z)} = -\frac{H}{p} \frac{\rho_0}{\rho_s} F_{(p)} = -\frac{H}{p} e^{-z/H} F_{(p)} = -\frac{H}{p_0} F_{(p)} \,\checkmark \tag{E.12}$$

Likewise, the EP flux divergence and associated zonal wind tendency term are given in A87 as

$$\nabla \cdot \widetilde{\mathbf{F}} = \frac{\partial \widetilde{F}_{(\phi)} \cos\phi}{a \cos\phi \partial\phi} + \frac{\partial \widetilde{F}_{(z)}}{\partial z}, \tag{E.13}$$

$$\left. \frac{\partial \widetilde{\overline{u}}}{\partial t} \right|_{\nabla \cdot \widetilde{\mathbf{F}}} = \frac{\nabla \cdot \widetilde{\mathbf{F}}}{\rho_0 a \cos\phi} \tag{E.14}$$

$$= \frac{1}{a \cos\phi} \left[\frac{\partial \rho_0^{-1} \widetilde{F}_{(\phi)} \cos\phi}{a \cos\phi \partial\phi} + \rho_0^{-1} \frac{\partial \widetilde{F}_{(z)}}{\partial z} \right] \tag{E.15}$$

141

$$= \frac{1}{a\cos\phi}\left[\frac{\partial F_{(\phi)}\cos\phi}{a\cos\phi\partial\phi} - \rho_0^{-1}\frac{p}{H}\frac{\partial F_{(p)}}{\partial p}\right]$$

$$= \frac{1}{a\cos\phi}\left[\frac{\partial F_{(\phi)}\cos\phi}{a\cos\phi\partial\phi} - \frac{\partial(p/(H\rho_0)\widetilde{F}_{(z)})}{\partial p}\right]$$

$$= \frac{1}{a\cos\phi}\left[\frac{\partial F_{(\phi)}\cos\phi}{a\cos\phi\partial\phi} + \frac{\partial F_{(p)}}{\partial p}\right] = \frac{\partial\overline{u}}{\partial t}\bigg|_{\nabla\cdot\mathbf{F}} \quad\checkmark$$

where we used the fact that the factor $p/(H\rho_0) = -p_0/(H\rho_s)$ is not a function of pressure, and so can be moved inside derivatives of p. The fact that the zonal-mean zonal-wind tendency is equivalent in either formulation makes sense, since whichever conventions we choose to use in the definition of the EP flux vector, it must not affect the physical forces on $\overline{u}$! This should also be true of the two advection terms of Eq. (E.6). To check this, we will first need the transformed residual velocities as given by A87. These turn out to be unaffected:

$$\widetilde{\overline{v}}^* = \overline{v} - \frac{1}{\rho_0}\frac{\partial}{\partial z}\frac{\rho_0\overline{v'\theta'}}{\partial\overline{\theta}/\partial z} \tag{E.16}$$

$$= \overline{v} - \frac{1}{\rho_0}\left(-\frac{p}{H}\right)\frac{\partial}{\partial p}\frac{\rho_0\overline{v'\theta'}}{-(p/H)\partial\overline{\theta}/\partial p}$$

$$= \overline{v} + \frac{\partial}{\partial p}\left(\frac{\cancel{p}}{\cancel{\rho_0}H}\right)\frac{\cancel{\rho_0}\overline{v'\theta'}}{-\cancel{(p/H)}\partial\overline{\theta}/\partial p}$$

$$= \overline{v} - \frac{\partial}{\partial p}\frac{\overline{v'\theta'}}{\partial\overline{\theta}/\partial p} = v^*$$

$$\widetilde{\overline{w}}^* = \overline{w} + \frac{\partial}{a\cos\phi\partial\phi}\frac{\overline{v'\theta'}}{\partial\overline{\theta}/\partial z}\cos\phi \tag{E.17}$$

$$= -\left(\frac{H}{p}\right)\overline{\omega} + \frac{\partial}{a\cos\phi\partial\phi}\frac{\overline{v'\theta'}}{-(p/H)\partial\overline{\theta}/\partial p}\cos\phi$$

$$= -\frac{H}{p}\omega^*$$

$$\implies \widetilde{\overline{w}}^* = w^*$$

Thus, the other terms of $\partial\overline{u}/\partial t$ transform simply:

$$\frac{\widetilde{\partial\overline{u}}}{\partial t}\bigg|_{\mathrm{adv}(v^*)} = \widetilde{\overline{v}}^*\left[f - \frac{\partial\overline{u}\cos\phi}{a\cos\phi\partial\phi}\right] = v^*\left[f - \frac{\partial\overline{u}\cos\phi}{a\cos\phi\partial\phi}\right] = \frac{\partial\overline{u}}{\partial t}\bigg|_{\mathrm{adv}(v^*)} \quad\checkmark \tag{E.18}$$

$$\left.\frac{\widetilde{\partial \overline{u}}}{\partial t}\right|_{\mathrm{adv}(\omega^*)} = -\widetilde{\overline{w}}^* \frac{\partial \overline{u}}{\partial z} = -w^* \frac{\partial \overline{u}}{\partial z} = -\left(-\frac{H}{p}\omega^*\right)\left(-\frac{p}{H}\right)\frac{\partial \overline{u}}{\partial p} = -\omega^* \frac{\partial \overline{u}}{\partial p} = \left.\frac{\partial \overline{u}}{\partial t}\right|_{\mathrm{adv}(\omega^*)} \checkmark$$

(E.19)

Now let's reverse-engineer the conversion from β-plane coordinates to spherical coordinates. The Beta-plane (hereafter denoted with superscript β) form of the TEM zonal-mean zonal wind tendency equation is given in Andrews and McIntyre (1976) as

$$\begin{aligned}
\frac{\partial \overline{u}^\beta}{\partial t} &= \overline{v}^{*\beta}\left[f - \frac{\partial \overline{u}}{\partial y}\right] - \overline{w}^{*\beta}\frac{\partial \overline{u}}{\partial z} + \nabla \cdot \mathbf{F}^\beta - \overline{X} \\
&= \overline{v}^{*\beta}\left[f - \frac{\partial \overline{u}}{\partial y}\right] - \overline{w}^{*\beta}\frac{\partial \overline{u}}{\partial z} + \left\{\frac{\partial}{\partial y}F_{(y)}^\beta + \frac{\partial}{\partial z}F_{(z)}^\beta\right\} - \overline{X}
\end{aligned}$$

(E.20)

where the components of the EP flux vector are

$$F_{(y)}^\beta = \frac{\partial \overline{u}}{\partial z}\frac{\overline{v'\theta'}}{\partial \overline{\theta}/\partial z} - \overline{u'v'},$$

(E.21)

$$F_{(z)}^\beta = \left(f - \frac{\partial \overline{u}}{\partial y}\right)\frac{\overline{v'\theta'}}{\partial \overline{\theta}/\partial z} - \overline{u'w'}$$

(E.22)

and the residual velocities are

$$\overline{v}^{*\beta} = \overline{v} - \frac{\partial}{\partial z}\frac{\overline{v'\theta'}}{\partial \overline{\theta}/\partial z}$$

(E.23)

$$\overline{w}^{*\beta} = \overline{w} + \frac{\partial}{\partial y}\frac{\overline{v'\theta'}}{\partial \overline{\theta}/\partial z}$$

(E.24)

In relaxing the beta-plane assumption (converting to more generic spherical coordinates), we should recover the equations given in GM16. The meridional residual velocity transforms simply, as it only involve derivatives in z:

$$\overline{v}^{*\beta} = \overline{v} - \frac{\partial}{\partial z}\frac{\overline{v'\theta'}}{\partial \overline{\theta}/\partial z} = \overline{v} - \left(\frac{p\!\!\!/}{H\!\!\!/}\right)\frac{\partial}{\partial p}\frac{\overline{v'\theta'}}{-(p\!\!\!/H\!\!\!/)\partial \overline{\theta}/\partial p} = \overline{v} - \frac{\partial}{\partial p}\frac{\overline{v'\theta'}}{\partial \overline{\theta}/\partial p} = v^* \checkmark$$

(E.25)

For the vertical residual velocity and EP flux components, we will need to proceed more carefully. Meridional derivatives are transformed using

$$\frac{\partial \alpha}{\partial y} = \frac{1}{a \cos \phi}\frac{\partial \alpha \cos \phi}{\partial \phi}$$

(E.26)

and components of a vector $\mathbf{A}$ moving from the β-plane to spherical coordinates involve a factor like

$$A_{(\phi)} = a \cos \phi A^{\beta}_{(y)} \tag{E.27}$$

$$A_{(p)} = a \cos \phi A^{\beta}_{(p)} \tag{E.28}$$

Using these rules, the vertical residual velocity transforms as

$$\overline{w}^{*\beta} = \overline{w} + \frac{\partial}{\partial y} \frac{\overline{v'\theta'}}{\partial \bar{\theta}/\partial z} = -\left(\frac{H}{p}\right)\overline{\omega} + \frac{1}{a\cos\phi}\frac{\partial}{\partial\phi}\frac{\overline{v'\theta'}}{-(p/H)\partial\bar{\theta}/\partial p}\cos\phi \tag{E.29}$$

$$= -\left(\frac{H}{p}\right)\left[\overline{\omega} + \frac{\partial}{a\cos\phi\partial\phi}\frac{\overline{v'\theta'}}{\partial\bar{\theta}/\partial p}\cos\phi\right]$$

$$= -\left(\frac{H}{p}\right)\omega^* = w^* ✔$$

and the components of the EP flux vector transform as

$$F^{\beta}_{(y)} = \frac{\partial\overline{u}}{\partial z}\frac{\overline{v'\theta'}}{\partial\bar{\theta}/\partial z} - \overline{u'v'} = \left(\frac{\cancel{p}}{\cancel{H}}\right)\frac{\partial\overline{u}}{\partial p}\frac{\overline{v'\theta'}}{\cancel{-(p/H)\partial\bar{\theta}/\partial p}} - \overline{u'v'} \tag{E.30}$$

$$= \frac{\partial\overline{u}}{\partial p}\frac{\overline{v'\theta'}}{\partial\bar{\theta}/\partial p} - \overline{u'v'}$$

$$\implies F_{(\phi)} = a\cos\phi F^{\beta}_{(y)} ✔$$

$$F^{\beta}_{(z)} = \left(f - \frac{\partial\overline{u}}{\partial y}\right)\frac{\overline{v'\theta'}}{\partial\bar{\theta}/\partial z} - \overline{u'w'} = \left(f - \frac{\partial\overline{u}\cos\phi}{a\cos\phi\partial\phi}\right)\frac{\overline{v'\theta'}}{\partial\bar{\theta}/\partial z} - \overline{u'w'} \tag{E.31}$$

$$= \left(f - \frac{\partial\overline{u}\cos\phi}{a\cos\phi\partial\phi}\right)\frac{\overline{v'\theta'}}{-(p/H)\partial\bar{\theta}/\partial p} - -\left(\frac{H}{p}\right)\overline{u'\omega'}$$

$$= -\left(\frac{H}{p}\right)\left[\left(f - \frac{\partial\overline{u}\cos\phi}{a\cos\phi\partial\phi}\right)\frac{\overline{v'\theta'}}{\partial\bar{\theta}/\partial p} - \overline{u'\omega'}\right]$$

$$= -\left(\frac{H}{p}\right)F^{\beta}_{(p)}$$

$$\implies F_{(p)} = a\cos\phi F^{\beta}_{(p)} ✔$$

E.2 Momentum and Tracer TEM Formulations

With all of this work done to understand the transformations between these formulations, we can now write the eddy transport vector consistently with GM16. The time tendency of a zonal-mean tracer mixing ratio field q in the TEM framework is that of A87 Eq. (9.4.13) (also Eq. (1) of Abalos et al. (2017)):

$$\frac{\partial \overline{q}}{\partial t} = \frac{\partial \overline{q}}{\partial t}\Big|_{\text{adv}(v^*)} + \frac{\partial \overline{q}}{\partial t}\Big|_{\text{adv}(w^*)} + \frac{\partial \overline{q}}{\partial t}\Big|_{\nabla \cdot \mathbf{M}} + \overline{S} \tag{E.32}$$

$$= -v^* \frac{\partial \overline{q}}{\partial y} - w^* \frac{\partial \overline{q}}{\partial z} + \frac{1}{\rho_0} \nabla \cdot \mathbf{M} + \overline{S}$$

where S are the *net* sources and sinks (including dissipation and other unresolved forcings), and $\mathbf{M}$ is the *eddy transport vector* or the *eddy tracer flux vector* (authors have used both terms). We immediately see that the structure of this equation is analogous to Eq. (E.6), where the eddy tracer flux divergence plays the role of the EP flux divergence, and S replaces X. The components of $\mathbf{M}$ are given in Appendix 9A of A87 as

$$M_{(y)}^{\beta} = \rho_0 \left[\frac{\partial \overline{q}}{\partial z} \frac{\overline{v'\theta'}}{\partial \overline{\theta}/\partial z} - \overline{q'v'} \right] \tag{E.33}$$

$$M_{(z)}^{\beta} = \rho_0 \left[-\frac{\partial \overline{q}}{\partial y} \frac{\overline{v'\theta'}}{\partial \overline{\theta}/\partial z} - \overline{q'w'} \right] \tag{E.34}$$

We have included superscripts to make it clear that these are given for Cartesian β-plane coordinates. Let's now make the necessary transformations. This involves (1) taking derivatives and vertical velocities from $z \to p$, (2) taking horizontal derivatives from $y \to \phi$, (3) applying vector component transformations from local β-plane coordinates to spherical coordinates, and (4) cancel factors of ρ_0 between $\mathbf{M}$ and $\partial \overline{q}/\partial t$. Explicitly, this is

$$\frac{\partial \overline{q}}{\partial t} = -v^* \frac{\partial \overline{q}}{\partial y} - \left(-\frac{\cancel{H}}{p} \right) \omega^* \left(-\frac{\cancel{p}}{H} \right) \frac{\partial \overline{q}}{\partial p} + \rho_0^{-1} \nabla \cdot \mathbf{M} + \overline{S} \tag{E.35}$$

$$= -v^* \frac{\partial \overline{q}}{\partial y} - \omega^* \frac{\partial \overline{q}}{\partial p} + \rho_0^{-1} \nabla \cdot \mathbf{M} + \overline{S}$$

$$= -v^* \frac{\partial \overline{q} \cos \phi}{a \cos \phi \partial \phi} - \omega^* \frac{\partial \overline{q}}{\partial p} + \rho_0^{-1} \nabla \cdot \mathbf{M} + \overline{S}$$

$$= -v^* \frac{\partial \overline{q} \cos \phi}{a \cos \phi \partial \phi} - \omega^* \frac{\partial \overline{q}}{\partial p} + \cancel{\rho_0}^{-1} \frac{1}{a \cos \phi} \nabla \cdot \mathbf{M} + \overline{S}$$

and

$$M_{(\phi)} = \rho_0 a \cos \phi M_{(y)}^{\beta} = \rho_0 a \cos \phi \left\{ -\left(\frac{H}{p}\right) \frac{\partial \overline{q}}{\partial p} \frac{\overline{v'\theta'}}{-(p/H)\partial \overline{\theta}/\partial p} - \overline{q'v'} \right\} \tag{E.36}$$

$$= a \cos \phi \left\{ \frac{\partial \overline{q}}{\partial p} \frac{\overline{v'\theta'}}{\partial \overline{\theta}/\partial p} - \overline{q'v'} \right\}$$

$$M_{(p)} = \rho_0 a \cos \phi M_{(p)}^{\beta} = \rho_0 a \cos \phi \left(-\frac{p}{H} \right) M_{(z)}^{\beta} \tag{E.37}$$

$$= \rho_0 a \cos \phi \left(-\frac{p}{H} \right) \left\{ -\frac{\partial \overline{q}}{\partial y} \frac{\overline{v'\theta'}}{\partial \overline{\theta}/\partial z} - \overline{q'w'} \right\}$$

$$= \rho_0 a \cos \phi \left(-\frac{p}{H} \right) \left\{ -\frac{\partial \overline{q} \cos \phi}{a \cos \phi \partial \phi} \frac{\overline{v'\theta'}}{-(p/H)\partial \overline{\theta}/\partial p} - \left(-\frac{H}{p} \right) \overline{q'\omega'} \right\}$$

$$= a \cos \phi \left\{ -\frac{\partial \overline{q} \cos \phi}{a \cos \phi \partial \phi} \frac{\overline{v'\theta'}}{\partial \overline{\theta}/\partial p} - \overline{q'\omega'} \right\}$$

The eddy tracer flux divergence is then (following GM16),

$$\nabla \cdot \mathbf{M} = \frac{\partial M_{(\phi)} \cos \phi}{a \cos \phi \partial \phi} + \frac{\partial M_{(p)}}{\partial p} \tag{E.38}$$

These forms are analogous to the EP flux vector components, where $\overline{q}$ replace $\overline{u}$, and the Coriolis force is discarded. In summary,

$$\frac{\partial \overline{q}}{\partial t} = \frac{\partial \overline{q}}{\partial t}\bigg|_{\mathrm{adv}(v^*)} + \frac{\partial \overline{q}}{\partial t}\bigg|_{\mathrm{adv}(\omega^*)} + \frac{\partial \overline{q}}{\partial t}\bigg|_{\nabla \cdot \mathbf{M}} + \overline{S} \tag{E.39}$$

$$= -v^* \frac{\partial \overline{q} \cos \phi}{a \cos \phi \partial \phi} - \omega^* \frac{\partial \overline{q}}{\partial p} + \frac{\nabla \cdot \mathbf{M}}{a \cos \phi} + \overline{S}$$

$$= -v^* \frac{\partial \overline{q} \cos \phi}{a \cos \phi \partial \phi} - \omega^* \frac{\partial \overline{q}}{\partial p} + \frac{1}{a \cos \phi} \left[\frac{\partial M_{(\phi)} \cos \phi}{a \cos \phi \partial \phi} + \frac{\partial M_{(p)}}{\partial p} \right] + \overline{S}$$

$$M_{(\phi)} = a \cos \phi \left\{ \frac{\partial \overline{q}}{\partial p} \frac{\overline{v'\theta'}}{\partial \overline{\theta}/\partial p} - \overline{q'v'} \right\} \tag{E.40}$$

$$M_{(p)} = a \cos \phi \left\{ -\frac{\partial \overline{q} \cos \phi}{a \cos \phi \partial \phi} \frac{\overline{v'\theta'}}{\partial \overline{\theta}/\partial p} - \overline{q'\omega'} \right\} \tag{E.41}$$

We can also instead write down the log-pressure versions of these vector components,

$$\widehat{M}_{(y)} = \frac{p}{p_0} M_{(y)} = \frac{p}{p_0} \frac{M_{(\phi)}}{a \cos \phi} \tag{E.42}$$

$$\widehat{M}_{(z)} = \frac{p}{p_0} M_{(z)} = -\frac{H}{p_0} \frac{M_{(p)}}{a \cos \phi} \tag{E.43}$$

Here we note that what is called the "eddy-flux components" in Dietmüller et al. (2017) and Abalos et al. (2013) differ from the conventions of GM16. They instead write the tracer tendency as

$$\frac{\partial \overline{q}}{\partial t} = \frac{\partial \overline{q}}{\partial t}\bigg|_{\mathrm{adv}(v^*)} + \frac{\partial \overline{q}}{\partial t}\bigg|_{\mathrm{adv}(w^*)} + \frac{\partial \overline{q}}{\partial t}\bigg|_{\nabla \cdot \mathbf{M}} + \overline{S} \tag{E.44}$$

$$= -v^* \frac{\partial \overline{q}}{\partial y} - w^* \frac{\partial \overline{q}}{\partial z} + \frac{p_0}{p} \nabla \cdot \widehat{\mathbf{M}} + \overline{S}$$

$$= -v^* \frac{\partial \overline{q}}{\partial y} - w^* \frac{\partial \overline{q}}{\partial z} + \frac{p_0}{p} \left[\frac{1}{\cos \phi} \frac{\partial \widehat{M}_{(y)} \cos \phi}{\partial y} + \frac{\partial \widehat{M}_{(z)}}{\partial z} \right] + \overline{S}$$

To see that this is equivalent to Eq. (E.39):

$$\frac{\partial \overline{q}}{\partial t} = -v^* \frac{\partial \overline{q}}{\partial y} - w^* \frac{\partial \overline{q}}{\partial z} + \frac{p_0}{p} \left[\frac{1}{\cos \phi} \frac{\partial \widehat{M}_{(y)} \cos \phi}{\partial y} + \frac{\partial \widehat{M}_{(z)}}{\partial z} \right] + \overline{S} \tag{E.45}$$

$$= -v^* \frac{\partial \overline{q} \cos \phi}{\cos \phi \partial \phi} - w^* \frac{\partial \overline{q}}{\partial z} + \frac{p_0}{p} \left[\frac{1}{\cos \phi} \frac{\partial \widehat{M}_{(y)} \cos \phi}{\partial y} + \frac{\partial \widehat{M}_{(z)}}{\partial z} \right] + \overline{S}$$

$$= -v^* \frac{\partial \overline{q} \cos \phi}{\cos \phi \partial \phi} - \left(-\frac{\cancel{H}}{p} \right) \omega^* \left(-\frac{\cancel{p}}{H} \right) \frac{\partial \overline{q}}{\partial p} + \frac{p_0}{p} \left[\frac{1}{\cos \phi} \frac{\partial \widehat{M}_{(y)} \cos \phi}{\partial y} + \frac{\partial \widehat{M}_{(z)}}{\partial z} \right] + \overline{S}$$

$$= -v^* \frac{\partial \overline{q} \cos \phi}{\cos \phi \partial \phi} - \omega^* \frac{\partial \overline{q}}{\partial p} + \frac{\cancel{p_0}}{\cancel{p}} \left[\frac{1}{\cos \phi} \frac{\cancel{p}}{\cancel{p_0}} \frac{\partial M_{(y)} \cos \phi}{\partial y} + \frac{\cancel{p}}{\cancel{p_0}} \frac{\partial M_{(z)}}{\partial z} \right] + \overline{S}$$

$$= -v^* \frac{\partial \overline{q} \cos \phi}{\cos \phi \partial \phi} - \omega^* \frac{\partial \overline{q}}{\partial p} + \left[\frac{1}{\cos \phi} \frac{\partial \frac{M_{(\phi)}}{a \cos \phi} \cancel{\cos \phi}}{\partial y} + \left(-\frac{\cancel{p}}{H} \right) \frac{1}{a \cos \phi} \frac{\partial \left(-\frac{\cancel{H}}{p} \right) M_{(p)}}{\partial p} \right] + \overline{S}$$

$$= -v^* \frac{\partial \overline{q} \cos \phi}{\cos \phi \partial \phi} - \omega^* \frac{\partial \overline{q}}{\partial p} + \left[\frac{1}{a \cos \phi} \frac{\partial M_{(\phi)}}{\partial y} + \frac{1}{a \cos \phi} \frac{\partial M_{(p)}}{\partial p} \right] + \overline{S}$$

$$= -v^* \frac{\partial \overline{q} \cos \phi}{\cos \phi \partial \phi} - \omega^* \frac{\partial \overline{q}}{\partial p} + \left[\frac{1}{a \cos \phi} \frac{\partial M_{(\phi)} \cos \phi}{a \cos \phi \partial \phi} + \frac{1}{a \cos \phi} \frac{\partial M_{(p)}}{\partial p} \right] + \overline{S}$$

$$= -v^* \frac{\partial \overline{q} \cos \phi}{\cos \phi \partial \phi} - \omega^* \frac{\partial \overline{q}}{\partial p} + \frac{1}{a \cos \phi} \left[\frac{\partial M_{(\phi)} \cos \phi}{a \cos \phi \partial \phi} + \frac{\partial M_{(p)}}{\partial p} \right] + \overline{S} = \text{Eq. } (E.39) \checkmark$$

APPENDIX F

This appendix describes a simple method of implementing new tracer constituents in the E3SMv2 atmosphere model (EAM), which was used in implementing the SO_2, sulfate, ash, e90, and age-of-air (AoA) tracers used in teh analyses presented in Chapters 2 and 4.

This discussion is not complex, but is quite technical in its details, and so knowledge of Fortran and the structure of the E3SM and/or CESM model framework on the part of the reader is assumed. Some familiarity of the Common Infrastructure for Modeling the Earth (CIME; Foucar et al. (2017)) is also beneficial.

For a clone of the E3SM model in directory `./E3SM`, all paths in this appendix are written relative to the EAM source at `./E3SM/components/eam/` unless noted otherwise.

F.1 E3SM Tracers Overview

In the years both before and after E3SM's diversion from CESM (Golaz et al., 2019), developers have inserted routines for the definition, management, and evolution of many active and passive tracer species. These routines are locatable in the code base by `grep`'ing for keywords, which shows that the methods of implementation vary greatly; some packages decide to include the tracer logic alongside their other internal mechanisms, while some make more of an effort to encapsulate these routines (both of these approaches can be seen in the tracer-related codes that are scattered among the `src/chemistry` packages). By "definition" and "management", we refer to the plumbing required to ensure that the model and CIME infrastructure is aware of a given tracer, and that it is available as a history output to the user. By "evolution", we refer to the implementation of tracer mixing-ratio time-tendencies, which are passed to the semi-Lagrangian tracer transport scheme (Bradley et al., 2022) for advection.

A rather clean and well-encapsulated tracer implementation is seen in a module inherited from CAM at `src/physics/cam/aoa_tracers.F90` (where 'aoa' stands for "age of air", and implements a suite of age tracers; see Neu and Plumb (1999); Waugh and Hall (2002); Gerber (2012); Gupta et al. (2020)). This module provides as single place for reading namelist settings, registration and initialization of a tracer set, and passing tracer tendencies to the

transport solver. In what follows, we use this module as a template to describe the new inclusion of any arbitrary-length set of tracers into the model.

As a disclaimer; everything presented here was learned in some part by combing through in-line E3SM documentation, and through private communications with past developers, but mostly via manual inspection and reverse-engineering of the calling sequences in the model. If there are any issues with the material in this document, please let the author know.

The `aoa_tracers` module has the following structure of public and private interfaces:

module `aoa_tracers`:

    public subroutine `aoa_tracers_register()`
        registers constituents via the `cnst_add` interface of `physics/cam/constituen-ts.F90`

    public subroutine `aoa_tracers_readnl()`
        reads namelist options

    public subroutine `aoa_tracers_implements_cnst()`
        returns true if specified constituent is implemented by this package (queried by `dynamics/{dycore}/inidat.F90` for initialization)

    public subroutine `aoa_tracers_init()`
        initializes history fields, datasets

    public subroutine `aoa_tracers_init_cnst()`
        interface for initializing all constituents tracked by this package

        private subroutine `init_cnst_3d()`
            initializes 3D constituent field for single tracer

    public subroutine `aoa_tracers_timestep_init()`
        performs per-timestep initialization

    public subroutine `aoa_tracers_timestep_tend()`
        computes tracer tendencies

Again, all of these interfaces are required by the dynamical core and physics routines to ensure that the tracer species being included will be known to the model, will be evolved on the physics timesteps, and will be available for initialization and history file output. The two functions that contain the actual physical expressions of the tracers

are `aoa_tracers_timestep_tend()` (which gives the mixing-ratio temporal derivatives) and `init_cnst_3d()` (which gives the analytic initial condition of each species in the case that we do not read it from a data file). In addition, the following namelist settings are defined in `bld/namelist_files/namelist_definition.xml`:

> logical `aoa_tracers_flag`
>> If true, age of air tracers are included. This variable should not be set by the user. It will be set by build-namelist to be consistent with the `-age_of_air_trcs` argument specified to configure.
>
> logical `aoa_read_from_ic_file`
>> If true, age of air tracers are read from the initial conditions file, else they are analytically initialized by `aoa_tracers_init_cnst()`

as well as a configure option in `bld/config_files/definition.xml` (which is distinct from a namelist setting in that it is interpreted by EAM via `CAM_CONFIG_OPTS`)

> binary `age_of_air_trcs`
>> Switch on (off) age of air tracers: 0=off, 1=on. This will automatically set the `aoa_tracers_flag` namelist setting.

How to properly set these namelist and configure options will be described in Appendix F.3. For now, we assume these are provided correctly by the user, and discuss the subsequent order of operations by the model. These are:

1) Begin with `read_namelist()` from `src/control/runtime_opts.F90`, which calls `aoa_tracers_readnl()` to read in namelist settings and broadcast values to all processes. This depends on some namelist configuration at build time, which is found at:

  - `bld/configure`: interprets and sets the configure option `age_of_air_trcs` to enable/disable the tracer module
  - `bld/build-namelist`: updates the namelist setting `aoa_tracers_flag` by the configure option `age_of_air_trcs`

2) The coupler begins model initialization via `cam_init()` in `src/control/cam_comp.F90`. This performs the following steps:

  (a) Via `cam_initial()` in `src/dynamics/{dycore}/inital.F90`, call `phys_register()` in `src/physics/cam/physpkg.F90`, which invokes `aoa_tracers_register-()`, and applies the flag `aoa_read_from_ic_file` to each tracer field

(b) Via `cam_initial()` in `src/dynamics/{dycore}/inital.F90`, call `initial_con-ds()`, which in turn calls `read_inidat()` of `src/dynamics/{dycore}/inidat.F-90`. Internally, this function loops over all registered tracer constituents; for any constituent m where `aoa_tracer_implemented_cnst(m)` is `true`, either call `aoa_tracers_init_cnst()`, which performs the analytic initialization, or read the initial condition from file via `infld()`, depending on the namelist setting of `aoa_read_from_ic_file`.

(c) Via `phys_init()` in `src/physics/cam/physpkg.F90`, call `aoa_tracers_init()`, which adds the tracer fields as available history outputs via `addfld()`.

3) The coupler begins to cycle through all time steps in the atmosphere coupling interval. Each timestep begins with a call to `cam_run1()` of `src/control/cam_comp.F90` (containing a call to `phys_run1()` of `src/physics/cam/physpkg.F90`) for running the first phase of dynamics and physics before surface model updates. Here, the following happens:

(a) The timestep is initialized via `phys_timestep_init()` which calls `aoa_tracers_timestep_init()`, where per-timstep re-initializations of the tracer constituents can be implemented.

(b) tracer mixing ratios are written out via a call to `dig_phys_writeout()` from `physics/cam/cam_diagnostics.F90` (for the first timestep, this outputs the initial condition)

4) `cam_run1()` is followed by a call to to `cam_run2()` (containing a call to `phys_run2()`) for running the second phase of physics for methods that require surface model updates. The following steps will occur in `phys_run1()` → `phys_run1_adiabatic_or_ideal()` for `FIDEAL` runs, and in `phys_run2()` for any other compset, but are otherwise identical:

(a) Call `aoa_tracers_timestep_tend()`, which computes the tracer tendencies for the current timestep

(b) Call `physics_update()` from `physics/cam/physics_update_mod()`, passing the tendencies returned from the previous step

(c) Call `check_tracers_chng()` from `src/physics/cam/check_energy.F90`, passing the updated physics state from the previous step, which checks that the tracer mass changes match any boundary fluxes, ending the model run in the case of significant conservation errors

5) Repeat steps 3-4 for all timesteps, and finalize the model run via `cam_final()` in `src/control/cam_comp.F90`

Defining a new tracer module is then just a matter of replicating the structure of the `aoa_tracers` module, as well as all calls to it's public subroutines in the rest of the codebase. As long as that is done, then the steps 1-5 outlined above will be performed by the model run, and the output should be as expected. In Appendix F.2, we detail how this is done.

Of course, there is a much simpler and faster way to achieve a custom tracer in the model, without needing to do the busy work of defining a new module entirely, and without needing to know anything about the model's inner-workings. One could simply hijack the `aoa_tracers` module (or any other tracer-implementing module, e.g. a chemistry package) by redefining it's tracer constituent fields to obey the desired tendencies and initializations. This is bad practice (and ugly), but it can be a useful technique for preliminary development and testing.

F.2 Defining a New Tracer Module

Here we describe the implementation of a custom tracer module `cldera_passive_tracers` at `src/physics/cam/cldera_passive_tracers.F90`, which enables the use of a custom AoA tracer, as well as the e90 (Abalos et al., 2017) and ST80 (Eyring et al., 2013) tracers. These species are all passive, and below we refer to the three of them as a group as "passive" tracers. The code changes are available in our CLDERA E3SM fork on GitHub.

We will first detail everywhere that references and calls need to be made to the tracer module via it's subroutines and associated namelist/configure settings in Appendix F.2.1, and then discuss the contents of the module's subroutines themselves in Appendix F.2.2.

F.2.1 References to the module

As mentioned above, all we need do is mimic the structure of `aoa_tracers`, and all calls to it's subroutines elsewhere in the model. To determine where all of these changes will be needed, it is simple (if not sophisticated) to do a recursive search of all of the model code via

```
$ grep -R 'aoa\|age_of_air'
```

All relevant sections of code for the `aoa_tracers` module contain one of these two substrings. If this command is executed from the top directory of the model `./E3SM`, the resulting files containing matches should agree with the discussion of Appendix F.1, as follows:

For defining and reading namelist options:

`components/eam/bld/namelist_files/namelist_definition.xml`

`components/eam/bld/build-namelist`

`components/eam/src/control/runtime_opts.F90`

For setting configure flag:

`components/eam/bld/config_files/definition.xml`

`components/eam/bld/configure`

For initialization:

`components/eam/src/dynamics/se/inidat.F90`

`components/eam/src/dynamics/sld/inidat.F90`*

`components/eam/src/dynamics/fv/inidat.F90`*

`components/eam/src/dynamics/eul/inidat.F90`*

For calling the module from MMF physics:

`components/eam/src/physics/crm/physpkg.F90`*

For calling the module from CAM physics:

`components/eam/src/physics/cam/physpkg.F90`

In what follows, we do not consider any edits to the files marked with red asterisks* (that is, we will describe an implementation that works only for the SE dycore and CAM physics; extending this to more general use-cases should be straightforward).

Below is given each code snippet that needs to be *inserted* into the corresponding file. We do not display line numbers here, since they are bound to change; the precise position can be found by simply searching the file contents. Ellipses (...) indicate some separation between the surrounding line by (possibly lots of) other code.

1) In `components/eam/bld/config_files/definition.xml`, add a configure option definition:

```
...
<entry id="cldera_passive_trcs" valid_values="0,1" value="0">
Switch on (off) CLDERA aoa, e90, st80 tracers: 0=off, 1=on.
</entry>
...
```

2) In `components/eam/bld/configure`, add some logic for setting defaults and writing to the log:

153

```
...
OPTIONS
...
-cldera_passive_trcs Switch on idealized stratospheric aerosol injection tracers.
    Default: off
...
"cldera_passive_trcs!"        => \$opts{'cldera_passive_trcs'},
...
# Allow user to turn on the cldera passive tracers
if (defined $opts{'cldera_passive_trcs'}) {
    $cfg_ref->set('cldera_passive_trcs', $opts{'cldera_passive_trcs'});
}
my $cldera_passive__trcs = $cfg_ref->get('cldera_passive_trcs') ? "ON" : "OFF";
if ($print>=2) { print "CLDERA passive tracer package: $cldera_passive_trcs$eol"; }
...
if ($cldera_passive_trcs eq "ON") {
    $nadv += 3;
    if ($print>=2) { print "Advected constituents added by the CLDERA passive
        tracer package: 3$eol"; }
}
...
```

The last snippet above is important; it lets the model know that this module will be tracking 3 tracer species. via the increment to $nadv. This needs to be changed to however many tracers the module will implement (it is 4 for aoa_tracers).

3) In components/eam/bld/namelist_files/namelist_definition.xml, add the namelist definitions:

```
...
<entry id="cldera_passive_tracers_flag" type="logical" category="test_tracers"
        group="cldera_passive_tracers_nl" valid_values="" >
If true CLDERA aoa, e90, st80 tracers are included.
This variable should not be set by the user. It will be set by build-namelist
to be consistent with the '-cldera_passive_trcs' argument specified to configure.
Default: set by configure
</entry>

<entry id="cldera_passive_read_from_ic_file" type="logical" category="test_tracers"
        group="cldera_passive_tracers_nl" valid_values="" >
If true CLDERA aoa, e90, st80 tracers are read from the initial
conditions file. If this is not specified then they are not read from IC file.
Default: TRUE
</entry>
...
```

4) In components/eam/bld/build-namelist, add logic to automatically set the namelist setting for toggling the module on/off by the corresponding configure option at build time:

```
...
```

```
if ($cfg->get('cldera_passive_trcs')) { add_default($nl,
    'cldera_passive_tracers_flag', 'val'=>'.true.'); }
...
```

5) In `components/eam/src/control/runtime_opts.F90`, add a call to read the namelist settings:

```
...
use cldera_passive_tracers, only: cldera_passive_tracers_readnl
...
call cldera_passive_tracers_readnl(nlfilename)
...
```

6) In `components/eam/src/dynamics/se/inidat.F90`, add calls to the tracer initialization routine:

```
...
use cldera_passive_tracers,   only: cldera_passive_tracers_implements_cnst,
    cldera_passive_tracers_init_cnst
...
else if (cldera_passive_tracers_implements_cnst(cnst_name(m_cnst))) then
   call cldera_passive_tracers_init_cnst(cnst_name(m_cnst), qtmp, gcid)
    if(par%masterproc) write(iulog,*) '      ', cnst_name(m_cnst), &
        ' initialized by "cldera_passive_tracers_init_cnst"'
...
```

7) In `components/eam/src/physics/cam/physpkg.F90`, add calls to register and initialize the tracer module:

```
...
use cldera_passive_tracers, only: cldera_passive_tracers_register
...
! Register CLDERA stratospheric aerosol injection tracers
call cldera_passive_tracers_register()
...
use cldera_passive_tracers, only: cldera_passive_tracers_init
...
! CLDERA passive tracers
call cldera_passive_tracers_init()
...
```

In the same file, for ideal physics runs, in the subroutine `phys_run1_adiabatic_or_ideal()` (this snippet will not have an age-of-air parallel in a standard E3SM fork, since those tracers are not enabled for the `FIDEAL` compset; see the source of this file in the GitHub repository linked above for specifics), add the per-timestep calls to the tracer tendency function, and update physics:

```
...
! --JH--: adding to allow CLDERA passive tendencies
use cldera_passive_tracers,  only: cldera_passive_tracers_timestep_tend
```

```
...
! --JH--: Allow advancing of CLDERA passive tendencies if enabled
! the timestep_tend function automatically checks that these tracers are enabled
    for the run
call cldera_passive_tracers_timestep_tend(phys_state(c), ptend(c), ztodt,
    phys_state(c)%ncol)
call physics_update(phys_state(c), ptend(c), ztodt, phys_tend(c))
call check_tracers_chng(phys_state(c), tracerint,
    "cldera_passive_tracers_timestep_tend", nstep, ztodt, &
                        dummy_cflx)
...
```

In the same file, for full physics runs, in the subroutine `tphysac()`, add analogous code to that shown above:

```
...
use cldera_passive_tracers, only: cldera_passive_tracers_timestep_tend
...
call cldera_passive_tracers_timestep_tend(state, ptend, ztodt, ncol)
call physics_update(state, ptend, ztodt, tend)
call check_tracers_chng(state, tracerint, "cldera_passive_tracers_timestep_tend",
    nstep, ztodt, &
                        cam_in%cflx)
...
```

In the same file, in the subroutine `phys_timestep_init()`, add calls to the per-timestep initialization:

```
...
use cldera_passive_tracers, only: cldera_passive_tracers_timestep_init
...
! CLDERA passive tracers
call cldera_passive_tracers_timestep_init(phys_state)
...
```

F.2.2 Content of the module

Finally, we take a look at the actual content of the important subroutines. We will show here the modified functions of our custom `cldera_passive_tracers`, though they are just as legible for the aoa_tracers. Some of the subroutines are listed, but the code is not shown; these functions are generally trivial and uninteresting, and will be copied verbatim for most applications; see instead the source code at the GitHub repository (or in `aoa_tracers.F90`). In the snippets below, line numbers are relative to the code shown, and do not correspond to the source files.

1) In `cldera_passive_tracers_register()`, the constituents are registered via the `cnst_add` interface of `physucs/cam/constituents.F90`. See source code for details.

2) In `cldera_passive_tracers_readnl()`, the namelist options are read and broadcast to all MPI ranks. See source code for details.

3) In `cldera_passive_tracers_implements_cnst()`, return true if the specified constituent is implemented by this package. See source code for details.

4) In `cldera_passive_tracers_init()`, initialize history fields, datasets. See source code for details.

5) In `cldera_passive_tracers_timestep_init()`, perform per-timestep re-initialization of tracer fields. This module does not do this, but the template is retained (currently just returns). See source code for details.

6) In `cldera_passive_tracers_init_cnst()`, perform initialization of tracer fields via a call to `init_cnst_3d()`. This module initializes all three tracers, AoA, e90, and ST80 to zero everywhere. Here, line 20 aborts the initialization in the case that the `cldera_passive_tracers_flag` option is `.false.`, which would have been set at build-time by the `cldera_passive_trcs` configure option. Lines 54, 59, and 64 do the actual initialization to zero, on the mixing ratio field q:

```
1  ...
2  !================================================================================
3
4    subroutine cldera_passive_tracers_init_cnst(name, q, gcid)
5
6      !---------------------------------------------------------------------------
7      !
8      ! Purpose: initialize test tracers mixing ratio fields
9      !  This subroutine is called at the beginning of an initial run ONLY
10     !
11     !---------------------------------------------------------------------------
12
13     character(len=*), intent(in) :: name
14     real(r8),         intent(out) :: q(:,:) ! kg tracer/kg dry air (gcol, plev)
15     integer,          intent(in) :: gcid(:) ! global column id
16
17     integer :: m
18     !---------------------------------------------------------------------------
19
20     if (.not. cldera_passive_tracers_flag) return
21
22     do m = 1, ncnst
23        if (name == c_names(m)) then
24           ! pass global constituent index
```

```fortran
25            call init_cnst_3d(ifirst+m-1, q, gcid)
26          endif
27        end do
28
29     end subroutine cldera_passive_tracers_init_cnst
30
31   ...
32
33   !===============================================================================
34
35     subroutine init_cnst_3d(m, q, gcid)
36
37        use dyn_grid, only : get_horiz_grid_d, get_horiz_grid_dim_d
38        use dycore,   only : dycore_is
39
40        integer, intent(in) :: m      ! global constituent index
41        real(r8), intent(out) :: q(:,:) ! kg tracer/kg dry air (gcol,plev)
42        integer, intent(in) :: gcid(:) ! global column id
43
44        real(r8), allocatable :: lat(:)
45        integer :: plon, plat, ngcols
46        integer :: j, k, gsize
47        !-----------------------------------------------------------------------
48
49        if (masterproc) write(iulog,*) 'cldera_passive CONSTITUENTS: INITIALIZING
             ',cnst_name(m),m
50
51        ! ====== cldera_passive ======
52        if (m == ixaoa) then
53
54           q(:,:) = 0.0_r8
55
56        ! ====== e90 ======
57        else if (m == ixe90) then
58
59           q(:,:) = 0.0_r8
60
61        ! ====== ST80 ======
62        else if (m == ixst80) then
63
64           q(:,:) = 0.0_r8
65
66        end if
67
68     end subroutine init_cnst_3d
69
70   !==================================================================
```

7) In `cldera_passive_tracers_timestep_tend()`, compute the time tendencies of the mixing ratios at each timestep. Here we also perform operations on the mixing ratio

itself under some conditions. The AoA tracer q_1 has a source of

$$\frac{\partial q_1}{\partial t} = \frac{1}{86400} \frac{\text{day}}{\text{day}} \frac{1}{\text{s}} \tag{F.1}$$

everywhere above 700 hPa, where q_1 is interpreted as a "dimensionless mixing ratio" in units of day/day. Everywhere below 700 hPa, we set

$$\frac{\partial q_1}{\partial t} = 0 \frac{\text{day}}{\text{day}} \frac{1}{\text{s}} \tag{F.2}$$

$$q_1 = 0 \frac{\text{day}}{\text{day}} \tag{F.3}$$

That is, the tracer tendency describes a clock always "ticking" above the surface layer. The output will give average number of days since last contact with the surface layer for air in the grid cell. This is implemented in lines 80-87.

The e90 tracer q_2 is given a dissipation with an e-folding timescale of 90 days:

$$\frac{\partial q_2}{\partial t} = -\frac{1}{90 \times 86400} q_2 \frac{\text{kg}}{\text{kg}} \frac{1}{\text{s}} \tag{F.4}$$

It's emission is given as a *surface flux*, which is written to the `cflx` field of the input package tendency object `ptend`. The model will later handle turning this into an actual mixing ratio flux over the first model level in `src/physics/cam/diffusion_solver.F90`. The surface flux Φ_s is chosen to agree with Abalos et al. (2017):

$$\Phi_s = \left(2.7736 \times 10^{11} \frac{\text{molecules}}{\text{cm}^2 \text{ s}} \right) \left(\frac{1}{A} \frac{\text{mol}}{\text{molecules}} \right) \times 10000 \frac{1}{1000} \frac{\text{kg}}{\text{g}} \times \frac{\text{m}^2}{\text{cm}^2} \times 28 \frac{\text{g}}{\text{mol}} \tag{F.5}$$

where A is Avogadro's constant, and the last term is the molecular weight of carbon monoxide (CO), which is the molecular weight of e90 used in WACCM. This is implemented in lines 66–74, 90–92, and 113–115.

The ST80 tracer q_3 is given a dissipation with an e-folding timescale of 25 days below 80 hPa,

$$\frac{\partial q_3}{\partial t} = -\frac{1}{25 \times 86400} q_3 \frac{\text{kg}}{\text{kg}} \frac{1}{\text{s}} \tag{F.6}$$

and is held at a constant mixing ratio of 200 ppbv above 80 hPa,

$$\frac{\partial q_3}{\partial t} = 0 \, \frac{\text{kg}}{\text{kg}} \frac{1}{\text{s}} \tag{F.7}$$

$$q_3 = 200 \, \frac{\text{kg}}{\text{kg}} \tag{F.8}$$

This is implemented in lines 94–102.

```
1  ...
2
3  !======================================================================
4
5    subroutine cldera_passive_tracers_timestep_tend(state, ptend, cflx, dt)
6
7      use physics_types, only: physics_state, physics_ptend, physics_ptend_init
8      use phys_grid,    only: get_rlat_all_p , get_lat_all_p
9      use cam_history, only: outfld
10     use time_manager, only: get_nstep
11     use ref_pres,    only: pref_mid_norm
12     use time_manager, only: get_curr_time
13
14     ! Arguments
15     !type(physics_state), intent(in) :: state        ! state variables
16     type(physics_state), intent(inout) :: state      ! --JH--
17     type(physics_ptend), intent(out) :: ptend        ! package tendencies
18     real(r8),           intent(in)   :: dt           ! timestep
19     real(r8),           intent(inout) :: cflx(pcols,pcnst) ! Surface constituent
          flux (kg/m^2/s)
20
21     !---------------- Local workspace-----------------------------
22
23     integer :: i, k
24     integer :: lchnk          ! chunk identifier
25     integer :: ncol           ! no. of column in chunk
26     integer :: nstep          ! current timestep number
27
28     logical :: lq(pcnst)
29
30     integer :: day,sec        ! date variables
31     real(r8) :: t             ! tracer boundary condition
32     real(r8) :: aoa_scaling   ! scale AOA1 from nstep to time
33
34     real(r8) :: efold_st80    ! e-folding timescale for e90 in s
35     real(r8) :: efold_e90     ! e-folding timescale for e90 in s
36     real(r8) :: mweight_e90   ! molecular weight of e90 in g/mol
37     real(r8) :: sflx_e90      ! surface flux of e90 in mol cm^-2 s^-1
38
39     !-------------------------------------------------------------
40
41     if (.not. cldera_passive_tracers_flag) then
42        !Initialize an empty ptend for use with physics_update
43        call physics_ptend_init(ptend,state%psetcols,'cldera_passive_trc_ts')
```

```fortran
44        return
45     end if
46
47     lq(:)     = .FALSE.
48     lq(ixaoa) = .TRUE.
49     lq(ixe90) = .TRUE.
50     lq(ixst80) = .TRUE.
51     call physics_ptend_init(ptend,state%psetcols, 'cldera_passive_tracers', lq=lq)
52
53     nstep = get_nstep()
54     lchnk = state%lchnk
55     ncol = state%ncol
56
57     ! ---- compute AOA time scaling (1 s in days)
58     aoa_scaling = 1._r8/86400._r8
59
60     ! ---- e-folding times for e90 (90 days in s), st80 (80 days in s)
61     ! (reciprocals match WACCM 'e90_tau' and 'ST80_tau', and table A2 in
62     ! Tilmes+ (2016) Representation of CESM1 CAM4-chem within CCMI)
63     efold_e90 = 90._r8 * 86400._r8
64     efold_st80 = 25._r8 * 86400._r8
65
66     ! ---- molecular weight and surface flux for e90
67     ! (surface flux matches Abalos+ (2017), molecular weight is for CO, matches
68     !  WACCM surface emissions specification in
69     !  emissions_e90global_surface_1750-2100_0.9x1.25_c20170322.nc)
70     mweight_e90 = 28._r8
71     sflx_e90   = 2.7736e11_r8    ! [molecules cm^-2 s^-1]
72     sflx_e90   = sflx_e90 / 6.022141e23_r8            ! [moles cm^-2 s^-1]
73     ! convert mol to g, g to kg, cm^-2 to m^-2 for flux in [kg m^-2 s^-1]
74     sflx_e90   = sflx_e90 * mweight_e90 * (1._r8/1000._r8) * 10000._r8
75
76
77     ! -------------------- TRACER TENDENCIES --------------------
78     do k = 1, pver
79        do i = 1, ncol
80
81           ! ============ AOA ============
82           ! clock tracer with a source of 1 day/day everywhere above ~700hPa
83           if (pref_mid_norm(k) <= 0.7) then
84              ptend%q(i,k,ixaoa) = 1.0_r8 * aoa_scaling
85           else
86              ptend%q(i,k,ixaoa) = 0.0_r8
87              state%q(i,k,ixaoa) = 0.0_r8
88           end if
89
90           ! ============ e90 ============
91           ! dissipates with e-folding time of 90 days
92           ptend%q(i,k,ixe90) = -(1._r8 / efold_e90) * state%q(iu, k, ixe90)
93
94           ! ============ ST80 ============
95           ! dissipates with e-folding time of 25 days below ~80 hPa,
96           ! constant concentration of 200 ppbv above
97           if (pref_mid_norm(k) >= 0.08) then
```

161

```fortran
 98                  ptend%q(i,k,ixst80) = -(1._r8 / efold_st80) * state%q(iu, k, ixst80)
 99              else
100                  ptend%q(i,k,ixst80) = 0._r8
101                  state%q(i, k, ixst80) = 200e-9_r8 ! 200 ppbv to vmr
102              end if
103          end do
104      end do
105
106      ! ------------------- TRACER FLUXES -------------------
107      do i = 1, ncol
108
109          ! ====== AOA ======
110          ! no surface flux
111          !cflx(i,ixaoa) = 0._r8
112
113          ! ====== e90 ======
114          !cflx(i,ixe90) = sflx_e90
115          ptend%cflx(i,ixe90) = sflx_e90
116
117          ! ====== ST80 ======
118          ! no surface flux
119          !cflx(i,ixst80) = 0._r8
120
121      end do
122
123   end subroutine cldera_passive_tracers_timestep_tend
124
125 !===========================================================================
126
127 ...
```

F.3   Example Usage

On the user-side, all of the complexity described thus far is hidden (a worthwhile payoff of the implementation). After CIME case creation via create_case, simply turn on the configure option

```
./xmlchange --append --file env_build.xml --id CAM_CONFIG_OPTS --val
    "-cldera_passive_trcs"
```

and include something like the following in user_nl_eam:

```
empty_htapes    = .TRUE.              ! output only the varibales listed below
avgflag_pertape = 'A'                 ! hist file 1 is avg

! output a few quantities for frequently on their instantaneous values for SSW
    quantification
fincl1          = 'U','AOA','e90','ST80'

NHTFRQ          = -720        ! output frequency every 30 days
```

162

```
MFILT           = 12                  ! allow 12 time samples per hist file (1 year)
NDENS           = 2                    ! single-precision for each hist file

inithist='ENDOFRUN'

! activate built-in analytic init of cldera passive tracers (the default)
cldera_passive_read_from_ic_file = .TRUE.
```

If instead of allowing the analytic initialization, we want to read the initial condition of the tracer mixing ratios from a file (e.g. in the case of a restart), we instead insert

```
...

! provide initial data file
NCDATA='/path/to/data/somewhere.nc'

! deactivate built-in analytic init of cldera passive tracers
cldera_passive_read_from_ic_file = .TRUE.
```

BIBLIOGRAPHY

Abalos, M., Calvo, N., Benito-Barca, S., Garny, H., Hardiman, S. C., Lin, P., Andrews, M. B., Butchart, N., Garcia, R., Orbe, C., Saint-Martin, D., Watanabe, S., and Yoshida, K. (2021). The Brewer–Dobson circulation in CMIP6. *Atmospheric Chemistry and Physics*, 21(17):13571–13591.

Abalos, M., Orbe, C., Kinnison, D. E., Plummer, D., Oman, L. D., Jöckel, P., Morgenstern, O., Garcia, R. R., Zeng, G., Stone, K. A., and Dameris, M. (2020). Future trends in stratosphere-to-troposphere transport in CCMI models. *Atmospheric Chemistry and Physics*, 20(11):6883–6901.

Abalos, M., Randel, W. J., Kinnison, D. E., and Garcia, R. R. (2017). Using the Artificial Tracer e90 to Examine Present and Future UTLS Tracer Transport in WACCM. *Journal of the Atmospheric Sciences*, 74(10):3383–3403.

Abalos, M., Randel, W. J., Kinnison, D. E., and Serrano, E. (2013). Quantifying tracer transport in the tropical lower stratosphere using WACCM. *Atmospheric Chemistry and Physics*, 13(21):10591–10607.

American Meteorological Society (2013). Geoengineering the Climate System 2009. Technical report, American Meteorological Society. Available online at: https://www.ametsoc.org/index.cfm/ams/about-ams/ams-statements/archive-statements-of-the-ams/geoengineering-the-climate-system-2009/.

Andrews, D. G. (1987). On the interpretation of the eliassen-palm flux divergence. *Quarterly Journal of the Royal Meteorological Society*, 113(475):323–338.

Andrews, D. G., Holton, J. R., and Leovy, C. B. (1987). *Middle Atmosphere Dynamics*. Academic Press.

Andrews, D. G., Mahlman, J. D., and Sinclair, R. W. (1983). Eliassen-Palm Diagnostics of Wave-Mean Flow Interaction in the GFDL "SKYHI" General Circulation Model. *Journal of the Atmospheric Sciences*, 40(12):2768–2784.

Andrews, D. G. and McIntyre, M. E. (1976). Planetary Waves in Horizontal and Vertical Shear: The Generalized Eliassen-Palm Relation and the Mean Zonal Acceleration. *Journal of the Atmospheric Sciences*, 33(11):2031–2048.

Baldwin, M. P., Ayarzagüena, B., Birner, T., Butchart, N., Butler, A. H., Charlton-Perez, A. J., Domeisen, D. I. V., Garfinkel, C. I., Garny, H., Gerber, E. P., Hegglin, M. I., Langematz, U., and Pedatella, N. M. (2021). Sudden Stratospheric Warmings. *Reviews of Geophysics*, 59(1):e2020RG000708.

Baldwin, M. P. and Dunkerton, T. J. (1999). Propagation of the Arctic Oscillation from the stratosphere to the troposphere. *Journal of Geophysical Research: Atmospheres*, 104(D24):30937–30946.

Baldwin, M. P. and Dunkerton, T. J. (2001). Stratospheric Harbingers of Anomalous Weather Regimes. *Science*, 294(5542):581–584.

Baldwin, M. P., Gray, L. J., Dunkerton, T. J., Hamilton, K., Haynes, P. H., Randel, W. J., Holton, J. R., Alexander, M. J., Hirota, I., Horinouchi, T., Jones, D. B. A., Kinnersley, J. S., Marquardt, C., Sato, K., and Takahashi, M. (2001). The quasi-biennial oscillation. *Reviews of Geophysics*, 39(2):179–229.

Baran, A. J. and Foot, J. S. (1994). New application of the operational sounder HIRS in determining a climatology of sulphuric acid aerosol from the Pinatubo eruption. *Journal of Geophysical Research: Atmospheres*, 99(D12):25673–25679.

Barnes, E. A., Solomon, S., and Polvani, L. M. (2016). Robust Wind and Precipitation Responses to the Mount Pinatubo Eruption, as Simulated in the CMIP5 Models. *Journal of Climate*, 29(13):4763–4778.

Barnes, J. E. and Hofmann, D. J. (1997). Lidar measurements of stratospheric aerosol over Mauna Loa Observatory. *Geophysical Research Letters*, 24(15):1923–1926.

Bednarz, E. M., Visioni, D., Kravitz, B., Jones, A., Haywood, J. M., Richter, J., MacMartin, D. G., and Braesicke, P. (2023). Climate response to off-equatorial stratospheric sulfur injections in three Earth system models – Part 2: Stratospheric and free-tropospheric response. *Atmospheric Chemistry and Physics*, 23(1):687–709.

Bekki, S. (1995). Oxidation of volcanic SO2: A sink for stratospheric OH and H2O. *Geophysical Research Letters*, 22(8):913–916.

Bekki, S. and Pyle, J. A. (1994). A two-dimensional modeling study of the volcanic eruption of Mount Pinatubo. *Journal of Geophysical Research: Atmospheres*, 99(D9):18861–18869.

Birner, T. and Bönisch, H. (2011). Residual circulation trajectories and transit times into the extratropical lowermost stratosphere. *Atmospheric Chemistry and Physics*, 11(2):817–827.

Bittner, M., Timmreck, C., Schmidt, H., Toohey, M., and Krüger, K. (2016). The impact of wave-mean flow interaction on the Northern Hemisphere polar vortex after tropical volcanic eruptions. *Journal of Geophysical Research: Atmospheres*, 121(10):5281–5297.

Bluth, G., Rose, W., Sprod, I., and Krueger, A. (1997). Stratospheric Loading of Sulfur from Explosive Volcanic Eruptions. *The Journal of Geology*, 105(6):671–684.

Boville, B. A. and Baumhefner, D. P. (1990). Simulated Forecast Error and Climate Drift Resulting from the Omission of the Upper Stratosphere in Numerical Models. *Monthly Weather Review*, 118(7):1517–1530.

Bradley, A. M., Bosler, P. A., and Guba, O. (2022). Islet: interpolation semi-Lagrangian element-based transport. *Geoscientific Model Development*, 15(16):6285–6310.

Brewer, A. W. (1949). Evidence for a world circulation provided by the measurements of helium and water vapour distribution in the stratosphere. *Quarterly Journal of the Royal Meteorological Society*, 75(326):351–363.

Brown, F., Marshall, L., Haynes, P. H., Garcia, R. R., Birner, T., and Schmidt, A. (2023). On the magnitude and sensitivity of the quasi-biennial oscillation response to a tropical volcanic eruption. *Atmospheric Chemistry and Physics*, 23(9):5335–5353.

Brown, H. Y., Wagman, B., Bull, D., Peterson, K., Hillman, B., Liu, X., Ke, Z., and Lin, L. (2024). Validating a microphysical prognostic stratospheric aerosol implementation in E3SMv2 using observations after the Mount Pinatubo eruption. *Geoscientific Model Development*, 17(13):5087–5121.

Bull, D., Peterson, K., Tezaur, I., Shand, L., Swiler, L., Salinger, A., Cook, B., and Leland, R. (2025). CLDERA Grand Challenge. Available at: https://www.sandia.gov/cldera/.

Burger, M., Wentz, J., and Horton, R. (2020). The Law and Science of Climate Change Attribution. *Columbia Journal of Environmental Law*, 45(1).

Butchart, N. (2014). The Brewer-Dobson circulation. *Reviews of Geophysics*, 52(2):157–184.

Butchart, N. (2022). The stratosphere: a review of the dynamics and variability. *Weather and Climate Dynamics*, 3(4):1237–1272.

Butler, A. H., Thompson, D. W. J., and Heikes, R. (2010). The Steady-State Atmospheric Circulation Response to Climate Change–like Thermal Forcings in a Simple General Circulation Model. *Journal of Climate*, 23(13):3474–3496.

Calvin, K., Dasgupta, D., Krinner, G., Mukherji, A., Thorne, P. W., Trisos, C., Romero, J., Aldunce, P., Barrett, K., Blanco, G., Cheung, W. W., Connors, S., Denton, F., Diongue-Niang, A., Dodman, D., Garschagen, M., Geden, O., Hayward, B., Jones, C., Jotzo, F., Krug, T., Lasco, R., Lee, Y.-Y., Masson-Delmotte, V., Meinshausen, M., Mintenbeck, K., Mokssit, A., Otto, F. E., Pathak, M., Pirani, A., Poloczanska, E., Pörtner, H.-O., Revi, A., Roberts, D. C., Roy, J., Ruane, A. C., Skea, J., Shukla, P. R., Slade, R., Slangen, A., Sokona, Y., Sörensson, A. A., Tignor, M., Van Vuuren, D., Wei, Y.-M., Winkler, H., Zhai, P., Zommers, Z., Hourcade, J.-C., Johnson, F. X., Pachauri, S., Simpson, N. P., Singh, C., Thomas, A., Totin, E., Arias, P., Bustamante, M., Elgizouli, I., Flato, G., Howden, M., Méndez-Vallejo, C., Pereira, J. J., Pichs-Madruga, R., Rose, S. K., Saheb, Y., Sánchez Rodríguez, R., Ürge Vorsatz, D., Xiao, C., Yassaa, N., Alegría, A., Armour, K., Bednar-Friedl, B., Blok, K., Cissé, G., Dentener, F., Eriksen, S., Fischer, E., Garner, G., Guivarch, C., Haasnoot, M., Hansen, G., Hauser, M., Hawkins, E., Hermans, T.,

Kopp, R., Leprince-Ringuet, N., Lewis, J., Ley, D., Ludden, C., Niamir, L., Nicholls, Z., Some, S., Szopa, S., Trewin, B., Van Der Wijst, K.-I., Winter, G., Witting, M., Birt, A., Ha, M., Romero, J., Kim, J., Haites, E. F., Jung, Y., Stavins, R., Birt, A., Ha, M., Orendain, D. J. A., Ignon, L., Park, S., Park, Y., Reisinger, A., Cammaramo, D., Fischlin, A., Fuglestvedt, J. S., Hansen, G., Ludden, C., Masson-Delmotte, V., Matthews, J. R., Mintenbeck, K., Pirani, A., Poloczanska, E., Leprince-Ringuet, N., and Péan, C. (2023). IPCC, 2023: Climate Change 2023: Synthesis Report. Contribution of Working Groups I, II and III to the Sixth Assessment Report of the Intergovernmental Panel on Climate Change [Core Writing Team, H. Lee and J. Romero (eds.)]. IPCC, Geneva, Switzerland. Technical report, Intergovernmental Panel on Climate Change (IPCC). Edition: First.

Casadevall, T. J. (1991). Aerial view to the south of Pinatubo crater.

Chabrillat, S., Vigouroux, C., Christophe, Y., Engel, A., Errera, Q., Minganti, D., Monge-Sanz, B. M., Segers, A., and Mahieu, E. (2018). Comparison of mean age of air in five reanalyses using the BASCOE transport model. *Atmospheric Chemistry and Physics*, 18(19):14715–14735.

Charney, J. G. and Drazin, P. G. (1961). Propagation of planetary-scale disturbances from the lower into the upper atmosphere. *Journal of Geophysical Research (1896-1977)*, 66(1):83–109.

Christiansen, B. (2008). Volcanic Eruptions, Large-Scale Modes in the Northern Hemisphere, and the El Niño–Southern Oscillation. *Journal of Climate*, 21(5):910–922.

Clyne, M., Lamarque, J.-F., Mills, M. J., Khodri, M., Ball, W., Bekki, S., Dhomse, S. S., Lebas, N., Mann, G., Marshall, L., Niemeier, U., Poulain, V., Robock, A., Rozanov, E., Schmidt, A., Stenke, A., Sukhodolov, T., Timmreck, C., Toohey, M., Tummon, F., Zanchettin, D., Zhu, Y., and Toon, O. B. (2021). Model physics and chemistry causing intermodel disagreement within the VolMIP-Tambora Interactive Stratospheric Aerosol ensemble. *Atmospheric Chemistry and Physics*, 21(5):3317–3343.

Cook, K. H. (2003). Role of Continents in Driving the Hadley Cells. *Journal of the Atmospheric Sciences*, 60(7):957–976.

Crutzen, P. J. (2006). Albedo Enhancement by Stratospheric Sulfur Injections: A Contribution to Resolve a Policy Dilemma? *Climatic Change*, 77(3):211.

DallaSanta, K., Gerber, E. P., and Toohey, M. (2019). The Circulation Response to Volcanic Eruptions: The Key Roles of Stratospheric Warming and Eddy Interactions. *Journal of Climate*, 32(4):1101–1120.

DallaSanta, K., Orbe, C., Rind, D., Nazarenko, L., and Jonas, J. (2021). Response of the Quasi-Biennial Oscillation to Historical Volcanic Eruptions. *Geophysical Research Letters*, 48(20):e2021GL095412.

Danabasoglu, G., Lamarque, J.-F., Bacmeister, J., Bailey, D. A., DuVivier, A. K., Edwards, J., Emmons, L. K., Fasullo, J., Garcia, R., Gettelman, A., Hannay, C., Holland, M. M.,

Large, W. G., Lauritzen, P. H., Lawrence, D. M., Lenaerts, J. T. M., Lindsay, K., Lipscomb, W. H., Mills, M. J., Neale, R., Oleson, K. W., Otto-Bliesner, B., Phillips, A. S., Sacks, W., Tilmes, S., Kampenhout, L. v., Vertenstein, M., Bertini, A., Dennis, J., Deser, C., Fischer, C., Fox-Kemper, B., Kay, J. E., Kinnison, D., Kushner, P. J., Larson, V. E., Long, M. C., Mickelson, S., Moore, J. K., Nienhouse, E., Polvani, L., Rasch, P. J., and Strand, W. G. (2020). The Community Earth System Model Version 2 (CESM2). *Journal of Advances in Modeling Earth Systems*, 12(2):e2019MS001916.

Davis, N. A., Visioni, D., Garcia, R. R., Kinnison, D. E., Marsh, D. R., Mills, M., Richter, J. H., Tilmes, S., Bardeen, C. G., Gettelman, A., Glanville, A. A., MacMartin, D. G., Smith, A. K., and Vitt, F. (2023). Climate, Variability, and Climate Sensitivity of "Middle Atmosphere" Chemistry Configurations of the Community Earth System Model Version 2, Whole Atmosphere Community Climate Model Version 6 (CESM2(WACCM6)). *Journal of Advances in Modeling Earth Systems*, 15(9):e2022MS003579.

Defant, M. J., Jacques, D., Maury, R. C., de Boer, J., and Joron, J.-L. (1989). Geochemistry and tectonic setting of the Luzon arc, Philippines. *Geological Society of America Bulletin*, 101:663–672. ADS Bibcode: 1989GSAB..101..663D.

Dietmüller, S., Garny, H., Plöger, F., Jöckel, P., and Cai, D. (2017). Effects of mixing on resolved and unresolved scales on stratospheric age of air. *Atmospheric Chemistry and Physics*, 17(12):7703–7719.

Dobson, G. M. B. (1956). Origin and distribution of the polyatomic molecules in the atmosphere. *Proceedings of the Royal Society of London. Series A. Mathematical and Physical Sciences*, 236(1205):187–193.

Driscoll, S., Bozzo, A., Gray, L. J., Robock, A., and Stenchikov, G. (2012). Coupled Model Intercomparison Project 5 (CMIP5) simulations of climate following volcanic eruptions. *Journal of Geophysical Research: Atmospheres*, 117(D17).

Dunkerton, T., Hsu, C.-P. F., and McIntyre, M. E. (1981). Some Eulerian and Lagrangian Diagnostics for a Model Stratospheric Warming. *Journal of the Atmospheric Sciences*, 38(4):819–844.

Dunkerton, T. J. (1983). Modification of stratospheric circulation by trace constituent changes? *Journal of Geophysical Research: Oceans*, 88(C15):10831–10836.

Dunkerton, T. J. (1997). The role of gravity waves in the quasi-biennial oscillation. *Journal of Geophysical Research: Atmospheres*, 102(D22):26053–26076.

Dutton, E. G. and Christy, J. R. (1992). Solar radiative forcing at selected locations and evidence for global lower tropospheric cooling following the eruptions of El Chichón and Pinatubo. *Geophysical Research Letters*, 19(23):2313–2316.

Díaz-Durán, A., Serrano, E., Ayarzagüena, B., Abalos, M., and de la Cámara, A. (2017). Intra-seasonal variability of extreme boreal stratospheric polar vortex events and their precursors. *Climate Dynamics*, 49:3473–3491.

Edmon, H. J., Hoskins, B. J., and McIntyre, M. E. (1980). Eliassen-Palm Cross Sections for the Troposphere. *Journal of the Atmospheric Sciences*, 37(12):2600–2616.

Ehrmann, T., Wagman, B., Bull, D., Hillman, B., and Hollowed, J. (2024). Identifying Northern Hemisphere Stratospheric and Surface Temperature Responses to the Mt. Pinatubo Eruption within E3SMv2-SPA. Technical Report SAND2024-12730, Sandia National Laboratories.

Eluszkiewicz, J., Crisp, D., Zurek, R., Elson, L., Fishbein, E., Froidevaux, L., Waters, J., Grainger, R. G., Lambert, A., Harwood, R., and Peckham, G. (1996). Residual Circulation in the Stratosphere and Lower Mesosphere as Diagnosed from Microwave Limb Sounder Data. *Journal of the Atmospheric Sciences*, 53(2):217–240.

Eyring, V., Lamarque, J.-F., Hess, P., Arfeuille, F., Bowman, K., Duncan, B., Fiore, A., Gettelman, A., Giorgetta, M. A., Granier, C., Hegglin, M., Kinnison, D., Kunze, M., Langematz, U., Luo, B., Martin, R., Matthes, K., Newman, P. A., Peter, T., Robock, A., Ryerson, T., Saiz-Lopez, A., Salawitch, R., Schultz, M., Shepherd, T. G., Shindell, D., Staehelin, J., Thomason, L., Tilmes, S., Vernier, J.-P., Waugh, D. W., and Young, P. J. (2013). Overview of IGAC/SPARC Chemistry-Climate Model Initiative (CCMI) Community Simulations in Support of Upcoming Ozone and Climate Assessments. *SPARC Newsletter*, 40:48–66.

Fasullo, J. T., Caron, J. M., Phillips, A., Li, H., Richter, J. H., Neale, R. B., Rosenbloom, N., Strand, G., Glanville, S., Li, Y., Lehner, F., Meehl, G., Golaz, J.-C., Ullrich, P., Lee, J., and Arblaster, J. (2024). Modes of Variability in E3SM and CESM Large Ensembles. *Journal of Climate*, 37(8):2629–2653.

Fisher, B. L., Krotkov, N. A., Bhartia, P. K., Li, C., Carn, S. A., Hughes, E., and Leonard, P. J. T. (2019). A new discrete wavelength backscattered ultraviolet algorithm for consistent volcanic SO2 retrievals from multiple satellite missions. *Atmospheric Measurement Techniques*, 12(9):5137–5153.

Fleming, E. L., Chandra, S., Barnett, J. J., and Corney, M. (1990). Zonal mean temperature, pressure, zonal wind and geopotential height as functions of latitude. *Advances in Space Research*, 10(12):11–59.

Foucar, J. G., Salinger, A. G., and Deakin, M. (2017). CIME, Common Infrastructure for Modeling the Earth v. 5.0. Technical Report CIME, Sandia National Lab. (SNL-NM), Albuquerque, NM (United States).

Frazer, M. E. and Ming, Y. (2022). Understanding Controlling Factors of Extratropical Humidity and Clouds with an Idealized General Circulation Model. *Journal of Climate*, 35(16):5321–5337.

Frierson, D. M. W., Held, I. M., and Zurita-Gotor, P. (2006). A Gray-Radiation Aquaplanet Moist GCM. Part I: Static Stability and Eddy Scale. *Journal of the Atmospheric Sciences*, 63(10):2548–2566.

Fujiwara, M., Manney, G. L., Gray, L. J., and Wright, J. S. E. (2022). SPARC Reanalysis Intercomparison Project (S-RIP) Final Report. *SPARC Report No. 10, WCRP-6/2021*.

Fulton, D. J. and Hegerl, G. C. (2021). Testing Methods of Pattern Extraction for Climate Data Using Synthetic Modes. *Journal of Climate*, 34(18):7645–7660.

Fyfe, J. C., von Salzen, K., Cole, J. N. S., Gillett, N. P., and Vernier, J.-P. (2013). Surface response to stratospheric aerosol changes in a coupled atmosphere–ocean model. *Geophysical Research Letters*, 40(3):584–588.

Gao, C., Robock, A., and Ammann, C. (2008). Volcanic forcing of climate over the past 1500 years: An improved ice core-based index for climate models. *Journal of Geophysical Research: Atmospheres*, 113(D23).

Garcia, R. R., Marsh, D. R., Kinnison, D. E., Boville, B. A., and Sassi, F. (2007). Simulation of secular trends in the middle atmosphere, 1950–2003. *Journal of Geophysical Research: Atmospheres*, 112(D9).

Garcia, R. R., Randel, W. J., and Kinnison, D. E. (2011). On the Determination of Age of Air Trends from Atmospheric Trace Species. *Journal of the Atmospheric Sciences*, 68(1):139–154.

Garfinkel, C. I., Aquila, V., Waugh, D. W., and Oman, L. D. (2017). Time-varying changes in the simulated structure of the Brewer–Dobson Circulation. *Atmospheric Chemistry and Physics*, 17(2):1313–1327.

Garny, H., Birner, T., Bönisch, H., and Bunzel, F. (2014). The effects of mixing on age of air. *Journal of Geophysical Research: Atmospheres*, 119(12):7015–7034.

Gelaro, R., McCarty, W., Suárez, M. J., Todling, R., Molod, A., Takacs, L., Randles, C. A., Darmenov, A., Bosilovich, M. G., Reichle, R., Wargan, K., Coy, L., Cullather, R., Draper, C., Akella, S., Buchard, V., Conaty, A., Silva, A. M. d., Gu, W., Kim, G.-K., Koster, R., Lucchesi, R., Merkova, D., Nielsen, J. E., Partyka, G., Pawson, S., Putman, W., Rienecker, M., Schubert, S. D., Sienkiewicz, M., and Zhao, B. (2017). The Modern-Era Retrospective Analysis for Research and Applications, Version 2 (MERRA-2). *Journal of Climate*, 30(14):5419–5454.

Gerber, E. P. (2012). Stratospheric versus Tropospheric Control of the Strength and Structure of the Brewer–Dobson Circulation. *Journal of the Atmospheric Sciences*, 69(9):2857–2877.

Gerber, E. P. and Manzini, E. (2016). The Dynamics and Variability Model Intercomparison Project (DynVarMIP) for CMIP6: assessing the stratosphere–troposphere system. *Geoscientific Model Development*, 9(9):3413–3425.

Gerber, E. P. and Polvani, L. M. (2009). Stratosphere–Troposphere Coupling in a Relatively Simple AGCM: The Importance of Stratospheric Variability. *Journal of Climate*, 22(8):1920–1933.

Gerber, E. P., Voronin, S., and Polvani, L. M. (2008). Testing the Annular Mode Autocorrelation Time Scale in Simple Atmospheric General Circulation Models. *Monthly Weather Review*, 136(4):1523–1536.

Golaz, J.-C., Caldwell, P. M., Van Roekel, L. P., Petersen, M. R., Tang, Q., Wolfe, J. D., Abeshu, G., Anantharaj, V., Asay-Davis, X. S., Bader, D. C., Baldwin, S. A., Bisht, G., Bogenschutz, P. A., Branstetter, M., Brunke, M. A., Brus, S. R., Burrows, S. M., Cameron-Smith, P. J., Donahue, A. S., Deakin, M., Easter, R. C., Evans, K. J., Feng, Y., Flanner, M., Foucar, J. G., Fyke, J. G., Griffin, B. M., Hannay, C., Harrop, B. E., Hoffman, M. J., Hunke, E. C., Jacob, R. L., Jacobsen, D. W., Jeffery, N., Jones, P. W., Keen, N. D., Klein, S. A., Larson, V. E., Leung, L. R., Li, H.-Y., Lin, W., Lipscomb, W. H., Ma, P.-L., Mahajan, S., Maltrud, M. E., Mametjanov, A., McClean, J. L., McCoy, R. B., Neale, R. B., Price, S. F., Qian, Y., Rasch, P. J., Reeves Eyre, J. E. J., Riley, W. J., Ringler, T. D., Roberts, A. F., Roesler, E. L., Salinger, A. G., Shaheen, Z., Shi, X., Singh, B., Tang, J., Taylor, M. A., Thornton, P. E., Turner, A. K., Veneziani, M., Wan, H., Wang, H., Wang, S., Williams, D. N., Wolfram, P. J., Worley, P. H., Xie, S., Yang, Y., Yoon, J.-H., Zelinka, M. D., Zender, C. S., Zeng, X., Zhang, C., Zhang, K., Zhang, Y., Zheng, X., Zhou, T., and Zhu, Q. (2019). The DOE E3SM Coupled Model Version 1: Overview and Evaluation at Standard Resolution. *Journal of Advances in Modeling Earth Systems*, 11(7):2089–2129.

Golaz, J.-C., Van Roekel, L. P., Zheng, X., Roberts, A. F., Wolfe, J. D., Lin, W., Bradley, A. M., Tang, Q., Maltrud, M. E., Forsyth, R. M., Zhang, C., Zhou, T., Zhang, K., Zender, C. S., Wu, M., Wang, H., Turner, A. K., Singh, B., Richter, J. H., Qin, Y., Petersen, M. R., Mametjanov, A., Ma, P.-L., Larson, V. E., Krishna, J., Keen, N. D., Jeffery, N., Hunke, E. C., Hannah, W. M., Guba, O., Griffin, B. M., Feng, Y., Engwirda, D., Di Vittorio, A. V., Dang, C., Conlon, L. M., Chen, C.-C.-J., Brunke, M. A., Bisht, G., Benedict, J. J., Asay-Davis, X. S., Zhang, Y., Zhang, M., Zeng, X., Xie, S., Wolfram, P. J., Vo, T., Veneziani, M., Tesfa, T. K., Sreepathi, S., Salinger, A. G., Reeves Eyre, J. E. J., Prather, M. J., Mahajan, S., Li, Q., Jones, P. W., Jacob, R. L., Huebler, G. W., Huang, X., Hillman, B. R., Harrop, B. E., Foucar, J. G., Fang, Y., Comeau, D. S., Caldwell, P. M., Bartoletti, T., Balaguru, K., Taylor, M. A., McCoy, R. B., Leung, L. R., and Bader, D. C. (2022). The DOE E3SM Model Version 2: Overview of the Physical Model and Initial Model Evaluation. *Journal of Advances in Modeling Earth Systems*, 14(12):e2022MS003156.

Graf, H.-F., Perlwitz, J., and Kirchner, I. (1994). Northern Hemisphere tropospheric mid-latitude circulation after violent volcanic eruptions. *Contributions to Atmospheric Physics*, 67:3–13.

Guo, S., Bluth, G. J. S., Rose, W. I., Watson, I. M., and Prata, A. J. (2004a). Re-evaluation of SO2 release of the 15 June 1991 Pinatubo eruption using ultraviolet and infrared satellite sensors. *Geochemistry, Geophysics, Geosystems*, 5(4).

Guo, S., Rose, W. I., Bluth, G. J. S., and Watson, I. M. (2004b). Particles in the great Pinatubo volcanic cloud of June 1991: The role of ice. *Geochemistry, Geophysics, Geosystems*, 5(5).

Gupta, A., Gerber, E. P., and Lauritzen, P. H. (2020). Numerical impacts on tracer transport: A proposed intercomparison test of Atmospheric General Circulation Models. *Quarterly Journal of the Royal Meteorological Society*, 146(733):3937–3964.

Gupta, A., Gerber, E. P., Plumb, R. A., and Lauritzen, P. H. (2021). Numerical Impacts on Tracer Transport: Diagnosing the Influence of Dynamical Core Formulation and Resolution on Stratospheric Transport. *Journal of the Atmospheric Sciences*, 78(11):3575–3592.

Hal Holbrook, R. W. (1993). In the Path of a Killer Volcano. ISBN: 9781578070398.

Hall, T. M. and Plumb, R. A. (1994). Age as a diagnostic of stratospheric transport. *Journal of Geophysical Research: Atmospheres*, 99(D1):1059–1070.

Hall, T. M. and Prather, M. J. (1993). Simulations of the trend and annual cycle in stratospheric CO_2. *Journal of Geophysical Research: Atmospheres*, 98(D6):10573–10581.

Hannah, W. M., Bradley, A. M., Guba, O., Tang, Q., Golaz, J.-C., and Wolfe, J. (2021). Separating Physics and Dynamics Grids for Improved Computational Efficiency in Spectral Element Earth System Models. *Journal of Advances in Modeling Earth Systems*, 13(7):e2020MS002419.

Hansen, J., Lacis, A., Ruedy, R., and Sato, M. (1992). Potential climate impact of Mount Pinatubo eruption. *Geophysical Research Letters*, 19(2):215–218.

Harris, L., Chen, X., Putman, W., Zhou, L., and Chen, J.-H. (2021). A Scientific Description of the GFDL Finite-Volume Cubed-Sphere Dynamical Core. Technical Memorandum GFDL2021001, Geophysical Fluid Dynamics Laboratory, Princeton, New Jersey.

Hegerl, G. C., Hoegh-Guldberg, O., Casassa, G., Hoerling, M., Kovats, S., Parmesan, C., Pierce, D., and Stott, P. (2010). Good Practice Guidance Paper on Detection and Attribution Related to Anthropogenic Climate Change. In *Meeting Report of the Intergovernmental Panel on Climate Change Expert Meeting on Detection and Attribution of Anthropogenic Climate Change*. IPCC Working Group I Technical Support Unit, University of Bern, Bern, Switzerland.

Heidinger, A. K., Foster, M. J., Walther, A., and Zhao, X. T. (2014). The Pathfinder Atmospheres–Extended AVHRR Climate Dataset. *Bulletin of the American Meteorological Society*, 95(6):909–922.

Held, I. M. and Suarez, M. J. (1994). A Proposal for the Intercomparison of the Dynamical Cores of Atmospheric General Circulation Models. *Bulletin of the American Meteorological Society*, 75(10):1825–1830.

Henry, M., Bednarz, E. M., and Haywood, J. (2024). How does the latitude of stratospheric aerosol injection affect the climate in UKESM1? *Atmospheric Chemistry and Physics*, 24(23):13253–13268.

Henry, M., Haywood, J., Jones, A., Dalvi, M., Wells, A., Visioni, D., Bednarz, E. M., Mac-Martin, D. G., Lee, W., and Tye, M. R. (2023). Comparison of UKESM1 and CESM2 simulations using the same multi-target stratospheric aerosol injection strategy. *Atmospheric Chemistry and Physics*, 23(20):13369–13385.

Herrington, A. R., Lauritzen, P. H., Reed, K. A., Goldhaber, S., and Eaton, B. E. (2019). Exploring a Lower-Resolution Physics Grid in CAM-SE-CSLAM. *Journal of Advances in Modeling Earth Systems*, 11(7):1894–1916.

Hollowed, J. P., Jablonowski, C., Brown, H. Y., Hillman, B. R., Bull, D. L., and Hart, J. L. (2024). HSW-V v1.0: localized injections of interactive volcanic aerosols and their climate impacts in a simple general circulation model. *Geoscientific Model Development*, 17(15):5913–5938.

Holton, J. R. and Hakim, G. J. (2013). Chapter 10 - The General Circulation. In Holton, J. R. and Hakim, G. J., editors, *An Introduction to Dynamic Meteorology (Fifth Edition)*, pages 325–375. Academic Press, Boston.

Holton, J. R. and Tan, H.-C. (1980). The Influence of the Equatorial Quasi-Biennial Oscillation on the Global Circulation at 50 mb. *Journal of the Atmospheric Sciences*, 37(10):2200–2208.

Hoskins, B. J., Yang, G.-Y., and Fonseca, R. M. (2020). The detailed dynamics of the June–August Hadley Cell. *Quarterly Journal of the Royal Meteorological Society*, 146(727):557–575.

Hourdin, F., Mauritsen, T., Gettelman, A., Golaz, J.-C., Balaji, V., Duan, Q., Folini, D., Ji, D., Klocke, D., Qian, Y., Rauser, F., Rio, C., Tomassini, L., Watanabe, M., and Williamson, D. (2017). The Art and Science of Climate Model Tuning. *Bulletin of the American Meteorological Society*, 98(3):589–602.

Hughes, O. K. and Jablonowski, C. (2023). A mountain-induced moist baroclinic wave test case for the dynamical cores of atmospheric general circulation models. *Geoscientific Model Development*, 16(22):6805–6831.

Jablonowski, C. and Williamson, D. (2011). The Pros and Cons of Diffusion, Filters and Fixers in Atmospheric General Circulation Models. In Lauritzen, P. H., Jablonowski, C., Taylor, M. A., and Nair, R. D., editors, *Numerical Techniques for Global Atmospheric Models*, volume 80 of *Lecture Notes in Computational Science and Engineering*, pages 381–493. Springer.

Jucker, M. (2021). Scaling of Eliassen-Palm flux vectors. *Atmospheric Science Letters*, 22(4):e1020.

Karami, K., Garcia, R., Jacobi, C., Richter, J. H., and Tilmes, S. (2023). The Holton–Tan mechanism under stratospheric aerosol intervention. *Atmospheric Chemistry and Physics*, 23(6):3799–3818.

Karpechko, A. Y., Gillett, N. P., Dall'Amico, M., and Gray, L. J. (2010). Southern Hemisphere atmospheric circulation response to the El Chichón and Pinatubo eruptions in coupled climate models. *Quarterly Journal of the Royal Meteorological Society*, 136(652):1813–1822.

Kinne, S., Toon, O. B., and Prather, M. J. (1992). Buffering of stratospheric circulation by changing amounts of tropical ozone a Pinatubo Case Study. *Geophysical Research Letters*, 19(19):1927–1930.

Kodera, K. (1994). Influence of volcanic eruptions on the troposphere through stratospheric dynamical processes in the northern hemisphere winter. *Journal of Geophysical Research: Atmospheres*, 99(D1):1273–1282.

Konopka, P., Ploeger, F., Tao, M., Birner, T., and Riese, M. (2015). Hemispheric asymmetries and seasonality of mean age of air in the lower stratosphere: Deep versus shallow branch of the Brewer-Dobson circulation. *Journal of Geophysical Research: Atmospheres*, 120(5):2053–2066.

Kovilakam, M., Thomason, L. W., Ernest, N., Rieger, L., Bourassa, A., and Millán, L. (2020). The Global Space-based Stratospheric Aerosol Climatology (version 2.0): 1979–2018. *Earth System Science Data*, 12(4):2607–2634.

Kremser, S., Thomason, L. W., von Hobe, M., Hermann, M., Deshler, T., Timmreck, C., Toohey, M., Stenke, A., Schwarz, J. P., Weigel, R., Fueglistaler, S., Prata, F. J., Vernier, J.-P., Schlager, H., Barnes, J. E., Antuña-Marrero, J.-C., Fairlie, D., Palm, M., Mahieu, E., Notholt, J., Rex, M., Bingen, C., Vanhellemont, F., Bourassa, A., Plane, J. M. C., Klocke, D., Carn, S. A., Clarisse, L., Trickl, T., Neely, R., James, A. D., Rieger, L., Wilson, J. C., and Meland, B. (2016). Stratospheric aerosol—Observations, processes, and impact on climate. *Reviews of Geophysics*, 54(2):278–335.

Labitzke, K. and McCormick, M. P. (1992). Stratospheric temperature increases due to Pinatubo aerosols. *Geophysical Research Letters*, 19(2):207–210.

Lauritzen, P. H., Conley, A. J., Lamarque, J.-F., Vitt, F., and Taylor, M. A. (2015). The terminator "toy" chemistry test: a simple tool to assess errors in transport schemes. *Geoscientific Model Development*, 8(5):1299–1313.

Liu, X., Ma, P.-L., Wang, H., Tilmes, S., Singh, B., Easter, R. C., Ghan, S. J., and Rasch, P. J. (2016). Description and evaluation of a new four-mode version of the Modal Aerosol Module (MAM4) within version 5.3 of the Community Atmosphere Model. *Geoscientific Model Development*, 9(2):505–522.

Lu, H., Hitchman, M. H., Gray, L. J., Anstey, J. A., and Osprey, S. M. (2020). On the role of Rossby wave breaking in the quasi-biennial modulation of the stratospheric polar vortex during boreal winter. *Quarterly Journal of the Royal Meteorological Society*, 146(729):1939–1959.

MacDonald, C. G. and Ming, Y. (2022). Tropical Intraseasonal Variability Response to Zonally Asymmetric Forcing in an Idealized Moist GCM. *Journal of Climate*, 35(24):8079–8101.

Mamalakis, A., Ebert-Uphoff, I., and Barnes, E. A. (2022). Neural Network Attribution Methods for Problems in Geoscience: A Novel Synthetic Benchmark Dataset. *Environmental Data Science*, 1:e8.

Marshall, L. R., Maters, E. C., Schmidt, A., Timmreck, C., Robock, A., and Toohey, M. (2022). Volcanic effects on climate: recent advances and future avenues. *Bulletin of Volcanology*, 84(5):54.

Matthes, K., Marsh, R., Garcia, R., Kinnison, E., Sassi, F., and Walters, S. (2010). Role of the QBO in modulating the influence of the 11 year solar cycle on the atmosphere using constant forcings. *Journal of Geophysical Research*.

McClelland, L. (1991). Global Volcanism Program Report on Pinatubo (Philippines). Technical Report 16:7, Smithsonian Institution.

McClernon, K., Goode, K., and Ries, D. (2024). A comparison of model validation approaches for echo state networks using climate model replicates. *Spatial Statistics*, 59:100813.

McCormick, M. P., Thomason, L. W., and Trepte, C. R. (1995). Atmospheric effects of the Mt Pinatubo eruption. *Nature*, 373(6513):399–404.

McCusker, K., Battisti, D., and Bitz, C. (2012). The Climate Response to Stratospheric Sulfate Injections and Implications for Addressing Climate Emergencies. *Journal of Climate*, 25:3096–3116.

Mcfarlane, N. (2011). Parameterizations: Representing key processes in climate models without resolving them. *Wiley Interdisciplinary Reviews: Climate Change*, 2.

McIntyre, M. E. and Palmer, T. N. (1984). The 'surf zone' in the stratosphere. *Journal of Atmospheric and Terrestrial Physics*, 46(9):825–849.

McNeill, V. F. (2017). Atmospheric Aerosols: Clouds, Chemistry, and Climate. *Annual Review of Chemical and Biomolecular Engineering*, 8(Volume 8, 2017):427–444. Publisher: Annual Reviews.

Mills, M. J., Richter, J. H., Tilmes, S., Kravitz, B., MacMartin, D. G., Glanville, A. A., Tribbia, J. J., Lamarque, J.-F., Vitt, F., Schmidt, A., Gettelman, A., Hannay, C., Bacmeister, J. T., and Kinnison, D. E. (2017). Radiative and Chemical Response to Interactive Stratospheric Sulfate Aerosols in Fully Coupled CESM1(WACCM). *Journal of Geophysical Research: Atmospheres*, 122(23):13,061–13,078.

Mills, M. J., Schmidt, A., Easter, R., Solomon, S., Kinnison, D. E., Ghan, S. J., Neely, R. R., Marsh, D. R., Conley, A., Bardeen, C. G., and Gettelman, A. (2016). Global volcanic aerosol properties derived from emissions, 1990–2014, using CESM1(WACCM). *Journal of Geophysical Research: Atmospheres*, 121(5):2332–2348.

Ming, Y. and Held, I. M. (2018). Modeling Water Vapor and Clouds as Passive Tracers in an Idealized GCM. *Journal of Climate*, 31(2):775–786.

Muthers, S., Kuchar, A., Stenke, A., Schmitt, J., Anet, J. G., Raible, C. C., and Stocker, T. F. (2016). Stratospheric age of air variations between 1600 and 2100. *Geophysical Research Letters*, 43(10):5409–5418.

Naeg/AFP, A. (1991). Mt. Pinatubo eruption.

National Academies of Sciences, and Medicine, E. (2021). *Reflecting Sunlight: Recommendations for Solar Geoengineering Research and Research Governance*. The National Academies Press, Washington, DC.

Neu, J. L. and Plumb, R. A. (1999). Age of air in a "leaky pipe" model of stratospheric transport. *Journal of Geophysical Research: Atmospheres*, 104(D16):19243–19255.

Office of Science and Technology Policy (OSTP) (2023). Congressionally-Mandated Report on Solar Radiation Modification | OSTP.

Oort, A. H. and Yienger, J. J. (1996). Observed Interannual Variability in the Hadley Circulation and Its Connection to ENSO. *Journal of Climate*, 9(11):2751–2767.

Petty, G. W. (2006). *A first course in atmospheric radiation*. Madison, Wis: Sundog Pub, 2nd edition.

Pikovnik, M., Zaplotnik, Z., Boljka, L., and Z, N. (2022). Metrics of the Hadley circulation strength and associated circulation trends. *Weather and Climate Dynamics*, 3(2):625–644.

Pitari, G. (1993). A Numerical Study of the Possible Perturbation of Stratospheric Dynamics Due to Pinatubo Aerosols: Implications for Tracer Transport. *Journal of the Atmospheric Sciences*, 50(15):2443–2461.

Pitari, G., Cionni, I., Di Genova, G., Visioni, D., Gandolfi, I., and Mancini, E. (2016). Impact of Stratospheric Volcanic Aerosols on Age-of-Air and Transport of Long-Lived Species. *Atmosphere*, 7(11):149.

Ploeger, F., Abalos, M., Birner, T., Konopka, P., Legras, B., Müller, R., and Riese, M. (2015a). Quantifying the effects of mixing and residual circulation on trends of stratospheric mean age of air. *Geophysical Research Letters*, 42(6):2047–2054.

Ploeger, F., Legras, B., Charlesworth, E., Yan, X., Diallo, M., Konopka, P., Birner, T., Tao, M., Engel, A., and Riese, M. (2019). How robust are stratospheric age of air trends from different reanalyses? *Atmospheric Chemistry and Physics*, 19(9):6085–6105.

Ploeger, F., Riese, M., Haenel, F., Konopka, P., Müller, R., and Stiller, G. (2015b). Variability of stratospheric mean age of air and of the local effects of residual circulation and eddy mixing. *Journal of Geophysical Research: Atmospheres*, 120(2):716–733.

Plumb, R. A. (2007). Tracer interrelationships in the stratosphere. *Reviews of Geophysics*, 45(4).

Polvani, L. M., Banerjee, A., and Schmidt, A. (2019). Northern Hemisphere continental winter warming following the 1991 Mt. Pinatubo eruption: reconciling models and observations. *Atmospheric Chemistry and Physics*, 19(9):6351–6366. Publisher: Copernicus GmbH.

Polvani, L. M. and Kushner, P. J. (2002). Tropospheric response to stratospheric perturbations in a relatively simple general circulation model. *Geophysical Research Letters*, 29(7):18–1–18–4.

Ramachandran, S., Ramaswamy, V., Stenchikov, G. L., and Robock, A. (2000). Radiative impact of the Mount Pinatubo volcanic eruption: Lower stratospheric response. *Journal of Geophysical Research: Atmospheres*, 105(D19):24409–24429.

Randall, D. (2010). The Evolution of Complexity In General Circulation Models.

Reed, K. A. and Jablonowski, C. (2012). Idealized tropical cyclone simulations of intermediate complexity: A test case for AGCMs. *Journal of Advances in Modeling Earth Systems*, 4(2).

Richter, J. H., Tilmes, S., Mills, M. J., Tribbia, J. J., Kravitz, B., MacMartin, D. G., Vitt, F., and Lamarque, J.-F. (2017). Stratospheric Dynamical Response and Ozone Feedbacks in the Presence of SO2 Injections. *Journal of Geophysical Research: Atmospheres*, 122(23):12,557–12,573.

Richter, J. H., Visioni, D., MacMartin, D. G., Bailey, D. A., Rosenbloom, N., Dobbins, B., Lee, W. R., Tye, M., and Lamarque, J.-F. (2022). Assessing Responses and Impacts of Solar climate intervention on the Earth system with stratospheric aerosol injection (ARISE-SAI): protocol and initial results from the first simulations. *Geoscientific Model Development*, 15(22):8221–8243.

Rieger, L. A., Cole, J. N. S., Fyfe, J. C., Po-Chedley, S., Cameron-Smith, P. J., Durack, P. J., Gillett, N. P., and Tang, Q. (2020). Quantifying CanESM5 and EAMv1 sensitivities to Mt. Pinatubo volcanic forcing for the CMIP6 historical experiment. *Geoscientific Model Development*, 13(10):4831–4843.

Robock, A. (2000). Volcanic Eruptions and Climate. *Reviews of Geophysics*, 38:191–219.

Robock, A. (2002). The Climatic Aftermath. *Science*, 295(5558):1242–1244.

Rosen, J. M. (1971). The Boiling Point of Stratospheric Aerosols. *Journal of Applied Meteorology and Climatology*, 10(5):1044–1046.

Rudolph, D. K. and Guard, C. P. (1995). 1991 Annual Tropical Cyclone Report. Technical report, Naval Oceanography Command Center, Joint Typhoon Warning Center, San Francisco.

Sato, M., Hansen, J. E., McCormick, M. P., and Pollack, J. B. (1993). Stratospheric aerosol optical depths, 1850–1990. *Journal of Geophysical Research: Atmospheres*, 98(D12):22987–22994.

Scaife, A. A., Baldwin, M. P., Butler, A. H., Charlton-Perez, A. J., Domeisen, D. I. V., Garfinkel, C. I., Hardiman, S. C., Haynes, P., Karpechko, A. Y., Lim, E.-P., Noguchi, S., Perlwitz, J., Polvani, L., Richter, J. H., Scinocca, J., Sigmond, M., Shepherd, T. G., Son, S.-W., and Thompson, D. W. J. (2022). Long-range prediction and the stratosphere. *Atmospheric Chemistry and Physics*, 22(4):2601–2623.

Schneider, T. (2006). The General Circulation of the Atmosphere. *Annual Review of Earth and Planetary Sciences*, 34:655–688.

Schneider, T., Bischoff, T., and Haug, G. H. (2014). Migrations and dynamics of the intertropical convergence zone. *Nature*, 513(7516):45–53.

Schurer, A., Hegerl, G., Mann, M., Tett, S., and Phipps, S. (2013). Separating Forced from Chaotic Climate Variability over the Past Millennium. *Journal of Climate*, 26:6954–6973.

Self, S., Zhao, J.-X., Holasek, R. E., Torres, R. C., King, A. J., Zhao, J.-X., Holasek, R. E., Torres, R. C., and King, A. J. (1997). The Atmospheric Impact of the 1991 Mount Pinatubo Eruption. In Newhall, C. G. and Punongbayan, R. S., editors, *Fire and Mud: Eruptions and Lahars of Mount Pinatubo, Philippines*. Philippine Institute of Volcanology and Seismology and University of Washington Press.

Sheng, J.-X., Weisenstein, D. K., Luo, B.-P., Rozanov, E., Arfeuille, F., and Peter, T. (2015). A perturbed parameter model ensemble to investigate Mt. Pinatubo's 1991 initial sulfur mass emission. *Atmospheric Chemistry and Physics*, 15(20):11501–11512.

Shepherd, J. and Rayner, S. (2009). Geoengineering the climate: science, governance and uncertainty. Technical report, Royal Society of London. Available online at: https://royalsociety.org/news-resources/publications/2009/geoengineering-climate/.

Sheshadri, A., Plumb, R. A., and Gerber, E. P. (2015). Seasonal Variability of the Polar Stratospheric Vortex in an Idealized AGCM with Varying Tropospheric Wave Forcing. *Journal of the Atmospheric Sciences*, 72(6):2248–2266.

Sierra, A. (2023). Lake Pinatubo from above.

Simpson, I. R., Tilmes, S., Richter, J. H., Kravitz, B., MacMartin, D. G., Mills, M. J., Fasullo, J. T., and Pendergrass, A. G. (2019). The Regional Hydroclimate Response to Stratospheric Sulfate Geoengineering and the Role of Stratospheric Heating. *Journal of Geophysical Research: Atmospheres*, 124(23):12587–12616.

Stenchikov, G., Hamilton, K., Stouffer, R. J., Robock, A., Ramaswamy, V., Santer, B., and Graf, H.-F. (2006). Arctic Oscillation response to volcanic eruptions in the IPCC AR4 climate models. *Journal of Geophysical Research: Atmospheres*, 111(D7).

Stenchikov, G., Kirchner, I., Robock, A., Graf, H.-F., Antuña-Marrero, J. C., Grainger, R., Lambert, A., and Thomason, L. (1998). Radiative forcing from the 1991 Mount Pinatubo volcanic eruption. *Journal of Geophysical Research*, 1031:13837–13858.

Stenchikov, G., Robock, A., Ramaswamy, V., Schwarzkopf, M. D., Hamilton, K., and Ramachandran, S. (2002). Arctic Oscillation response to the 1991 Mount Pinatubo eruption: Effects of volcanic aerosols and ozone depletion. *Journal of Geophysical Research: Atmospheres*, 107(D24):ACL 28–1–ACL 28–16.

Stenchikov, G., Ukhov, A., Osipov, S., Ahmadov, R., Grell, G., Cady-Pereira, K., Mlawer, E., and Iacono, M. (2021). How Does a Pinatubo-Size Volcanic Cloud Reach the Middle Stratosphere? *Journal of Geophysical Research: Atmospheres*, 126(10):e2020JD033829.

Taylor, K. E., Stouffer, R. J., and Meehl, G. A. (2012). An Overview of CMIP5 and the Experiment Design. *Bulletin of the American Meteorological Society*, 93(4):485–498.

Taylor, M. A., Guba, O., Steyer, A., Ullrich, P. A., Hall, D. M., and Eldred, C. (2020). An Energy Consistent Discretization of the Nonhydrostatic Equations in Primitive Variables. *Journal of Advances in Modeling Earth Systems*, 12(1):e2019MS001783.

Thatcher, D. R. and Jablonowski, C. (2016). A moist aquaplanet variant of the Held–Suarez test for atmospheric model dynamical cores. *Geoscientific Model Development*, 9(4):1263–1292.

Thomas, M. A., Giorgetta, M. A., Timmreck, C., Graf, H.-F., and Stenchikov, G. (2009). Simulation of the climate impact of Mt. Pinatubo eruption using ECHAM5 – Part 2: Sensitivity to the phase of the QBO and ENSO. *Atmospheric Chemistry and Physics*, 9(9):3001–3009.

Thomason, L. W., Ernest, N., Millán, L., Rieger, L., Bourassa, A., Vernier, J.-P., Manney, G., Luo, B., Arfeuille, F., and Peter, T. (2018). A global space-based stratospheric aerosol climatology: 1979–2016. *Earth System Science Data*, 10(1):469–492.

Tilmes, S., Richter, J. H., Kravitz, B., MacMartin, D. G., Mills, M. J., Simpson, I. R., Glanville, A. S., Fasullo, J. T., Phillips, A. S., Lamarque, J.-F., Tribbia, J., Edwards, J., Mickelson, S., and Ghosh, S. (2018). CESM1(WACCM) Stratospheric Aerosol Geoengineering Large Ensemble Project. *Bulletin of the American Meteorological Society*, 99(11):2361–2371.

Tilmes, S., Richter, J. H., Mills, M. J., Kravitz, B., MacMartin, D. G., Vitt, F., Tribbia, J. J., and Lamarque, J.-F. (2017). Sensitivity of Aerosol Distribution and Climate Response to Stratospheric SO2 Injection Locations. *Journal of Geophysical Research: Atmospheres*, 122(23):12,591–12,615.

Timmreck, C. (2012). Modeling the climatic effects of large explosive volcanic eruptions. *WIREs Climate Change*, 3(6):545–564.

Toohey, M., Krüger, K., Bittner, M., Timmreck, C., and Schmidt, H. (2014). The impact of volcanic aerosol on the Northern Hemisphere stratospheric polar vortex: mechanisms and sensitivity to forcing structure. *Atmospheric Chemistry and Physics*, 14(23):13063–13079.

Toohey, M., Krüger, K., Niemeier, U., and Timmreck, C. (2011). The influence of eruption season on the global aerosol evolution and radiative impact of tropical volcanic eruptions. *Atmospheric Chemistry and Physics*, 11(23):12351–12367.

Toohey, M., Stevens, B., Schmidt, H., and Timmreck, C. (2016). Easy Volcanic Aerosol (EVA v1.0): an idealized forcing generator for climate simulations. *Geoscientific Model Development*, 9(11):4049–4070.

Waugh, D. and Hall, T. (2002). Age Of Stratospheric Air: Theory, Observations, And Models: Age Of Stratospheric Air. *Reviews of Geophysics*, 40(4):1–1–1–26.

Williamson, D. (2007). The Evolution of Dynamical Cores for Global Atmospheric Models. *J. Royal Met. Soc. Japan*, 85B:241–269.

Williamson, D., Olson, J. G., and Boville, B. A. (1998). A Comparison of Semi-Lagrangian and Eulerian Tropical Climate Simulations. *Monthly Weather Review*, 126(4):1001–1012.

Wolfe, E. W. and Hoblitt, R. P. (1997). Overview of the Eruptions. In *Fire and Mud: Eruptions and Lahars of Mount Pinatubo, Philippines*. Philippine Institute of Volcanology and Seismology and University of Washington Press.

Yao, W. and Jablonowski, C. (2016). The Impact of GCM Dynamical Cores on Idealized Sudden Stratospheric Warmings and Their QBO Interactions. *Journal of the Atmospheric Sciences*, 73(9):3397–3421.

Yu, W., Hannah, W. M., Benedict, J. J., Chen, C.-C., and Richter, J. H. (2024). Improving the QBO Forcing by Resolved Waves with Vertical Grid Refinement in E3SMv2. *ESSS Open Archive*.

Yue, G. K., Poole, L. R., Wang, P.-H., and Chiou, E. W. (1994). Stratospheric aerosol acidity, density, and refractive index deduced from SAGE II and NMC temperature data. *Journal of Geophysical Research: Atmospheres*, 99(D2):3727–3738.

Zanchettin, D., Khodri, M., Timmreck, C., Toohey, M., Schmidt, A., Gerber, E. P., Hegerl, G., Robock, A., Pausata, F. S. R., Ball, W. T., Bauer, S. E., Bekki, S., Dhomse, S. S., LeGrande, A. N., Mann, G. W., Marshall, L., Mills, M., Marchand, M., Niemeier, U., Poulain, V., Rozanov, E., Rubino, A., Stenke, A., Tsigaridis, K., and Tummon, F. (2016). The Model Intercomparison Project on the climatic response to Volcanic forcing (VolMIP): experimental design and forcing input data for CMIP6. *Geoscientific Model Development*, 9(8):2701–2719.

Zhao, T. X.-P., Chan, P. K., and Heidinger, A. K. (2013). A global survey of the effect of cloud contamination on the aerosol optical thickness and its long-term trend derived from operational AVHRR satellite observations. *Journal of Geophysical Research: Atmospheres*, 118(7):2849–2857.